

DEVELOPMENT OF A THERMODYNAMIC MODEL FOR THE PURIFICATION OF 1-HEXENE

by

Ranjeetha Hirawan [BSc. Eng]

Submitted in fulfilment of the academic requirements for the degree Master of Science in Chemical Engineering, University of KwaZulu-Natal, Durban 2007. All the work presented in this dissertation is original unless otherwise stated and has not (in whole or part) been submitted previously to any tertiary institute as part of a degree.

As the candidate's supervisor, I approve this dissertation for submission

Prof. D Ramjugernath

As the candidate's co-supervisor, I approve this dissertation for submission

Prof. JD Raal

The financial assistance of the National Research Foundation (NRF) towards this research is hereby acknowledged. Opinions expressed and conclusions arrived at, are those of the author and not necessarily to be attributed to the NRF.

ABSTRACT

The South African based petrochemical company, SASOL, operates three large plants for the recovery and purification of the chemical 1-hexene. The thermodynamic models available in commercial simulation packages fail to predict or correlate the plant data presently observed by SASOL. The focus of this project is the accrument of comprehensive and accurate modelling parameters that would assist SASOL in optimizing the operation of the three plants and meet their purity specifications.

The experimental requirements of the project are the measurement of isothermal vapour-liquid equilibrium (VLE) data for selected binary systems, using a dynamic still. The binary systems investigated were 1-hexene + n-methylpyrrolidone (NMP) at 40, 62 and 90 °C, water + NMP at 70, 90 and 107 °C and 1-hexene + 3methylcyclopentene (3MCP) at 40, 50 and 60 °C.

With respect to the modelling of the VLE data, the combined (γ - ϕ) and direct (ϕ - ϕ) regression procedures were utilized. The results of the analysis show the combined method as the more flexible of the two, when used for low pressure systems.

The excess Gibbs energy correlations investigated were the Margules, Van Laar, Wilson, NRTL and UNIQUAC. The NRTL and Van Laar models dominated the

modelling results across the range of temperatures for each binary system and for both the direct and combined methods of data regression.

The experimental data for the systems of water (1) + NMP (2) at 107 °C and at 70 °C were compared to literature data. The first system showed excellent correlation with the literature results while the second plot at 70 °C showed a positive bias of the experimental data between x_1 of 0.3 and 0.8.

Thermodynamic consistency tests for the VLE data are also required to verify the accuracy of the data. For this project, the point and direct (Van Ness) consistency tests were used as the area test was considered as too mild. All systems passed the point and direct tests for the combined method and therefore verify the thermodynamic consistency of the experimental data. The systems failed in most cases for the direct method as the combined method is the more flexible of the two modelling methods.

ACKNOWLEDGEMENTS

I would like to acknowledge the following people for their contribution in making this project a success:

- First and foremost, my supervisors, Professor J.D Raal and Professor D. Ramjugernath for their guidance and the knowledge that they have shared.
- My peers especially Minal Soni and Prathieka Naidoo for their unfailing help and friendship.
- The technical and laboratory staff for their assistance.
- NRF for their financial contributions.
- My parents Anitha and Vishnu Hirawan, for giving me the strength and support to pursue my dreams.

TABLE OF CONTENTS

CHAPTER ONE	
INTRODUCTION.....	1
CHAPTER TWO	
REVIEW OF THE THEORETICAL THERMODYNAMIC ASPECTS OF	
PHASE EQUILIBRIA.....	3
2.1 Thermodynamic relationships and equilibrium	4
2.1.1 Equilibrium	4
2.1.2 Fugacity and activity coefficient.....	4
2.1.3 Infinite dilution activity coefficients.....	5
2.2 Analytical methods: The direct and combined methods.....	7
2.2.1 The direct method	7
2.2.2 The combined (gamma-phi) method.....	10
2.3 Activity coefficient models	11
2.3.1 The Margules equation	11
2.3.2 The Van Laar equation	14
2.3.3 The Wilson equation.....	14
2.3.4 The NRTL equation (Non-Random Two Liquid Model)	15
2.3.5 The UNIQUAC model: (Universal Quasi-Chemical Theory).....	16
2.4 Equations of state (EOS).....	17
2.4.1 Virial Equation of State	21
2.4.2 The van der Waals family of cubic equations of state.....	23
2.4.2.1 <i>The van der Waals EOS</i>	24
2.4.2.2 <i>The Soave-Redlich-Kwong (SRK) EOS</i>	25
2.4.2.3 <i>The Peng-Robinson (PR) EOS</i>	26
2.5 Mixing rules.....	29
2.6 Vapour-liquid equilibrium data reduction.....	39
2.6.1 Barkers Method.....	40
2.7 Thermodynamic consistency tests	41
2.7.1 Area test	42
2.7.2 Point test	43
2.7.3 The Direct Test	44
CHAPTER THREE	
EQUIPMENT AND PROCEDURE.....	46
3.1 Equipment	46
3.1.1 Vapour-liquid equilibrium still	47
3.2 Procedure.....	50
3.2.1 Detection of leaks	50
3.2.2 Cleaning of the VLE still.....	51
3.2.3 Calibration of the pressure sensor.....	51
3.2.4 Calibration of the temperature sensor.....	52
3.2.5 Calibration of the gas chromatographs (GCs)	52
3.2.6 Procedure to obtain isothermal or isobaric measurements	55

CHAPTER FOUR	
EXPERIMENTAL RESULTS	56
4.1 Data for Test System: Cyclohexane +Ethanol.....	56
4.2 Data for System: Water +NMP	59
4.3 Data for System: 1-Hexene +NMP	64
4.4 Data for System: 1-Hexene +3MCP	68
CHAPTER FIVE	
DISCUSSION.....	73
5.1 Chemicals.....	73
5.2 Thermodynamic Modelling.....	74
5.2.1 The Combined Method	81
5.2.2 The Direct Method: Wong-Sandler-SRK	90
5.2.3 The Direct Method: Wong-Sandler-PRSV	99
5.2.4 The Direct Method: Twu-Coon-SRK	108
5.2.5 Direct Method- Twu-Coon PRSV	117
5.3 Thermodynamic Consistency Tests.....	126
5.3.1 Thermodynamic Consistency Tests for Combined Method	127
5.4 Temperature Dependence of Thermodynamic Modelled Parameters.....	137
5.4.1 Temperature Dependence of Thermodynamic Modelled Parameter- Combined Method	127
5.5 Verification of Available Experimental Data.....	145
CHAPTER SIX	
CONCLUSION.....	147
REFERENCES.....	148
APPENDIX A	
THERMODYNAMIC RELATIONSHIPS	153
A.1 Energy Functions	153
A.2 Chemical potential	154
A.3 Fugacity.....	155
A.4 Excess Properties	156
A.5 Formulation of the Wong-Sandler Mixing Rule	157
APPENDIX B	
THERMODYNAMIC CONSISTENCY TESTS	160
B.1 Thermodynamic Consistency Tests for Wong-Sandler-SRK	160
B.2 Thermodynamic Consistency Tests for Direct Method: Wong-Sandler-PRSV.....	170
B.3 Thermodynamic Consistency Tests for Direct Method: Twu-Coon-SRK.....	179
B.4 Thermodynamic Consistency Tests for Direct Method: Twu-Coon-PRSV	189
APPENDIX C	
GAS CHROMATOGRAPH CALIBRATIONS	199

APPENDIX D
TEMPERATURE DEPENDENCE OF THERMODYNAMIC MODELLED
PARAMETERS

**D.1 Temperature Dependence of Thermodynamic Modelled Parameters-Wong
Sandler-SRK.....204**

**D.2 Temperature Dependence of Thermodynamic Modelled Parameters-Wong
Sandler-PRSV.....212**

**D.3 Temperature Dependence of Thermodynamic Modelled Parameters-Twu-
Coon-SRK.....220**

**D.4 Temperature Dependence of Thermodynamic Modelled Parameters-Twu-
Coon-PRSV.....228**

LIST OF FIGURES

Figure 2.1: Isothermal bubble pressure calculation for the direct method

Figure 2.2: Isothermal bubble pressure calculation for the combined method

Figure 3.1: Vapour-liquid equilibrium still as designed by Raal

Figure 3.2: Plot of P_{actual} vs. P_{read} on KNF pressure controller

Figure 3.3: Plot of T_{actual} of Pt-100 sensor vs. T_{read} on display

Figure 3.4: Plot of A_1/A_2 vs. x_1/x_2 for cyclohexane + ethanol

Figure 3.5: Plot of A_2/A_1 vs. x_2/x_1 for cyclohexane + ethanol

Figure 4.1: Plot of P vs. x, y for cyclohexane (1) + ethanol (2) at 50 °C

Figure 4.2: Plot of y vs. x for cyclohexane (1) + ethanol (2) at 50 °C

Figure 4.3: Plot of P vs. x, y for cyclohexane (1) + ethanol (2) at 40 kPa

Figure 4.4: Plot of y vs. x for cyclohexane (1) + ethanol (2) at 40 kPa

Figure 4.5: Plot of P vs. x, y for water (1) +NMP (2) at 70 °C

Figure 4.6: Plot of y vs. x for water (1) +NMP (2) at 70 °C

Figure 4.7: Plot of P vs. x, y for water (1) +NMP (2) at 90 °C

Figure 4.8: Plot of y vs. x for water (1)-NMP (2) at 90 °C

Figure 4.9: Plot of P vs. x, y for water (1) +NMP (2) at 107 °C

Figure 4.10: Plot of y vs. x for water (1) +NMP (2) at 107 °C

Figure 4.11: Plot of P vs. x, y for 1-hexene (1) +NMP (2) at 40 °C

Figure 4.12: Plot of y vs. x for 1-hexene (1) +NMP (2) at 40 °C

Figure 4.13: Plot of P vs. x, y for 1-hexene (1) +NMP (2) at 62 °C

Figure 4.14: Plot of y vs. x for 1-hexene (1) +NMP (2) at 62 °C

Figure 4.15: Plot of P vs. x, y for 1-hexene (1) +NMP (2) at 90 °C

Figure 4.16: Plot of y vs. x for 1-hexene (1) +NMP (2) at 90 °C

Figure 4.17: Plot of P vs. x, y for 1-hexene (1) +3MCP (2) at 40 °C

Figure 4.18: Plot of y vs. x for 1-hexene (1) +3MCP (2) at 40 °C

Figure 4.19: Plot of P vs. x, y for 1-hexene (1) +3MCP (2) at 50 °C

Figure 4.20: Plot of y vs. x for 1-hexene (1) +3MCP (2) at 50 °C

Figure 4.21: Plot of P vs. x, y for 1-hexene (1) +3MCP (2) at 60 °C

Figure 4.22: Plot of y vs. x for 1-hexene (1) +3MCP (2) at 60 °C

Figure 5. 1: Plot of P vs. x, y for NRTL fit of Water (1) + NMP (2) at 70 °C

Figure 5. 2: Plot of y vs. x for NRTL fit of Water (1) + NMP (2) at 70 °C

Figure 5. 3 Plot of P vs. x, y for NRTL fit of Water (1) + NMP (2) at 90 °C

Figure 5. 4: Plot of y vs. x for NRTL fit of Water (1) + NMP (2) at 90 °C

Figure 5. 5: Plot of P vs. x, y for NRTL fit of Water (1) + NMP (2) at 107 °C

Figure 5. 6: Plot of y vs. x for NRTL fit of Water (1) + NMP (2) at 107 °C

Figure 5. 7: Plot of P vs. x, y for NRTL fit of Hexene (1) + NMP (2) at 40 °C

Figure 5. 8: Plot of y vs. x for NRTL fit of Hexene (1) + NMP (2) at 40 °C

Figure 5. 9: Plot of P vs. x, y for NRTL fit of Hexene (1) + NMP (2) at 62 °C

Figure 5. 10: Plot of y vs. x for NRTL fit of Hexene (1) + NMP (2) at 62 °C

Figure 5. 11: Plot of P vs. x, y for NRTL fit of Hexene (1) + NMP (2) at 90 °C

Figure 5. 12: Plot of y vs. x for NRTL fit of Hexene (1) + NMP (2) at 90 °C

Figure 5. 13: Plot of P vs. x, y for NRTL fit of Hexene (1) + 3MCP (2) at 40 °C

Figure 5. 14: Plot of y vs. x for NRTL fit of Hexene (1) + 3MCP (2) at 40 °C

Figure 5. 15: Plot of P vs. x, y for NRTL fit of Hexene (1) + 3MCP (2) at 50 °C

Figure 5. 16: Plot of y vs. x for NRTL fit of Hexene (1) + 3MCP (2) at 50 °C
Figure 5. 17: Plot of P vs. x, y for NRTL fit of Hexene (1) + 3MCP (2) at 60 °C
Figure 5. 18: Plot of y vs. x for NRTL fit of Hexene (1) + 3MCP (2) at 60 °C
Figure 5. 19: Plot of P vs. x, y for Van Laar fit of Water (1) + NMP (2) at 70 °C
Figure 5. 20: Plot of y vs. x for Van Laar fit of Water (1) + NMP (2) at 70 °C
Figure 5. 21: Plot of P vs. x, y for Van Laar fit of Water (1) + NMP (2) at 90 °C
Figure 5. 22: Plot of y vs. x for Van Laar fit of Water (1) + NMP (2) at 90 °C
Figure 5. 23: Plot of P vs. x, y for Van Laar fit of Water (1) + NMP (2) at 107 °C
Figure 5. 24: Plot of y vs. x for Van Laar fit of Water (1) + NMP (2) at 107 °C
Figure 5. 25: Plot of P vs. x, y for NRTL fit of Hexene (1) + NMP (2) at 40 °C
Figure 5. 26: Plot of y vs. x for NRTL fit of Hexene (1) + NMP (2) at 40 °C
Figure 5. 27: Plot of P vs. x, y for NRTL fit of Hexene (1) + NMP (2) at 62 °C
Figure 5. 28: Plot of y vs. x for NRTL fit of Hexene (1) + NMP (2) at 62 °C
Figure 5. 29: Plot of P vs. x, y for Uniquac fit of Hexene (1) + NMP (2) at 90 °C
Figure 5. 30: Plot of y vs. x for Uniquac fit of Hexene (1) + NMP (2) at 90 °C
Figure 5. 31: Plot of P vs. x, y for Van Laar fit of Hexene (1) + 3MCP (2) at 40 °C
Figure 5. 32: Plot of y vs. x for Van Laar fit of Hexene (1) + 3MCP (2) at 40 °C
Figure 5. 33: Plot of P vs. x, y for NRTL fit of Hexene (1) + 3MCP (2) at 50 °C
Figure 5. 34: Plot of y vs. x for NRTL fit of Hexene (1) + 3MCP (2) at 50 °C
Figure 5. 35: Plot of P vs. x, y for Van Laar fit of Hexene (1) + 3MCP (2) at 60 °C
Figure 5. 36: Plot of y vs. x for Van Laar fit of Hexene (1) + 3MCP (2) at 60 °C
Figure 5. 37: Plot of P vs. x, y for Uniquac fit of Water (1) + NMP (2) at 70 °C
Figure 5. 38: Plot of y vs. x for Uniquac fit of Water (1) + NMP (2) at 70 °C
Figure 5. 39: Plot of P vs. x, y for Van Laar fit of Water (1) + NMP (2) at 90 °C
Figure 5. 40: Plot of y vs. x for Van Laar fit of Water (1) + NMP (2) at 90 °C
Figure 5. 41: Plot of P vs. x, y for Van Laar fit of Water (1) + NMP (2) at 107 °C
Figure 5. 42: Plot of y vs. x for Van Laar fit of Water (1) + NMP (2) at 107 °C
Figure 5. 43: Plot of P vs. x, y for Wilson fit of Hexene (1) + NMP (2) at 40 °C
Figure 5. 44: Plot of y vs. x for Wilson fit of Hexene (1) + NMP (2) at 40 °C
Figure 5. 45: Plot of P vs. x, y for NRTL fit of Hexene (1) + NMP (2) at 62 °C
Figure 5. 46: Plot of y vs. x for NRTL fit of Hexene (1) + NMP (2) at 62 °C
Figure 5. 47: Plot of P vs. x, y for Uniquac fit of Hexene (1) + NMP (2) at 90 °C
Figure 5. 48: Plot of y vs. x for Uniquac fit of Hexene (1) + NMP (2) at 90 °C
Figure 5. 49: Plot of P vs. x, y for NRTL fit of Hexene (1) + 3MCP (2) at 40 °C
Figure 5. 50: Plot of y vs. x for NRTL fit of Hexene (1) + 3MCP (2) at 40 °C
Figure 5. 51: Plot of P vs. x, y for Van Laar fit of Hexene (1) + 3MCP (2) at 50 °C
Figure 5. 52: Plot of y vs. x for Van Laar fit of Hexene (1) + 3MCP (2) at 50 °C
Figure 5. 53: Plot of P vs. x, y for Van Laar fit of Hexene (1) + 3MCP (2) at 60 °C
Figure 5. 54: Plot of y vs. x for Van Laar fit of Hexene (1) + 3MCP (2) at 60 °C
Figure 5. 55: Plot of P vs. x, y for NRTL fit of Water (1) + NMP (2) at 70 °C
Figure 5. 56: Plot of y vs. x for NRTL fit of Water (1) + NMP (2) at 70 °C
Figure 5. 57: Plot of P vs. x, y for NRTL fit of Water (1) + NMP (2) at 90 °C
Figure 5. 58: Plot of y vs. x for NRTL fit of Water (1) + NMP (2) at 90 °C
Figure 5. 59: Plot of P vs. x, y for NRTL fit of Water (1) + NMP (2) at 107 °C
Figure 5. 60: Plot of y vs. x for NRTL fit of Water (1) + NMP (2) at 107 °C
Figure 5. 61: Plot of P vs. x, y for NRTL fit of Hexene (1) + NMP (2) at 40 °C
Figure 5. 62: Plot of y vs. x for NRTL fit of Hexene (1) + NMP (2) at 40 °C
Figure 5. 63: Plot of P vs. x, y for Uniquac fit of Hexene (1) + NMP (2) at 62 °C
Figure 5. 64: Plot of y vs. x for Uniquac fit of Hexene (1) + NMP (2) at 62 °C
Figure 5. 65: Plot of P vs. x, y for NRTL fit of Hexene (1) + NMP (2) at 90 °C

Figure 5. 66: Plot of y vs. x for NRTL fit of Hexene (1) + NMP (2) at 90 °C
Figure 5. 67: Plot of P vs. x, y for Van Laar fit of Hexene (1) + 3MCP (2) at 40 °C
Figure 5. 68: Plot of y vs. x for Van Laar fit of Hexene (1) + 3MCP (2) at 40 °C
Figure 5. 69: Plot of P vs. x, y for Van Laar fit of Hexene (1) + 3MCP (2) at 50 °C
Figure 5. 70: Plot of y vs. x for Van Laar fit of Hexene (1) + 3MCP (2) at 50 °C
Figure 5. 71: Plot of P vs. x, y for Van Laar fit of Hexene (1) + 3MCP (2) at 60 °C
Figure 5. 72: Plot of y vs. x for Van Laar fit of Hexene (1) + 3MCP (2) at 60 °C
Figure 5. 73: Plot of P vs. x, y for NRTL fit of Water (1) + NMP (2) at 70 °C
Figure 5. 74: Plot of y vs. x for NRTL fit of Water (1) + NMP (2) at 70 °C
Figure 5. 75: Plot of P vs. x, y for NRTL fit of Water (1) + NMP (2) at 90 °C
Figure 5. 76: Plot of y vs. x for NRTL fit of Water (1) + NMP (2) at 90 °C
Figure 5. 77: Plot of P vs. x, y for NRTL fit of Water (1) + NMP (2) at 107 °C
Figure 5. 78: Plot of y vs. x for NRTL fit of Water (1) + NMP (2) at 107 °C
Figure 5. 79: Plot of P vs. x, y for NRTL fit of Hexene (1) + NMP (2) at 40 °C
Figure 5. 80: Plot of y vs. x for NRTL fit of Hexene (1) + NMP (2) at 40 °C
Figure 5. 81: Plot of P vs. x, y for Uniquac fit of Hexene (1) + NMP (2) at 62 °C
Figure 5. 82: Plot of y vs. x for Uniquac fit of Hexene (1) + NMP (2) at 62 °C
Figure 5. 83: Plot of P vs. x, y for Van Laar fit of Hexene (1) + NMP (2) at 90 °C
Figure 5. 84: Plot of y vs. x for Van Laar fit of Hexene (1) + NMP (2) at 90 °C
Figure 5. 85: Plot of P vs. x, y for NRTL fit of Hexene (1) + 3MCP (2) at 40 °C
Figure 5. 86: Plot of y vs. x for NRTL fit of Hexene (1) + 3MCP (2) at 40 °C
Figure 5. 87: Plot of P vs. x, y for Van Laar fit of Hexene (1) + 3MCP (2) at 50 °C
Figure 5. 88: Plot of y vs. x for Van Laar fit of Hexene (1) + 3MCP (2) at 50 °C
Figure 5. 89: Plot of P vs. x, y for Van Laar fit of Hexene (1) + 3MCP (2) at 60 °C
Figure 5. 90: Plot of y vs. x for Van Laar fit of Hexene (1) + 3MCP (2) at 60 °C
Figure 5. 91: Point Test for Water (1) + NMP (2) at 70 °C
Figure 5. 92: Direct Test for Water (1) + NMP (2) at 70 °C
Figure 5. 93: Point Test for Water (1) + NMP (2) at 90 °C
Figure 5. 94: Direct Test for Water (1) + NMP (2) at 90 °C
Figure 5. 95: Point Test for Water (1) + NMP (2) at 107 °C
Figure 5. 96: Direct Test for Water (1) + NMP (2) at 107 °C
Figure 5. 97: Point Test for Hexene (1) + NMP (2) at 40 °C
Figure 5. 98: Direct Test for Hexene (1) + NMP (2) at 40 °C
Figure 5. 99: Point Test for Hexene (1) + NMP (2) at 62 °C
Figure 5. 100: Direct Test for Hexene (1) + NMP (2) at 62 °C
Figure 5. 101: Point Test for Hexene (1) + NMP (2) at 90 °C
Figure 5. 102: Direct Test for Hexene (1) + NMP (2) at 90 °C
Figure 5. 103: Point Test for Hexene (1) + 3MCP (2) at 40 °C
Figure 5. 104: Direct Test for Hexene (1) + 3MCP (2) at 40 °C
Figure 5. 105: Point Test for Hexene (1) + 3MCP (2) at 50 °C
Figure 5. 106: Direct Test for Hexene (1) + 3MCP (2) at 50 °C
Figure 5. 107: Point Test for Hexene (1) + 3MCP (2) at 60 °C
Figure 5. 108: Direct Test for Hexene (1) + 3MCP (2) at 60 °C
Figure 5. 109: Plot of T vs. Van Laar modelled parameters for system 1-hexene (1) +
NMP(2)
Figure 5. 110: Plot of T vs. Uniquac modelled parameters for system 1-hexene (1) +
NMP (2)
Figure 5. 111: Plot of T vs. Wilson modelled parameters for system 1-hexene (1) +
NMP (2)

Figure 5. 112a: Plot of T vs. NRTL modelled parameters for system 1-hexene (1) + NMP (2)

Figure 5. 112b: Plot of T vs. NRTL modelled parameters for system 1-hexene (1) + NMP (2)

Figure 5. 113: Plot of T vs. Van Laar modelled parameters for system water (1) + NMP (2)

Figure 5. 114: Plot of T vs. Uniquac modelled parameters for system water (1) + NMP (2)

Figure 5. 115: Plot of T vs. Wilson modelled parameters for system water (1) + NMP (2)

Figure 5. 116a: Plot of T vs. NRTL modelled parameters for system water (1) + NMP (2)

Figure 5. 116b: Plot of T vs. NRTL modelled parameters for system water (1) + NMP (2)

Figure 5. 117a: Plot of T vs. Van Laar modelled parameters for system 1-hexene (1) + 3MCP (2)

Figure 5. 117b: Plot of T vs. Van Laar modelled parameters for system 1-hexene (1) + 3MCP (2)

Figure 5. 118: Plot of T vs. Uniquac modelled parameters for system 1-hexene (1) + 3MCP (2)

Figure 5. 119: Plot of T vs. Wilson modelled parameters for system 1-hexene (1) + 3MCP (2)

Figure 5. 120a: Plot of T vs. NRTL modelled parameters for system 1-hexene (1) + 3MCP (2)

Figure 5. 120b: Plot of T vs. NRTL modelled parameters for system 1-hexene (1) + 3MCP (2)

Figure 5. 121: Plot of P vs. x for available data of Water (1) + NMP (2) at 107 °C

Figure 5. 122: Plot of P vs. x for available data of Water (1) + NMP (2) at 70 °C

Figure B.1: Point Test for Water (1) + NMP (2) at 70 °C

Figure B.2: Direct Test for Water (1) + NMP (2) at 70 °C

Figure B.3: Point Test for Water (1) + NMP (2) at 90 °C

Figure B.4: Direct Test for Water (1) + NMP (2) at 90 °C

Figure B.5: Point Test for Water (1) + NMP (2) at 107 °C

Figure B.6: Direct Test for Water (1) + NMP (2) at 107 °C

Figure B.7: Point Test for Hexene (1) + NMP (2) at 40 °C

Figure B.8: Direct Test for Hexene (1) + NMP (2) at 40 °C

Figure B.9: Point Test for Hexene (1) + NMP (2) at 62 °C

Figure B.10: Direct Test for Hexene (1) + NMP (2) at 62 °C

Figure B.11: Point Test for Hexene (1) + NMP (2) at 90 °C

Figure B.12: Direct Test for Hexene (1) + NMP (2) at 90 °C

Figure B.13: Point Test for Hexene (1) + 3MCP (2) at 40 °C

Figure B.14: Direct Test for Hexene (1) + 3MCP (2) at 40 °C

Figure B.15: Point Test for Hexene (1) + 3MCP (2) at 50 °C

Figure B.16: Direct Test for Hexene (1) + 3MCP (2) at 50 °C

Figure B.17: Point Test for Hexene (1) + 3MCP (2) at 60 °C

Figure B.18: Direct Test for Hexene (1) + 3MCP (2) at 60 °C

Figure B.19: Point Test for Water (1) + NMP (2) at 70 °C

Figure B.20: Direct Test for Water (1) + NMP (2) at 70 °C

Figure B.21: Point Test for Water (1) + NMP (2) at 90 °C

Figure B.22: Direct Test for Water (1) + NMP (2) at 90 °C

Figure B.21: Point Test for Water (1) + NMP (2) at 90 °C
Figure B.22: Direct Test for Water (1) + NMP (2) at 90 °C
Figure B.23: Point Test for Water (1) + NMP (2) at 107 °C
Figure B.24: Direct Test for Water (1) + NMP (2) at 107 °C
Figure B.25: Point Test for Hexene (1) + NMP (2) at 40 °C
Figure B.26: Direct Test for Hexene (1) + NMP (2) at 40 °C
Figure B.27: Point Test for Hexene (1) + NMP (2) at 62 °C
Figure B.28: Direct Test for Hexene (1) + NMP (2) at 62 °C
Figure B.29: Point Test for Hexene (1) + NMP (2) at 90 °C
Figure B.30: Direct Test for Hexene (1) + NMP (2) at 90 °C
Figure B.31: Point Test for Hexene (1) + 3MCP (2) at 40 °C
Figure B.32: Direct Test for Hexene (1) + 3MCP (2) at 40 °C
Figure B.33: Point Test for Hexene (1) + 3MCP (2) at 50 °C
Figure B.34: Direct Test for Hexene (1) + 3MCP (2) at 50 °C
Figure B.35: Point Test for Hexene (1) + 3MCP (2) at 60 °C
Figure B.36: Direct Test for Hexene (1) + 3MCP (2) at 60 °C
Figure B.37: Point Test for Water (1) + NMP (2) at 70 °C
Figure B.38: Direct Test for Water (1) + NMP (2) at 70 °C
Figure B.39: Point Test for Water (1) + NMP (2) at 90 °C
Figure B.40: Direct Test for Water (1) + NMP (2) at 90 °C
Figure B.41: Point Test for Water (1) + NMP (2) at 107 °C
Figure B.42: Direct Test for Water (1) + NMP (2) at 107 °C
Figure B.43: Point Test for Hexene (1) + NMP (2) at 40 °C
Figure B.44: Direct Test for Hexene (1) + NMP (2) at 40 °C
Figure B.45: Point Test for Hexene (1) + NMP (2) at 62 °C
Figure B.46: Direct Test for Hexene (1) + NMP (2) at 62 °C
Figure B.47: Point Test for Hexene (1) + NMP (2) at 90 °C
Figure B.48: Direct Test for Hexene (1) + NMP (2) at 90 °C
Figure B.49: Point Test for Hexene (1) + 3MCP (2) at 40 °C
Figure B.50: Direct Test for Hexene (1) + 3MCP (2) at 40 °C
Figure B.51: Point Test for Hexene (1) + 3MCP (2) at 50 °C
Figure B.52: Direct Test for Hexene (1) + 3MCP (2) at 50 °C
Figure B.53: Point Test for Hexene (1) + 3MCP (2) at 60 °C
Figure B.54: Direct Test for Hexene (1) + 3MCP (2) at 60 °C
Figure B.55: Point Test for Water (1) + NMP (2) at 70 °C
Figure B.56: Direct Test for Water (1) + NMP (2) at 70 °C
Figure B.57: Point Test for Water (1) + NMP (2) at 90 °C
Figure B.58: Direct Test for Water (1) + NMP (2) at 90 °C
Figure B.59: Point Test for Water (1) + NMP (2) at 107 °C
Figure B.60: Direct Test for Water (1) + NMP (2) at 107 °C
Figure B.61: Point Test for Hexene (1) + NMP (2) at 40 °C
Figure B.62: Direct Test for Hexene (1) + NMP (2) at 40 °C
Figure B.63: Point Test for Hexene (1) + NMP (2) at 62 °C
Figure B.64: Direct Test for Hexene (1) + NMP (2) at 62 °C
Figure B.65: Point Test for Hexene (1) + NMP (2) at 90 °C
Figure B.66: Direct Test for Hexene (1) + NMP (2) at 90 °C
Figure B.67: Point Test for Hexene (1) + 3MCP (2) at 40 °C
Figure B.68: Direct Test for Hexene (1) + 3MCP (2) at 40 °C
Figure B.69: Point Test for Hexene (1) + 3MCP (2) at 50 °C
Figure B.70: Direct Test for Hexene (1) + 3MCP (2) at 50 °C

Figure B.71: Point Test for Hexene (1) + 3MCP (2) at 60 °C
Figure B.72: Direct Test for Hexene (1) + 3MCP (2) at 60 °C

Figure C.1: Plot of A_1/A_2 vs. x_1/x_2 for 1-hexene (1) + NMP (2)
Figure C.2: Plot of A_2/A_1 vs. x_2/x_1 for 1-hexene (1) + NMP (2)
Figure C.3: Plot of A_1/A_2 vs. x_1/x_2 for water (1) + NMP (2)
Figure C.4: Plot of A_2/A_1 vs. x_2/x_1 for water (1) + NMP (2)
Figure C.5: Plot of A_1/A_2 vs. x_1/x_2 for 1-hexene (1) + 3MCP (2)
Figure C.6: Plot of A_2/A_1 vs. x_2/x_1 for 1-hexene (1) + 3MCP (2)

Figure D.1: Plot of T vs. Van Laar modelled parameters for system 1-hexene (1) + NMP (2)
Figure D.2: Plot of T vs. Uniquac modelled parameters for system 1-hexene (1) + NMP (2)
Figure D.3: Plot of T vs. Wilson modelled parameters for system 1-hexene (1) + NMP (2)
Figure D.4a: Plot of T vs. NRTL modelled parameters for system 1-hexene (1) + NMP (2)
Figure D.4b: Plot of T vs. NRTL modelled parameters for system 1-hexene (1) + NMP (2)
Figure D.5: Plot of T vs. Van Laar modelled parameters for system water (1) + NMP (2)
Figure D.6: Plot of T vs. Uniquac modelled parameters for system water (1) + NMP (2)
Figure D.7: Plot of T vs. Wilson modelled parameters for system water (1) + NMP (2)
Figure D.8a: Plot of T vs. NRTL modelled parameters for system water (1) + NMP (2)
Figure D.8b: Plot of T vs. NRTL modelled parameters for system water (1) + NMP (2)
Figure D.9a: Plot of T vs. Van Laar modelled parameters for system 1-hexene (1) + 3MCP (2)
Figure D.9b: Plot of T vs. Van Laar modelled parameters for system 1-hexene (1) + 3MCP (2)
Figure D.10: Plot of T vs. Uniquac modelled parameters for system 1-hexene (1) + 3MCP (2)
Figure D.11: Plot of T vs. Wilson modelled parameters for system 1-hexene (1) + 3MCP (2)
Figure D.12a: Plot of T vs. NRTL modelled parameters for system 1-hexene (1) + 3MCP (2)
Figure D.12b: Plot of T vs. NRTL modelled parameters for system 1-hexene (1) + 3MCP (2)
Figure D.13: Plot of T vs. Van Laar modelled parameters for system 1-hexene (1) + NMP (2)
Figure D.14: Plot of T vs. Uniquac modelled parameters for system 1-hexene (1) + NMP (2)
Figure D.15: Plot of T vs. Wilson modelled parameters for system 1-hexene (1) + NMP (2)
Figure D.16a: Plot of T vs. NRTL modelled parameters for system 1-hexene (1) + NMP (2)
Figure D.16b: Plot of T vs. NRTL modelled parameters for system 1-hexene (1) + NMP (2)
Figure D.17: Plot of T vs. Van Laar modelled parameters for system water (1) + NMP (2)

Figure D.18: Plot of T vs. Uniquac modelled parameters for system water (1) + NMP (2)

Figure D.19: Plot of T vs. Wilson modelled parameters for system water (1) + NMP (2)

Figure D.20a: Plot of T vs. NRTL modelled parameters for system water (1) + NMP (2)

Figure D.20b: Plot of T vs. NRTL modelled parameters for system water (1) + NMP (2)

Figure D.21a: Plot of T vs. Van Laar modelled parameters for system 1-hexene (1) + 3MCP (2)

Figure D.21b: Plot of T vs. Van Laar modelled parameters for system 1-hexene (1) + 3MCP (2)

Figure D.22: Plot of T vs. Uniquac modelled parameters for system 1-hexene (1) + 3MCP (2)

Figure D.23: Plot of T vs. Wilson modelled parameters for system 1-hexene (1) + 3MCP (2)

Figure D.24a: Plot of T vs. NRTL modelled parameters for system 1-hexene (1) + 3MCP (2)

Figure D.24b: Plot of T vs. NRTL modelled parameters for system 1-hexene (1) + 3MCP (2)

Figure D.25: Plot of T vs. Van Laar modelled parameters for system 1-hexene (1) + NMP (2)

Figure D.26: Plot of T vs. Uniquac modelled parameters for system 1-hexene (1) + NMP (2)

Figure D.27: Plot of T vs. Wilson modelled parameters for system 1-hexene (1) + NMP (2)

Figure D.28a: Plot of T vs. NRTL modelled parameters for system 1-hexene (1) + NMP (2)

Figure D.28b: Plot of T vs. NRTL modelled parameters for system 1-hexene (1) + NMP (2)

Figure D.29: Plot of T vs. Van Laar modelled parameters for system water (1) + NMP (2)

Figure D.30: Plot of T vs. Uniquac modelled parameters for system water (1) + NMP (2)

Figure D.31: Plot of T vs. Wilson modelled parameters for system water (1) + NMP (2)

Figure D.32a: Plot of T vs. NRTL modelled parameters for system water (1) + NMP (2)

Figure D.32b: Plot of T vs. NRTL modelled parameters for system water (1) + NMP (2)

Figure D.33: Plot of T vs. Van Laar modelled parameters for system 1-hexene (1) + 3MCP (2)

Figure D.34: Plot of T vs. Uniquac modelled parameters for system 1-hexene (1) + 3MCP (2)

Figure D.35: Plot of T vs. Wilson modelled parameters for system 1-hexene (1) + 3MCP (2)

Figure D.36a: Plot of T vs. NRTL modelled parameters for system 1-hexene (1) + 3MCP (2)

Figure D.36b: Plot of T vs. NRTL modelled parameters for system 1-hexene (1) + 3MCP (2)

Figure D.37: Plot of T vs. Van Laar modelled parameters for system 1-hexene (1) + NMP (2)

Figure D.38: Plot of T vs. Uniquac modelled parameters for system 1-hexene (1) + NMP (2)

Figure D.39: Plot of T vs. Wilson modelled parameters for system 1-hexene (1) + NMP (2)

Figure D.40a: Plot of T vs. NRTL modelled parameters for system 1-hexene (1) + NMP (2)

Figure D.40b: Plot of T vs. NRTL modelled parameters for system 1-hexene (1) + NMP (2)

Figure D.41: Plot of T vs. Van Laar modelled parameters for system water (1) + NMP (2)

Figure D.42: Plot of T vs. Uniquac modelled parameters for system water (1) + NMP (2)

Figure D.43: Plot of T vs. Wilson modelled parameters for system water (1) + NMP (2)

Figure D.44a: Plot of T vs. NRTL modelled parameters for system water (1) + NMP (2)

Figure D.44b: Plot of T vs. NRTL modelled parameters for system water (1) + NMP (2)

Figure D.45: Plot of T vs. Van Laar modelled parameters for system 1-hexene (1) + 3MCP (2)

Figure D.46: Plot of T vs. Uniquac modelled parameters for system 1-hexene (1) + 3MCP (2)

Figure D.47: Plot of T vs. Wilson modelled parameters for system 1-hexene (1) + 3MCP (2)

Figure D.48a: Plot of T vs. NRTL modelled parameters for system 1-hexene (1) + 3MCP (2)

Figure D.48b: Plot of T vs. NRTL modelled parameters for system 1-hexene (1) + 3MCP (2)

Table 2.1:	Activity Coefficient Expressions for Binary Systems
Table 2.2:	Equation of State Parameters and Fugacity Coefficient Expressions
Table 2.3:	Parameters \bar{a}_i and \bar{b}_i for the mixing rules used
Table 2.4:	The Direct Test Scale
Table 3.1:	Gas chromatograph specifications and operating conditions
Table 4.1:	VLE data for cyclohexane (1) + ethanol (2) at 50 °C
Table 4.2:	VLE data for cyclohexane (1) + ethanol (2) at 40 kPa
Table 4.3:	VLE data for water (1) +NMP (2) at 70 °C
Table 4.4:	VLE data for water (1) +NMP (2) at 90 °C
Table 4.5:	VLE data for water (1) +NMP (2) at 107 °C
Table 4.6:	VLE data for 1-hexene (1) +NMP (2) at 40 °C
Table 4.7:	VLE data for 1-hexene (1) +NMP (2) at 62 °C
Table 4.8:	VLE data for 1-hexene (1) +NMP (2) at 90 °C
Table 4.9:	VLE data for 1-hexene (1) +3mcp (2) at 40 °C
Table 4.10:	VLE data for 1-hexene (1) +3mcp (2) at 50 °C
Table 4.11:	VLE data for 1-hexene (1) +3mcp (2) at 60 °C
Table 5.1:	Chemical Analysis
Table 5.2:	Pure Component Properties
Table 5.3:	Summary of the Best Fit Models
Table 5.4:	Thermodynamic modelled parameters for the Combined Method
Table 5.5:	Thermodynamic modelled parameters for the Direct Method: Wong-Sandler-SRK
Table 5.6:	Thermodynamic modelled parameters for the Direct Method: Wong-Sandler-PRSV

Table 5.6:	Thermodynamic modelled parameters for the Direct Method: Wong-Sandler-PRSV
Table 5.7:	Thermodynamic modelled parameters for the Direct Method i.e. Twu-Coon-SRK
Table 5.8:	Thermodynamic modelled parameters for the Direct Method i.e. Twu-Coon-PRSV
Table 5.9:	Direct Test Scale for the Combined Method
Table B.1:	Direct Test Scale for the Direct Method: Wong-Sandler-SRK
Table B.2:	Direct Test Scale for the Direct Method: Wong-Sandler-PRSV
Table B.3:	Direct Test Scale for the Direct Method: Twu-Coon-SRK
Table B.4:	Direct Test Scale for the Direct Method: Twu-Coon-PRSV

NOMENCLATURE

A	Helmholtz free energy
B_{ii}	Pure component second virial coefficient
B_{ij}	Cross second virial coefficient
C_P	Heat capacity at constant pressure
C_V	Heat capacity at constant volume
C_{iL}	concentration of solute in the bulk liquid phase
C_{iG}	concentration of solute in the gas bubble
$C_{i,sL}$	concentration of solute in liquid phase of the boundary layer
$C_{i,sG}$	concentration of solute in vapour phase of the boundary layer
D	Volumetric flow rate
D_{ijL}	Liquid phase diffusion coefficient
D_{ijG}	Gas phase diffusion coefficient
d_b	Diameter of the bubble
f	pure component fugacity
f_i	Fugacity of species i in solution
G	Gibbs energy
H	Enthalpy
M	Molecular mass
M_i	Partial molar property of species i in solution
m	mass
N	Number of moles of solute
n	Number of moles of solute
P	Pressure
Q	Heat

R	Universal gas constant
S	Entropy
T	Temperature
U	Internal energy
V	Molar volume
V_i	Partial Molar volume
x	liquid mole fraction
y	vapour mole fraction
Z	Compressibility factor
F	Correction term for vapour-phase non-ideality
f	Pure component fugacity coefficient
f	Fugacity coefficient of species i in solution
γ	Activity coefficient
μ	Chemical potential
ω	acentric factor
E	Excess property
$i.d.$	Property value for an ideal solution
δ	Property value at infinitely dilute concentration
$i.g.$	Property value for an ideal gas
L	Liquid phase property
R	Residual property ($M^R = M - M^{i.g.}$) refer to Section 3.5
sat	Property value at saturation
t	Total system property
V	Vapour phase property
Z	Compressibility factor

INTRODUCTION

Many age-old human activities such as brewing, soap making and alchemy involved applications of chemical engineering, however the industrial revolution (18th century to the present), necessitated George Davis, an unremarkable alkali inspector in 1880, England to actually define the scope of a chemical engineer.

At present, although chemical engineering has diversified to “engineering” on a molecular level in areas as diverse as biosensors, it was and is tailored to fulfil the needs of the chemical and petroleum industry where separation methods such as distillation, filtration, crystallization and extraction dominate. Knowledge of the thermodynamic behaviour of the systems becomes invaluable for the design and optimisation of separation processes controlled by equilibrium.

SASOL, a South African based petrochemical company currently runs three plants for the recovery and purification of 1-hexene. The thermodynamic models presently available in commercial simulation packages fail to accurately predict or correlate the plant data obtained by SASOL. The University of KwaZulu-Natal’s School of Chemical Engineering (Howard College Campus) was approached to:

- 1) Verify experimental data that is currently available.
- 2) Measure full vapour-liquid equilibrium (VLE) data sets (P-T-x-y) for the binary combinations 1-hexene + n-methylpyrrolidone (NMP), water + NMP and 1-hexene + 3-methylcyclopentene (3MCP) utilising the vapour-liquid equilibrium still as designed by Raal [Raal & Muhlbauer, 1998].
- 3) Undertake comprehensive correlations of measured data using various Gibbs excess energy models e.g. Wilson, NRTL, van Laar and Uniquac models within VLE methods such as the direct (ϕ - ϕ) and combined (γ - ϕ) methods.
- 4) Test the thermodynamic consistency of measured VLE data using consistency tests such as the point and direct tests.

REVIEW OF THE THEORETICAL THERMODYNAMIC ASPECTS OF PHASE EQUILIBRIA

The various separation processes in industry that generally involve multi-component streams require intimate knowledge of the vapour-liquid equilibrium (VLE) dynamics of the system to obtain separation of any use. The measurement of this data is expensive and time-consuming and it is therefore necessary to obtain experimental data of the highest quality. Accurate interpretation of the data is also necessary to interpolate and extrapolate the measured information to new conditions from the minimum amount of experimental data.

This chapter's intention is to provide a brief summary of the thermodynamic theory behind the data interpretation and modelling. A detailed review of thermodynamic behaviour can be found in Smith & Van Ness [1996] and Raal & *Mühlbauer* [1998]. The symbols, notation and phraseology used for the various thermodynamic properties in this review are similar to those of Smith & Van Ness [1996].

2.1 Thermodynamic relationships and equilibrium

2.1.1 Equilibrium

Thermodynamic equilibrium as defined in Appendix A.1 is represented by the equality of temperature and pressure, as well as the fugacity of component i , f_i in all phases. For a liquid and vapour phase in equilibrium:

$$\hat{f}_i^L = \hat{f}_i^V \quad (2-1)$$

Two approaches are commonly used in expressing the equality of the fugacities in VLE: the equation of state (EOS) and the gamma-phi approach. Before a discussion of these two methods are undertaken, a definition of the auxiliary functions, fugacity and activity coefficient of component i as well as the calculation procedure for infinite dilution activity coefficients, is required.

2.1.2 Fugacity and activity coefficient

The vapour phase non-ideality is represented by the fugacity coefficient and for component i in solution, is defined as:

$$\hat{\phi}_i = \frac{\hat{f}_i^V}{y_i P} \quad (2-2)$$

where, y_i represents the composition of component i in the vapour phase and P is the system pressure. Under ideal gas conditions, the fugacity coefficient equals unity. The greater the fugacity coefficient deviates from unity, the greater the system deviates from ideal gas behaviour.

The liquid phase non-ideality is represented by activity coefficient for component i in solution and is defined as:

$$\gamma_i = \frac{\hat{f}_i^L}{x_i f_i} \quad (2-3)$$

where, x_i represents the composition of component i in the liquid phase and f_i is the fugacity of pure component i .

Using the concept of excess properties (see Appendix A.2); we define the activity coefficient, γ_i with respect to the excess Gibbs energy, G^E as:

$$\ln \gamma_i = \frac{\overline{G}_i^E}{RT} \quad (2-4)$$

The activity coefficient γ_i can be determined from an expression for G^E as a function of composition:

$$\frac{G^E}{RT} = \sum x_i \frac{\overline{G}_i^E}{RT} = \sum x_i \ln \gamma_i \quad (2-5)$$

2.1.3 Infinite dilution activity coefficients

From equation (2-3), as the mole fraction of component 1 approaches zero in solution, its activity coefficient approaches a definite limit and is known as the activity coefficient of component 1 at infinite dilution (γ_i^∞). The infinite dilution activity coefficients are extremely important in separation processes especially when the compound of interest occurs in minute concentrations. They can be determined experimentally by methods such as ebulliometry and inert gas stripping. A full analysis of the many methods is undertaken in Raal & Mühlbauer [1998].

Carlson [1942] calculated an “apparent” activity coefficient by using an isothermal pressure-composition diagram or an isobaric temperature-composition diagram and then by extrapolating it to $x_i = 0$, obtained γ_i^∞ . Unfortunately, extrapolation usually leads to large errors. Also, important components are frequently found in very low concentrations in the liquid phase. Therefore Gautreau and Coates [1955] developed

exact thermodynamic relations for the activity coefficient at infinite dilution by relating the infinite dilution activity coefficient to pressure with respect to liquid composition. Privald *et al.* [1992], using the virial equation of state truncated at the second virial coefficient converts the equation of Gautreau and Coates for component 1 to:

$$\gamma_1^\infty = \varepsilon_1^\infty \left(\frac{P_2^{Sat}}{P_1^{Sat}} \right) \left\{ 1 + \beta_2 \left(\frac{1}{P_2^{Sat}} \right) \left(\frac{\partial P}{\partial x_1} \right)_{T, x_1=0} \right\} \quad (2-6)$$

where,

$$\varepsilon_1^\infty = \exp \left[\frac{(B_{11} - V_1)(P_2^{Sat} - P_1^{Sat}) + \delta_{12} P_2^{Sat}}{RT} \right] \quad (2-7)$$

$$\beta_2 = 1 + p_2^{Sat} \left(\frac{B_{22} - V_2}{RT} \right) \quad (2-8)$$

$$\delta_{12} = 2B_{12} - B_{11} - B_{22} \quad (2-9)$$

P_i^{Sat} and V_i are the vapour pressure and liquid molar volume of component i , B_{ii} and B_{ij} are the second virial coefficient of pure i and the i - j interaction respectively. Detailed analysis of the virial equation of state can be found in Section 2.4.2. The liquid molar volume of component i , V_i is calculated from the Rackett [1970] equation:

$$V_i = V_{ci} Z_{ci}^{(1-T_r)} \quad (2-10)$$

where, V_{ci} is the critical molar volume of component i , Z_{ci} is the critical compressibility factor of component i and T_{ri} is the reduced temperature of component i , calculated from T/T_{ci} . T_{ci} is the critical temperature of component i .

An estimate of the partial derivative was obtained from the graphical method of Ellis and Jonah [1962], as modified by Maher and Smith [1979]. The P versus x_1 data are converted to P_D versus x_1 values using:

$$P_D = P - [P_2^{Sat} + (P_1^{Sat} - P_2^{Sat})x_1] \quad (2-11)$$

Differentiating Equation (2-11) and taking the limit as $x_1 \rightarrow 0$, the following is obtained:

$$\left(\frac{\partial P}{\partial x_1} \right)_{x_1=0} = \left(\frac{P_D}{x_1 x_2} \right)_{x_1=0} - P_1^s + P_2^s \quad (2-12)$$

The term on the left-hand side of Equation (2-12) is determined by extrapolating a plot of $P_D / x_1 x_2$ versus x_1 to $x_1 = 0$. Van Ness [1964] stated that this short extrapolation is superior to the lengthy one needed when tangents are drawn. If the slope of $P_D / x_1 x_2$ is not linear, then Maher and Smith [1979] suggest that $x_1 x_2 / P_D$ be plotted against x_1 . The partial derivative and hence γ_1^∞ can be determined. Similarly a calculation for γ_2^∞ is carried out.

2.2 Analytical methods: The direct and combined methods

The direct and combined (gamma-phi) regression procedures will be reviewed in the isothermal forms i.e. bubble pressure calculations.

2.2.1 The direct method

In the direct regression method, referred as such by Wichterle [1978a], the non-idealities of both the vapour and liquid phase are described by fugacity coefficients represented by equations of state (EOS). Equation (2-1) requires that for vapour-liquid equilibrium, the fugacity of a component in the vapour phase must be equal to the fugacity of the component in the liquid phase. By substituting into this equation the definition of the fugacity coefficient (Equation 2-2), the relationship becomes:

$$x_i \hat{\phi}_i^L = y_i \hat{\phi}_i^V \quad (2-13)$$

The fugacity coefficients are calculated using the exact thermodynamic relationships [Prausnitz *et al.*, 1986]:

$$\ln \hat{\phi}_i^V = \frac{1}{RT} \int_{V_T^V}^{\infty} \left[\left(\frac{\partial P}{\partial n_i} \right)_{T, V_T, n_j} - \frac{RT}{V_T} \right] dV_T - \ln \left[\frac{PV^V}{RT} \right] \quad (2-14a)$$

$$\ln \hat{\phi}_i^L = \frac{1}{RT} \int_{V_T^L}^{\infty} \left[\left(\frac{\partial P}{\partial n_i} \right)_{T, V_T, n_j} - \frac{RT}{V_T} \right] dV_T - \ln \left[\frac{PV^L}{RT} \right] \quad (2-14b)$$

where, the superscripts V and L denote vapour and liquid phase properties, n is the number of moles of material, V_T is the total volume and V is the molar volume. Equations (2-14a) and (2-14b) require a pressure explicit EOS in the form $P = P(V, T)$ with suitable mixing rules applicable to all the mixture's components and their interactions over the entire vapour to liquid density range.

The difficulties related to the direct method are [Raal & Muhlbauer, 1998; Ramjugernath & Raal, 1999]:

- 1) The choice of EOS that best describes both the liquid and vapour phase non-idealities. The main criterion is the flexibility of the EOS in describing the system P-V-T behaviour for both phases within the temperature and pressure range required.
- 2) The choice of mixing rules which is required to extend EOS's to mixtures. Majority of mixing rules are empirical and can describe only specific systems.
- 3) The location of appropriate roots for liquid and vapour molar densities when using EOS's that are of higher mathematical order than the cubic EOS.

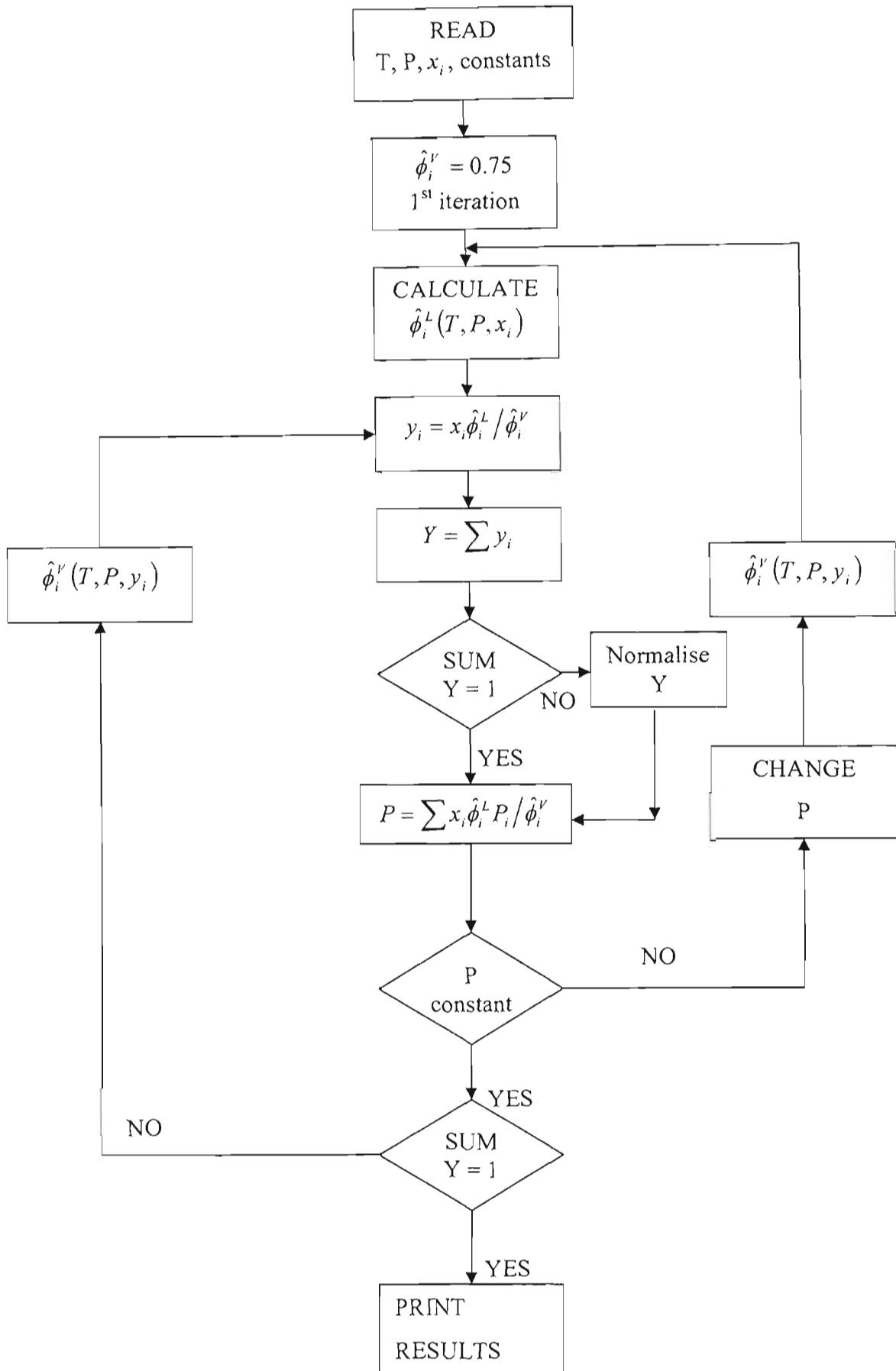


Figure 2.1: Isothermal bubble pressure calculation for the direct method (Raal & Muhlbauer [1998]).

2.2.2 The combined (gamma-phi) method

In the combined regression method, called such by Wichterle [1978b], the non-ideality of the vapour phase is described by a fugacity coefficient but the non-ideality of the liquid phase is described by an activity coefficient. The fugacity and activity coefficient from Equations (2-2) and (2-3) substituted into the equilibrium constraint of Equation (2-1) translates into:

$$y_i \hat{\phi}_i P = x_i \gamma_i f_i \quad (2-15)$$

Re-arrangement of Equation (2-15) gives:

$$y_i = \frac{x_i \gamma_i f_i}{\hat{\phi}_i P} \quad (2-16)$$

Substituting f_i as defined in Appendix A.3 into Equation (2-16) yields:

$$y_i = \frac{x_i \gamma_i \phi_i^{sat} P_i^{sat} \exp\left[\frac{V_i^L (P - P_i^{sat})}{RT}\right]}{\hat{\phi}_i P} \quad (2-17)$$

By defining,

$$\Phi_i = \frac{\hat{\phi}_i}{\phi_i^{sat}} \exp\left[\frac{-V_i^L (P - P_i^{sat})}{RT}\right] \quad (2-18)$$

Equation (2-17) reduces to:

$$y_i P \Phi_i = x_i \gamma_i P_i^{sat} \quad (2-19)$$

The vapour phase fugacity coefficient is calculated using a suitable EOS that describes the vapour phase behaviour and the liquid phase activity coefficient is calculated using a suitable activity coefficient model.

Some of the difficulties associated with the combined method follow [Raal & Muhlbauer, 1995; Ramjugemath & Raal, 1999]:

- 1) Since the vapour phase is represented by an EOS and the liquid phase by an activity coefficient model, there is a large number of parameters to be regressed from experimental data
- 2) Liquid-phase pure-component molar volumes V_i^L and the partial molar volumes \overline{V}_i^L have to be calculated.
- 3) A suitable Gibbs energy model is required so that expressions for the activity coefficients can be derived from the Gibbs-Duhem equation.

2.3 Activity coefficient models

The basis of the combined method of data reduction is to find an accurate form of G^E/RT and therefore the activity coefficient. Binary data for many different types of mixtures cannot be represented with the same equation [Renon and Prausnitz, 1968] and therefore in order to obtain the best fit for a particular data set, various G^E expressions have to be considered. Any form of the excess Gibbs energy can be used, as long as it is accurate, and as long as it has the correct pure component limits [Gess & Danner, 1991] i.e. as x_1 and x_2 approach zero, G^E must approach zero. Some of the more successful G^E models have been those that can be derived from series expansions.

A brief review of the activity coefficient correlations widely used today follows.

2.3.1 The Margules equation

The Margules equation, derived from the Redlich-Kister expansion was originally proposed in 1895:

$$\frac{G^E}{RT} = x_1 x_2 [A + B(x_1 - x_2) + C(x_1 - x_2)^2 + \dots] \quad (2-20)$$

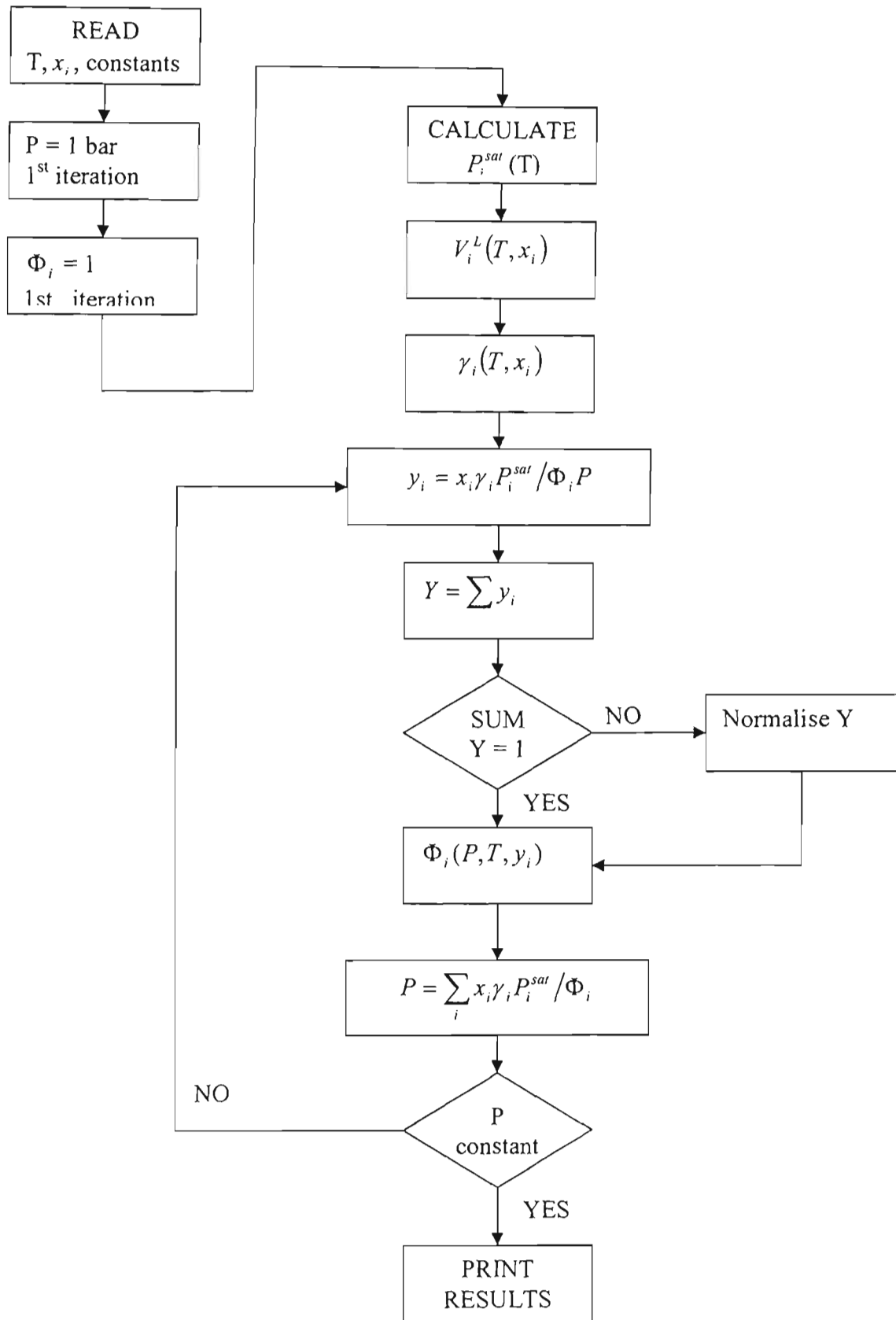


Figure 2.2: Isothermal bubble pressure calculation for the combined method.(Raal & Muhlbauer [1998]).

The simplest form of the Margules equation ignores the higher order terms of the expansion by setting $B = C = 0$:

$$\frac{G^E}{RT} = x_1 x_2 A \quad (2-21)$$

Equation (2-21) is known as the two-suffix Margules equation, because the Gibbs energy is a second order function of x_1 . The applicability of this equation is limited because of its simplicity. Only mixtures of chemically similar molecules conform to this correlation.

The function is symmetric in the relationship between x_1 and G^E , but most real systems exhibit asymmetric behaviour, making the equation inadequate in the representation of non-ideal systems. Although its accuracy is limited, the equation can be used to estimate how much the system deviates from ideal conditions [Gess & Danner, 1991]. For ideal systems, the excess Gibbs energy is zero, while more complicated interactions give rise to values of the excess Gibbs energy both greater and less than zero. This model is generally used to estimate the non-ideality of systems.

To account for more complicated behaviour, the higher order terms of the Redlich-Kister expansion must be included. Letting C and higher terms to be set to zero, and multiply A by $(x_1 + x_2)$, and letting $A_{21} = A + B$ and $A_{12} = A - B$, the three-suffix Margules equation is obtained:

$$\frac{G^E}{RT} = x_1 x_2 [A_{21} x_1 + A_{12} x_2] \quad (2-22)$$

A four-suffix Margules equation is obtained by including the C term in the Redlich-Kister expansion and a similar manipulation as above:

$$\frac{G^E}{RT} = x_1 x_2 [A_{12} x_2 + A_{12} x_1 - C x_1 x_2] \quad (2-23)$$

Van Ness et al. [1973] recommend this form for the testing of VLE data for thermodynamic consistency. The higher order Margules equations are effective in representing certain non-ideal systems.

Malanowski and Anderko [1992] stated that poor performance of the equations can be attributed to the assumption of equal sized molecules. They recommended the equations be used in binary systems. The constants are temperature independent which limits the equation's ability to treat isobaric systems. If too many terms are included in an expansion there is a possibility that the equation will attempt to describe random experimental errors, producing artificial curvature or inflection points [Malanowski and Anderko, 1992].

2.3.2 The Van Laar equation

The van Laar model was developed in 1910 to incorporate the size difference of molecules:

$$\frac{G^E}{RTx_1x_2} = \frac{A_{12}A_{21}}{A_{12}x_1 + A_{21}x_2} \quad (2-24)$$

In rare cases the constants A_{21} and A_{12} are of opposite sign and the denominator, zero [Raal & Mulbauer, 1998]. This is unacceptable if the data is to be represented over the entire composition range. The van Laar model performed poorly in representing highly non-ideal systems, which indicates a more advanced model is needed to represent the interaction of the components in the liquid phase. The constants of this relationship are not temperature dependent as well.

2.3.3 The Wilson equation

In 1964, G. M. Wilson developed a new model that considered the energy of interaction between two molecules as well as the molecule size. The derivation was based on local composition. For a binary system:

$$\frac{G^E}{RT} = -x_1 \ln(x_1 + x_2 G_{12}) - x_2 \ln(x_2 + x_1 G_{21}) \quad (2-25)$$

$$G_{12} = \frac{V_2^L}{V_1^L} \exp\left(-\frac{a_{12}}{RT}\right) \quad (2-26)$$

$$G_{21} = \frac{V_1^L}{V_2^L} \exp\left(-\frac{a_{21}}{RT}\right) \quad (2-27)$$

where, V_i^L is the liquid molar volume for the two pure components and a_{ij} are parameters characterizing molecular interactions but are used as empirical correlating constants. The G_{ij} parameters incorporate temperature dependence and can represent multi-component behaviour with only binary parameters. Orye [1965] showed the applicability of the Wilson's equation data for a wide variety of liquid mixtures. The disadvantages of the Wilson equation, which are not serious for our purposes are firstly, that the maxima or minima cannot be reproduced on the $\ln \gamma$ vs. x_1 curve and secondly, that the equation is not suitable for mixtures of partially miscible liquids.

2.3.4 The NRTL equation (Non-Random Two Liquid Model)

Renon and Prausnitz [1968] published the NRTL model, based on Scott's two-liquid model and included a term to represent the non-randomness of a solution as well as the local composition model. It is particularly suitable for highly non-ideal systems.

$$\frac{G^E}{RTx_1x_2} = \frac{\tau_{21}G_{21}}{x_1 + x_2G_{21}} + \frac{\tau_{12}G_{12}}{x_2 + x_1G_{12}} \quad (2-28)$$

$$G_{12} = \exp(-\alpha_{12}\tau_{12}) \quad (2-29)$$

$$G_{21} = \exp(-\alpha_{12}\tau_{21}) \quad (2-30)$$

The τ_{ij} 's are related to the "energy parameters" g_{ij} by:

$$\tau_{12} = \frac{g_{12} - g_{22}}{RT} \quad (2-31)$$

$$\tau_{21} = \frac{g_{21} - g_{11}}{RT} \quad (2-32)$$

The equations have three adjustable parameters, the two Δg_{ij} and α_{12} . The g_{ij} parameters represent the interaction between components i and j, whereas α_{ij} , which equals α_{ji} , is the non-randomness parameter. When α_{ji} is zero, the mixture is completely random. The value of α_{ji} extends the equation to represent a large variety of mixtures. The τ_{ij} 's introduce temperature dependence and the NRTL is also applicable to multi-component mixtures with only binary parameters.

2.3.5 The UNIQUAC model: (Universal Quasi-Chemical Theory)

Abrams and Prausnitz [1975] derived a semi-theoretical model for the excess Gibbs energy that extended the quasi-chemical lattice theory of Guggenheim. The basis of the model is the assumption that a liquid can be represented by a three dimensional lattice, where each lattice site is occupied by a segment of a molecule, with a total of r_i segments for each molecule of type i. The model consists of two parts, namely, a combinatorial part that represents the athermal (no energy of interaction between the segments) contribution and a residual part that accounts for the energy of interaction between the segments. The combinatorial part is a function of concentration, the size parameter and the area parameter q i.e. it is based solely from structural considerations. The residual part is a function of temperature and the energy parameters ($u_{ji} - u_{ii}$). The UNIQUAC equation uses only two adjustable parameters per binary and an extension to non-polar and polar multi-component systems requires no higher parameters. For a binary system:

$$G^E = G^E(\text{combinatorial}) + G^E(\text{residual}) \quad (2-33)$$

where,

$$\frac{G^E(\text{combinatorial})}{RT} = \sum_i x_i \ln \frac{\Phi_i}{x_i} + \frac{z}{2} \sum_i q_i x_i \ln \frac{\theta_i}{\Phi_i} \quad (2-34)$$

$$\frac{G^E(\text{residual})}{RT} = -\sum_i q_i' x_i \ln \left(\sum_j \theta_j' \tau_{ji} \right) \quad (2-35)$$

The parameters r and q are pure component molecular structure constants. In the original formulation of Abrams and Prausnitz [1975], $q_i = q_i'$. To obtain better agreement with water or alcohols, q_i' for water and alcohols was introduced empirically to give an optimum fit [Anderson and Prausnitz, 1978].

See Table 3-1 for definition of symbols and the corresponding activity coefficients for the G^E models discussed.

2.4 Equations of state (EOS)

The P-V-T relations i.e. the equations of state (EOS) for pure substances and their mixtures are vital for the calculation of a wide range of thermodynamic properties e.g. critical properties, vapour pressures and densities.

EOS's were originally used for pure compounds and when initially applied to mixtures, the equations were restricted to describing non-polar and slightly polar compounds. Recently there have been a multitude of papers published that extend EOS to strongly polar compounds.

Sandler et al., [1994] and Raal & Mühlbauer, [1998] classify EOS as follows:

- 1) Family of virial EOS's
- 2) EOS's in a corresponding states format
- 3) van der Waals family of cubic EOS's
- 4) EOS's derived from statistical thermodynamics based on lattice models, perturbation theory or integral equation theory.
- 5) EOS's derived from fitting computer simulation data.

Table 2.1
Activity Coefficient Expressions for Binary Systems

Margules 2-suffix

$$\ln \gamma_1 = A x_2^2 \quad (2-36)$$

$$\ln \gamma_2 = A x_1^2 \quad (2-37)$$

A = adjustable parameters

Margules 3-suffix

$$\ln \gamma_1 = [A_{12} + 2(A_{21} - A_{12})x_1]x_2^2 \quad (2-38)$$

$$\ln \gamma_2 = [A_{21} + 2(A_{12} - A_{21})x_2]x_1^2 \quad (2-39)$$

A_{12}, A_{21} = adjustable parameters

Margules 4-suffix

$$\ln \gamma_1 = [A_{12} + 2(A_{21} - A_{12} - C)x_1 + 3Cx_1^2]x_2^2 \quad (2-40)$$

$$\ln \gamma_2 = [A_{21} + 2(A_{12} - A_{21} - C)x_2 + 3Cx_2^2]x_1^2 \quad (2-41)$$

A_{12}, A_{21}, C = adjustable parameters

Van Laar

$$\ln \gamma_1 = A_{12} \left(\frac{A_{21}x_2}{A_{12}x_1 + A_{21}x_2} \right)^2 \quad (2-42)$$

$$\ln \gamma_2 = A_{21} \left(\frac{A_{12}x_1}{A_{12}x_1 + A_{21}x_2} \right)^2 \quad (2-43)$$

A_{12}, A_{21} = adjustable parameters

Table 2.1 (Continued)

Activity Coefficient Expressions for Binary Systems

Wilson

$$\ln \gamma_1 = -\ln(x_1 + G_{12}x_2) + x_2 \left(\frac{G_{12}}{x_1 + G_{12}x_2} - \frac{G_{21}}{x_2 + G_{21}x_1} \right) \quad (2-44)$$

$$\ln \gamma_2 = -\ln(x_2 + G_{21}x_1) - x_1 \left(\frac{G_{12}}{x_1 + G_{12}x_2} - \frac{G_{21}}{x_2 + G_{21}x_1} \right) \quad (2-45)$$

$$G_{ij} = \frac{V_j^L}{V_i^L} \exp \left(-\frac{a_{ij}}{RT} \right) \quad (2-46)$$

V_i^L = molar volume of pure liquid component

a_{ij} = adjustable parameters

UNIQUAC

$$\ln \gamma_1 = \ln \frac{\Phi_1}{x_1} + \frac{Z}{2} q_1 n \frac{\theta_1}{\Phi_1} + \Phi_2 \left(l_1 - \frac{r_1}{r_2} l_2 \right) - q_1 \ln(\theta_1 + \theta_2 \tau_{21}) + \theta_2 q_1 \left(\frac{\tau_{21}}{\theta_1 + \theta_2 \tau_{21}} - \frac{\tau_{12}}{\theta_2 + \theta_1 \tau_{12}} \right) \quad (2-47)$$

$$\ln \gamma_2 = \ln \frac{\Phi_2}{x_2} + \frac{Z}{2} q_2 n \frac{\theta_2}{\Phi_2} + \Phi_1 \left(l_2 - \frac{r_2}{r_1} l_1 \right) - q_2 \ln(\theta_2 + \theta_1 \tau_{12}) + \theta_1 q_2 \left(\frac{\tau_{12}}{\theta_2 + \theta_1 \tau_{12}} - \frac{\tau_{21}}{\theta_1 + \theta_2 \tau_{21}} \right) \quad (2-48)$$

$$\tau_{ji} = \exp \left(\frac{-(u_{ji} - u_{ii})}{RT} \right) \quad (2-49)$$

u_{ji} = parameter of interaction between component j and I

z = coordination number; $\frac{z}{2} = 5$

q_i = area parameter of component I

r_i = size parameter of component I

Z = coordination number and is equal to 10

$$l_i = \frac{Z}{2} (r_i - q_i) - (r_i - 1) \quad (2-50)$$

Table 2.1 (Continued)

Activity Coefficient Expressions for Binary Systems

$$\Phi_i = \frac{x_i r_i}{x_1 r_1 + x_2 r_2} \quad (\text{the average segment fraction of component } i) \quad (2-51)$$

$$\theta_i = \frac{x_i q_i}{x_1 q_1 + x_2 q_2} \quad \text{and} \quad \theta'_i = \frac{x_i q_i}{x_1 q_1 + x_2 q_2} \quad (2-52)$$

$(u_{12} - u_{22}), (u_{21} - u_{11}) = \text{adjustable parameters}$

NRTL

$$\ln \gamma_1 = x_2^2 \left[\tau_{21} \left(\frac{G_{21}}{x_1 + x_2 G_{21}} \right)^2 + \frac{\tau_{12} G_{12}}{(x_2 + x_1 G_{12})^2} \right] \quad (2-53)$$

$$\ln \gamma_2 = x_1^2 \left[\tau_{12} \left(\frac{G_{12}}{x_2 + x_1 G_{12}} \right)^2 + \frac{\tau_{212} G_{21}}{(x_1 + x_2 G_{21})^2} \right] \quad (2-54)$$

$$\tau_{ij} = \frac{g_{ij} - g_{jj}}{RT} \quad (2-55)$$

$$G_{ij} = \exp(-\alpha_{ij} \tau_{ij}) \quad (2-56)$$

Δg_{ij} and $\alpha_{12} = \text{adjustable parameters}$

Of interest in this project are the family of virial EOS's and the van der Waals family of cubic EOS's.

2.4.1 Virial Equation of State

The virial equation of state is extremely attractive due to its simplicity, which is highly advantageous in iterative procedures and the direct relation of the parameters to intermolecular forces. The equation is also easily extended to mixtures.

Abbott [1986] recommends the use of the equation for pressures up to about 5 bar. Smith and Van Ness [1987] suggest that the truncated two-and three-parameter virial EOS be used for pressures up to 15 and 50 bars respectively. The accuracy of the calculation of the fugacity is about the same for the pressure-explicit and density-explicit equations truncated at the second virial coefficient, and the systems are usually specified by temperature, pressure and composition. The most convenient form of the virial EOS is as follows:

$$Z = 1 + \frac{BP}{RT} \quad (2-57)$$

where, Z is the compressibility factor PV/RT and B is the second virial coefficient. Walas [1985] recommends the equation for pressures corresponding to $P/P_C \leq 0.5T/T_C$.

For a pure vapour, the virial coefficients are functions of only of temperature. For a mixture, the coefficients are dependent on temperature and composition:

$$B_{mixture}(T, y) = \sum_{i=1}^m \sum_{j=1}^m y_i y_j B_{ij}(T) \quad (2-58a)$$

where, m is the number of components and B_{ij} is the virial coefficient characterising pair interactions between an i and a j molecule.

For a binary system, the exact expression is:

$$B_{mix} = \sum_{i=1}^2 \sum_{j=1}^2 y_i y_j B_{ij} = y_1^2 B_{11} + 2y_1 y_2 B_{12} + y_2^2 B_{22} \quad (2-58b)$$

With the use of the virial EOS, Equation (2-18) transforms into:

$$\Phi_i = \exp \left[\frac{(B_{ii} - V_i)(P - P_i^{sat}) + P y_j \delta_{ij}}{RT} \right] \quad (2-59)$$

where, as in Equation (2-9)

$$\delta_{ij} = 2B_{ij} - B_{ii} - B_{jj}$$

Experimental virial coefficients for the pure components B_{ii} and mixtures B_{ij} can be found in Dymond and Smith [1980] and Cholinski *et al.* [1986]. For prediction of these coefficients, correlations such as Tsonopoulos [1974], Haydon & O'Connell [1975], Nothnagel *et al.* [1973], Black [1958] and O'Connell & Prausnitz [1967] are available. The method of Haydon & O'Connell was utilised in this project as it offers the most reliable prediction of coefficients and is simple and highly accurate for complex systems [Haydon & O'Connell, 1975]. The Haydon & O'Connell method is a predictive method, with the virial coefficients being functions of dipole moments, temperature, pressure, critical temperature, critical pressure and the degree of association between the interacting components

The truncated form of the virial expansion can describe only the vapour phase behaviour. In the direct method, the equation must be able to describe both the liquid and vapour behaviour. Thus, the virial EOS cannot be used in the direct case.

A number of equations of state have been proposed over the years but the cubic equation of state (CEOS) is the simplest polynomial form capable of yielding the ideal gas limit at $V \rightarrow \infty$ and of representing both liquid and gas phases.

2.4.2 The van der Waals family of cubic equations of state

The most general form of a cubic equation of state (CEOS) contains five parameters and takes the form:

$$P = \frac{RT}{V-b} - \frac{a(V-\theta)}{(V-b)(V^2 + \zeta V + \psi)} \quad (2-60)$$

where the adjustable parameters a , b , θ , ζ and ψ are in general functions of temperature [Abbott, 1979].

The cubic equation in its general form has been analysed by Martin [1967 and 1979], Abbott [1973] and Vera et al. [1984] but the forms that have achieved widespread usage and acceptance are the Soave-Redlich-Kwong(SRK) and the Peng-Robinson (PR) modifications of the van der Waals equation of state.

The van der Waals family of CEOS contain only the two parameters a and b , where Equation (2-60) reduces to:

$$P = \frac{RT}{V-b} - \frac{a}{g(V)} \quad (2-61)$$

where $g(V)$ is a generalised function of molar volume.

The parameter b represents a rough measure of the size of the molecule whereas the parameter a is a measure of the attractive forces of the molecules. The pressure of the system is then thought of as the sum of repulsive and attractive terms:

$$P = P_{repulsive} + P_{attractive} \quad (2-62)$$

$$P_{repulsive} = \frac{RT}{V-b} \quad (2-63)$$

$$P_{attractive} = -\frac{a}{g(V)} \quad (2-64)$$

Two methods are available for determination of the attractive and co-volume parameters. The first is to choose the parameters to fit experimental data such as pure compound vapour pressure and liquid or vapour densities. The second method is to fit the parameters to the critical point using the EOS and the critical point conditions as given by:

$$\left(\frac{\delta P}{\delta V}\right)_{T,\text{critical point}} = \left(\frac{\delta^2 P}{\delta V^2}\right)_{T,\text{critical point}} = 0 \quad (2-65)$$

2.4.2.1 The van der Waals EOS

In 1873 van der Waals proposed the first equation of state that represented both gas and liquid phases. The equation took into account intermolecular forces to describe the volumetric behaviour of fluids:

$$P = \frac{RT}{V-b} - \frac{a}{V^2} \quad (2-66)$$

Due to the simplicity in the treatment of intermolecular forces of the van der Waals equation, accurate results cannot be made.

In 1949 Redlich and Kwong modified the equation and hence the accuracy by introducing temperature dependence and an extra size parameter into the denominator of the second (attractive) term:

$$P = \frac{RT}{V-b} - \frac{a}{T^{0.5}V(V+b)} \quad (2-67)$$

Although the Redlich-Kwong (R-K) equation has limited accuracy, and is generally useful only for nearly ideal systems, the success of the R-K EOS stimulated numerous investigators to propose various methods for improving the equation. A comprehensive review was undertaken by Horvath in 1974 of these modifications up to the early 1970's.

Improvements of the R-K EOS fall within two main trends of research; they either adopt a better temperature dependence of parameters or change the functional form of the $g(V)$ dependence [Anderko, 1990].

The temperature dependence of the “a” parameter is essential for the reproduction of vapour pressures [Wichterle, 1978]. The first method for expressing the temperature dependence was proposed by Soave in 1972 and it gained extensive popularity due to its accuracy and simplicity.

2.4.2.2 The Soave-Redlich-Kwong (SRK) EOS

In 1972, Soave incorporated the temperature dependence that Redlich-Kwong had introduced into the attraction parameter and developed the following equation:

$$P = \frac{RT}{V-b} - \frac{a(T,\omega)}{V(V+b)} \quad (2-68)$$

Many methods were introduced for adjusting the parameters to enable the EOS to match experimental vapour pressures. Wilson in 1964 first introduced the following form of the temperature dependence of the “a” parameter for both phases:

$$a(T) = a_c \alpha(T)$$

$$\alpha(T) = T_R (1 + (1.57 + 1.62\omega)) (T_R^{-1}) \quad (2-69)$$

$$b(T) = b_c \quad (2-70)$$

where a_c and b_c are the values at the critical point and $T_R = \frac{T}{T_C}$.

The first method for expressing the temperature dependence that gained widespread popularity due to its accuracy and simplicity was proposed by Soave [1972] for non-polar substances:

$$\sqrt{\alpha_i} = 1 + \kappa_i (1 - \sqrt{T_{ri}}) \quad (2-71)$$

where κ_i was expressed as a quadratic function of the acentric factor. Soave correlated κ_i against the acentric factors of the compounds examined:

$$\kappa_i = 0.48 + 1.5\omega - 0.1\omega^2 \quad (2-72)$$

Soave's function was found to be incorrect at high-reduced temperatures, as it does not always decrease monotonically. The full set of equation can be found in Table 2.

Soave calculated the vapour pressures of several hydrocarbons and compared these with experimental data. In contrast to the original R-K EOS, which yielded vapour pressures diverging sharply from experimental values, especially for compounds with large acentric factors, Soave's modification fitted the experimental curve well. In addition, the SRK EOS has proved successful in correlating the phase behaviour of multi-component systems containing non-polar and slightly polar substances. Despite its successes, the SRK EOS always predicts liquid-phase specific volumes that are greater than literature values (Peng & Robinson, 1976].

The solution of Equation (2-87) in Table 3-2 has either one or three real roots. If the solution has three real roots, the highest root corresponds to the compressibility factor of the vapour and the lowest positive root, the liquid.

2.4.2.3 The Peng-Robinson (PR) EOS

While an appropriate temperature dependence of the "a" parameter is sufficient for representing accurately the vapour pressure, modifications of the $g(V)$ functional dependence are necessary to improve the prediction of volumetric properties. The simplest approach is to change the form of the attractive term of the R-K EOS without adding parameters. In 1976, Peng and Robinson recognized that the critical compressibility factor, Z_c of the R-K EOS was overestimated thus impairing the liquid volume calculations. The critical compressibility factor, Z_c is defined at the critical point as $Z_c = P_c V_c / RT_c$. They postulated an equation reducing Z_c :

$$P = \frac{RT}{V-b} - \frac{a(T, \omega)}{V(V+b) + b(V-b)} \quad (2-73)$$

To calculate the fugacity coefficient of the Peng-Robinson EOS, with respect to the compressibility factor, the following equation is derived:

$$z^3 - (1-B)z^2 + z(A - 2B - 3B^2) - (AB - B^2 - B^3) = 0 \quad (2-74)$$

Similarly, for three roots, the highest root corresponds to the compressibility factor of the vapour and the lowest positive root, the liquid.

The full set of equations for the Peng-Robinson EOS can be found in Table 2-2. Although both SRK and PR EOS's use the same equations for α and κ as a function of ω , there is a difference with respect to the κ function. For a CEOS, at $T_r = 0.7$, α is uniquely determined by ω from the definition of the acentric factor:

$$\log(P_r^s)_{T_r=0.7} = -(\omega + 1) \quad (2-75)$$

where P_r^s is the reduced saturation pressure.

Therefore, for each EOS, there is a κ that exactly reproduces the value of the vapour pressure at $T_r = 0.7$. Soave computed α values at $T_r = 0.7$ over a range of ω without experimental points. On the other hand, Peng and Robinson failed to satisfy Equation (2-75) as they fitted the vapour pressure from the normal boiling point to the critical point for a large number of compounds to obtain the coefficients. This resulted in poor representation of the PR EOS for polar compounds.

Numerous modifications were proposed for the Peng-Robinson EOS but the most widely used modification was that of Stryjek and Vera [1986]. The equation, which modified the α function, is highly desirable as it is a one-parameter form. The alpha function as in Equation (2-71) remains the same:

$$\alpha = \left[1 + \kappa(1 - \sqrt{T_r})\right]^2$$

$$\kappa = \kappa_o + \kappa_1(1 + \sqrt{T_r})(0.7 - T_r) \quad (2-76)$$

$$\kappa_o = 0.378 + 1.489\omega + 0.17\omega^2 + 0.019\omega^3 \quad (2-77)$$

Table 2.2
Equation of State Parameters and Fugacity Coefficient Expressions

For pure species i, the general EOS can be represented by:

$$Z_i = \frac{PV_i}{RT} = \frac{V_i}{V_i - b_i} - \frac{a_i(T)V_i}{RT(V_i + c_1b_i)(V_i + c_2b_i)} \quad (2-78)$$

where:

$$a_i = a_{ci}\alpha_i \quad (2-79)$$

$$a_{ci}(T) = \frac{\Omega_a R^2 T_{ci}^2}{P_{ci}} \quad (2-80)$$

$$b_i = \frac{\Omega_b RT_{ci}}{P_{ci}} \quad (2-81)$$

Parameters	SRK EOS	PR EOS
c_1	0	$1 - \sqrt{2}$
c_2	1	$1 + \sqrt{2}$
Ω_a	0.424747	0.45724
Ω_b	0.08664	0.07780

with α defined as in Equation (2-71):

$$\sqrt{\alpha_i} = 1 + \kappa_i(1 - \sqrt{T_{ri}}) \quad (2-82)$$

where:

$$\text{SRK EOS} : \kappa_i = 0.480 + 1.574\omega_i - 0.176\omega_i^2 \quad (2-83)$$

$$\text{PR EOS} : \kappa_i = 0.374 + 1.542\omega_i - 0.269\omega_i^2 \quad (2-84)$$

To solve for the pure component fugacity coefficient:

$$\text{SRK EOS} : \ln \phi = z - 1 - \ln(z - B) - \frac{A}{B} \ln\left(\frac{z + B}{z}\right) \quad (2-85)$$

$$\text{PR EOS} : \ln \phi = z - 1 - \ln(z - B) - \frac{A}{2\sqrt{2}B} \ln\left(\frac{z + \frac{(1 + \sqrt{2})B}{2}}{z + \frac{(1 - \sqrt{2})B}{2}}\right) \quad (2-86)$$

To evaluate z, Equation (2-78) is simplified to:

$$\text{SRK EOS} : z^3 - z^2 + z(A - B - B^2) - AB = 0 \quad (2-87)$$

$$\text{PR EOS} : z^3 - (1 - B)z^2 + z(A - 2B - 3B^2) - D = 0 \quad (2-88)$$

With: $D = AB - B^2 - B^3$

The constants A and B can be calculated from:

$$A = \frac{a_i P}{R^2 T^2} \quad (2-89)$$

$$B = \frac{b_i P}{RT} \quad (2-90)$$

with:

$$z = \frac{PV}{RT} \quad (2-91)$$

2.5 Mixing rules

To extend pure substance EOS to mixtures, a mixing rule has to be incorporated into the modelling. There are essentially two basic methods of applying a cubic EOS to a mixture, Method A and Method B [Walas, 1985].

In Method A, a mixture's EOS a_m and b_m parameters are calculated from critical properties e.g. T_{cm} and P_{cm} determined from combining rules. The simplest combining rules are mole-fraction-weighted sums of the property parameter for the components of the mixture. The various combining rules will not be further discussed, as they are not that commonly used in phase equilibrium calculations. A full discussion can be found in Walas [1985].

The most common method is Method B, where the pure component a_i and b_i parameters are calculated using pure component properties e.g. T_{ci} and P_{ci} . Mixing

rules are then only employed to express the EOS a_m and b_m (also written as a and b) parameters as some function of composition and pure component a_i and b_i parameters.

For a mixture Equation (2-78) in its general form:

$$Z_{mi} = \frac{PV_{mi}}{RT} = \frac{V_{mi}}{V_m - b_m} - \frac{a_m(T)V_m}{RT(V_m + c_1 b_m)(V_m + c_2 b_m)} \quad (2-92)$$

The values of a_m and b_m are mixture values related to the pure component parameters a_i and b_i through a mixing rule.

The general expression for the fugacity coefficient of compound i in a mixture:

$$\ln \hat{\phi}_i = \frac{\bar{b}_i}{\bar{b}_m} (Z_m - 1) - \ln \frac{(V_m - b_m)Z_m}{V_m} + \frac{a_m / b_m RT}{c_1 - c_2} * \left(1 + \frac{\bar{a}_i}{a_m} - \frac{\bar{b}_i}{b_m} \right) \ln \frac{V_m + c_2 b_m}{V_m + c_1 b_m} \quad (2-93)$$

In this equation, \bar{a}_i and \bar{b}_i are “partial parameters” for component i :

$$\bar{a}_i \equiv \left[\frac{\partial(na_m)}{\partial n_i} \right]_{T, n_j, i} \quad (2-94)$$

$$\bar{b}_i \equiv \left[\frac{\partial(nb_m)}{\partial n_i} \right]_{T, n_j, i} \quad (2-95)$$

At a given temperature and pressure, the solution for $\hat{\phi}_i$ from Equation (2-93) requires prior solution of Equation (2-92) for V_m (the mixture molar volume) and from that Z_m (the mixture compressibility factor). The parameters \bar{a}_i and \bar{b}_i can be found in Table 3-3 for the mixing rules used in this project.

The simplest mixing rule is the van der Waals one-fluid mixing rules:

$$a_m = \sum \sum x_i x_j a_{ij} \quad (2-96)$$

$$b_m = \sum \sum x_i x_j b_{ij} \quad (2-97)$$

The combining rules for a_{ij} and b_{ij} are:

$$a_{ij} = \sqrt{a_i a_j} (1 - k_{ij}) \quad (2-98)$$

$$b_{ij} = \frac{1}{2} (b_i + b_j) (1 - l_{ij}) \quad (2-99)$$

where k_{ij} and l_{ij} are the binary interaction parameters obtained by fitting EOS predictions to experimental VLE data for k_{ij} or VLE and density data for k_{ij} and l_{ij} .

Generally, l_{ij} is set zero, leading to:

$$b_m = \sum x_i b_i \quad (2-100)$$

The justification of the van der Waals one-fluid mixing rule stems from the virial EOS. By expanding the van Waals equation in powers of (b/V) , we obtain:

$$\frac{PV_m}{RT} = 1 + \sum_{n=1}^{\infty} \left(\frac{b_m}{V} \right)^n - \frac{a_m}{V_m RT} \quad (2-101)$$

From statistical mechanics and Equation (2-58a),

$$B_{mixture}(T, y) = \sum_{i=1}^m \sum_{j=1}^m y_i y_j B_{ij}(T) = \sum_{i=1}^m \sum_{j=1}^m y_i y_j \left(b_{ij} - \frac{a_{ij}}{RT} \right) = b_m - \frac{a_m}{RT} \quad (2-102)$$

A sufficient, but not necessary condition is that the cubic EOS parameters satisfy the van der Waals one-fluid mixing rule, as the low-density composition dependence of a cubic EOS has to be the same as the theoretically correct virial expansion.

The van der Waals one-fluid mixing rule is only effective in describing mixtures near ideality. To encompass mixtures that deviate widely from ideality, Vidal [1978] and Huron and Vidal [1979] developed a mixing rule that incorporated activity coefficient models based on an infinite reference pressure. Activity coefficient models are used to effectively describe mixtures that are highly non-ideal. Huron and Vidal considered the

excess Gibbs free energy given by a van der Waals type of CEOS at the limit of infinite pressure:

$$G_{EOS}^E(T, P \rightarrow \infty, x_i) = \Lambda \left[\frac{a_m}{b_m} - \sum_i x_i \frac{a_i}{b_i} + P \sum_i x_i (b_m - b_i) \right] \quad (2-103)$$

The constant Λ depends on the EOS:

$$\text{SRK EOS: } \Lambda = -\ln(2) \quad (2-104)$$

$$\text{PR EOS: } \Lambda = \frac{1}{\sqrt{2}} \ln(\sqrt{2} - 1) \quad (2-105)$$

They assumed that at infinite pressure the excess Gibbs free energy obtained from an EOS equals the excess Gibbs energy calculated from the liquid phase activity coefficient model:

$$G_{EOS}^E(T, P \rightarrow \infty, x_i) = G_\gamma^E(T, P \rightarrow \infty, x_i) \quad (2-106)$$

Also the co-volume parameter b equals the volume V at infinite pressure:

$$\lim_{P \rightarrow \infty} \frac{V_i}{b_i} = \lim_{P \rightarrow \infty} \frac{V_m}{b_m} = 1 \quad (2-107)$$

and the excess volume, V^E , is zero.

Therefore Equation (2-106) reduces to:

$$a_m = b_m \left[\sum_i x_i \frac{a_i}{b_i} + \frac{G_\gamma^E(T, P \rightarrow \infty, x_i)}{\Lambda} \right] \quad (2-108)$$

The above-derived equation together with Equation (2-100) form the original Huron-Vidal (OHV) mixing rule and is able to correlate highly polar and asymmetric systems.

The fugacity coefficient for Peng-Robinson EOS is then given by:

$$\ln \phi_i = \frac{b_i}{b_m} (Z - 1) - \ln(Z - B) - \frac{1}{2\sqrt{2}} \left[\frac{a_i}{b_i RT} + \frac{\ln \gamma_i}{C^*} \right] \ln \left\{ \frac{Z + (1 + \sqrt{2})B}{Z + (1 - \sqrt{2})B} \right\} \quad (2-109)$$

The difficulties associated with the OHV mixing rule was examined by Sandler [1992] and Sandler et al. [1994]:

- 1) The mixing rule may not be successful in describing non-polar hydrocarbon systems.
- 2) The OHV mixing rule does not satisfy the quadratic composition dependence required of the second virial coefficient at the low-density limit
- 3) Even though the Huron-Vidal approach allows the use of G^E models with EOS's, the parameters are not the same as those obtained when correlating data directly with the activity coefficient model as G^E is a function of pressure and even at a fixed temperature, its low-pressure value is not the same as at infinite pressure. As a result, one cannot use parameter tables e.g. the DECHEMA Data Series developed for excess Gibbs free energy models at low pressure with this EOS model.

The mixing rule as developed by Wong and Sandler uses the excess Helmholtz free energy A^E as opposed to G^E in the OHV mixing rule [Wong and Sandler, 1992]. In addition:

- 1) It allows the use of existing G^E parameter tables [Wong and Sandler, 1992];
- 2) Allows extrapolation over wide ranges of temperature and pressure [Huang and Sandler, 1993]
- 3) Provides the simplest method of extending UNIFAC or other low-pressure prediction methods to high temperatures and pressures [Orbey et al., 1993].

The new mixing rules of Wong and Sandler are based on the following important observations:

- 1) Although the van der Waals one-fluid mixing rule is a sufficient condition to ensure the proper composition dependence of the second virial coefficient, it is not a necessary condition.

The van der Waals one-fluid mixing rule places constraints on two functions, a and b , to satisfy the single relation of Equation (2-102). The mixing rule of Wong and Sandler uses the last equality of Equation (2-102) as one of the restrictions on the EOS a and b parameters together with the following combining rule:

$$b_{ij} - \frac{a_{ij}}{RT} = \frac{1}{2} \left[\left(\frac{b_i - a_i}{RT} \right) + \left(\frac{b_j - a_j}{RT} \right) \right] (1 - k_{ij}) \quad (2-110)$$

where k_{ij} is a second virial coefficient binary interaction parameter.

- 2) The excess Helmholtz free energy on mixing is much less pressure dependent than the excess Gibbs free energy.

The second equation for the a and b parameters then come from the condition that:

$$\begin{aligned} A_{EOS}^E(T, P = \infty, x_i) &= A^E(T, P = \infty, x_i) \\ &= A^E(T, lowP, x_i) \\ &= G^E(T, lowP, x_i) \end{aligned} \quad (2-111)$$

where the subscript EOS refers to the Helmholtz free energy derived from an EOS, while A^E and G^E without the subscripts indicate the free energy from activity coefficient models.

The advantages of the Wong-Sandler mixing rule were summarized as follows by Sandler et al. [1994]:

- 1) It extends the range and applicability of equations of state to mixtures that previously could only be correlated with activity coefficient models.
- 2) Activity coefficient parameters reported in databanks can be used directly and with good accuracy.
- 3) In many mixtures the free-energy model parameters in the EOS can be taken to be independent of temperatures, thereby allowing extrapolation over large ranges of temperature and pressure.
- 4) The mixing rule can be used to make predictions at high pressure based on low-pressure prediction techniques, such as UNIFAC and other group contribution methods.

The full formulation of the Wong-Sandler mixing rule appears in Appendix A.

An extensive review of the mixing rules was undertaken by Raal and Muhlbauer [1998], where the mixing rules were divided into five main categories: classical (CMR), density-dependent (DDMR), composition-dependent (CDMR), local composition (LCMR) and density-independent (DIMR). Raal and Muhlbauer [1998] stated that the density-independent mixing rule of Wong and Sandler (W-S) is the most appealing and promising mixing rule.

The WS mixing rule does not correlate non-polar mixtures better than van der Waals mixing rule and it encounters singularity problem for mixtures on non-polar compounds with light gases. The WSMR does not reduce to the CMR when the interaction parameters in the excess free energy model are set equal to zero.

Numerous modifications have been undertaken on the Wong-Sandler mixing rule. Orbey and Sandler [1995(a)] reformulated the mixing rule by eliminating one of its parameters. Satyro and Trebble [1998] showed that at extremely high pressures i.e. in the order of 15 000 bar, the Wong and Sandler mixing rules produced negative heat capacities. They modified the Wong and Sandler mixing rule, however at the expense of maintaining the quadratic compositional relationship of the predicted second virial coefficient.

Twu and Coon [1996] recently developed a mixing rule that they claim is more flexible than the Wong-Sandler mixing rules and avoids the problems associated with the Wong-Sandler mixing rules. The mixing rule depends only on composition and temperature and is based on the equation:

$$A_{nr}^E = \Delta A - \Delta A_{vdW} \quad (2-112)$$

where A_{nr}^E is the excess Helmholtz free energy obtained using non-random liquid theory based on the local-composition concept, ΔA is the Helmholtz-free-energy departure function (i.e. the difference between the molar Helmholtz free energy of a mixture and that of the same mixture of an ideal gas at the same temperature, pressure and composition), and ΔA_{vdW} is the Helmholtz free-energy departure function evaluated for a van der Waals fluid.

If ΔA and ΔA_{vdW} are evaluated using a two-parameter CEOS, then at the limit of infinite pressure ($P \rightarrow \infty$), Equation (2-112) yields:

$$\frac{A_{nr}^E}{RT} = \Lambda \cdot \left(\frac{a_m^*}{b_m^*} - \frac{a_{m,vdW}^*}{b_{m,vdW}^*} \right) \quad (2-113)$$

where the constant Λ is defined in Equation (2-104) and (2-105) and the reduced properties a_m^* and b_m^* are defined in Equations (2-89) and (2-90) as A and B. The evaluation of the parameters $a_{m,vdW}^*$ and $b_{m,vdW}^*$ requires evaluation of Equations (2-96) and (2-97).

The use of a two-parameter CEOS allows two degrees of freedom to choose the two mixture parameters a_m and b_m . Application of the infinite-pressure limit to arrive at Equation (2-113) utilises one degree of freedom. As Wong and Sandler [1992], Twu and Coon used the remaining degree of freedom to satisfy the second virial coefficient

boundary condition. Substitution of the combining rules for a_{ij} and b_{ij} from the van der Waals Equations (2-98) and (2-99) into Equation (2-102) yields:

$$b_m = b_{m,vdW} + \frac{1}{RT} \cdot (a_m - a_{m,vdW}) \quad (2-114)$$

If Equations (2-113) and (2-114) are solved simultaneously for the mixture parameters a_m and b_m , we obtain the Twu-Coon mixing rule (TCMR):

$$a^* = \frac{aP}{R^2T^2} = b^* \cdot \left(\frac{a_{vdW}^*}{b_{vdW}^*} + \frac{1}{\Lambda} \cdot \frac{A_{nr}^E}{RT} \right) \quad (2-115)$$

$$b^* = \frac{bP}{RT} = \frac{b_{vdW}^* - a_{vdW}^*}{1 - \left(\frac{a_{vdW}^*}{b_{vdW}^*} + \frac{1}{\Lambda} \cdot \frac{A_{nr}^E}{RT} \right)} \quad (2-116)$$

Any Helmholtz free energy model may be used for A_{nr}^E above. The TCMR has two second virial coefficient binary interaction parameters, k_{ij} and l_{ij} . This extra parameter provides the TCMR with immense flexibility in regression of VLE data.

Table 2.3

Parameters \bar{a}_i and \bar{b}_i for the mixing rules used

Huron-Vidal Original Mixing rule (OHVMR):

$$\bar{a}_i = \frac{a_i b_m}{b_i} + \frac{a_m b_i}{b_m} - a_m + \frac{b_m RT \ln \gamma_i^{P_\infty}}{\Lambda} \quad (2-117)$$

$$\bar{b}_i = b_i \quad (2-118)$$

Wong-Sandler Mixing Rule (WSMR):

$$\bar{a}_i = b_m RT \left[\frac{a_i}{b_i RT} + \frac{\ln \gamma_i}{\Lambda} \right] + a_m \left[\frac{\bar{b}_i}{b_m} - 1 \right] \quad (2-119)$$

$$\bar{b}_i = \frac{2 \sum_j x_j \left(b - \frac{a}{RT} \right)_{ij} - b_m \left(1 - \frac{\ln \gamma_i^{P_\infty}}{\Lambda} - \frac{a_i}{b_i RT} \right)}{1 - \frac{1}{\Lambda} \cdot \frac{G_y^E(T, P^*, x_i)}{RT} - \sum_j x_j \frac{a_j}{b_j RT}} \quad (2-120)$$

Twu-Coon Mixing Rule (TCMR):

$$\bar{a}_i = a_m \left(\frac{\bar{b}_i}{b_m} + \frac{\bar{D}_i}{D_m} - 1 \right) \quad (2-121)$$

$$\bar{b}_i = b_m \left[\frac{2 \sum_j x_j (b_{ij}^* - a_{ij}^*)}{\sum_i \sum_j x_i x_j (b_{ij}^* - a_{ij}^*)} - \frac{1}{1 - D_m} (1 - \bar{D}_i) \right] \quad (2-122)$$

where D_m and \bar{D}_i are:

$$D_m \equiv \frac{a_{m,vdW}^*}{b_{m,vdW}^*} + \frac{1}{\Lambda} \cdot \frac{A_{nr}^E}{RT} \quad (2-123)$$

$$\bar{D}_i \equiv \left[\frac{\partial(nD_m)}{\partial n_i} \right]_{T, n_j, x_i} = \frac{a_{m,vdW}^*}{b_{m,vdW}^*} \left[\frac{2}{a_{m,vdW}^*} \sum_j x_j a_{ij} - \frac{2}{b_{m,vdW}^*} \sum_j x_j b_{ij} + 1 \right] + \frac{\ln \gamma_{i,nr}}{\Lambda} \quad (2-124)$$

2.6 Vapour-liquid equilibrium data reduction

Abbot & Van Ness [1975(III)] stated that Barker's method, which is a least squares reduction procedure, is a most attractive procedure as it is a single step analytical fitting technique, that makes direct use of the measured data. Silverman & Tassios [1984] also found that Barker's method produced very good results. The goal of a least squares method is to choose the set of parameter estimates that minimize the sum of the squares of the errors between one or more experimental and calculated quantities. The objective function is the sum of the squares of the errors. The most reliable estimates of the parameters are obtained from multiple measurements, usually a series of vapour-liquid equilibrium T, P, x and y [Prausnitz, Anderson, Grens, 1980].

In data reduction, various combinations of the variables P, T, x and y may be known and the missing ones are calculated using appropriate equations and correlations. When a binary liquid phase is in equilibrium with its vapour, there are two degrees of freedom [Van Ness, 1995]. Thus when temperature is fixed i.e. for isothermal data, then for any value of x_1 , we can calculate values for y_1 and pressure. This is termed a bubble point pressure calculation. Similarly when pressure is fixed i.e. for the isobaric case, a bubble point temperature calculation is performed where vapour mole fractions and temperatures are calculated from liquid mole fractions and pressure.

Both of these routine engineering calculations are based on an ability to evaluate G^E/RT , P_i^{sat} and Φ_i which are variables required in both the combined and direct method [Smith & Van Ness, 1987]. Data reduction for the isothermal case is far simpler as the temperature dependence of the parameters in the activity coefficient models reduces them to constants. The feasibility of VLE determination from measurements at constant temperature is shown in Ljunglin & Van Ness [1962]. We assume the availability of an expression for G^E/RT as a function of x_1 and T that is inherently capable of correlating the data to within their experimental precision.

If a full set of P-x-y data is obtained experimentally, y is the least reliable, [Van Ness et al., 1973]. The large uncertainties associated with y will be propagated into larger uncertainties in the parameter estimates [Van Ness, 1978]. Byer et al. [1973]

demonstrated the effectiveness of the numerical procedure based on P-x data alone for various binary systems. The steps to the conventional Barker method follow below [Abbot & Van Ness, 1977].

2.6.1 Barker's Method

J. A. Barker, in 1953 established the first model-dependent method. For an isothermal set of P-x data:

- 1) A suitable expression for the excess Gibbs energy is selected. Barker [1953] employed the Scatchard [1949] polynomial, but any equation can be used.
- 2) The expression for the system pressure is given by:

$$P = \frac{x_1 \gamma_1 P_1^{sat}}{\Phi_1} + \frac{x_2 \gamma_2 P_2^{sat}}{\Phi_2} \quad (2-125)$$

- 3) The equations for the activity coefficients, γ_1 and γ_2 , in accordance with step (1), are substituted in Equation (2-125). This results in the pressure being a function of the unknown parameters of the activity coefficient model.
- 4) Utilizing a regression procedure, the unknown parameters that best fit the P-x data for the entire composition range are determined. The initial values of pressure are calculated with the correction factor, $\Phi_i=1$. The vapour mole fraction is then evaluated via Equation (2-19). These calculated values of pressure and vapour mole fraction are used to give new estimates of the correction factor. Iteration continues until there is no significant change in the calculated pressures.

Barker [1953] minimized the sum of the squares of the differences between the calculated and measured pressures in the determination of the unknown parameters. Van Ness et al. [1978] define this difference between the calculated value and the corresponding experimental value as a residual, denoted using the symbol, δ . Van Ness et al. [1978], upon comparison of different residuals, stated that the objective function $\sum(\delta P)^2$ utilized by Barker [1953] performed the best. The minimization of the pressure residual is also the simplest and the most direct method [Van Ness, 1995]. The non-linear regression technique of Marquardt [1963] was used in conjunction with

Barker's method in this project. For isobaric data reduction the residual of δT was used instead of δP .

The method of Barker was utilized with both the direct and combined method, modified accordingly as shown in Figure 2-1 and 2-2.

2.7 Thermodynamic consistency tests

VLE measurements are always liable to errors, depending on the instrumentation used, the accuracy of the experimental manipulation or the inadequacy of the thermodynamic functions G^E/RT and $\ln(\gamma_1/\gamma_2)$. To achieve data of high quality, the results need to be subjected to thermodynamic consistency tests. These tests are based on the Gibbs-Duhem equation. For a binary system, the equation is represented by:

$$\frac{H^E}{RT^2} dT - \frac{V^E}{RT} dP + x_1 d \ln \gamma_1 + x_2 d \ln \gamma_2 = 0 \quad (2-126)$$

For the isobaric system, the Gibbs-Duhem reduces to:

$$\frac{H^E}{RT^2} dT + x_1 d \ln \gamma_1 + x_2 d \ln \gamma_2 = 0 \quad (2-127)$$

For the isothermal system, it is assumed that the term $(V^E/RT)dP$ is negligible. The Gibbs-Duhem equation then reduces to:

$$x_1 d \ln \gamma_1 + x_2 d \ln \gamma_2 = 0 \quad (2-128)$$

For data to be consistent, the Gibbs-Duhem equation must hold true. The following thermodynamic consistency tests as described below stem from this equation.

2.7.1 Area test

One of the early procedures for testing thermodynamic consistency of VLE data is the area test, introduced by Redlich & Kister [1948]. The test involves the integration of Equation (2-87) over the entire composition range:

$$\int_0^1 \ln \left(\frac{\gamma_i}{\gamma_j} \right) dx_i = 0 \quad (2-129)$$

For thermodynamic consistency, the plot of $(\ln \gamma_1 / \gamma_2)$ vs x_1 must result in a net area of zero, i.e. the positive area (above the x axis) should equal the negative area (below the x axis).

Various extensions have been proposed e.g. Samuels et al. [1972] and Herington [1951]. Van Ness [1999] states that the area test is not a sufficient condition for a consistency test, as it is considered too mild. The reasons as stated by Van Ness [1995] are as follows:

- 1) The consistency criterion of the net area $\leq 10\%$ of the total area. This is not a stringent requirement.
- 2) For isobaric data, H^E , which is an important variable to take into consideration, is omitted, usually due to the unavailability of data.
- 3) For the isothermal case, the measured variable, P, cancels in the ratio of

$\frac{\gamma_1}{\gamma_2}$ [Van Ness, 1973]:

$$\frac{\gamma_1}{\gamma_2} = \frac{y_1 P \Phi_1 / x_1 P_1^{sat}}{y_2 P \Phi_2 / x_2 P_2^{sat}} = \frac{y_1 \Phi_1 x_2 P_2^{sat}}{y_2 \Phi_2 x_1 P_1^{sat}} \quad (2-130)$$

The area test is extremely sensitive to the values used for the pure component vapour pressures as all it is testing is whether $\frac{P_2^{sat}}{P_1^{sat}}$ is appropriate to the $y_i - x_i$ subset; it is otherwise worthless.

2.7.2 Point test

For testing the consistency of individual points, the Point test was developed. Different procedures for conducting the point test were conceived by Liebermann [1972], Van Ness et al. [1973], Dohnal [1985] and Kojima [1990]. The method of Van Ness was utilised as Van Ness *et al.* [1973] and Van Ness *et al.* [1975] recommends that from the P-T-x-y data set, P-T-x data be used to predict the y values. The thermodynamic consistency of the system is judged by the deviations between the predicted and experimental y values, as experimental uncertainty is likely greatest for y. The pressure is represented by Equation (2-125):

$$P^* = \frac{x_1 \gamma_1^* P_1^{sat}}{\Phi_1} + \frac{x_2 \gamma_2^* P_2^{sat}}{\Phi_2} \quad (2-131)$$

where the * denotes a calculated or predicted value.

After regression of the data, using Barker's method, to obtain the parameters that best fit the activity coefficient of choice, the values of y_1 are estimated by Equation (2-19).

$$y_1^* = \frac{x_1 \gamma_1^* P_1^{sat}}{P^*} \quad (2-132)$$

with the error represented by the residual:

$$\Delta y = y_1 - y_1^* \quad (2-133)$$

The quantity Δy is calculated for each data point and an average value established. The residuals reflect the systematic errors in the experimental data. To successfully pass the consistency test, the following two criteria must be met:

- 1) The average Δy values must be less than 0.02.
- 2) The value of Δy must randomly scatter about $\Delta y = 0$ as determined from a plot of Δy versus x.

2.7.3 The Direct Test

Van Ness, 1995 states that although the quantity $\ln(\gamma_1^*/\gamma_2^*)$ itself provides an area test of very limited values; the residuals $\delta(\ln(\gamma_1/\gamma_2))$ offer a unique opportunity for consistency testing. By using $\delta G^E/RT$ as the objective function, the isothermal case becomes:

$$\delta \ln\left(\frac{\gamma_1}{\gamma_2}\right) = x_1 \frac{d \ln \gamma_1^*}{dx_1} + x_2 \frac{d \ln \gamma_2^*}{dx_1} \quad (2-134)$$

The right hand side of this equation is exactly the quantity that Equation (2-128), the Gibbs-Duhem equation, requires to be zero for consistent data. The residual on the left is therefore a direct measure of deviations from the Gibbs-Duhem equation. The departure of the data from thermodynamic consistency is measured by the extent to which the values of this residual fail to scatter about zero.

Van Ness, 1995 show the direct relation of the direct test to the area test for the isothermal case, via the equation:

$$\int_0^1 \delta \ln\left(\frac{\gamma_1}{\gamma_2}\right) dx_1 = -\int_0^1 \left(\ln \frac{\gamma_1^*}{\gamma_2^*}\right) dx_1 \quad (2-135)$$

The integral on the right represents the area test therefore the left hand integral provides an alternate formulation of this test. For this form of the area test, a plot of the residual $\delta \ln(\gamma_1/\gamma_2)$ vs. x_1 is required. The objective function of $\sum [\delta \ln(\gamma_1/\gamma_2)]^2$ is used in the reduction of data, as this causes the residuals to scatter about a horizontal line. Its ordinate is zero when the test is satisfied.

Van Ness [1995] suggests establishing a scale to indicate the quality of a data set as judged by its departure from thermodynamic consistency. The appropriate measurement is the RMS value of $\delta \ln(\gamma_1/\gamma_2)$ from the direct test.

Table 2.4
The Direct Test Scale

Index	RMS $\delta \ln(\gamma_1/\gamma_2)$	Comments
1	$>0 \leq 0.025$	excellent
2	$>0.025 \leq 0.050$	very good
3	$>0.050 \leq 0.075$	good
4	$>0.075 \leq 0.100$	satisfactory
5	$>0.100 \leq 0.125$	poor
6	$>0.125 \leq 0.150$	very poor
7	$>0.150 \leq 0.175$	
8	$>0.175 \leq 0.200$	
9	$>0.200 \leq 0.225$	
10	$>0.225 \leq$	

Van Ness [1995] also recommends plotting experimental values of $\ln \gamma_1^*$, $\ln \gamma_2^*$ and $G^E/RT/x_1x_2$ vs. x_1 as one gets an immediate impression of the quality of a data set by the smoothness of the curves though not necessarily of its consistency.

EQUIPMENT AND PROCEDURE

In order to design effective vapour-liquid separations processes, highly accurate experimental determination of vapour-liquid equilibrium (VLE) data is needed. The equipment and method of measurement utilized to generate these experimental points has to be of the highest quality.

3.1 Equipment

Vapour-liquid equilibria at low pressures can be measured by two common types of equipment that differ in the way equilibrium between the phases is established i.e. dynamic and static equilibrium. For the equilibrium cell, in which static equilibrium between phases is attained, all one need do after loading the cell, is to place it in a constant-temperature bath, agitate to assure equilibrium, measure the pressure in the cell and sample the phases for analysis. However, there is a major disadvantage. The sample must be degassed i.e. freed of all non-condensable gases and the cell thoroughly evacuated before introduction of the sample [Van Ness & Abbott, 1982].

The dynamic equilibrium still as designed by Raal [Raal and Muhlbauer, 1998] was used in this project, as the equipment has proven its efficiency and accuracy in

numerous projects [Joseph, 2001]. Raal and Muhlbauer [1998] provide a detailed review on the development of both the static and dynamic method of measurement.

3.1.1 Vapour-liquid equilibrium still

The vapour-liquid equilibrium still as designed by Raal [Raal & Muhlbauer, 1998] embodies some of the features of the Yerazunis et al. [1964] design. A schematic diagram of the still can be found in Figure 3-1. A central feature of the design is the packed equilibrium chamber, which is concentric around a vacuum-insulated Cottrell tube. The Cottrell tube discharges onto a temperature-sensing element (e.g. Pt-100). Packing material of an open structure and therefore producing low-pressure drop, such as miniature stainless steel wire mesh cylinders of 3 mm dimensions, is used. An advantage of the design is that the packing is readily accessible by removal of the ground glass joint holding the temperature sensor, a feature that is not present in the Yerazunis et al. design. This allows an increase in the depth of the inert glass packing to accommodate systems that have difficulty in reaching equilibrium

An interesting feature of the central Cottrell tube design is that the equilibrium chamber is angularly symmetric and thus there is no preferred radial direction for the concentration or temperature gradients to develop. The equilibrium mixture exits through small holes in the bottom of the equilibrium chamber. Equilibrium liquid flows downward over a glass or stainless steel mixing spiral through a small liquid trap, and is returned to the boiling chamber. The disengaged equilibrium vapour flows upward around the equilibrium chamber and fulfils a vital thermal lagging function. The entire upper portion of the still is in addition insulated with a vacuum jacket.

The vacuum-jacketed Cottrell tube is a novel feature. In addition to reducing heat losses at its lower end, it serves the vital function of insulating the equilibrium region from any superheat effects associated with the upward flowing liquid-vapour mixture. Efficient magnetic stirring has been incorporated into both the condensate receiver and the boiling chamber, as they are vital for accurate functioning of any equilibrium still. Stirring in the condensate receiver eliminates temperature and any possible concentration gradients and leads to high reproducibility of sample concentrations.

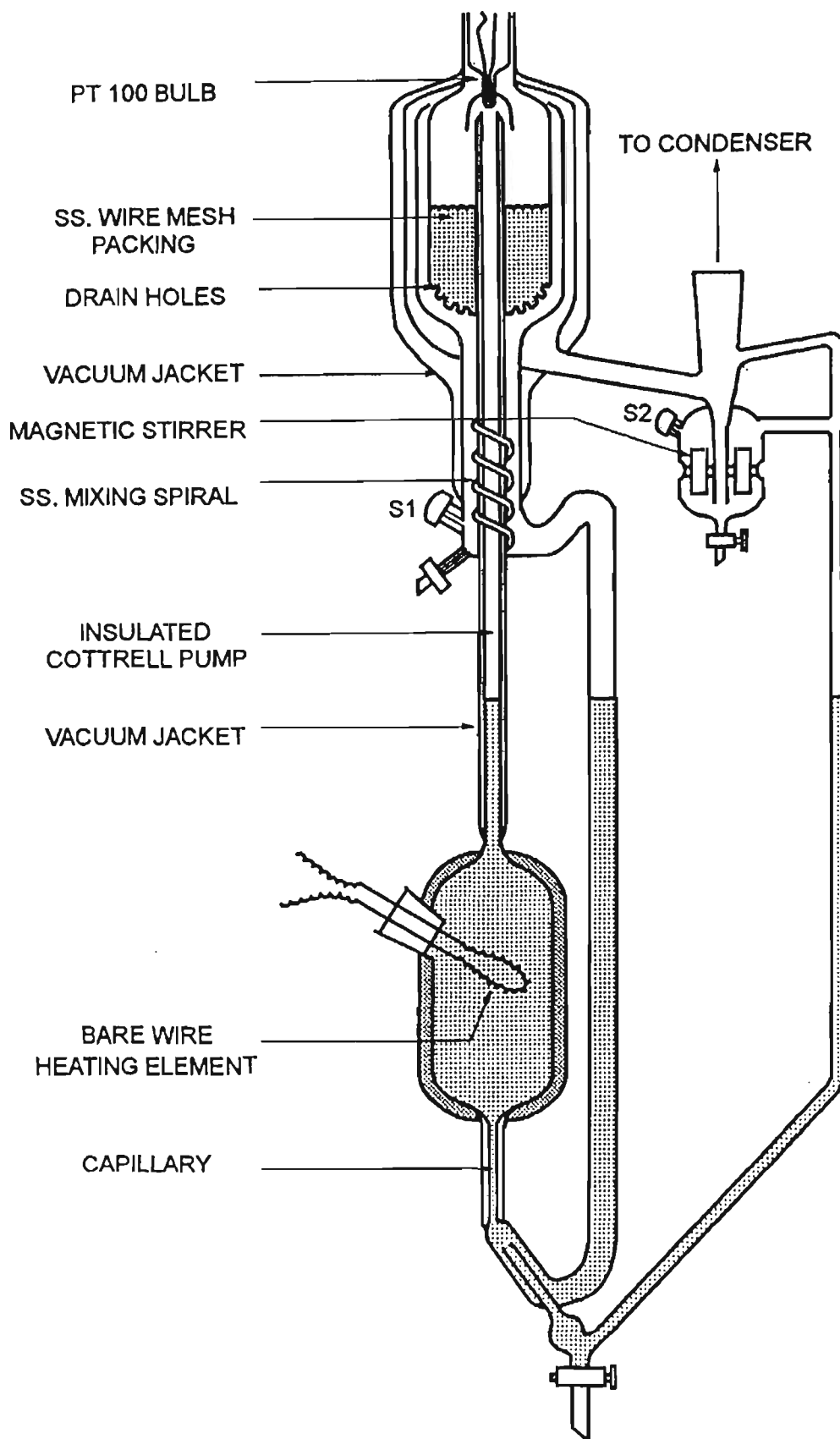


Figure 3.1: Vapour-liquid equilibrium still as designed by Raal [Raal & Muhlbauer, 1998]

The condensed vapour flows to the bottom of the condensate receiver via split downcomers. The stirrer paddle is made of a soft iron core encased in either stainless steel or glass and has a stainless steel spindle held in place by the glass dimples. Magnets, mounted on a small MAXXON DC stirring motors, drive the stirrers.

Stirring in the boiling chamber, effected by a stirrer similar to that for the condensate, rich in the more volatile component, is thoroughly mixed with other liquid before evaporation. This prevents flashing, a common problem in earlier designs.

The still has both external and internal heaters in the boiling chamber. The latter provides very rapid boiling, allows for very precise control of circulation rate, and offers nucleation sites for smooth boiling. The whole assembly is remarkably robust.

Liquid and vapour condensate samples are simultaneously taken with a gas-tight syringe using the sample septa, S1 and S2 as shown in Figure 3.1. Sampling presents no problems unless the system pressure is less than that can be achieved in the syringe. Sampling does not disturb operation of the still.

Pressure control, through the top of the condenser, is via an electronic manostat utilizing a pressure transducer and solenoid valve. A ballast flask together with a controller and a vacuum pump smooth any pressure fluctuations.

3.2 Procedure

3.2.1 Detection of leaks

Initially the vacuum pump withdrew air from the VLE still and controlled the pressure in the system to a specified value via a pressure controller. Once the pressure stabilised, the pump and controller were switched off and the equipment was isolated. An increase in pressure would give an indication of the presence of a leak in the still.

3.2.2 Cleaning of the VLE still

Cleaning of the apparatus is conducted by circulating acetone in the VLE still under isobaric control. Approximately 40 minutes of rapid boiling is required. The acetone is drained and the residual acetone flashed off with the aid of the vacuum pump. This procedure is repeated to ensure effective removal of all impurities.

3.2.3 Calibration of the pressure sensor

The pressure controller used for pressure control was the KNF vacuum pump-controller unit (type NC800). The controller was calibrated with the aid of a NIST (National Institute of Standards and Technology) certified electronic barometer (model PTB100A) and a differential mercury manometer, which was connected to the VLE still. During isobaric operation, the pressure difference between the barometer and manometer readings was compared to the pressure obtained by the vacuum pump. Using this relationship which can be found in Figure 3.2 below, the still could be operated at true pressure. The accuracy of the pressure measurement is approximately ± 0.05 kPa.

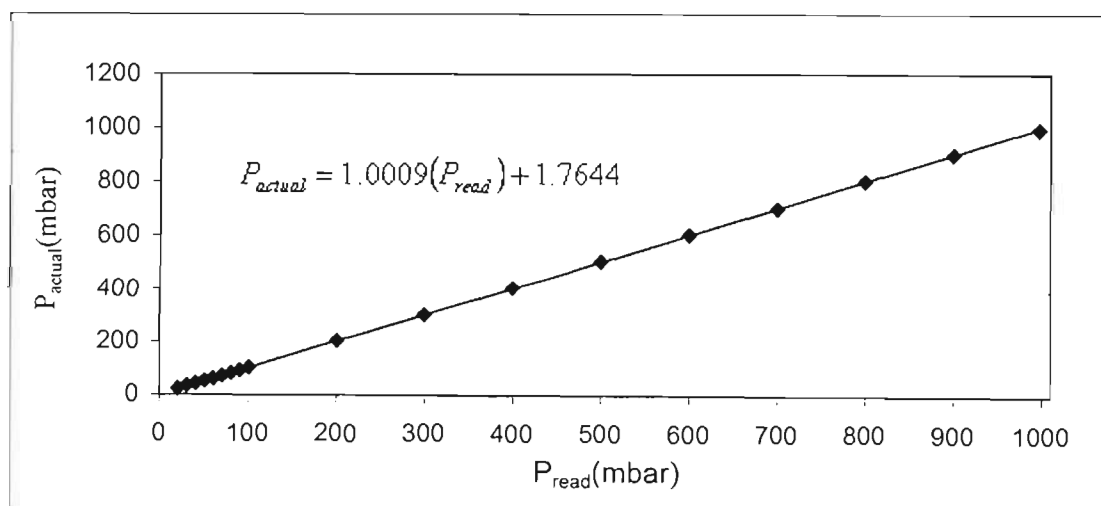


Figure 3.2: Plot of P_{actual} vs. P_{read} on KNF pressure controller

3.2.4 Calibration of the temperature sensor

The temperature of the component/s boiling in the still is obtained from the Pt-100 temperature sensor housed in the still. The temperature probe is connected to a display screen. The VLE still is filled with a chemical of purity greater than 99.6%. Under isobaric conditions, the vapour pressure of the chemical is measured and recorded at various pressures. These temperatures were compared to the temperatures predicted by the Reid equation and a relationship between the true and displayed temperature was formed. The accuracy of the temperature measurement is approximately ± 0.02 °C.

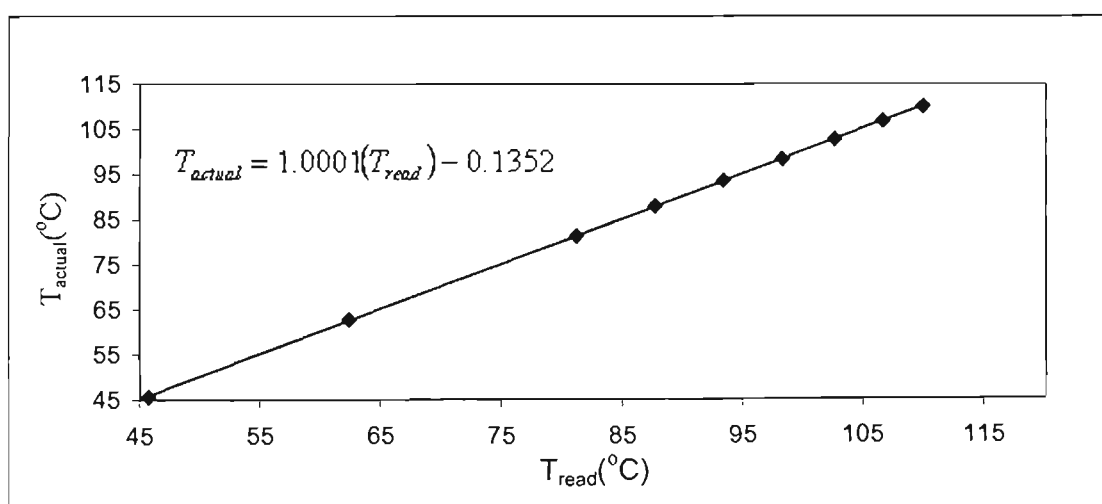


Figure 3.3: Plot of T_{actual} of Pt-100 sensor vs. T_{read} on display

3.2.5 Calibration of the gas chromatographs (GCs)

The response factor F is defined as the proportionality constant between the number of moles passing the detector and the peak area A , obtained from, e.g. an electronic integrator:

$$n_i = A_i F_i \quad (3-1)$$

Given that the area A depends on the amount of sample injected, which is not generally very reproducible, it is advisable to work only with area ratios:

$$\frac{n_1}{n_2} = \left(\frac{A_1}{A_2} \right) \left(\frac{F_1}{F_2} \right) = \frac{x_1}{x_2} \quad (3-2)$$

where x_i is the mole fraction of component i .

The response factor ratio (F_1/F_2) is not in general constant over large composition ranges, even when very small amounts of liquid sample are injected to avoid detector overloading. It is therefore advisable for mixture calibration to plot area ratios for pairs of components versus their mole fraction ratios over the entire composition range. A plot of (A_1/A_2) vs. (x_1/x_2) should extrapolate through the origin and the slope, (F_1/F_2) should equal the inverse of the slope (F_2/F_1). This implies the response factor ratios are exactly constant over the full composition range.

Plots of (A_1/A_2) vs. (x_1/x_2) for all binary systems measured can be found in Appendix C and the test system of cyclohexane + ethanol can be found in Figure 3.4 and 3.5. For each system, it can be seen that the gradient of (A_1/A_2) vs. (x_1/x_2) is sufficiently close in value to the reciprocal of (A_2/A_1) vs. (x_2/x_1). The accuracy of the composition measurement is approximately ± 0.001 mole fraction.

The specifications and operating conditions of the GCs used to analyse samples drawn from the VLE still are documented in Table 3.1.

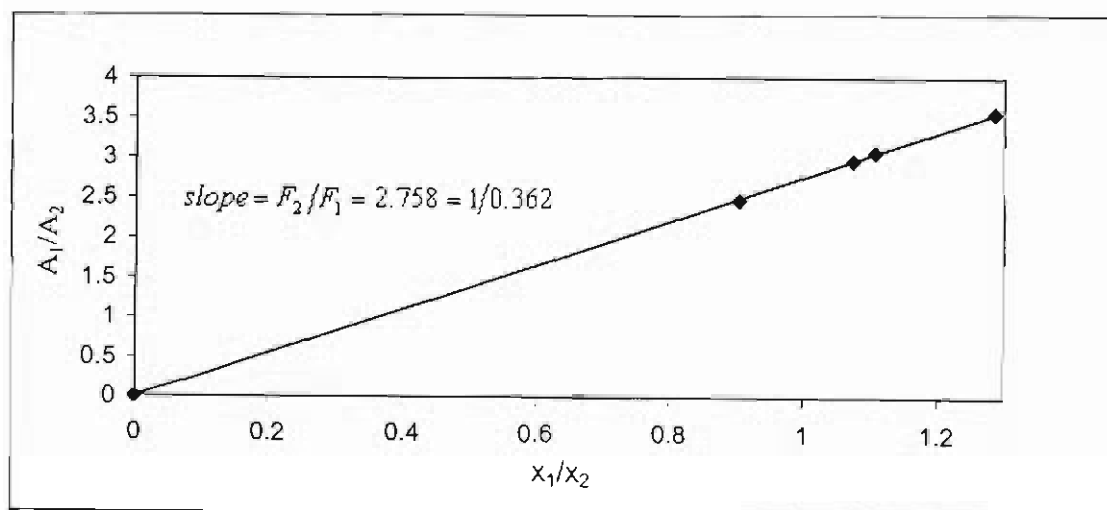


Figure 3.4: Plot of A_1/A_2 vs. x_1/x_2 for cyclohexane + ethanol

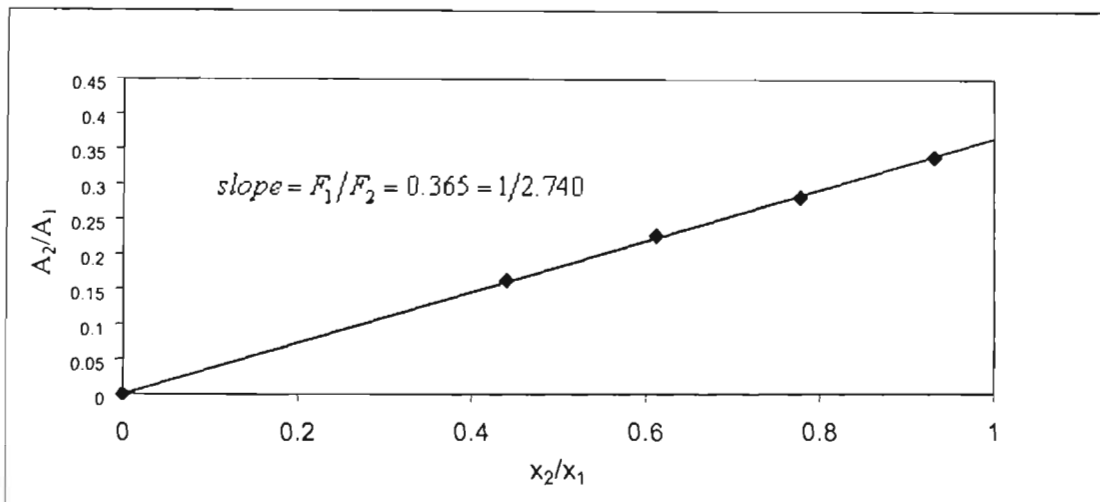


Figure 3.5: Plot of A_2/A_1 vs. x_2/x_1 for cyclohexane + ethanol

Table 3.1: Gas chromatograph specifications and operating conditions

System	GC	Column	Detector	Operating Conditions
1-hexene + NMP	Shimadzu GC-17A	Capillary Column	FID	Column Temperature 35 °C
		J&W Scientific GS-Q		Column Pressure 20 kPa
				Detector Temperature 200 °C
				Injector Temperature 200 °C
Water + NMP	Shimadzu GC-17A	Capillary Column	FID	Column Temperature 35 °C
		J&W Scientific GS-Q		Column Pressure 20 kPa
				Detector Temperature 200 °C
				Injector Temperature 200 °C
1-hexene + 3MCP	Chrompack 9000	Capillary Column	FID	Column Temperature 220 °C
		J&W Scientific GS-Q		Detector Temperature 150 °C
				Injector Temperature 100 °C

3.2.6 Procedure to obtain isothermal or isobaric measurements

Initially the VLE still was charged with a pure component. Once the cooling water supply, the vacuum pump, the temperature display and the Varian heaters were turned on, the voltage settings on the heaters and the pressure pump were manipulated to obtain the desired temperature in the isothermal case or pressure in the isobaric case. The power input to the boiling chamber was adjusted to the plateau region [Kneisl et al, 1989] to avoid erroneous boiling readings and to provide a good boil up rate. This ensured proper circulation and mixing of the components. The equilibration time differs for many binaries, therefore it was considered wiser to test the composition of the vapour and liquid at regular intervals. Once the results of the analyses were replicated, equilibrium had been reached and the final vapour and liquid compositions, together with the pressure and temperature of the system were recorded. To cover the entire composition range, in a binary system, the amount of the second component was increased in the still. For each addition, the above procedure was repeated.

EXPERIMENTAL RESULTS

Chapter four showcases the very heart of this thesis, the results obtained from the low pressure vapour liquid equilibrium experiments for the systems 1-hexene + NMP, water + NMP and 1-hexene + 3MCP. These results are preceded by isothermal and isobaric measurements for the system cyclohexane + ethanol which serve as a test of accuracy of the experimental equipment.

4.1 Data for Test System: Cyclohexane +Ethanol

The test system of cyclohexane +ethanol was measured at 50 °C and 40 kPa. The experimental data is shown in Table 4.1-4.2 and represented graphically in Figures 4.1-4.4.

Table 4.1: VLE data for cyclohexane (1) + ethanol (2) at 50 °C

P (kPa)	x_1	y_1	P (kPa)	x_1	y_1
29.15	0	0	56.95	0.728	0.617
39.35	0.052	0.236	56.45	0.805	0.628
45.29	0.080	0.379	55.15	0.899	0.648
53.05	0.184	0.508	49.85	0.970	0.751
56.15	0.399	0.555	47.45	0.985	0.789
56.65	0.423	0.567	38.15	1	0.963
57.05	0.507	0.574	36.35	1	1
57.35	0.549	0.582			
57.45	0.608	0.595			
57.35	0.659	0.602			

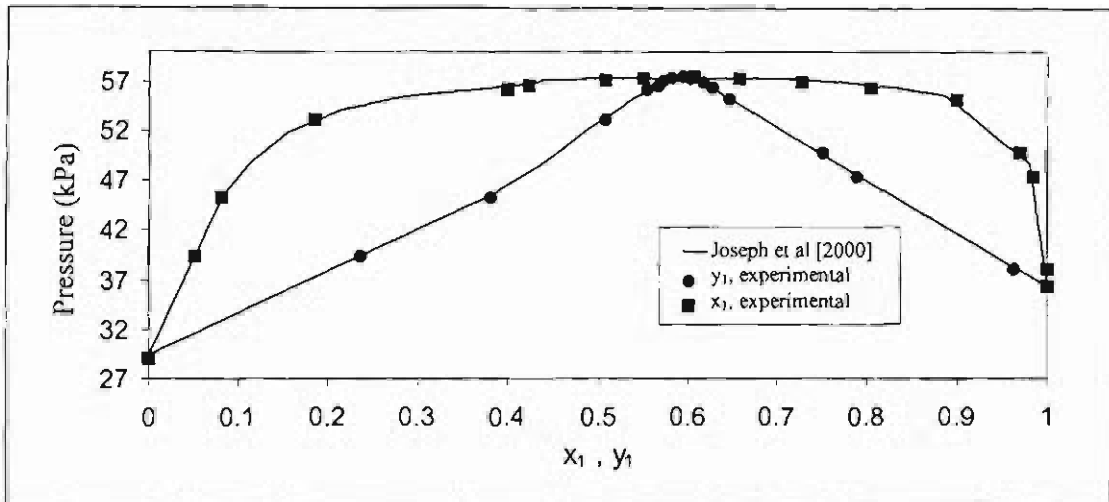


Figure 4.1: Plot of P vs. x, y for cyclohexane (1) + ethanol (2) at 50 °C

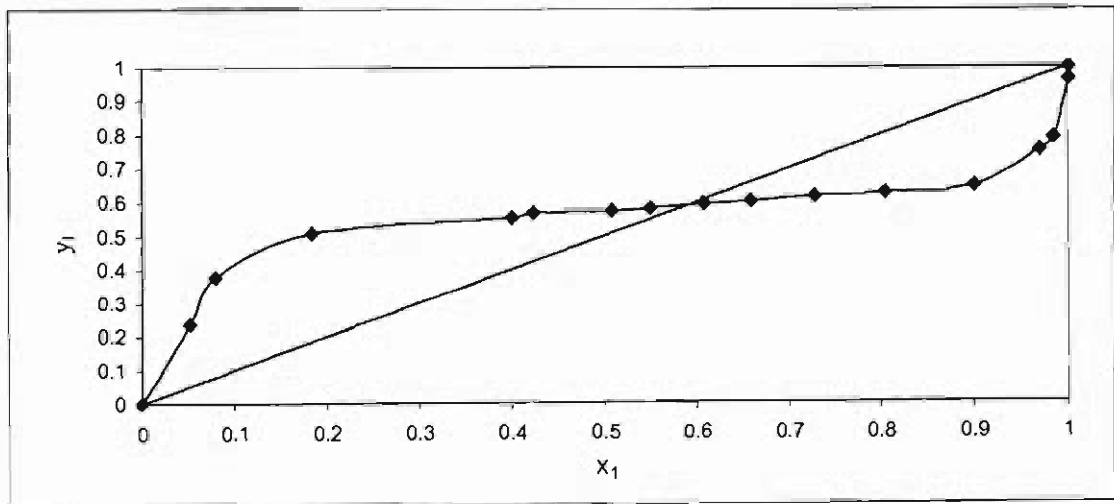


Figure 4.2: Plot of y vs. x for cyclohexane (1) + ethanol (2) at 50 °C

Table 4.2: VLE data for cyclohexane (1) + ethanol (2) at 40 kPa

T (K)	x_1	y_1	T(K)	x_1	y_1
329.52	0	0	314.60	0.616	0.629
325.84	0.023	0.162	314.64	0.718	0.623
323.69	0.042	0.248	317.71	0.962	0.746
319.79	0.096	0.388	318.77	0.979	0.777
316.34	0.199	0.527	322.86	0.989	0.907
315.74	0.248	0.554	324.23	0.997	0.947
314.69	0.472	0.627	325.67	1	1

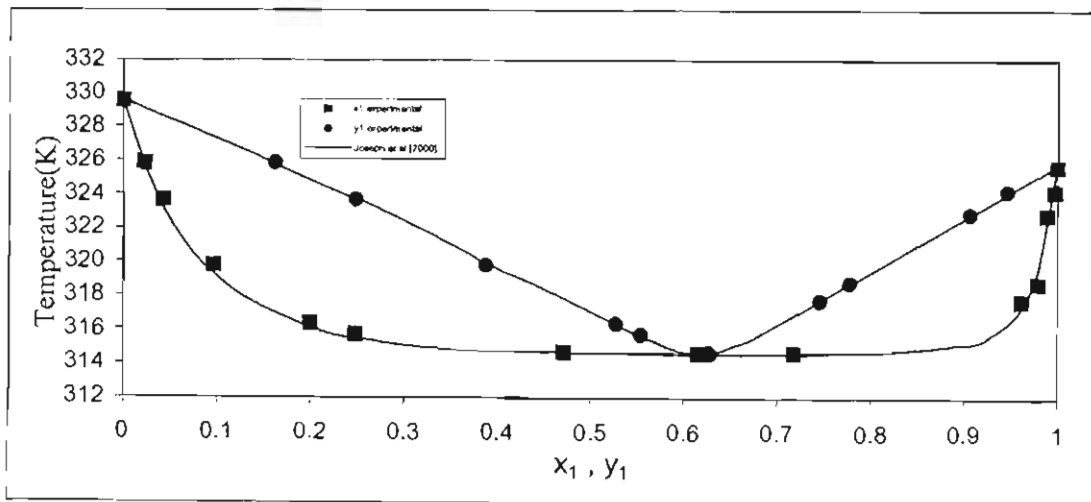


Figure 4.3: Plot of P vs. x, y for cyclohexane (1) + ethanol (2) at 40 kPa

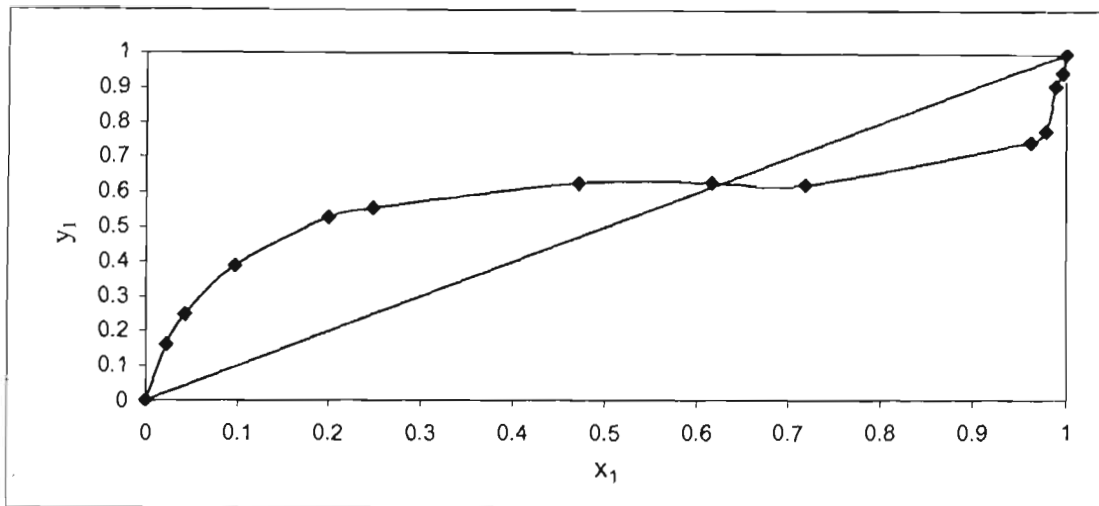


Figure 4.4: Plot of y vs. x for cyclohexane (1) + ethanol (2) at 40 kPa

4.2 Data for System: Water +NMP

The system of water + NMP was measured at 70, 90 and 107 °C. The experimental data is shown in Table 4.3-4.5 and represented graphically in Figures 4.5- 4.10.

Table 4.3: VLE data for water (1) +NMP (2) at 70 °C

P (mbar)	x_1	y_1	P (mbar)	x_1	y_1
7.94	0	0	192.94	0.657	0.993
90.12	0.340	0.948	216.97	0.733	0.994
126.88	0.462	0.968	248.99	0.812	0.996
147.89	0.523	0.980	284.02	0.923	0.996
174.92	0.605	0.989	311.04	1	1

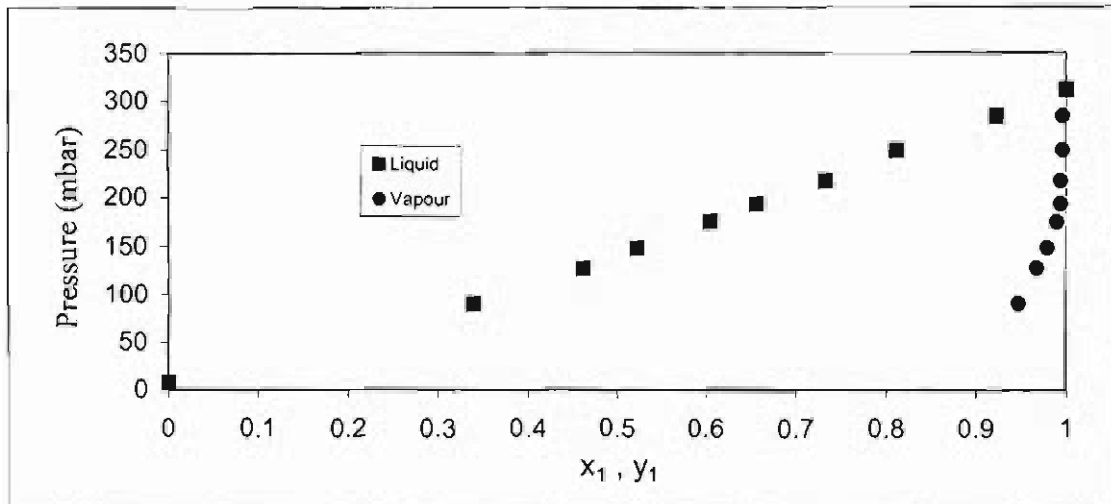


Figure 4.5: Plot of P vs. x, y for water (1) + NMP (2) at $70\text{ }^\circ\text{C}$

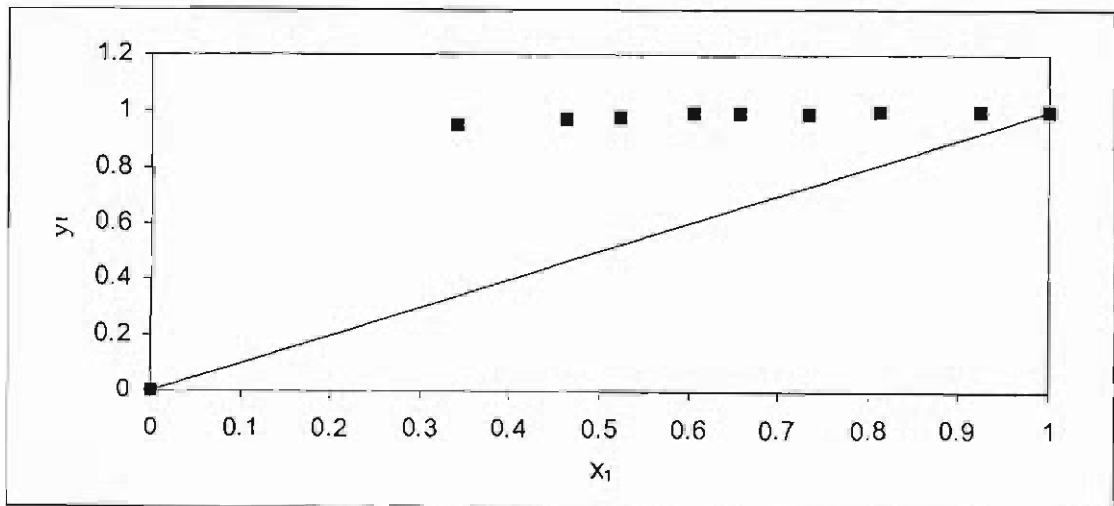


Figure 4.6: Plot of y vs. x for water (1) + NMP (2) at $70\text{ }^\circ\text{C}$

Table 4.4: VLE data for water (1) NMP (2) at 90 °C

P (mbar)	x_1	y_1	P (mbar)	x_1	y_1
21.7	0	0	452.17	0.674	0.991
113.86	0.182	0.843	540.42	0.782	0.995
208.95	0.322	0.936	617.32	0.879	0.997
260.93	0.407	0.954	672.37	0.959	0.998
348.08	0.519	0.971	701.39	1	1

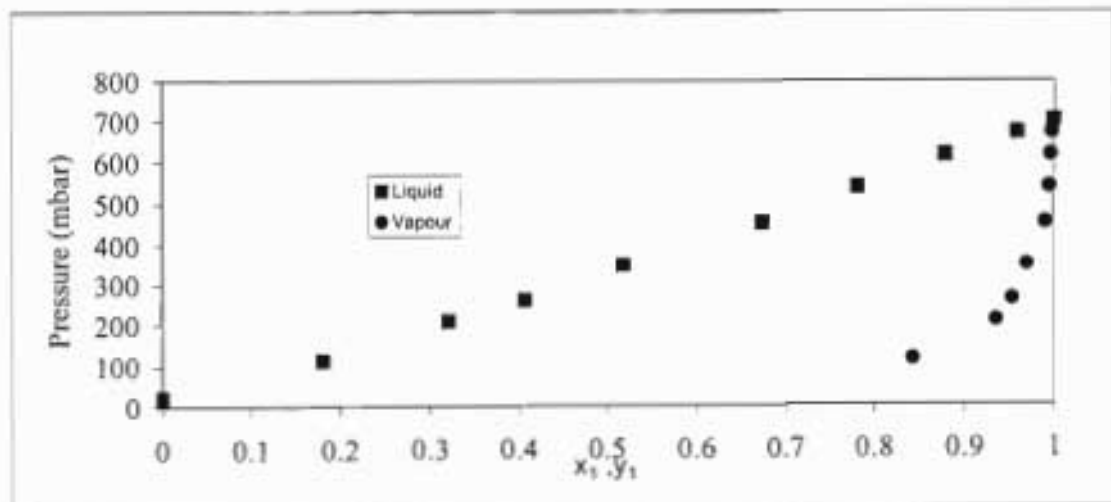


Figure 4.7: Plot of P vs. x, y for water (1) +NMP (2) at 90 °C

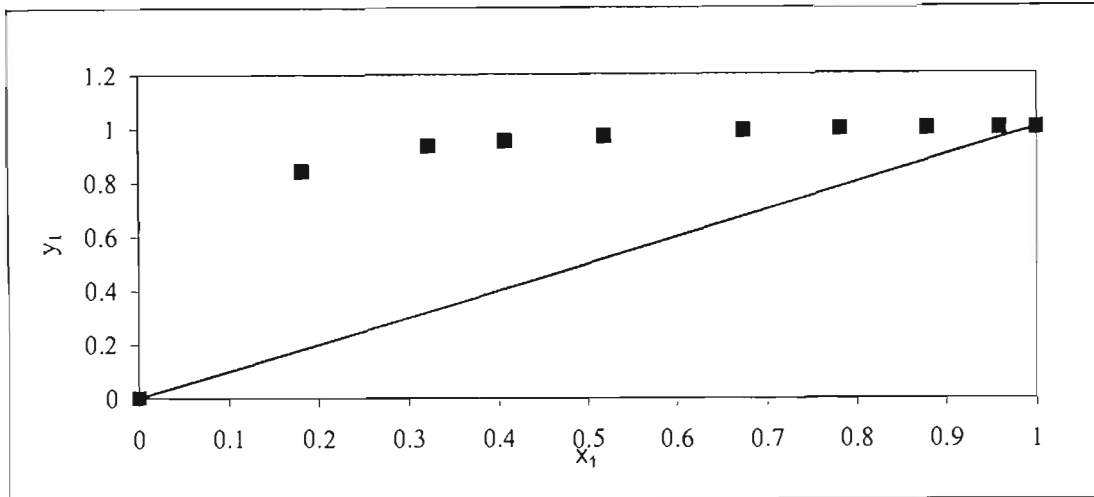


Figure 4.8: Plot of y vs. x for water (1)-NMP (2) at 90 °C

Table 4.5: VLE data for water (1) +NMP (2) at 107 °C

P (mbar)	x_1	y_1	P (mbar)	x_1	y_1
49.81	0	0	630.33	0.472	0.966
172.92	0.120	0.767	681.37	0.504	0.971
302.03	0.231	0.879	779.46	0.577	0.980
442.16	0.330	0.927	910.29	0.682	0.985
540.71	0.452	0.948	1299	1	1

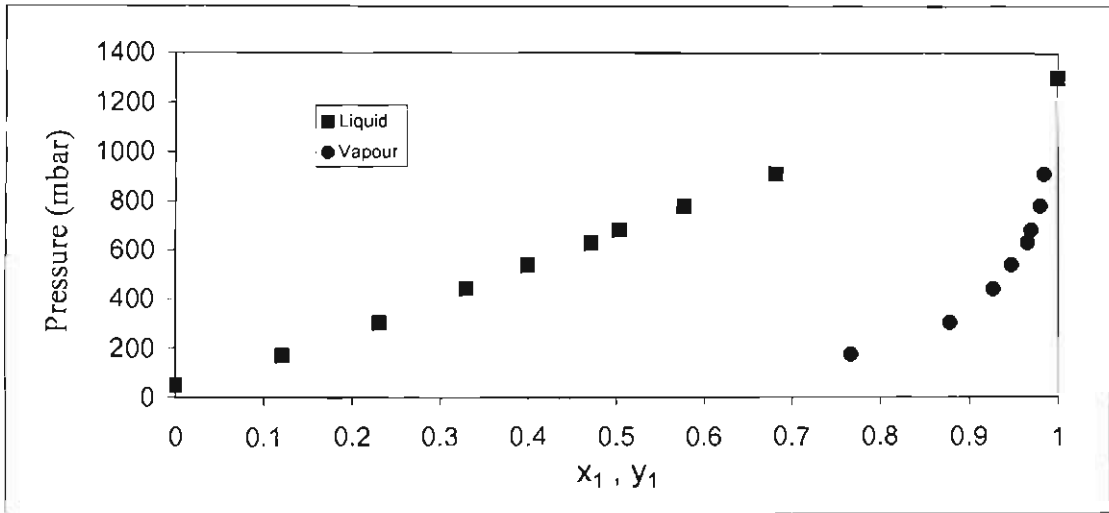


Figure 4.9: Plot of P vs. x, y for water (1) +NMP (2) at 107 °C

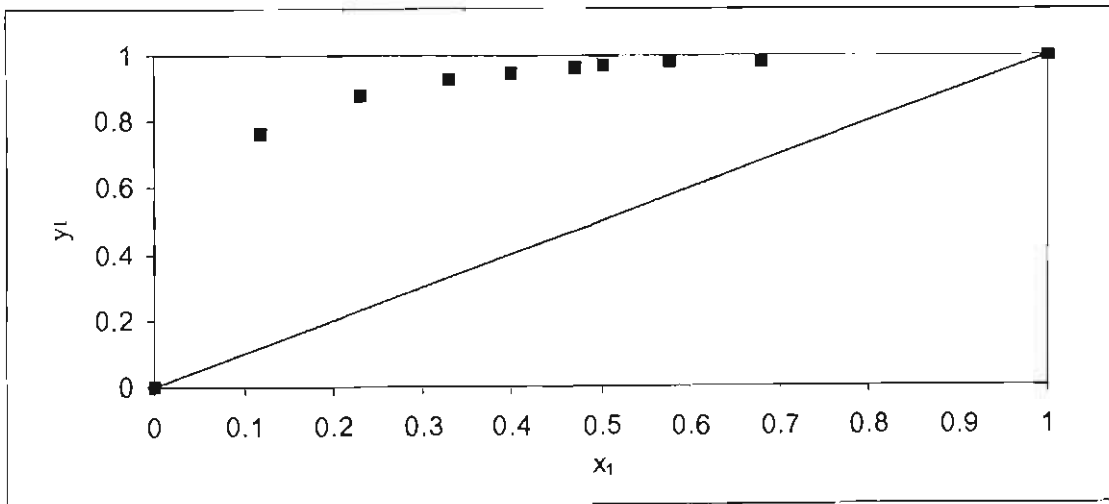


Figure 4.10: Plot of y vs. x for water (1) +NMP (2) at 107 °C

4.3 Data for System: 1-Hexene +NMP

The system of 1-hexene - NMP was measured at 40, 62 and 90 °C. The experimental data is shown in Table 4.6-4.8 and represented graphically in Figures 4.11 to 4.16.

Table 4.6: VLE data for 1-hexene +NMP at 40 °C

P (mbar)	x_1	y_1	P (mbar)	x_1	y_1
1.31	0	0	407.61	0.666	0.998
303.17	0.212	0.996	420.68	0.811	0.998
332.82	0.295	0.996	434.77	0.948	0.998
375.22	0.468	0.997	450.07	1	1
390.45	0.543	0.997			

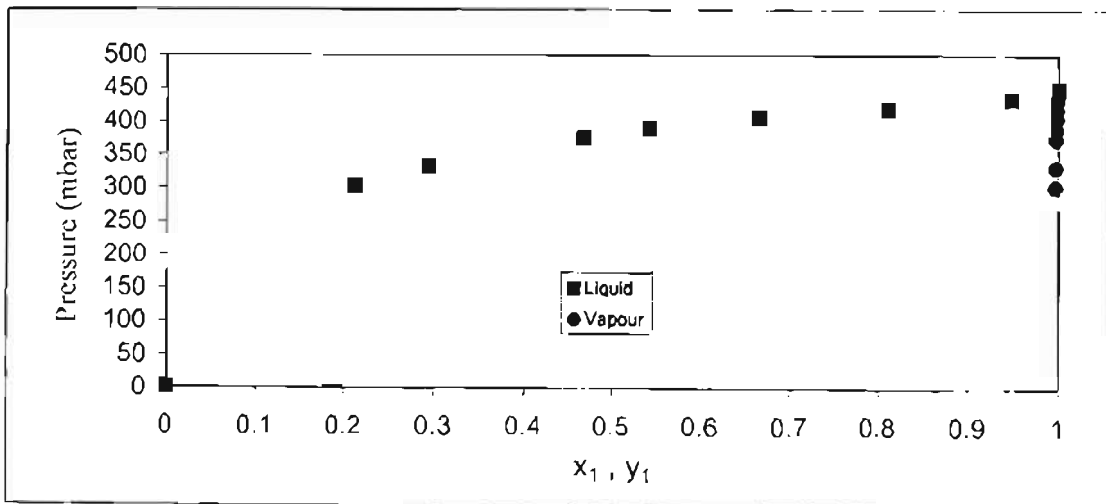


Figure 4.11: Plot of P vs. x_1, y_1 for 1-hexene (1) +NMP (2) at 40 °C

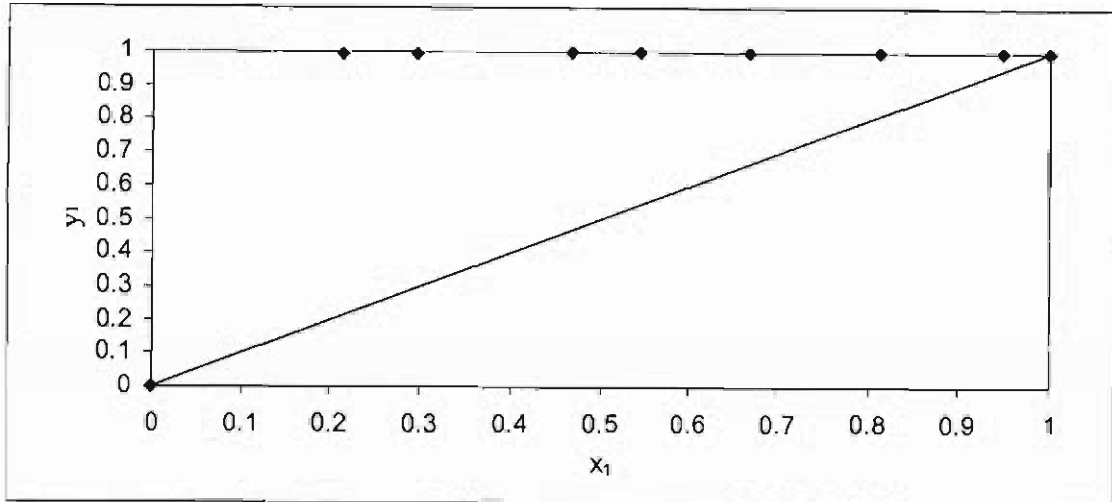


Figure 4.12: Plot of y vs. x for 1-hexene (1) +NMP (2) at 40 °C

Table 4.7: VLE data for 1-hexene (1) +NMP (2) at 62 °C

P (mbar)	x_1	y_1	P (mbar)	x_1	y_1
5.1	0	0	906.521	0.715	0.999
392.12	0.103	0.990	908.845	0.729	0.996
449.18	0.129	0.991	910.265	0.748	0.994
560.26	0.202	0.991	913.584	0.762	0.996
672.35	0.309	0.991	915.760	0.783	0.992
738.42	0.384	0.992	919.581	0.819	0.995
817.48	0.502	0.992	922.432	0.845	0.996
853.53	0.578	0.993	924.585	0.881	0.997
863.54	0.590	0.991	928.592	0.896	0.997
869.55	0.607	0.994	934.608	0.935	0.998
882.56	0.650	0.994	952.616	0.989	0.998
900.58	0.695	0.999	965.628	1	1

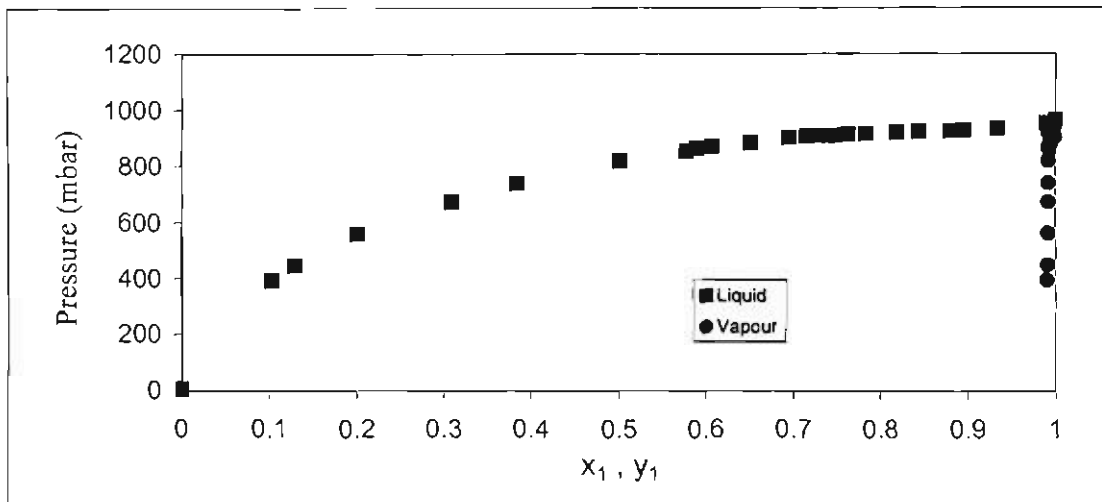


Figure 4.13: Plot of P vs. x, y for 1-hexene (1) +NMP (2) at 62 °C

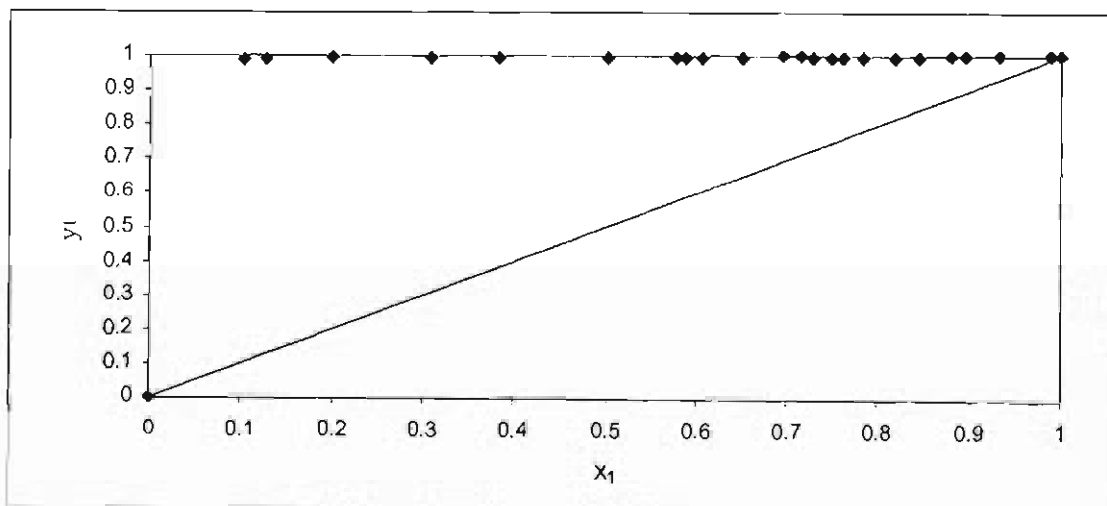


Figure 4.14: Plot of y vs. x for 1-hexene (1) +NMP (2) at 62 °C

Table 4.8: VLE data for 1-hexene (1) +NMP (2) at 90 °C

P (mbar)	x_1	y_1
21.78	0	0
138.89	0.013	0.845
256.99	0.027	0.915
352.01	0.038	0.941
544.09	0.064	0.969
719.41	0.091	0.971
853.00	0.110	0.978
962.63	0.133	0.980
2185.87	1	1

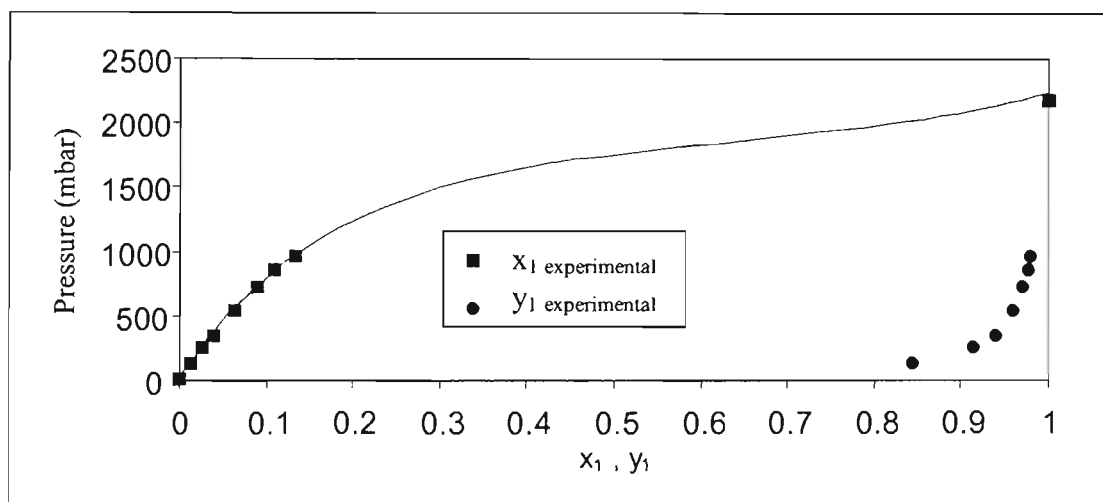


Figure 4.15: Plot of P vs. x, y for 1-hexene (1) +NMP (2) at 90 °C

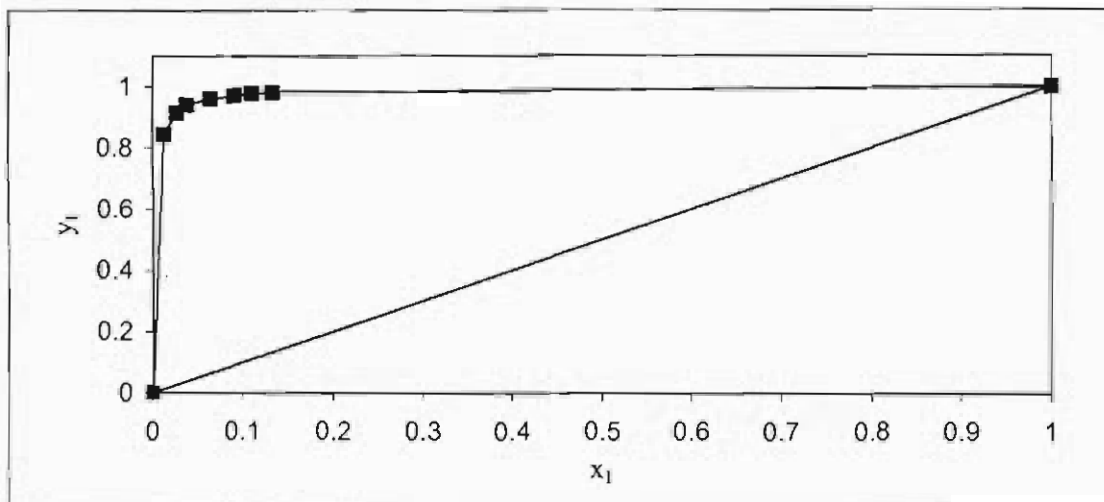


Figure 4.16: Plot of y_1 vs. x_1 for 1-hexene (1) + NMP (2) at 90 °C

4.4 Data for System: 1-Hexene +3MCP

The system of 1-hexene +3MCP was measured at 40, 50 and 60 °C. The experimental data is shown in Table 4.9-4.11 and represented graphically in Figures 4.17-4.22.

Table 4.9: VLE data for 1-hexene (1) +3MCP (2) at 40 °C

P (mbar)	x_1	y_1
428.40	0	0
442.82	0.729	0.729
445.66	0.847	0.845
446.89	0.894	0.898
448.34	0.933	0.933
449.21	0.963	0.960
450.07	1	1

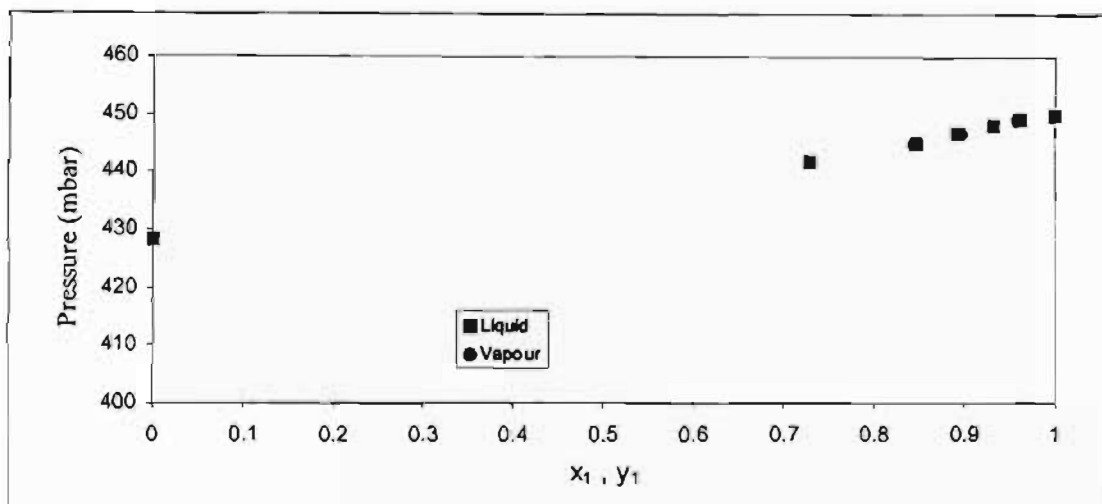


Figure 4.17: Plot of P vs. x, y for 1-hexene (1) +3MCP (2) at 40 °C

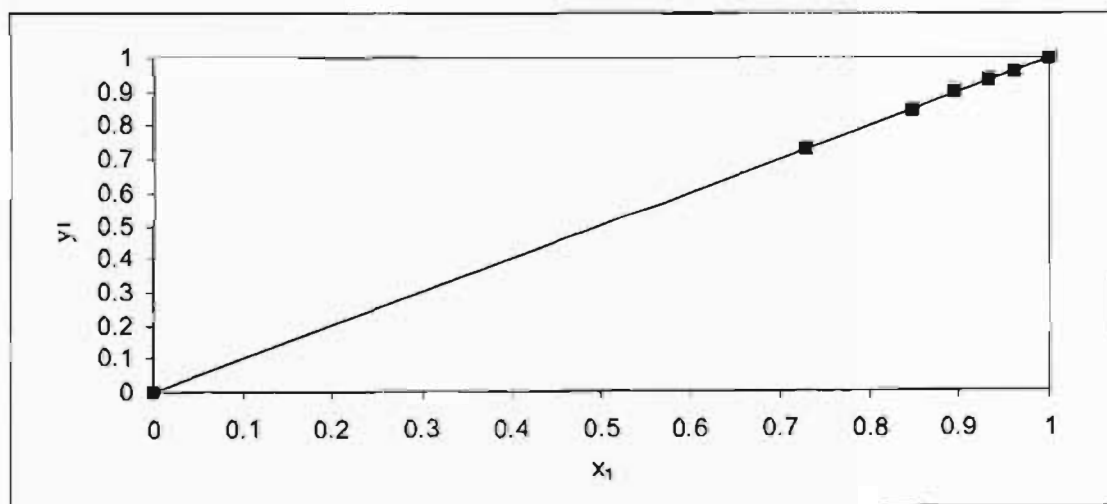


Figure 4.18: Plot of y vs. x for 1-hexene (1) +3MCP (2) at 40 °C

Table 4.10: VLE data for 1-hexene (1) +3MCP (2) at 50 °C

P (mbar)	x_1	y_1
615.80	0	0
637.33	0.817	0.820
638.03	0.851	0.860
639.34	0.897	0.896
641.64	0.938	0.938
643.85	0.974	0.975
646.35	1	1

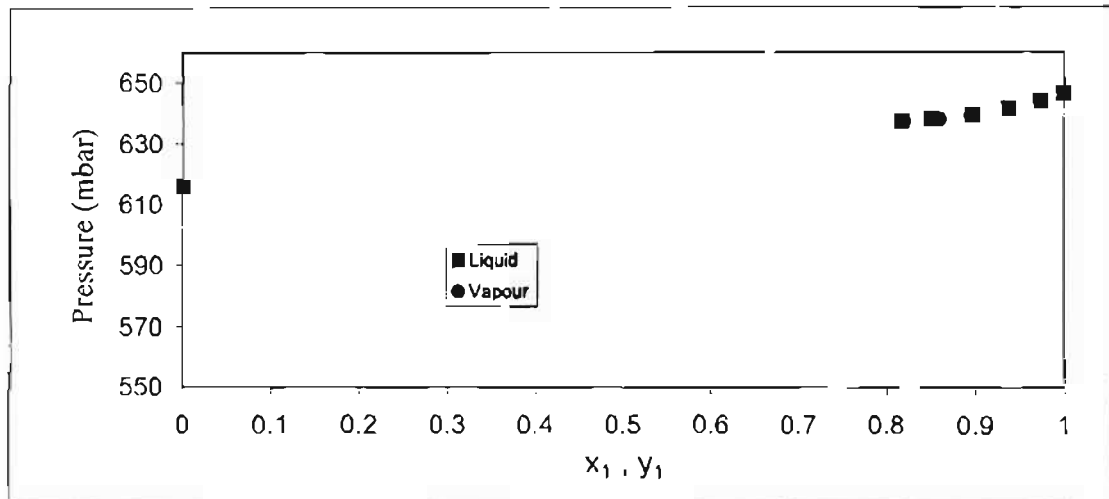


Figure 4.19: Plot of P vs. x, y for 1-hexene (1) +3MCP (2) at 50 °C

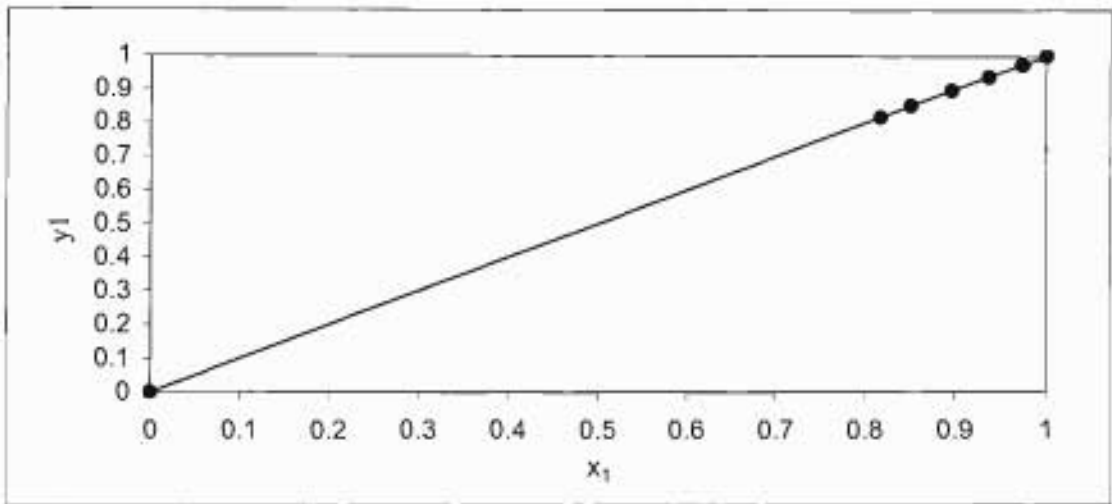


Figure 4.20: Plot of y vs. x for 1-hexene (1) +3MCP (2) at 50 °C

Table 4.11: VLE data for 1-hexene (1) +3MCP (2) at 60 °C

P(mbar)	x_1	y_1
863.03	0	0
893.80	0.855	0.862
896.57	0.896	0.904
899.57	0.943	0.938
902.72	0.977	0.977
905.83	1	1

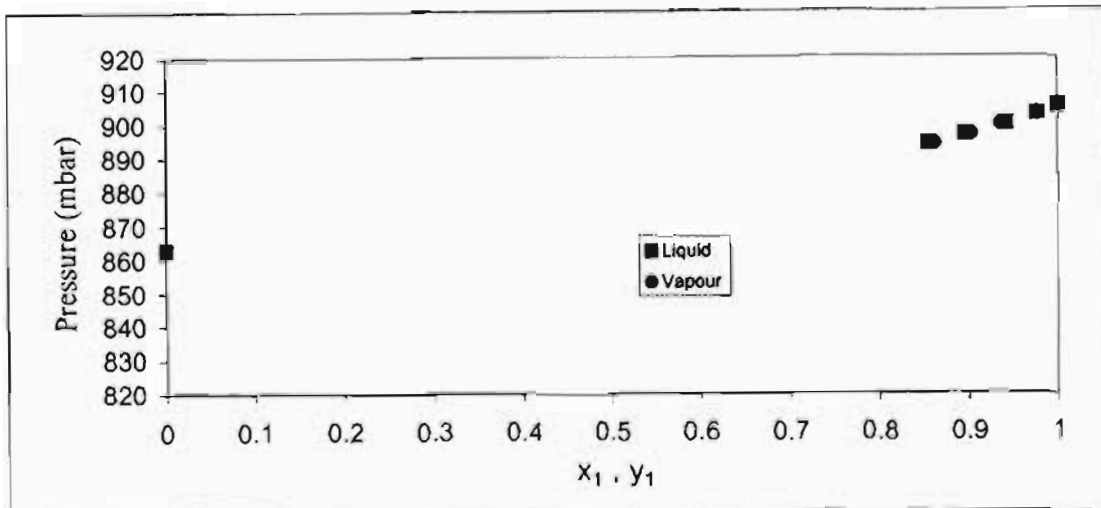


Figure 4.21: Plot of P vs. x,y for 1-hexene (1) +3MCP (2) at 60 °C

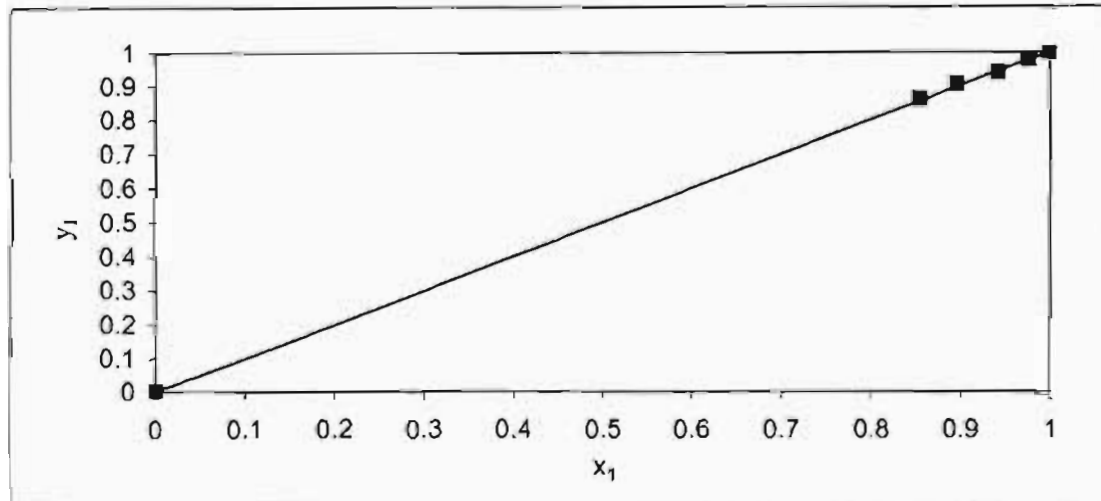


Figure 4.22: Plot of y vs. x for 1-hexene (1) +3MCP (2) at 60 °C

DISCUSSION

The following points were outlined as the objectives of this study and their results will be discussed in detail in this chapter:

- 1) Measure full Vapour-Liquid Equilibrium(VLE) data sets (P-T-x-y) for the binary combinations of 1-hexene + n-methylpyrrolidone(NMP), water + NMP and 1-hexene + 3methycyclopentene(3MCP)
- 2) Undertake comprehensive correlations of measured data using various Gibbs excess energy models and VLE methods such as the direct and combined (gamma-phi) methods.
- 3) Test the thermodynamic consistency of measured VLE data
- 4) Temperature dependence of thermodynamic modelled parameters
- 5) Verify experimental data that is currently available

5.1 Chemicals

Chemicals used in this study were 1-hexene, n-methylpyrrolidone (NMP), distilled water and 3-methycyclopentene (3MCP). Table 5.1 is a summary of the quality of the chemicals. For the chemicals 1-hexene and water, gas chromatograph (GC) analyses

show no significant impurities and the chemicals were used with no further purification. The chemical purity of 3-methylcyclopentene was found to be 96% from the GC analyses. High purity 3MCP was commercially unavailable but due to the necessity of measuring and modelling the 1-hexene + 3MCP system for the 1-hexene plant, VLE measurements and modelling was undertaken for the system.

Table 5.1: Chemical Analysis

Name	Formula	GC Peak Area %
1-hexene	C ₆ H ₁₂	99.09
NMP	C ₅ H ₉ NO	99.5
Water	H ₂ O	100
3MCP	C ₆ H ₁₀	96

5.2 Thermodynamic Modelling

The analysis of the experimental data was completed in two parts, the combined method and the direct method. A detailed breakdown of the equations and theory behind these methods are laid out in Chapter 2.

The combined (γ - ϕ) method accounts for the vapour phase deviation from ideal gas behaviour using the fugacity coefficient and accounts for the liquid phase deviation from ideal solution behaviour using the activity coefficient. In the direct regression method the non-idealities of both the vapour and liquid phase are described by fugacity coefficients represented by equations of state (EOS).

A comprehensive examination of the experimental results was undertaken for this project. Thermodynamic modelling included both the direct and combined method graphically shown in Chapter 2, Figures 2.1 and 2.2. Due to the iterative nature of the calculation, the Matlab program was used to perform the computations. In this section, Tables 5.4 to 5.8 document the results from these two methods, and include all activity coefficient model parameters at each temperature.

The activity coefficient models used in the modelling were the Wilson, NRTL, Van Laar and Uniquac models. The best fit model chosen to represent the system at a

specified temperature was based on the lowest optimised ΔP values. A summary of the modelled results is found below in Table 5.3. The NRTL model dominates the results as the model is the most flexible of all the activity coefficient models investigated due to the third alpha parameter it contains. The sections that follow i.e. 5.2.1 and 5.2.2 provide the graphical view of the experimental data against the regressed model. These plots are of pressure vs. composition (P vs. x, y) and y vs. x.

Both the direct and combined method of modelling requires pure component properties such as critical properties, dipole moments and accentric factors to accurately predict coefficients. These properties as well as their source of information can be found in Table 5.2 below.

Table 5.2: Pure Component Properties

Property	Source	1-Hexene	NMP	Water	3MCP
Critical Pressure (bar)	Reid et al.[1988]	31.7	44.6	221.2	37.78
Critical Temperature (K)	Reid et al.[1988]	504	721.7	647.3	523.2
Critical Volume (m ³ /kmol)	Reid et al.[1988]	350	310.8	57.1	306.8
Critical Compressibility Factor	Reid et al.[1988]	0.265	0.231	0.235	0.269
Dipole Moment (debyes)	Reid et al.[1988]	0.4	4.09	1.8	0
Accentric Factor	Prausnitz et al. [1980]	0.23	0.19	0.01	0.18

Table 5.3: Summary of the best fit models

Activity Coefficient Model	water (1) + NMP (2)			1-hexene(1) + NMP(2)			1-hexene(1) + 3MCP (2)		
	70	90	107	40	62	90	40	50	60
Combined Method	NRTL	NRTL	NRTL	NRTL	NRTL	NRTL	NRTL	NRTL	NRTL
Direct Method Wong Sandler-SRK	Van Laar	Van Laar	Van Laar	NRTL	NRTL	Uniquac	Van Laar	NRTL	Van Laar
Direct Method Wong-Sandler-PRSV	Uniquac	Van Laar	Van Laar	Wilson	NRTL	Uniquac	NRTL	Van Laar	Van Laar
Direct Method Twu-Coon-SRK	NRTL	NRTL	NRTL	NRTL	Uniquac	NRTL	Van Laar	Van Laar	Van Laar
Direct Method Twu-Coon-PRSV	NRTL	NRTL	NRTL	NRTL	Uniquac	Van Laar	NRTL	Van Laar	Van Laar

Table 5.4: Thermodynamic modelled parameters for the combined method

System	Activity Coefficient Model Parameters	System														
		l-hexene (1) + NMP (2)					water (1) + NMP (2)					l-hexene (1) + 3MCP (2)				
$T^{\circ}\text{C}$		40	62	90	70	90	107	40	50	60	40	50	60	40	50	60
Van Laar	A_{12} [J/mol]	1.573	1.351	1.529	-0.394	-0.325	-1.288	0.0237	-5.108	-9.302						
	A_{21} [J/mol]	2.281	2.531	2.041	-0.539	-0.360	-0.0753	0.0209	0.0073	0.0146						
	δP	0.0095	0.0305	0.0043	0.0012	0.0036	0.0125	2.07E-04	8.99E-04	5.6E-04						
	$\delta\gamma_1$	3.08E-07	2.56E-06	1.34E-06	2.84E-06	3.44E-06	6.09E-06	6.81E-06	5.16E-06	4.49E-06						
Uniquac	$u_{12} - u_{11}$ [J/mol]	2309.7	3265.7	2400.8	227.7	445.5	286.4	-2.242	137.324	86.438						
	$u_{12} - u_{22}$ [J/mol]	-416	-898.3	-412.5	-1873.5	-2001.9	-1603.6	-2.529	-149.299	-94.224						
	δP	0.009	0.0293	0.0043	0.0013	0.0038	0.0065	2.07E-04	9.14E-04	5.83E-04						
	$\delta\gamma_1$	3.01E-07	2.54E-06	1.35E-06	2.97E-06	4.06E-06	4.25E-06	6.82E-06	5.28E-06	4.54E-06						
Wilson	$L_{11} = \lambda_{12} - \lambda_{11}$ [J/mol]	1.600	644.7	482	1420.3	1764.6	2027.9	19.252	203.733	100						
	$L_{22} = \lambda_{12} - \lambda_{22}$ [J/mol]	6465.6	8570.3	13060	-1.1	-275.9	1610.1	56.221	-133.204	-21.442						
	δP	0.0041	0.0147	0.0044	0.0013	0.0038	0.0067	2.07E-04	9.12E-04	5.82E-04						
	$\delta\gamma_1$	2.16E-07	2.39E-06	1.41E-06	2.98E-06	4.06E-06	4.54E-06	6.81E-06	5.26E-06	4.53E-06						
NRTL	$g_{12} - g_{11}$ [J/mol]	5781	7069.1	483.6	-543.863	-957	25775.4	-916.9	-971.1	-950.1						
	$g_{12} - g_{22}$ [J/mol]	4263.2	3500.1	4118.6	-525.028	-4500	-20548.2	1014.5	2501.5	5595.5						
	alpha	0.5	0.6	-0.2	4.306	-1.7	3.25E-06	0.1	0.999	0.9						
	δP	2.46E-04	0.0023	0.0043	0.0012	0.0032	0.00336	2.07E-04	6.65E-04	3.38E-04						
$\delta\gamma_1$	1.33E-07	2.28E-06	1.34E-06	2.49E-06	4.21E-06	3.24E-06	6.81E-06	4.29E-06	4.33E-06							

Table 5.5: Thermodynamic modelled parameters for the Direct Method i.e. Wong-Sandler-SRK

Activity Coefficient Model Parameters	System												
	System	l-hexene (1) + NMP (2)				water (1) + NMP (2)				l-hexene (1) + 3MCP (2)			
		$T^{\circ}\text{C}$	40	62	90	70	90	107	40	50	60	40	50
Van Laar	A_{12} [J/mol]	1.626	1.565	1.168	1.135	1.457	2.198	0.0224	0.0212	0.646			
	A_{21} [J/mol]	2.853	3.377	1.243	8.464	11.237	14.415	179.949	3.866	-0.997			
	k_{12}	0.0123	-0.0205	0.254	-0.101	-0.338	-0.781	0.120	0.0845	0.563			
	δP	0.0116	0.0346	0.0029	0.0164	0.0295	0.0336	0.0308	0.0426	0.0618			
	δy_1	2.789E-04	0.0023	0.0033	0.0051	0.0147	0.0152	0.0117	0.0082	0.0200			
Uniquac	$u_{12} - u_{11}$ [J/mol]	3913.308	5167.785	355.032	-1160.830	-711.808	803.122	4001.682	3520.204	4002.450			
	$u_{12} - u_{22}$ [J/mol]	-546.534	-775.881	452.022	525.716	462.069	-516.957	-2391.060	-1578.656	-1281.636			
	k_{12}	-0.248	-0.304	0.356	0.461	0.410	0.388	0.231	-0.351	-0.756			
	δP	0.0106	0.0303	0.0029	0.0168	0.0331	0.0337	0.030	0.0426	0.0619			
	δy_1	2.5E-04	0.0023	0.0033	0.0043	0.0142	0.0147	0.015	0.0130	0.0089			
Wilson	$L_{11} = \lambda_{12} - \lambda_{11}$ [J/mol]	2390.292	17023.352	994.029	15274.150	2821.929	3993.267	-1453.554	-652.582	-2033.814			
	$L_{22} = \lambda_{12} - \lambda_{22}$ [J/mol]	25085.057	-1947.871	22168.099	-8893.964	18723.794	-430.172	4380.333	5325.176	5680.910			
	k_{12}	-0.00907	0.611	0.0641	0.620	0.426	0.503	-0.120	-0.394	-0.189			
	δP	0.0038	0.0443	0.0029	0.0171	0.0297	0.0337	0.0309	0.0426	0.0619			
	δy_1	1.738E-04	0.0022	0.0033	0.0035	0.0147	0.0146	0.0171	0.0128	0.0084			
NRTL	$g_{12} - g_{11}$ [J/mol]	7870.494	8488.486	700.427	30794.436	3816.159	7628.399	2046.797	1231.213	1093.666			
	$g_{12} - g_{22}$ [J/mol]	4667.047	3138.794	1847.019	-21637.975	-3819.409	-4903.681	-62.960	-10.827	-8.800			
	alpha	0.565	0.798	0.985	0.0381	-0.0700	0.103	0.200	0.215	0.205			
	k_{12}	0.136	0.320	0.456	0.499	0.560	0.537	0.0100	0.00984	0.00282			
	δP	0.0031	0.0109	0.0029	0.0171	0.0341	0.0338	0.0308	0.0426	0.0619			
δy_1	6.970E-05	0.0022	0.0034	0.0038	0.0141	0.0146	0.0164	0.0051	0.0031				

Table 5.6: Thermodynamic modelled parameters for the Direct Method i.e. Wong-Sandler-PRSV

Activity Coefficient Model	System	System											
		l-hexene (1) + NMP (2)				water (1) + NMP (2)				1-hexene (1) + 3MCP (2)			
	$T^{\circ}\text{C}$	40	62	90	70	90	107	40	50	60	40	50	60
Van Laar	A_{12} [J/mol]	1.371	0.214	0.685	0.754	0.971	0.672	0.00374	12.519	2.447	0.00374	12.519	2.447
	A_{21} [J/mol]	2.352	2.445	0.358	2.782	4.787	2.604	7.4555	0.0643	0.143	7.4555	0.0643	0.143
	k_{12}	0.0987	0.492	0.514	0.110	-0.0321	0.00687	-0.00270	-0.0220	0.378	-0.00270	-0.0220	0.378
	δP	0.0107	0.0376	0.957E-3	0.00759	0.00500	0.00574	0.0060	0.0154	0.0318	0.0060	0.0154	0.0318
	δy_1	0.00663	0.00308	0.00323	0.00607	0.0193	0.0195	0.0084	0.0045	0.0040	0.0084	0.0045	0.0040
Uniquac	$u_{12} - u_{11}$ [J/mol]	-2309.130	-2583.269	441.712	4419.575	884.692	611.527	-396.800	219.398	-50.554	-396.800	219.398	-50.554
	$u_{12} - u_{22}$ [J/mol]	7948.191	5801.969	364.800	-312.108	-622.712	-297.883	251.289	44.451	60.772	251.289	44.451	60.772
	k_{12}	0.636	0.673	0.359	-0.384	0.215	0.306	0.0761	-0.104	0.0199	0.0761	-0.104	0.0199
	δP	0.0101	0.0410	0.0011	0.0064	0.0053	0.0061	0.0060	0.0154	0.0318	0.0060	0.0154	0.0318
	δy_1	0.000673	0.0022	0.0028	0.0063	0.0161	0.0150	0.0073	0.0048	0.0042	0.0073	0.0048	0.0042
Wilson	$L_{11} = \lambda_{12} - \lambda_{11}$ [J/mol]	1970.714	291.518	1619.630	2646.477	4606.053	-84.489	646.660	289.97	76.053	646.660	289.97	76.053
	$L_{22} = \lambda_{12} - \lambda_{22}$ [J/mol]	6354.957	539.267	5376.879	-3276.39	-4004.650	1691.004	-1409.500	-17.991	43.011	-1409.500	-17.991	43.011
	k_{12}	0.0973	0.575	0.100	0.499	0.465	0.484	0.166	-0.000376	0.0281	0.166	-0.000376	0.0281
	δP	0.00595	0.0443	0.00387	0.0105	0.00986	0.00676	0.0060	0.0154	0.0318	0.0060	0.0154	0.0318
	δy_1	0.00909	0.00277	0.00360	0.00436	0.0192	0.0191	0.0081	0.0050	0.0042	0.0081	0.0050	0.0042
NRTL	$g_{12} - g_{11}$ [J/mol]	410.576	10900.26	2680.17	-2364.24	361.704	-248.105	-81.833	-52.352	10.474	-81.833	-52.352	10.474
	$g_{12} - g_{22}$ [J/mol]	2424.406	2925.48	1813.953	4819.202	933.244	1658.35	-82.728	84.520	-96.690	-82.728	84.520	-96.690
	alpha	0.3	0.4	0.3	0.3	0.3	0.3	0.0504	1.963	1.922	0.0504	1.963	1.922
	k_{12}	0.415	-0.0745	0.2	0.417	0.403	0.5	0.0416	0.0216	0.0497	0.0416	0.0216	0.0497
	δP	0.0121	0.0154	0.00239	0.00876	0.00535	0.00662	0.0060	0.0154	0.0318	0.0060	0.0154	0.0318
δy_1	0.00837	0.00289	0.00343	0.00625	0.0191	0.0195	0.0070	0.0050	0.0042	0.0070	0.0050	0.0042	

Table 5.7 Thermodynamic modelled parameters for the Direct Method i.e. Twu-Coon-SRK

Activity Coefficient Model	System												
	System	1-hexene (1) + NMP (2)				water (1) + NMP (2)				1-hexene (1) + 3MCP (2)			
		$T^{\circ}C$	40	62	90	70	90	107	40	50	60	40	50
Van Laar	A_{12} [J/mol]	6.8219	11.048	-1.456	-8.982	1168.7	0.3997	10.535	74,094	42,756			
	A_{21} [J/mol]	3.5674	10.331	-1.301	1.548	-1317.7	0.868	6.712	10,241	8,921			
	δP	0.0078	0.0214	0.0029	0.0159	0.0305	0.0336	0.0308	0.0426	0.0619			
	$\delta \gamma_1$	0.00024	0.0022	0.0033	0.0194	0.0144	0.0147	0.0112	0.0045	0.0044			
	k_{12}	0.0852	-0.214	0.121	-0.900	-0.2	-0.101	-0.128	-0.0982	-0.0971			
	l_{12}	0.228	0.205	0	-0.637	0	0.109	0.265	0.573	0.517			
		4216	6690.379	508.703	-82.213	126.350	-540.777	1631.961	1200.216	1567.659			
Uniquac	$u_{12} - u_{11}$ [J/mol]	3254	2239.636	449.688	-2712.778	-2645.299	1454.026	1856.185	4145.565	2284.937			
	$u_{12} - u_{22}$ [J/mol]	0.0049	0.0022	0.0029	0.0164	0.0306	0.0337	0.0309	0.0426	0.0619			
	δP	0.00016	0.0022	0.0029	0.0056	0.0144	0.0147	0.0164	0.0130	0.0097			
	$\delta \gamma_1$	-0.148	-0.255	0.0372	-0.300	-0.214	-0.101	-0.0143	0.0978	0.0821			
	k_{12}	0.0724	-0.00530	0.0459	-0.127	-0.0447	0.145	0.181	0.351	0.325			
		12641	6606.467	2474.404	-1166.921	-1691.4	-3371.277	3422.949	2936.154	3121.012			
		18408.7	21298.225	4273.300	2553.925	352.6	-256.138	3824.498	4822.062	4539.125			
Wilson	$L_{11} - \lambda_{12} - \lambda_{11}$ [J/mol]	0.0025	0.0070	0.0029	0.0164	0.0317	0.0337	0.0309	0.0426	0.0619			
	$L_{22} - \lambda_{12} - \lambda_{22}$ [J/mol]	0.0002	0.0022	0.0033	0.0054	0.0147	0.0146	0.0167	0.0133	0.0081			
	δP	-0.0311	-0.00724	0.0377	-0.250	-0.1001	-0.0195	-0.00549	-0.0452	-0.00702			
	$\delta \gamma_1$	0.0299	0.0661	0.0715	-0.104	0.0103	-0.0168	0.0945	0.0718	0.122			
		8068	10760.175	28504.23	1675.439	-146.1	3418.9	2814.481	2998.497	8522.308			
		4519	5065.335	4130.075	-10223.751	-1871.5	676.5	3029.327	1059.929	1523.143			
		0.64	0.431	0.325	0.437	2.2	0.4	0.777	1.050	0.0534			
NRTL	$g_{12} - g_{11}$ [J/mol]	0.0029	0.0023	0.0029	0.0164	0.0308	0.0309	0.0426	0.0619	0.0153			
	$g_{12} - g_{22}$ [J/mol]	7.7E-05	0.0022	0.0033	0.0054	0.0143	0.0165	0.0133	0.0101	0.0155			
	alpha	0.0036	-0.0377	0.0192	0.0447	-0.204	-0.102	0.0355	0.0219	-0.0459			
	δP	0.022	0.0245	0.0605	-0.212	0.00281	0.210	0.109	0.0842	0.180			

Table 5.8 Thermodynamic modelled parameters for the Direct Method i.e. Twu-Coon-PRSV

Activity Coefficient Model	System											
	System	l-hexene (1) + NMP (2)			water (1) + NMP (2)			l-hexene (1) + 3MCP (2)				
		$T^{\circ}C$	40	62	90	70	90	107	40	50	60	
Van Laar	A_{12} [J/mol]	6.18	11.048	-1.678	-0.239	0.978	0.7412	6.185	12.183	99.362		
	A_{21} [J/mol]	3.07	10.331	-1.408	-11.846	2.684	1.500	3.079	5.650	7.989		
	δP	0.0054	0.021	0.0011	4.391 E-04	0.0046	0.0055	0.0054	0.0154	0.0317		
	δy_1	0.00036	0.0022	0.003	0.0050	0.0160	0.0150	3.579E-04	0.0038	0.0054		
	k_{12}	0.0919	-0.214	0.123	-0.0964	-0.109	-0.0722	0.0919	-0.108	-0.0676		
	l_{12}	0.2121	0.205	-0.007	0.108	0.167	0.164	0.212	0.266	0.499		
	Uniquac	$u_{12} - u_{11}$ [J/mol]	3344	6342.320	876.519	-1603.977	1215.084	1394.531	3344.298	-18.640	362.483	
		$u_{12} - u_{22}$ [J/mol]	3345	2259.243	533.025	-6289.154	-3.553	423.803	3345.036	-550.528	-686.593	
		δP	0.033	0.0017	0.0011	0.0017	0.0047	0.0054	0.0033	0.0154	0.0318	
		δy_1	0.00033	0.0021	0.0031	0.0053	0.0161	0.0150	3.29E-004	0.0047	0.0041	
k_{12}		-0.100	-0.241	0.0267	-0.0438	-0.207	-0.140	-0.100	0.111	0.0695		
l_{12}		0.0999	-0.000450	0.0554	-0.0969	0.0929	0.146	0.0999	0.0892	0.0538		
Wilson		$L_{11} - \lambda_{12} - \lambda_{11}$ [J/mol]	10095	6128.916	2023.071	-3714.509	-3164.991	1336.335	10095.256	2359.700	3209.456	
		$L_{22} - \lambda_{12} - \lambda_{22}$ [J/mol]	9909	18525.250	3430.582	3708.261	299.262	451.054	9909.422	1103.103	2674.482	
		δP	0.00099	0.0064	0.0011	0.0028	0.0066	0.0054	9.921E-04	0.0154	0.0318	
		δy_1	0.00033	0.0022	0.0031	0.0047	0.0162	0.0150	3.359E-004	0.0052	0.0046	
	k_{12}	-0.0285	-0.01104	0.0404	0.00593	-0.0836	-0.139	-0.0285	-0.00773	0.0917		
	l_{12}	0.0298	0.0597	0.0614	0.0728	-0.0229	0.147	0.0298	0.0544	0.0804		
	NRTL	$g_{12} - g_{11}$ [J/mol]	6319	10900.070	28400.291	9637.271	14476.339	9478.9	6319.091	3605.467	627.034	
		$g_{12} - g_{22}$ [J/mol]	5197	5256.775	4551.565	-9795.089	-3131.684	-1315.8	5197.051	-4165.176	0.948	
		alpha	0.71	0.382	0.305	0.539	0.157	0.300	0.708	0.00596	0.948	
		δP	0.00045	0.0016	0.0011	0.0043	0.0045	0.0052	4.547E-04	0.0154	0.0318	
δy_1		0.00025	0.0022	0.0031	0.0044	0.0159	0.0151	2.515E-04	0.0048	0.0043		
k_{12}		0.0112	-0.0590	0.0195	0.150	-0.0746	-1.005	0.0112	0.0299	0.0331		
l_{12}		0.0245	0.0140	0.0687	0.131	0.216	0.283	0.0245	0.0224	0.0576		

5.2.1 The Combined Method

From Table 5.3, for the combined method, the NRTL activity coefficient model dominates for all systems at all temperatures. This model proves that it is particularly suitable for highly non-ideal systems. Figures 5.1 to 5.18 alternate between P vs. x, y and y vs. x for each system at each temperature.

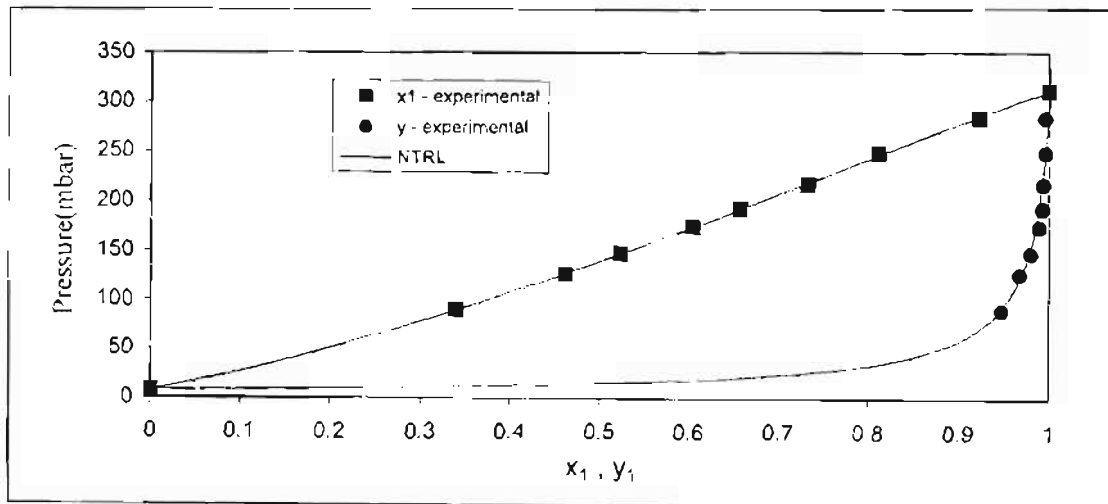


Figure 5.1: Plot of P vs. x, y for NRTL fit of Water (1) + NMP (2) at 70 °C

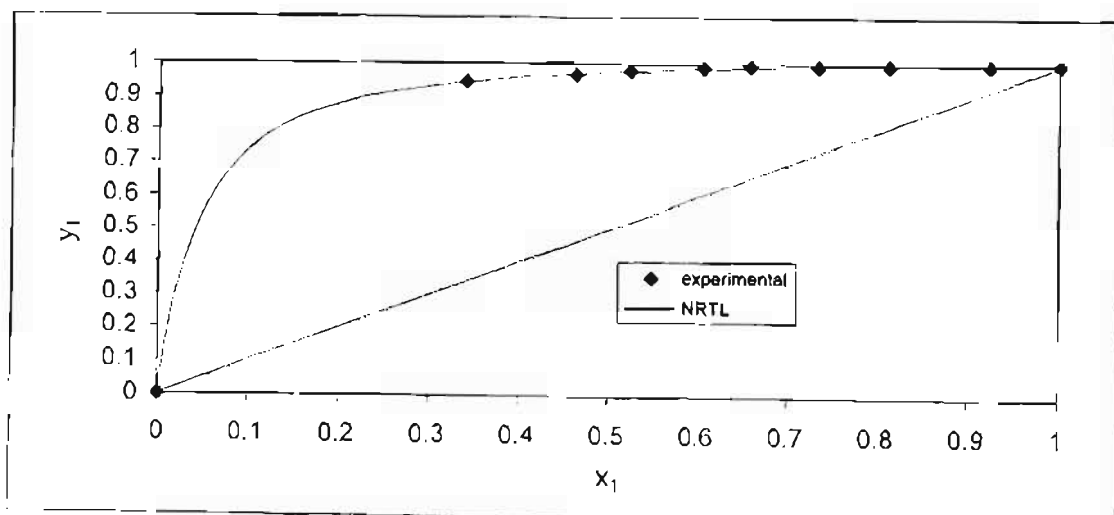


Figure 5.2: Plot of y vs. x for NRTL fit of Water (1) + NMP (2) at 70 °C

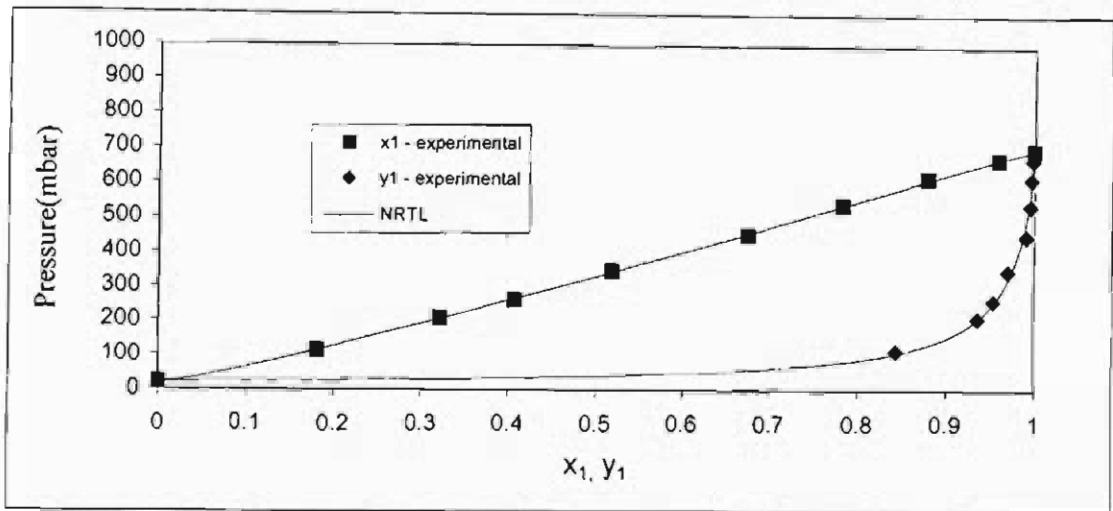


Figure 5. 3 Plot of P vs. x, y for NRTL fit of Water (1) + NMP (2) at 90 °C

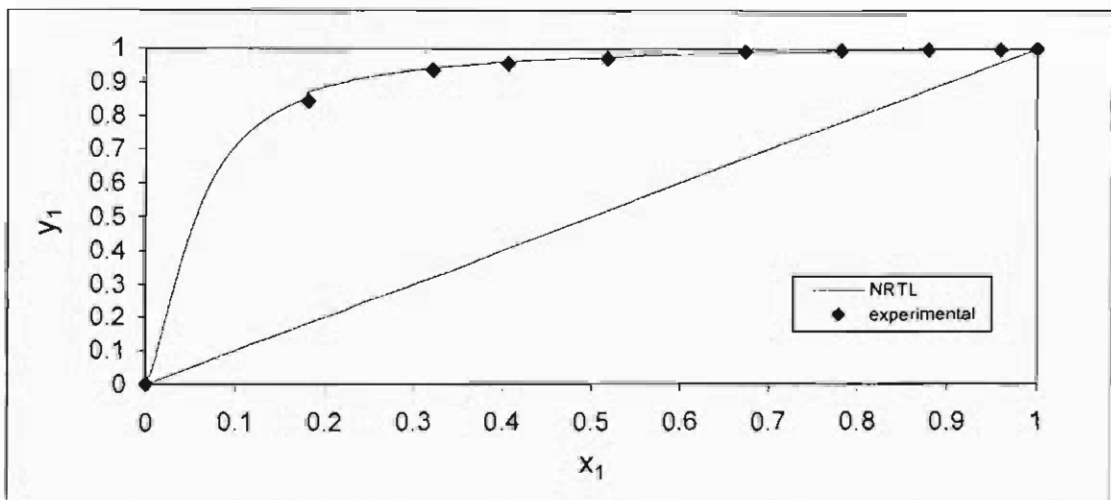


Figure 5. 4: Plot of y vs. x for NRTL fit of Water (1) + NMP (2) at 90 °C

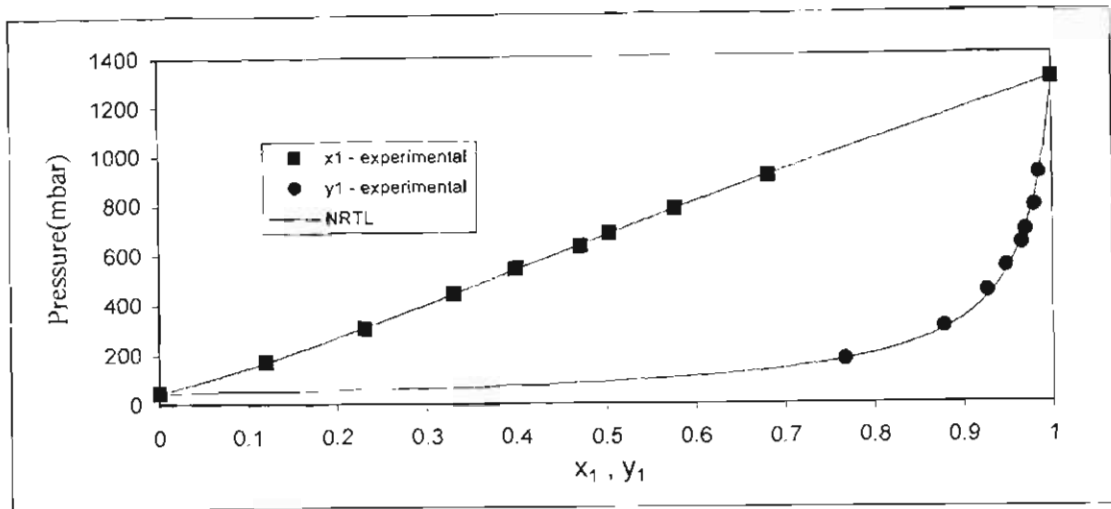


Figure 5. 5: Plot of P vs. x, y for NRTL fit of Water (1) + NMP (2) at 107 °C

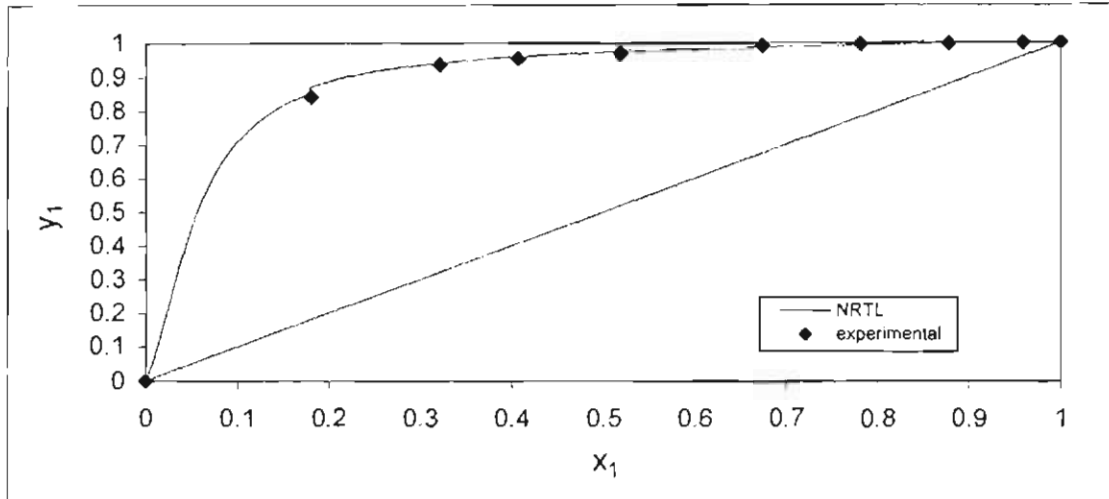


Figure 5. 6: Plot of y vs. x for NRTL fit of Water (1) + NMP (2) at 107 °C

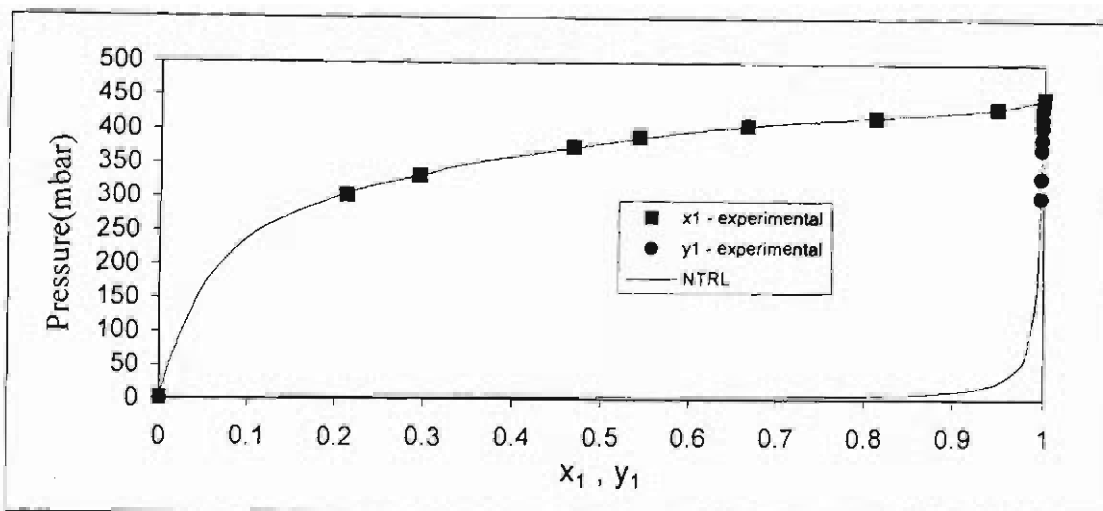


Figure 5. 7: Plot of P vs. x, y for NRTL fit of Hexene (1) + NMP (2) at 40 °C

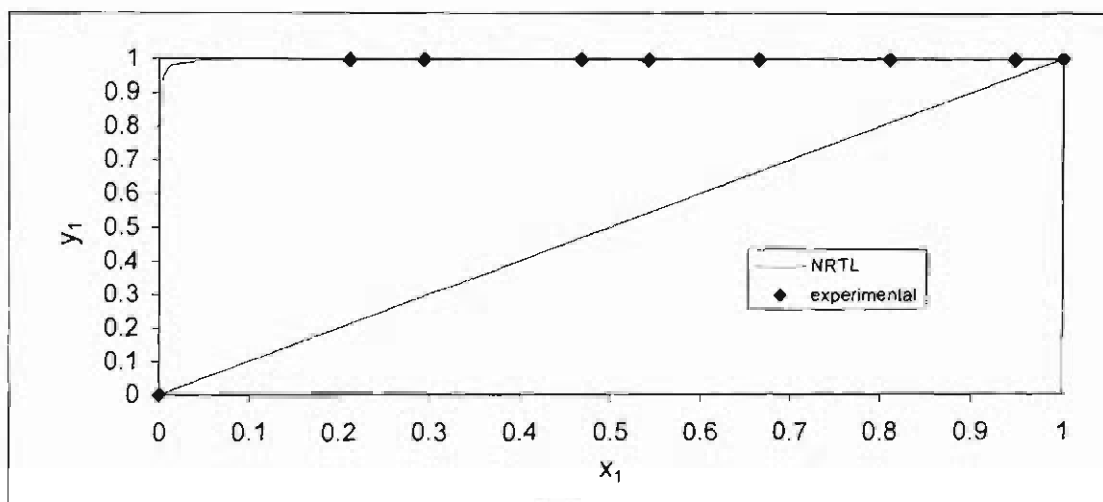


Figure 5. 8: Plot of y vs. x for NRTL fit of Hexene (1) + NMP (2) at 40 °C

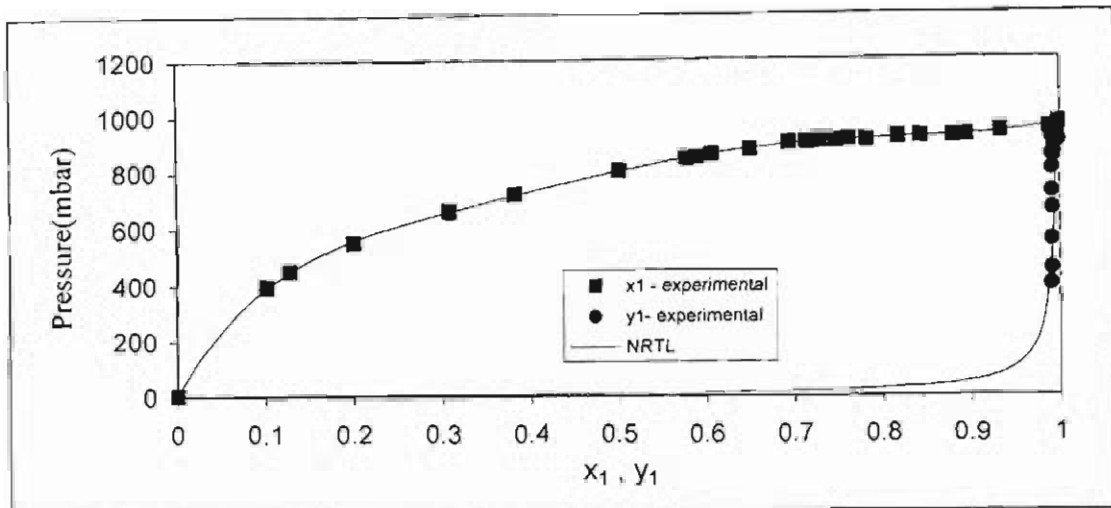


Figure 5. 9: Plot of P vs. x, y for NRTL fit of Hexene (1) + NMP (2) at 62 °C

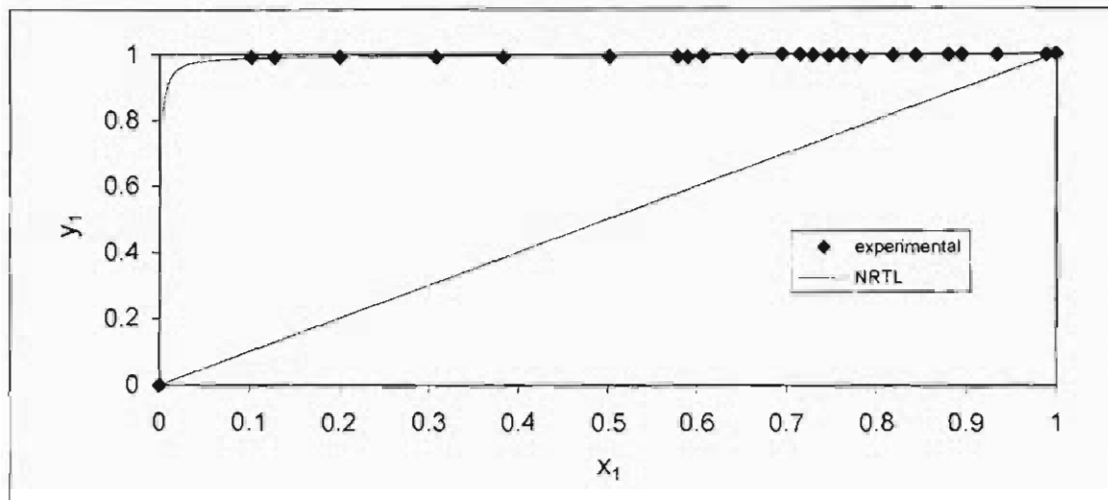


Figure 5. 10: Plot of y vs. x for NRTL fit of Hexene (1) + NMP (2) at 62 °C

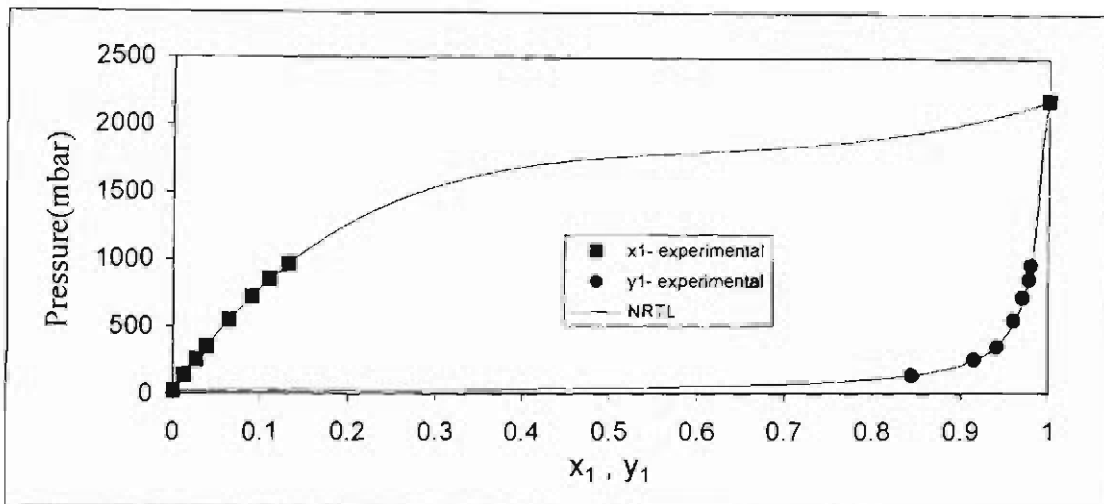


Figure 5. 11: Plot of P vs. x, y for NRTL fit of Hexene (1) + NMP (2) at 90 °C

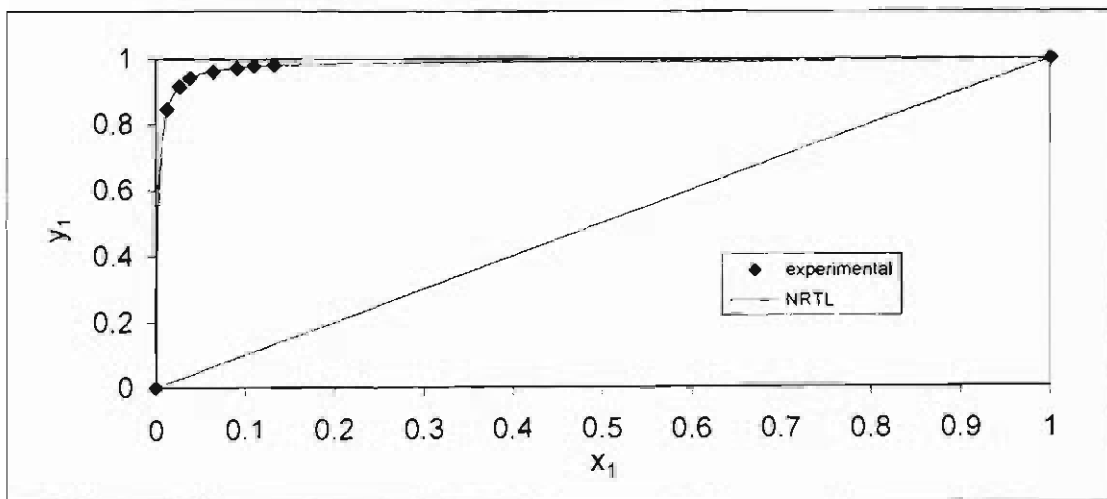


Figure 5. 12: Plot of y vs. x for NRTL fit of Hexene (1) + NMP (2) at 90 °C

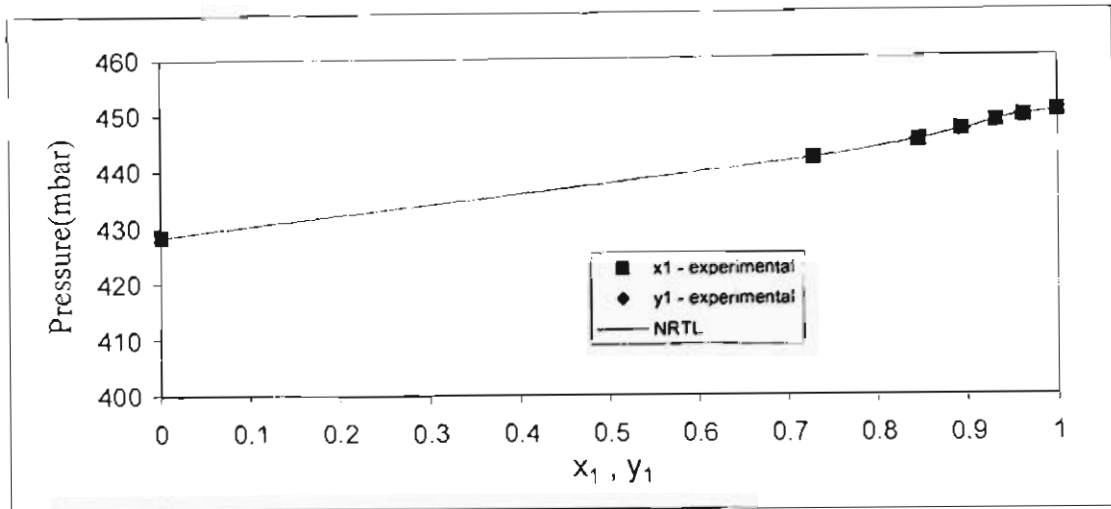


Figure 5.13: Plot of P vs. x, y for NRTL fit of Hexene (1) + 3MCP (2) at 40 °C

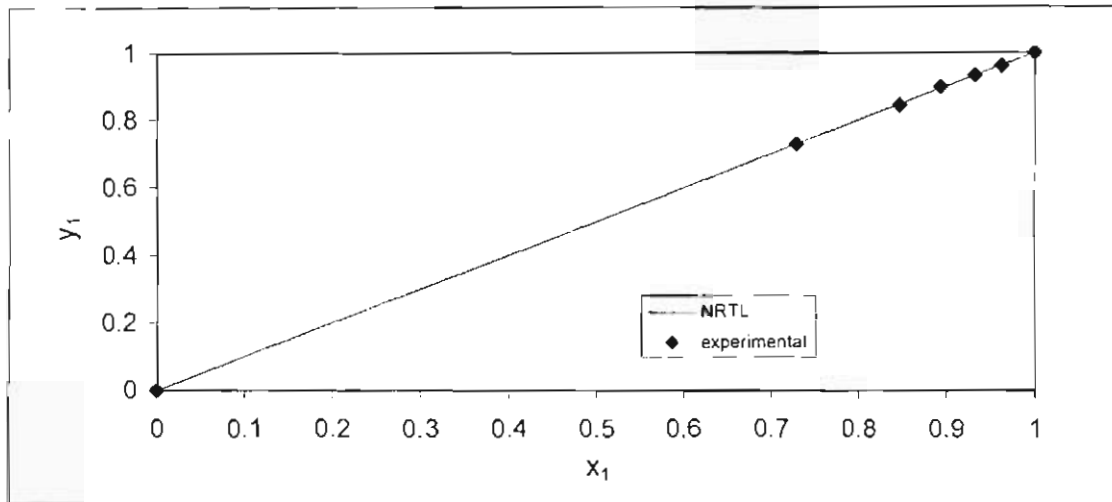


Figure 5.14: Plot of y vs. x for NRTL fit of Hexene (1) + 3MCP (2) at 40 °C

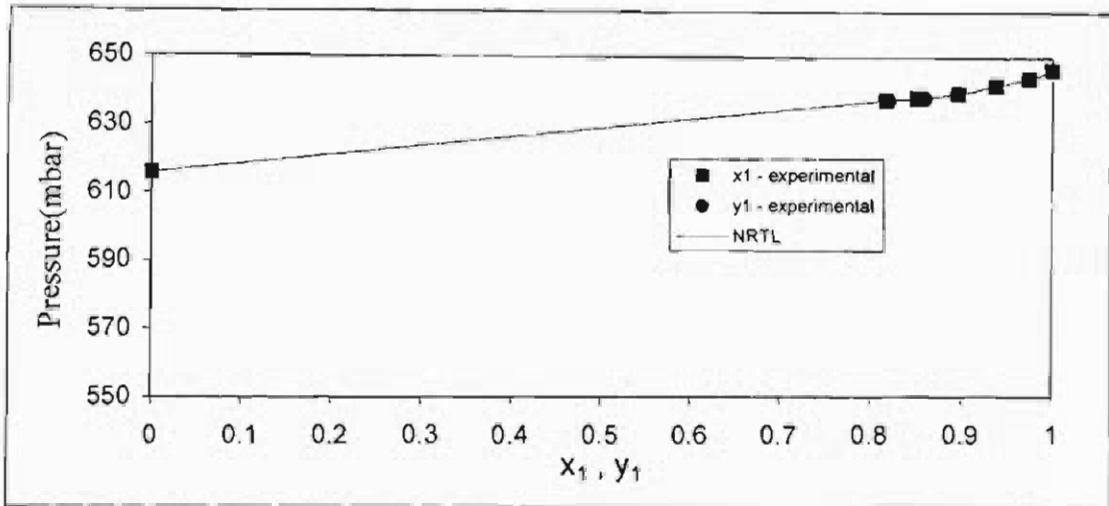


Figure 5. 15: Plot of P vs. x, y for NRTL fit of Hexene (1) + 3MCP (2) at 50 °C

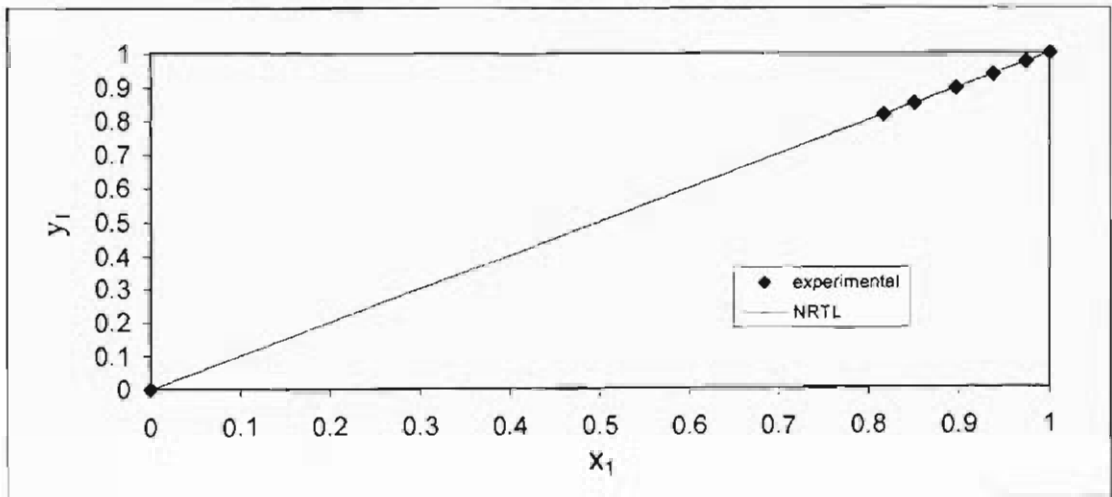


Figure 5. 16: Plot of y vs. x for NRTL fit of Hexene (1) + 3MCP (2) at 50 °C

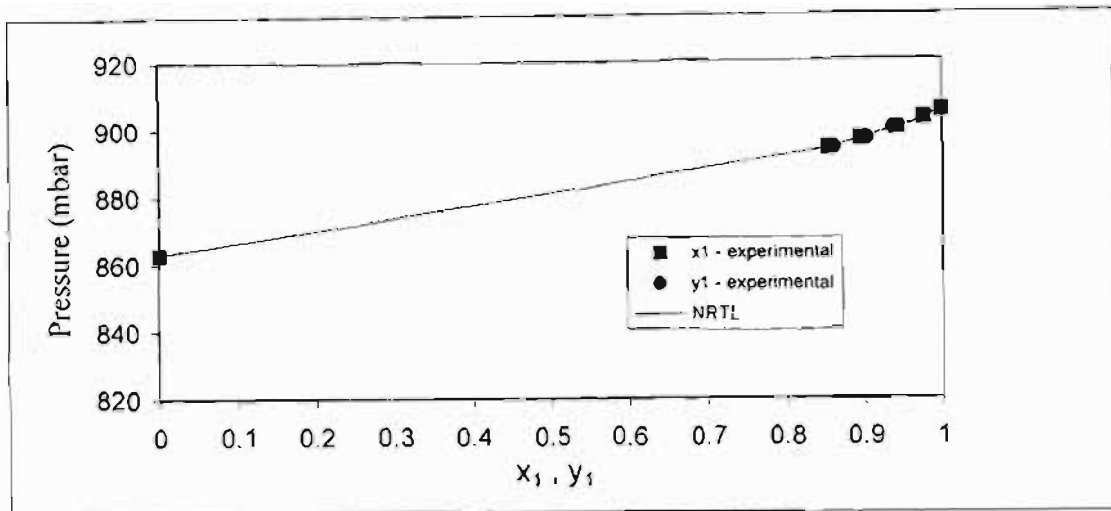


Figure 5. 17: Plot of P vs. x, y for NRTL fit of Hexene (1) + 3MCP (2) at 60 °C

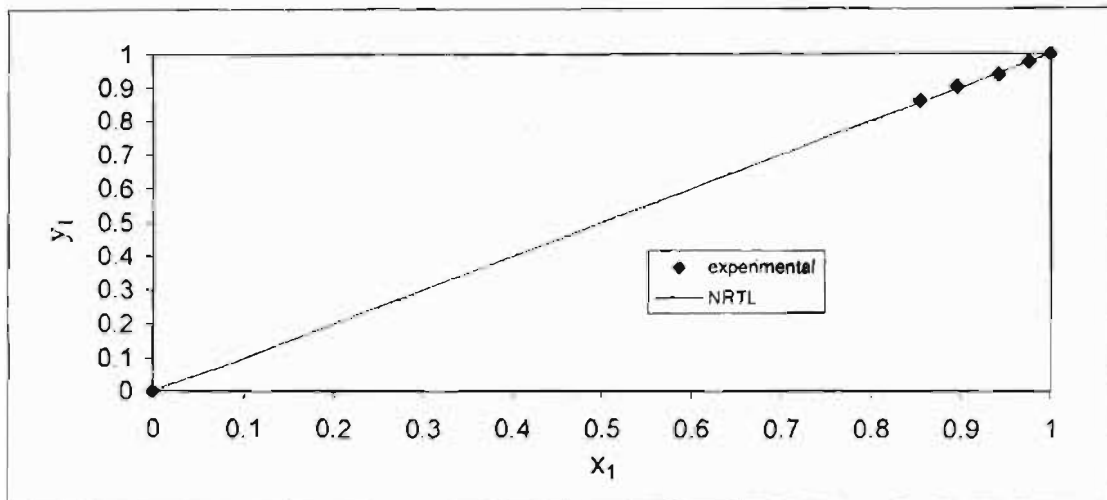


Figure 5. 18: Plot of y vs. x for NRTL fit of Hexene (1) + 3MCP (2) at 60 °C

5.2.2 The Direct Method: Wong-Sandler-SRK

From Table 5.3, for the Wong-Sandler-SRK model in the direct method, the NRTL, Van Laar and Uniquac activity coefficient models stand out as the best fit models. Figures 5.19 to 5.36 alternate between P vs. x, y and y vs. x for each system at each temperature.

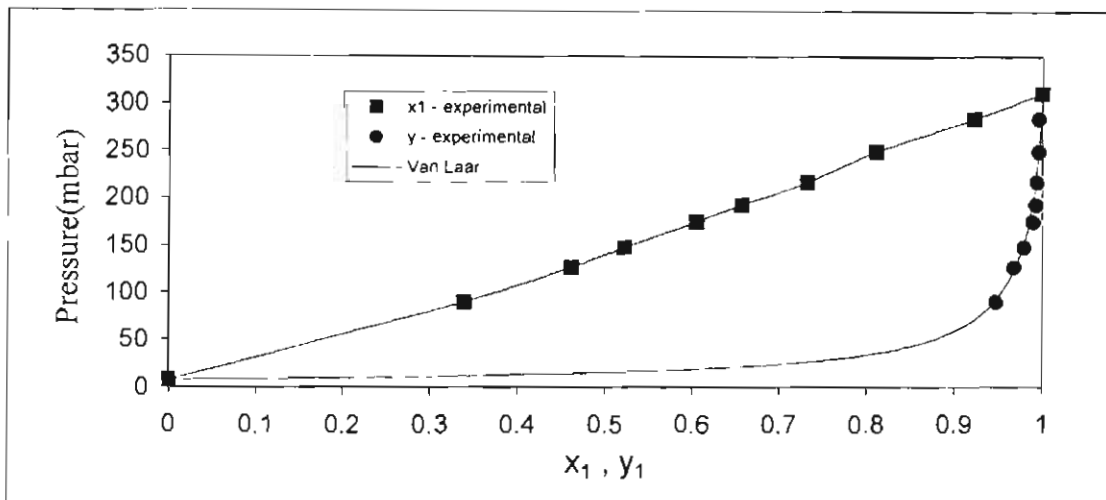


Figure 5. 19: Plot of P vs. x, y for Van Laar fit of Water (1) + NMP (2) at 70 °C

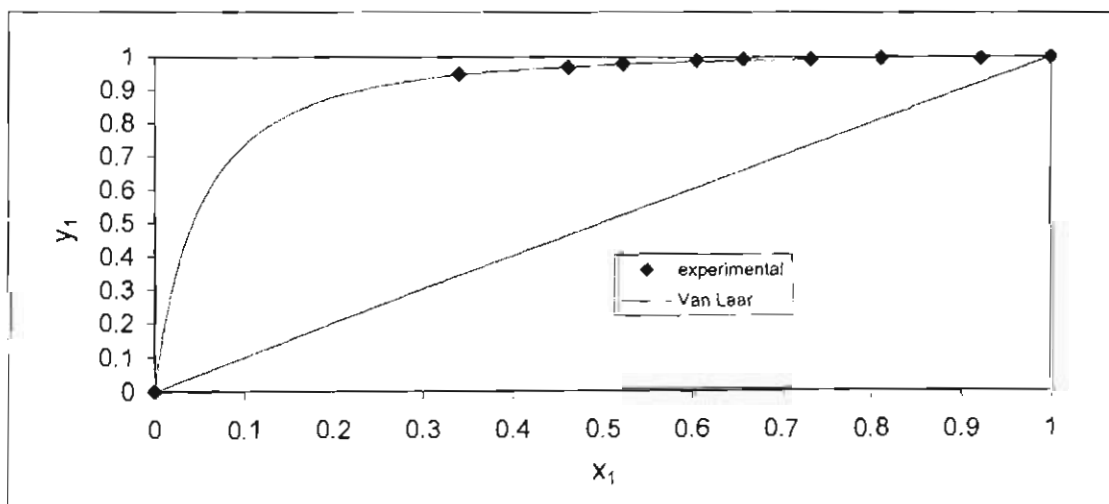


Figure 5. 20: Plot of y vs. x for Van Laar fit of Water (1) + NMP (2) at 70 °C

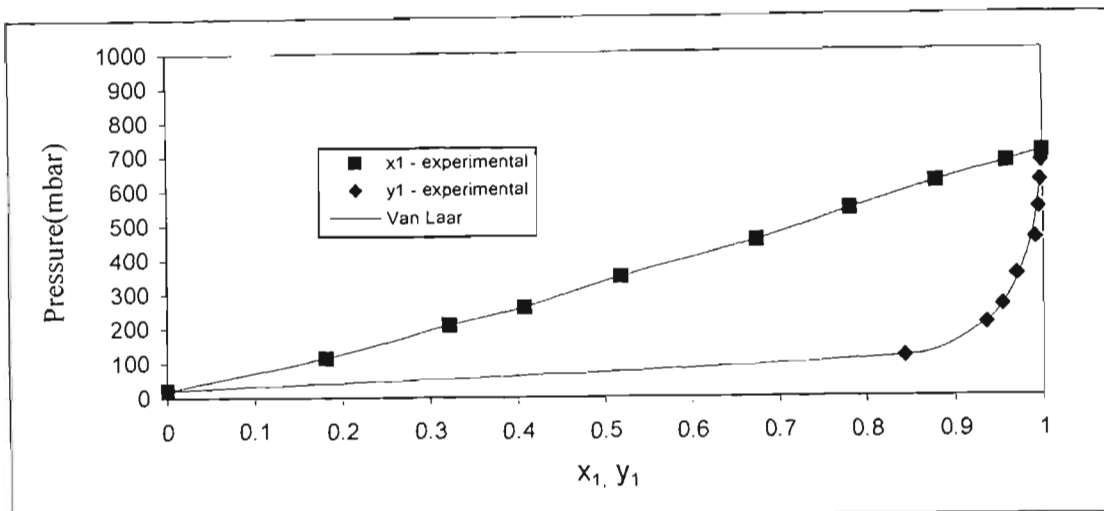


Figure 5. 21: Plot of P vs. x, y for Van Laar fit of Water (1) + NMP (2) at 90 °C

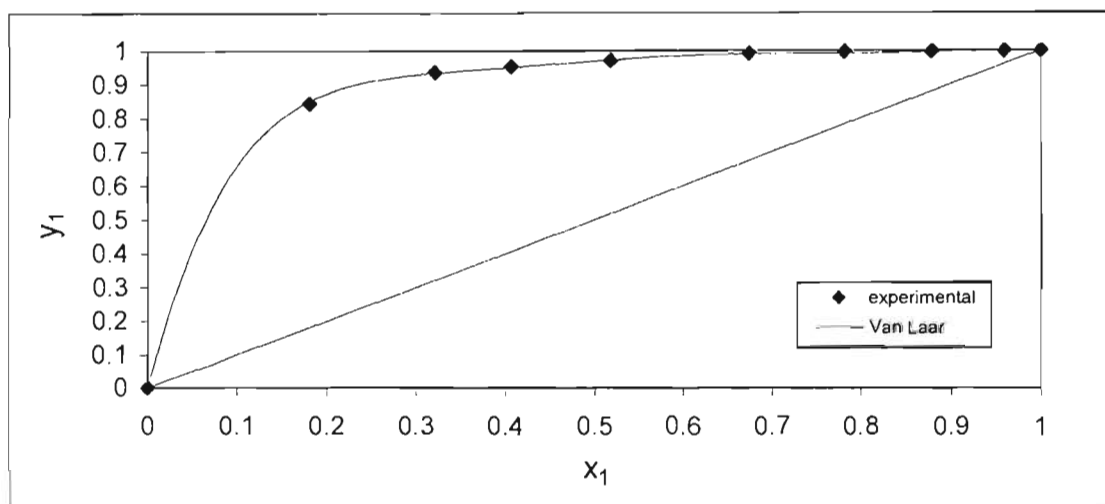


Figure 5. 22: Plot of y vs. x for Van Laar fit of Water (1) + NMP (2) at 90 °C

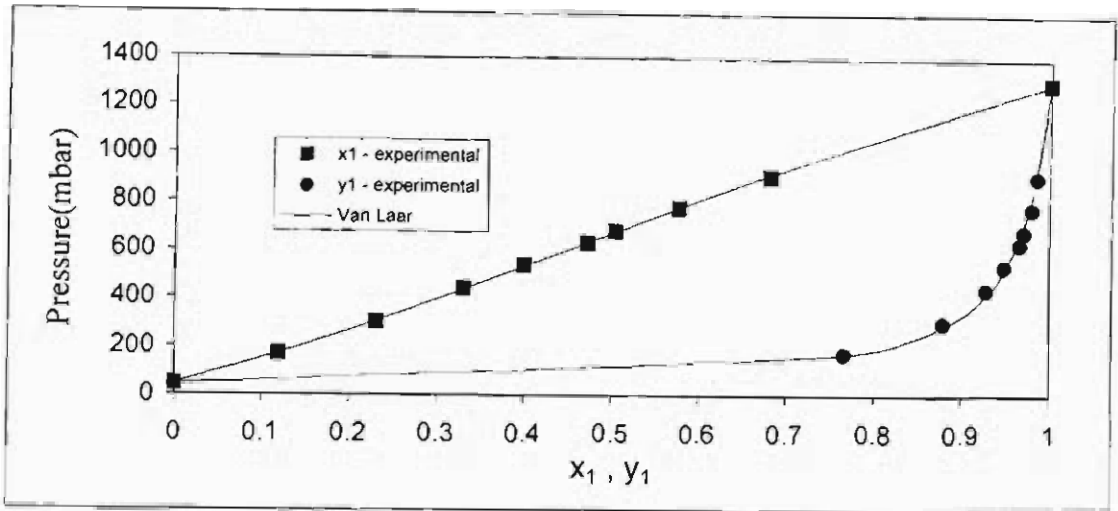


Figure 5.23: Plot of P vs. x, y for Van Laar fit of Water (1) + NMP (2) at 107 °C

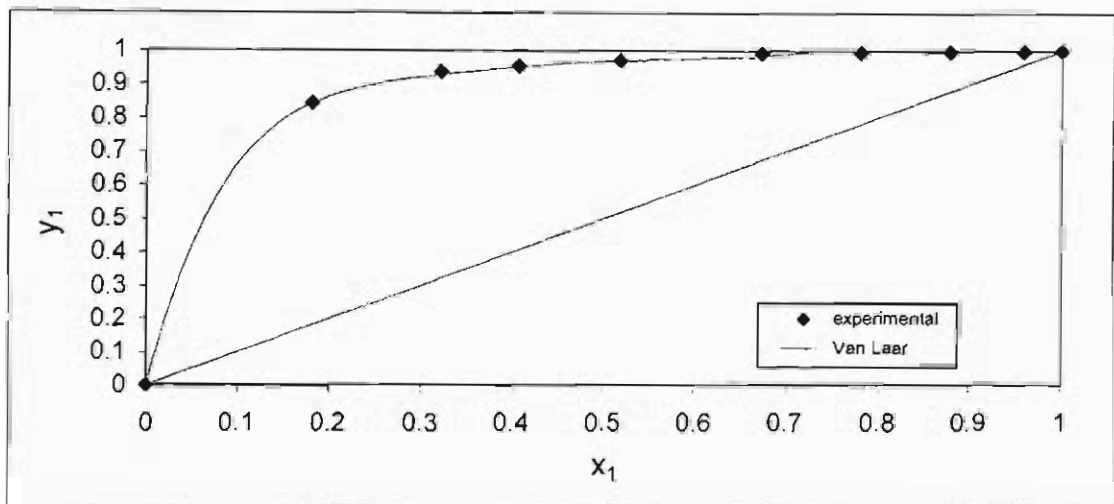


Figure 5.24: Plot of y vs. x for Van Laar fit of Water (1) + NMP (2) at 107 °C

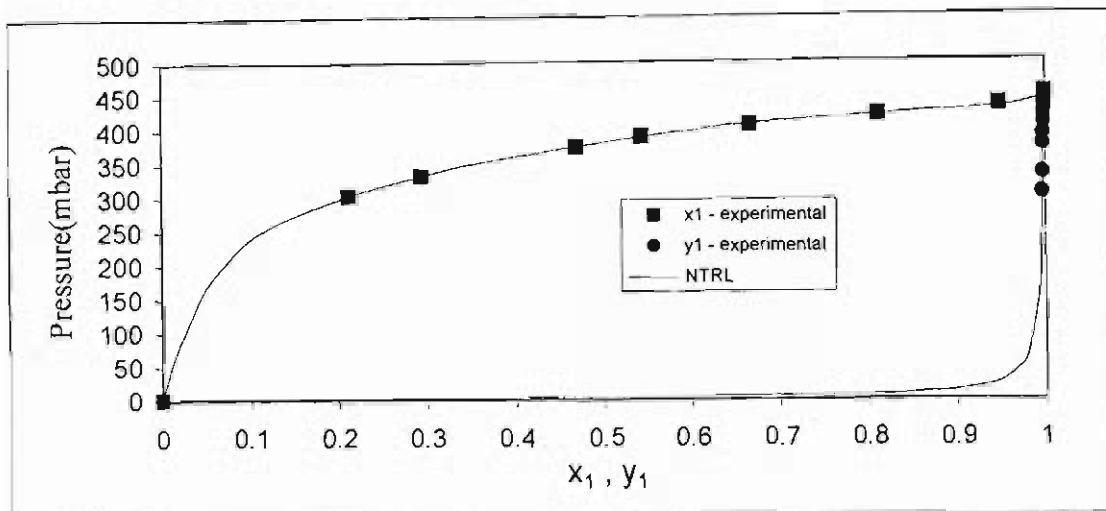


Figure 5. 25: Plot of P vs. x, y for NRTL fit of Hexene (1) + NMP (2) at 40 °C

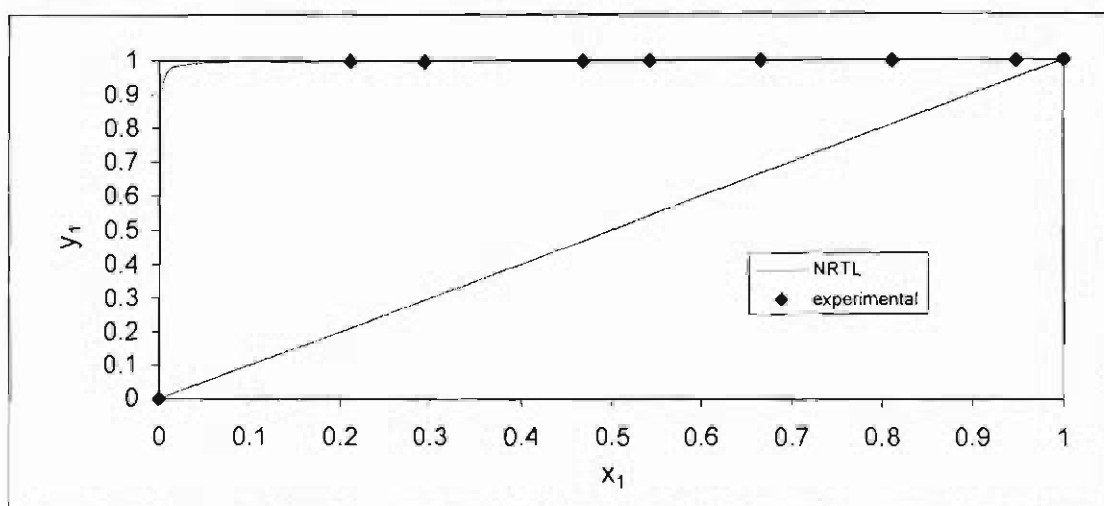


Figure 5. 26: Plot of y vs. x for NRTL fit of Hexene (1) + NMP (2) at 40 °C

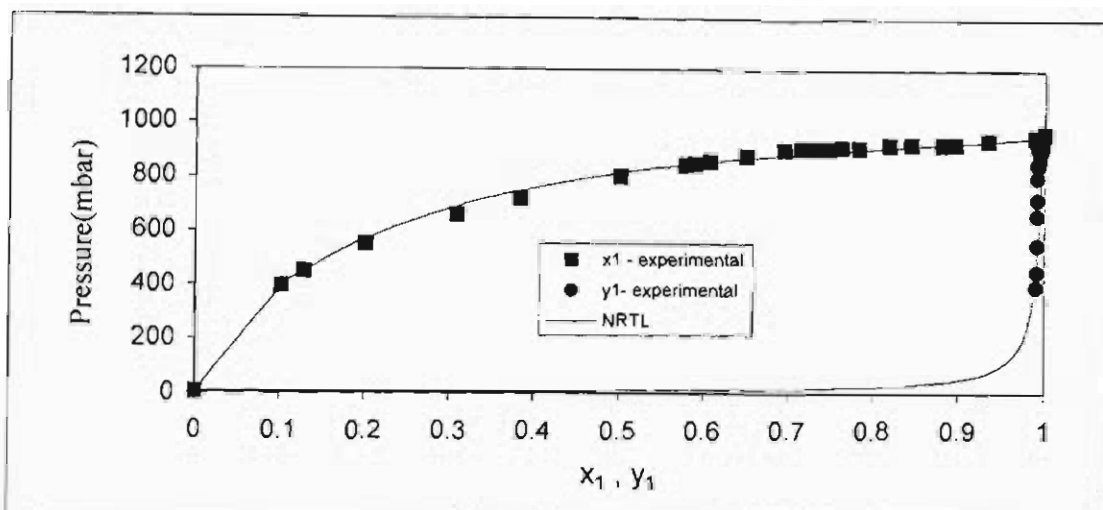


Figure 5. 27: Plot of P vs. x, y for NRTL fit of Hexene (1) + NMP (2) at 62 °C

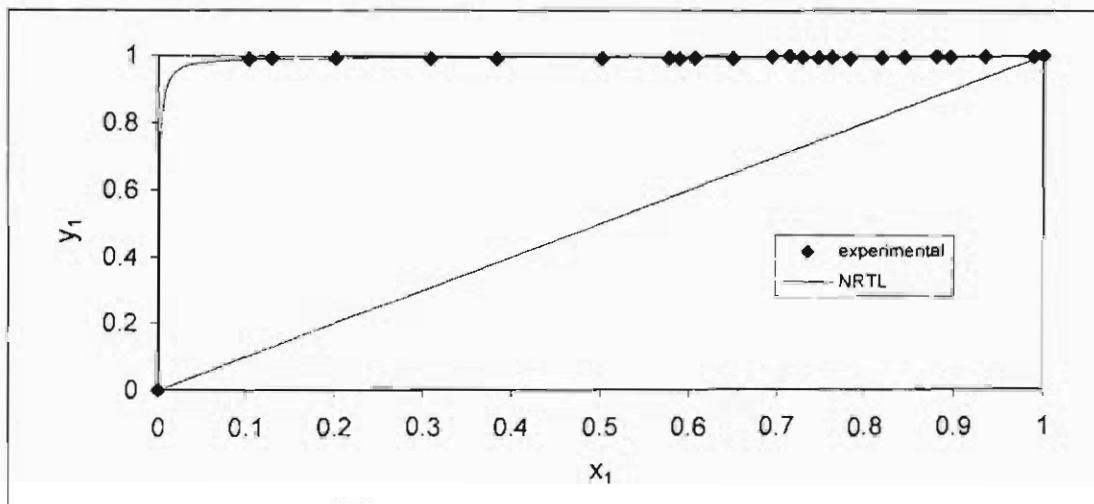


Figure 5. 28: Plot of y vs. x for NRTL fit of Hexene (1) + NMP (2) at 62 °C

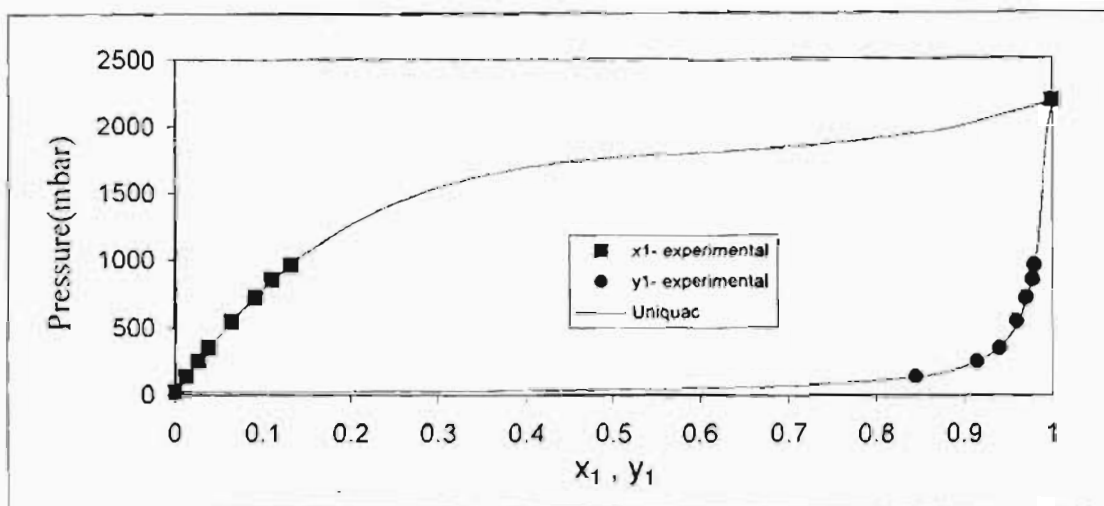


Figure 5. 29: Plot of P vs. x, y for Uniquac fit of Hexene (1) + NMP (2) at 90 °C

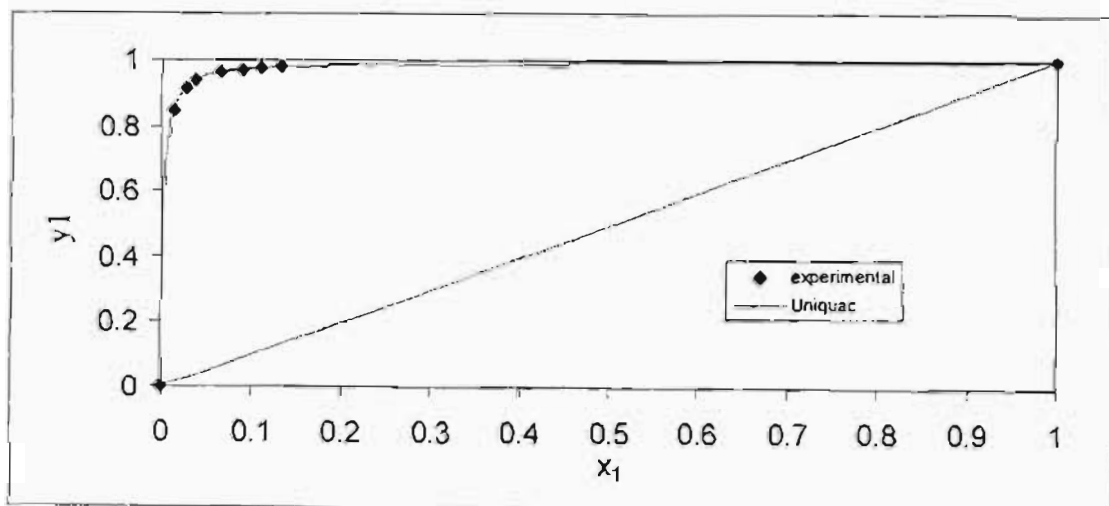


Figure 5. 30: Plot of y vs. x for Uniquac fit of Hexene (1) + NMP (2) at 90 °C

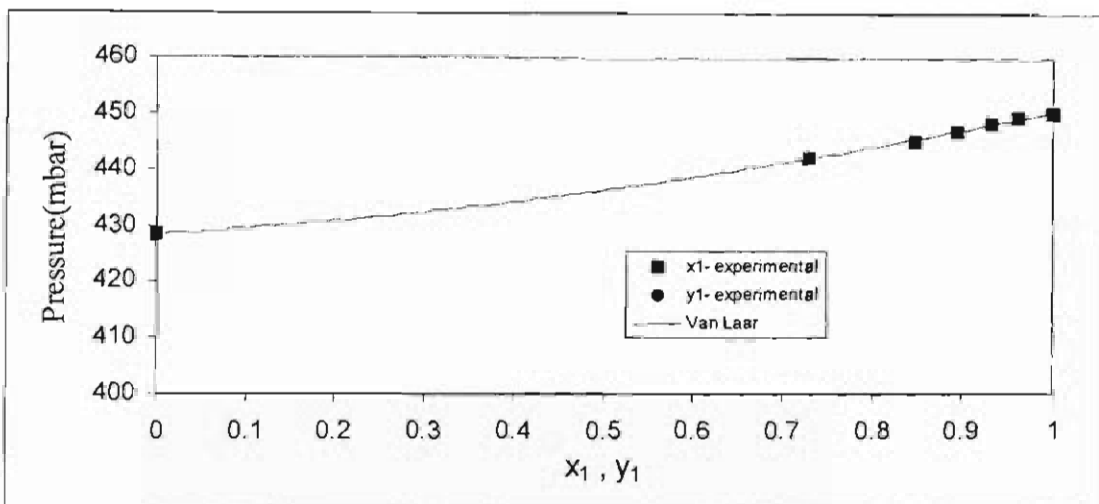


Figure 5. 31: Plot of P vs. x, y for Van Laar fit of Hexene (1) + 3MCP (2) at 40 °C

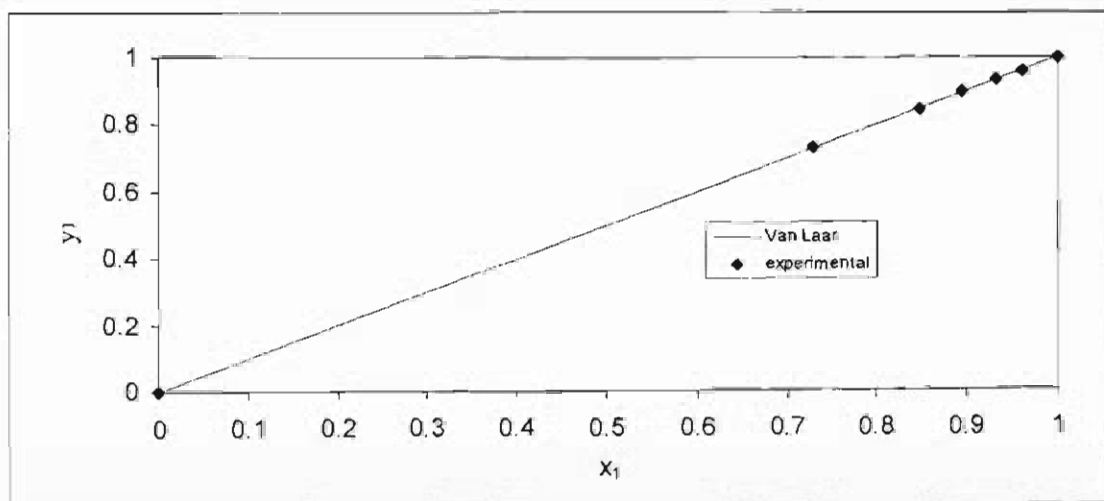


Figure 5. 32: Plot of y vs. x for Van Laar fit of Hexene (1) + 3MCP (2) at 40 °C

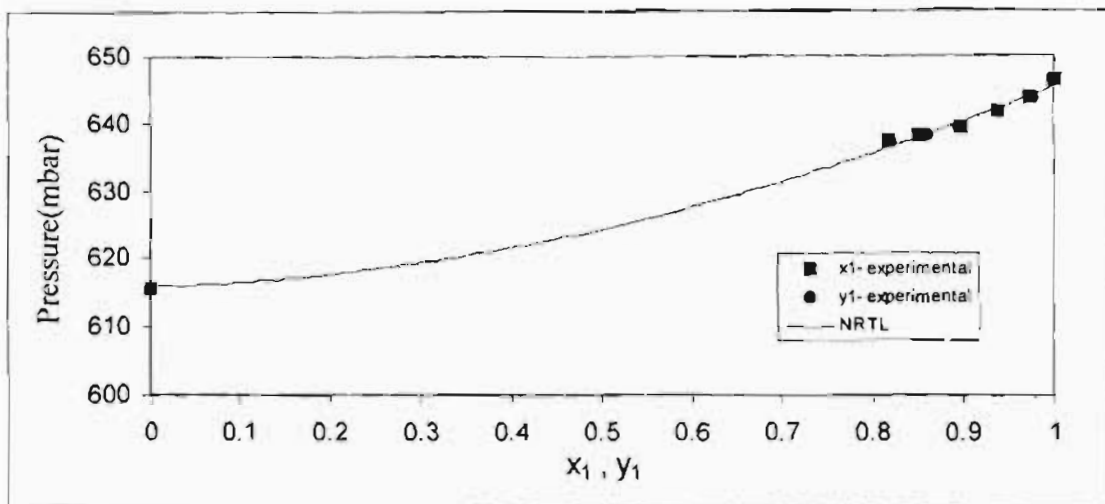


Figure 5. 33: Plot of P vs. x, y for NRTL fit of Hexene (1) + 3MCP (2) at 50 °C

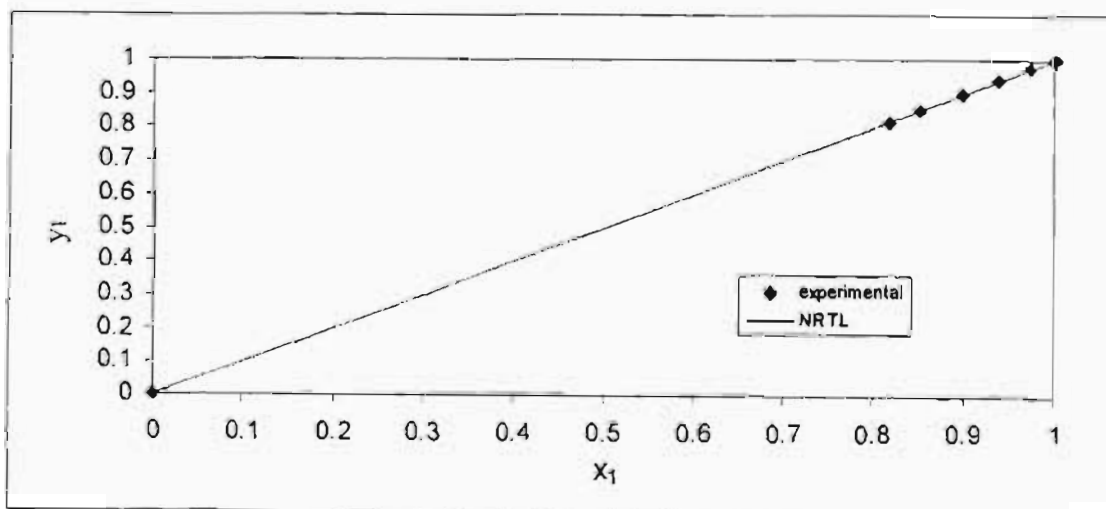


Figure 5. 34: Plot of y vs. x for NRTL fit of Hexene (1) + 3MCP (2) at 50 °C

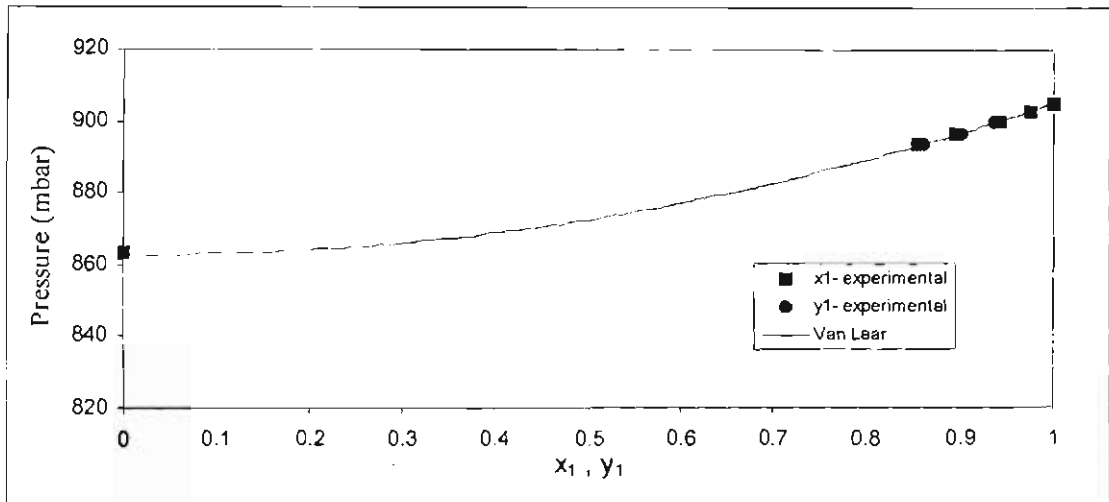


Figure 5. 35: Plot of P vs. x, y for Van Laar fit of Hexene (1) + 3MCP (2) at 60 °C

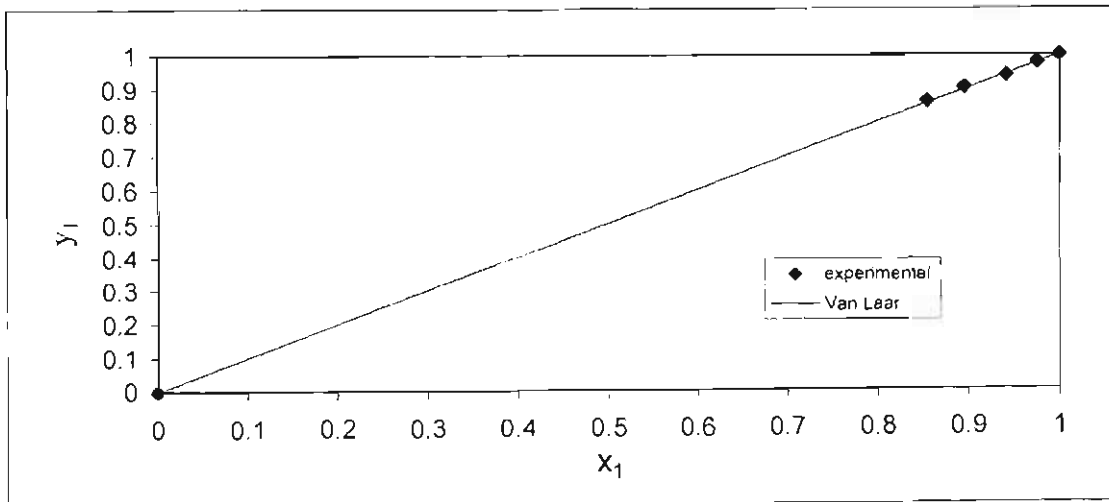


Figure 5. 36: Plot of y vs. x for Van Laar fit of Hexene (1) + 3MCP (2) at 60 °C

5.2.3 The Direct Method: Wong-Sandler-PRSV

From Table 5.3, for the Wong-Sandler-PRSV model in the direct method, the activity coefficient models vary from the NRTL, Van Laar, Wilson and Uniquac. Figures 5.37 to 5.54 alternate between P vs. x, y and y vs. x for each system at each temperature.

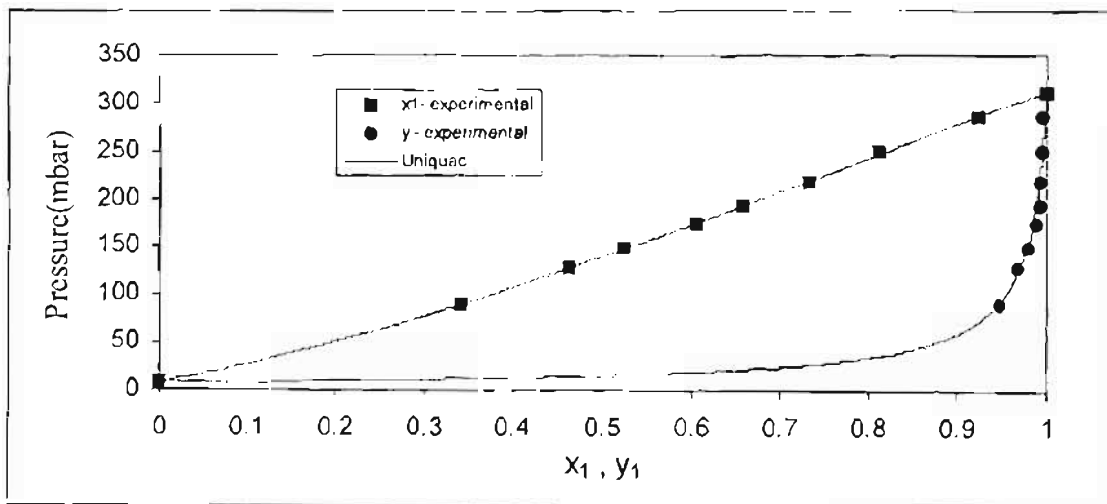


Figure 5. 37: Plot of P vs. x, y for Uniquac fit of Water (1) + NMP (2) at 70 °C

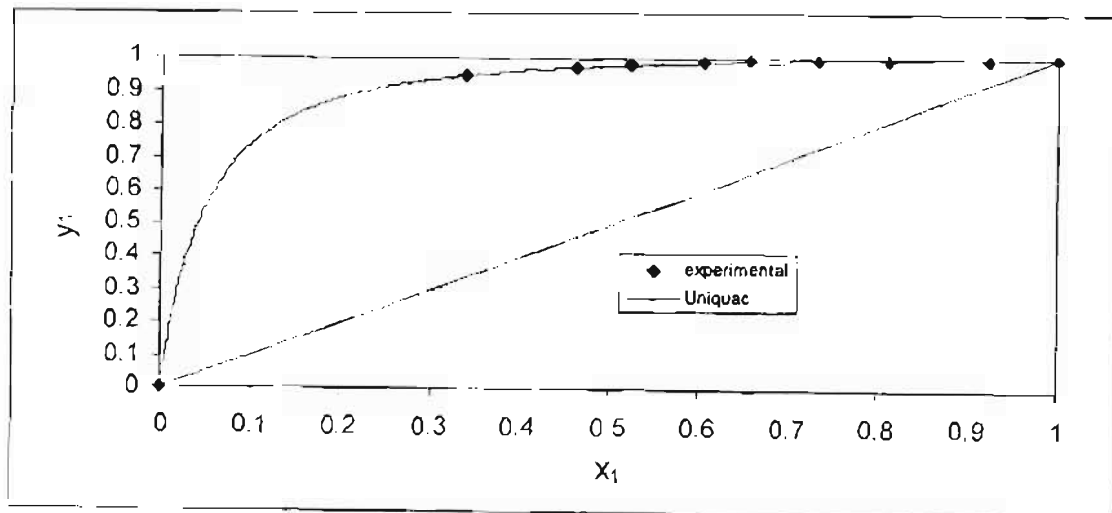


Figure 5. 38: Plot of y_1 vs. x_1 for Uniquac fit of Water (1) + NMP (2) at 70 °C

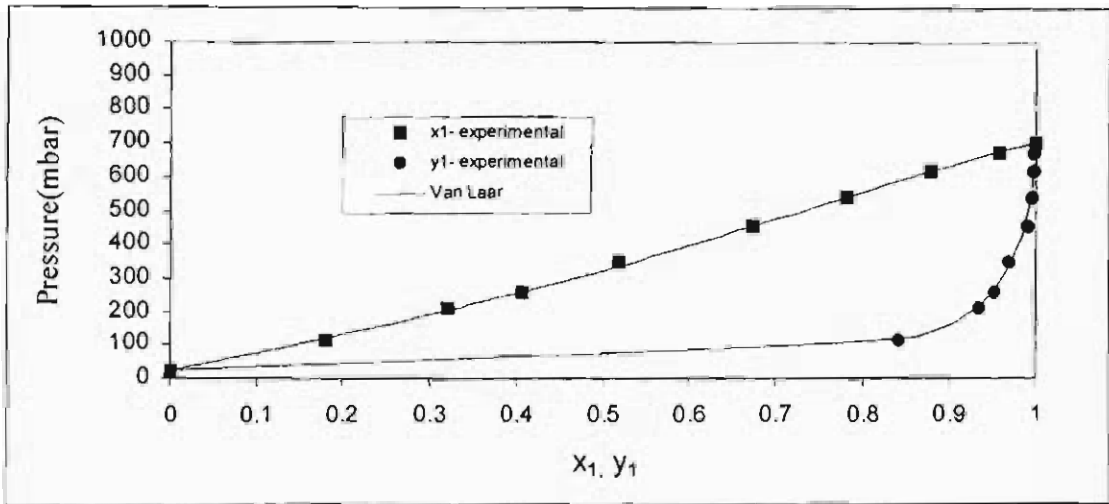


Figure 5. 39: Plot of P vs. x, y for Van Laar fit of Water (1) + NMP (2) at 90 °C

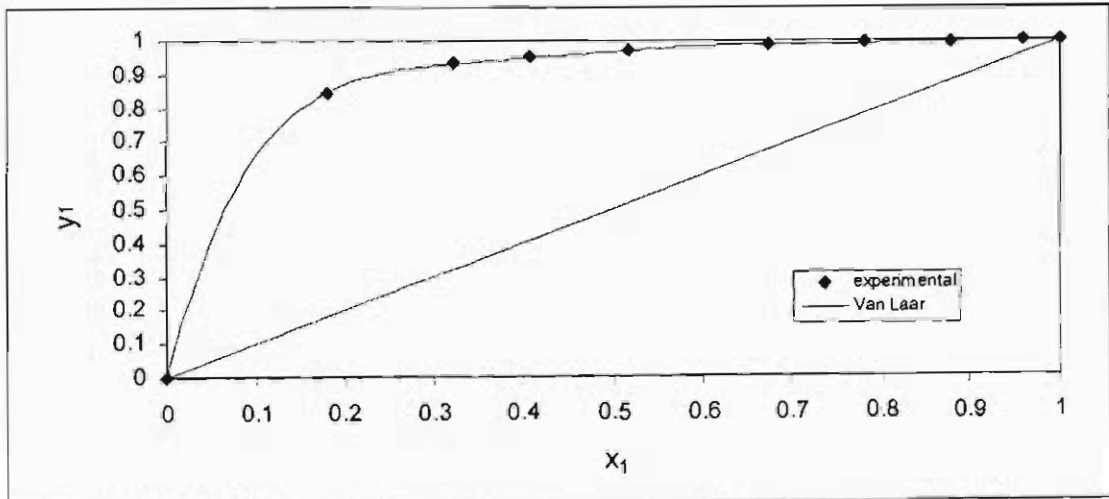


Figure 5. 40: Plot of y vs. x for Van Laar fit of Water (1) + NMP (2) at 90 °C

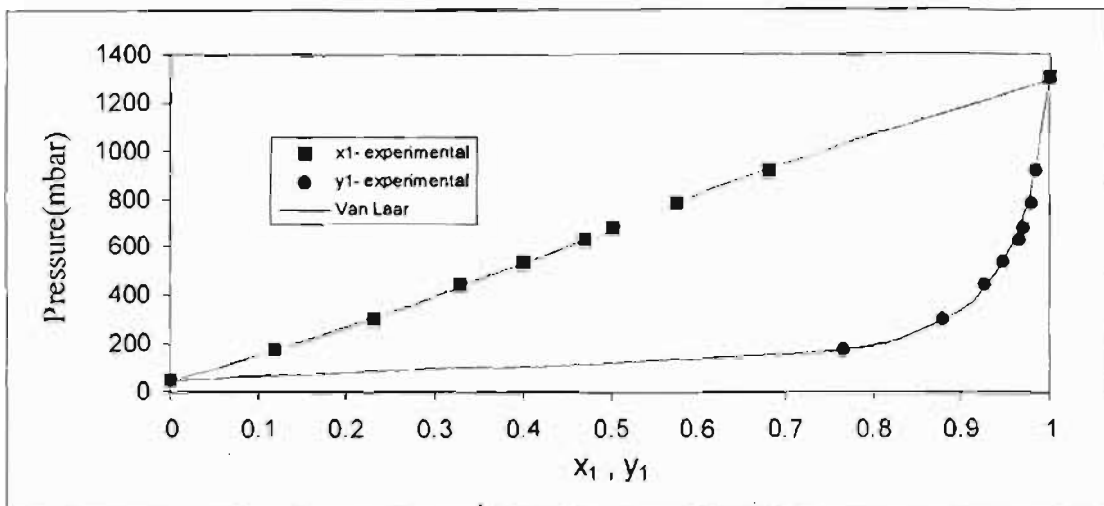


Figure 5.41: Plot of P vs. x, y for Van Laar fit of Water (1) + NMP (2) at 107 °C

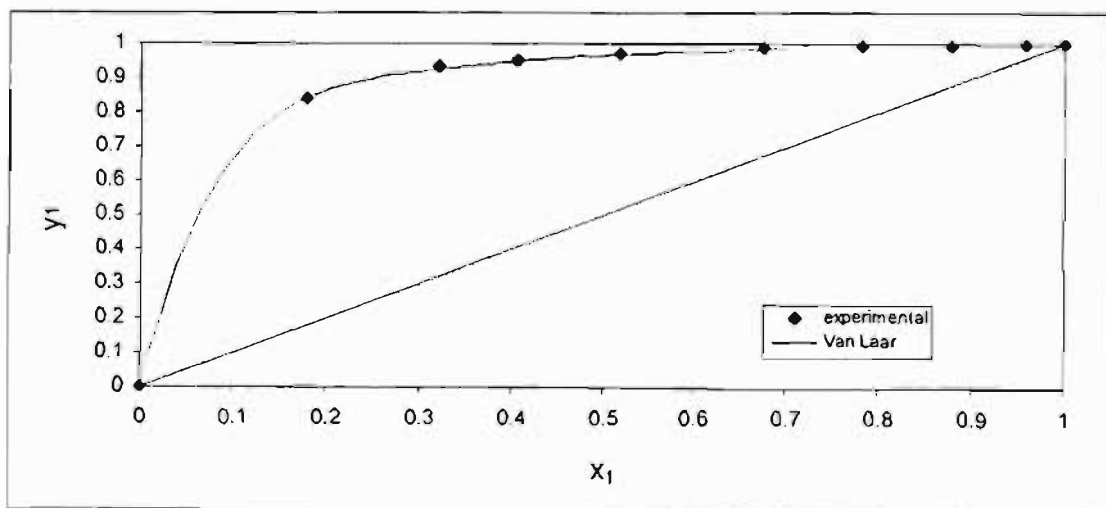


Figure 5.42: Plot of y vs. x for Van Laar fit of Water (1) + NMP (2) at 107 °C

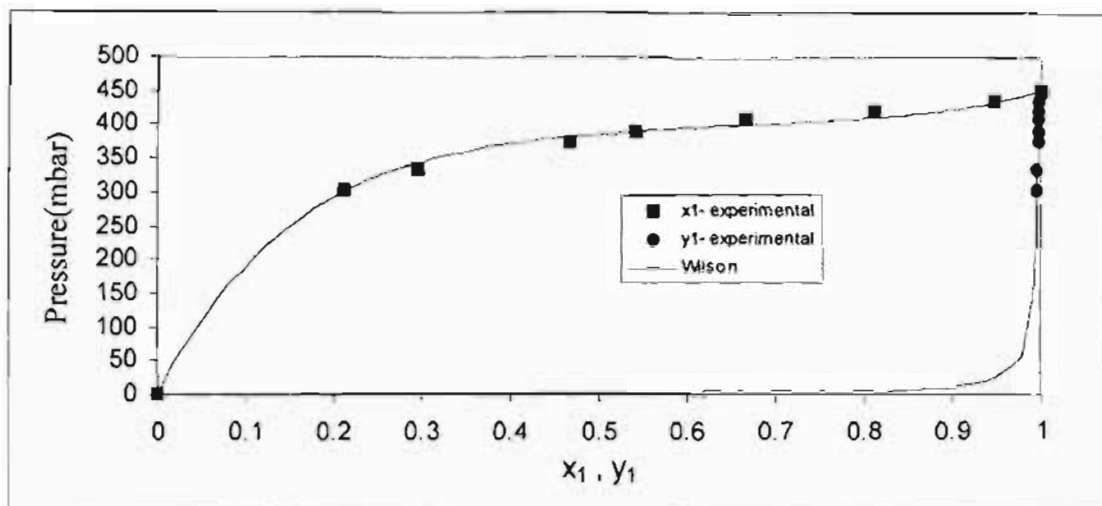


Figure 5. 43: Plot of P vs. x, y for Wilson fit of Hexene (1) + NMP (2) at 40 °C

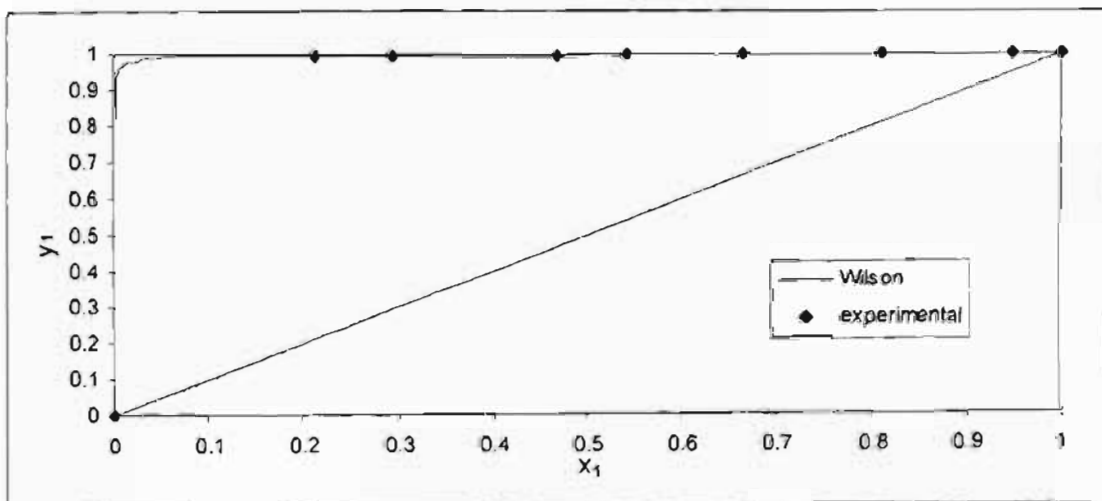


Figure 5. 44: Plot of y vs. x for Wilson fit of Hexene (1) + NMP (2) at 40 °C

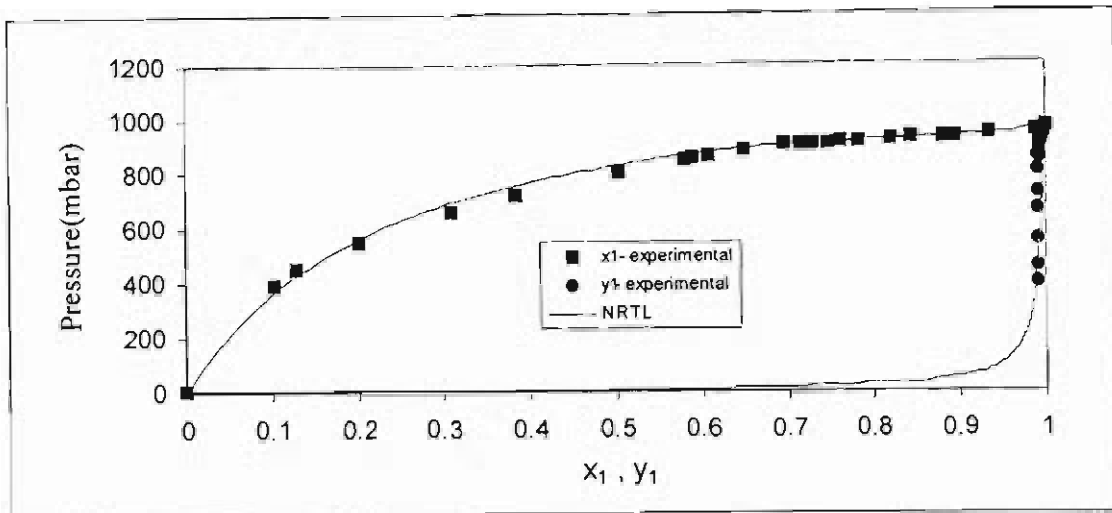


Figure 5. 45: Plot of P vs. x, y for NRTL fit of Hexene (1) + NMP (2) at 62 °C

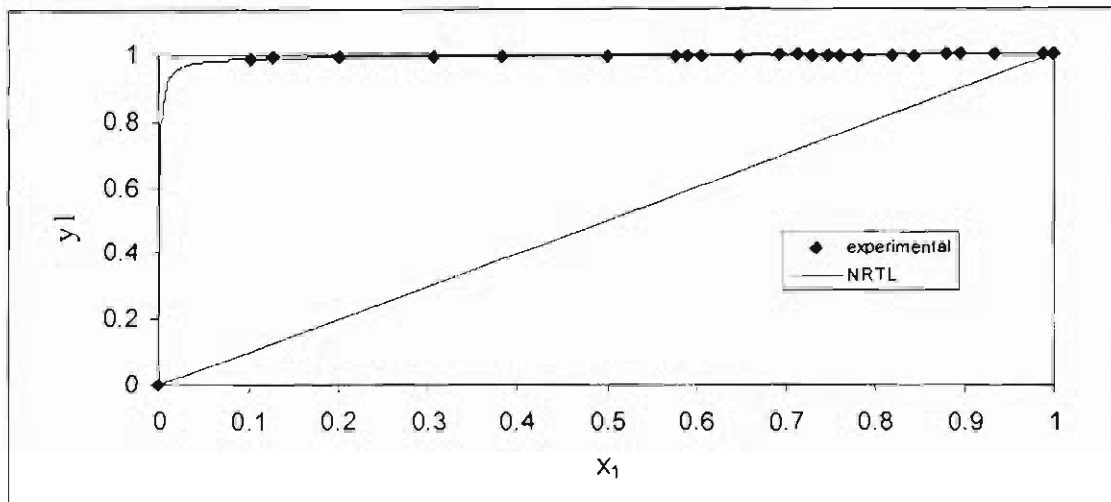


Figure 5. 46: Plot of y vs. x for NRTL fit of Hexene (1) + NMP (2) at 62 °C

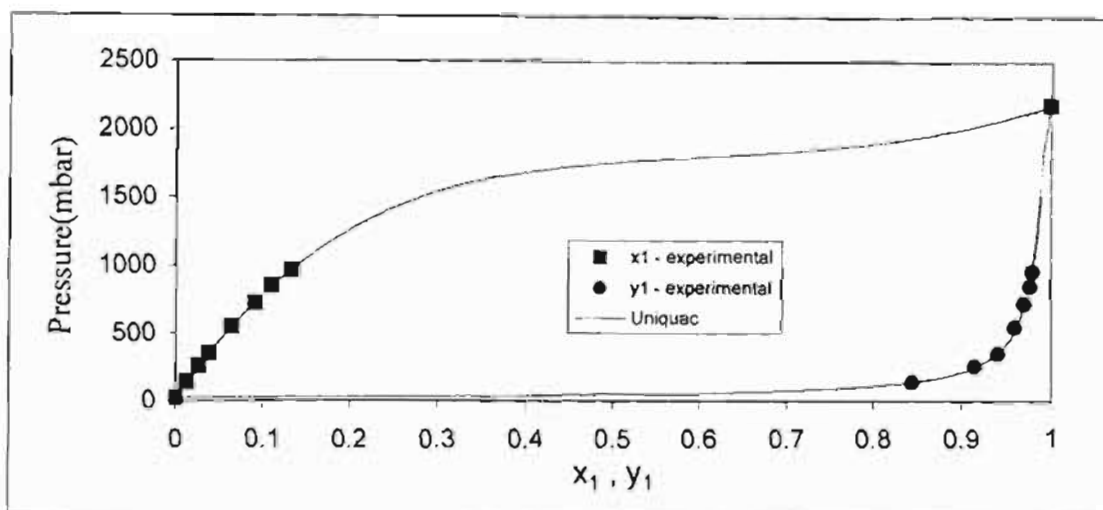


Figure 5. 47: Plot of P vs. x, y for Uniquac fit of Hexene (1) + NMP (2) at 90 °C

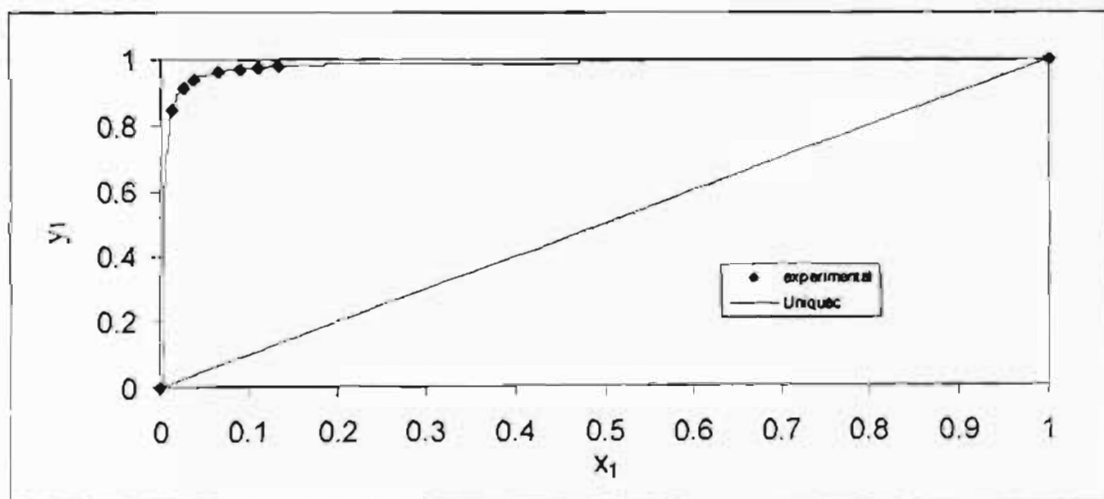


Figure 5. 48: Plot of y vs. x for Uniquac fit of Hexene (1) + NMP (2) at 90 °C

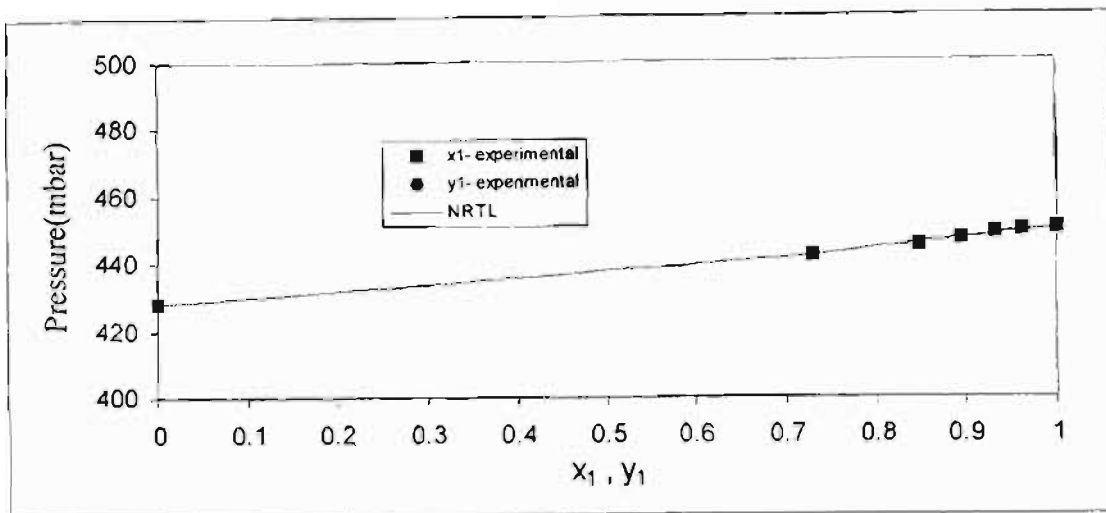


Figure 5. 49: Plot of P vs. x, y for NRTL fit of Hexene (1) + 3MCP (2) at 40 °C

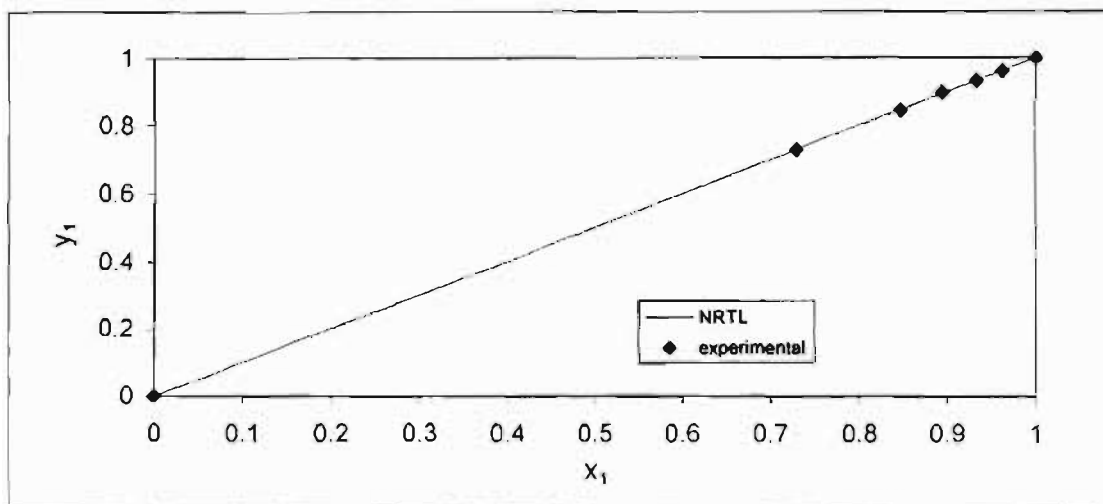


Figure 5. 50: Plot of y vs. x for NRTL fit of Hexene (1) + 3MCP (2) at 40 °C

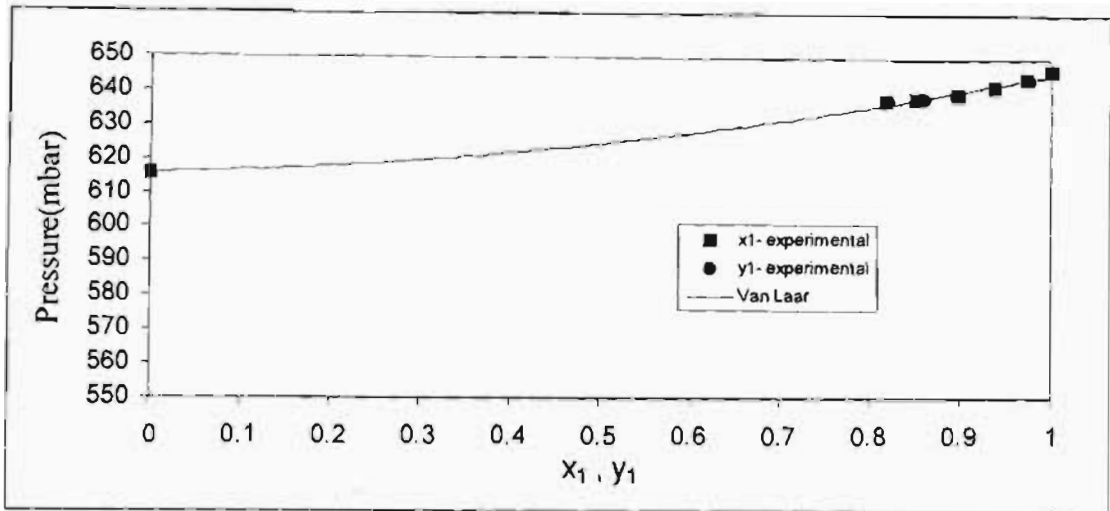


Figure 5. 51: Plot of P vs. x, y for Van Laar fit of Hexene (1) + 3MCP (2) at 50 °C

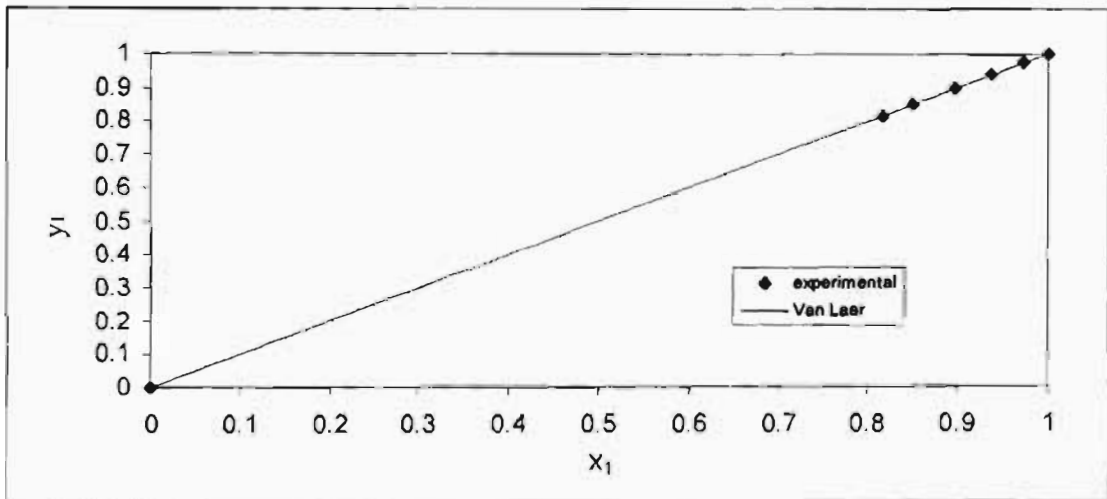


Figure 5. 52: Plot of y vs. x for Van Laar fit of Hexene (1) + 3MCP (2) at 50 °C

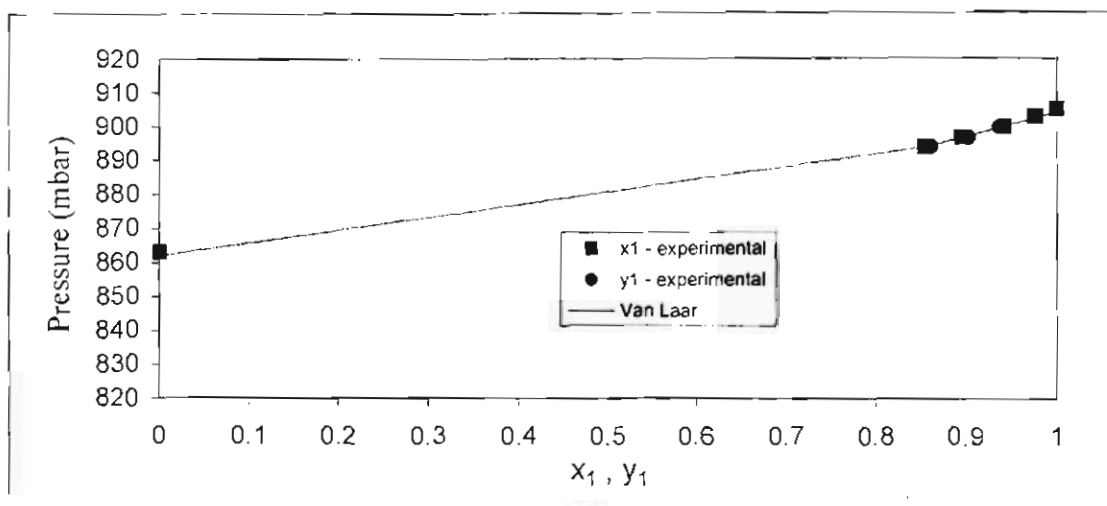


Figure 5.53: Plot of P vs. x, y for Van Laar fit of Hexene (1) + 3MCP (2) at 60 °C

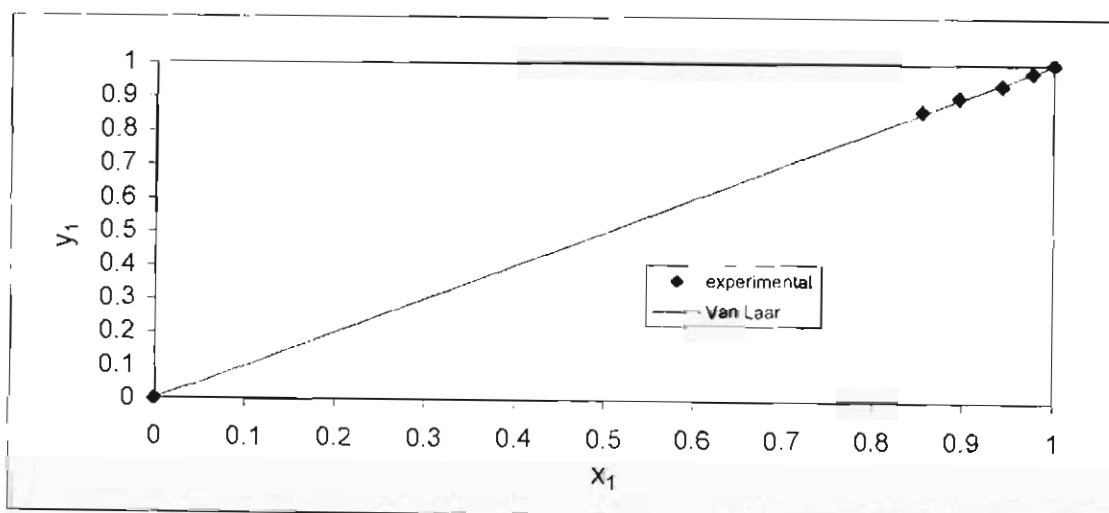


Figure 5.54: Plot of y vs. x for Van Laar fit of Hexene (1) + 3MCP (2) at 60 °C

5.2.4 The Direct Method: Twu-Coon-SRK

From Table 5.3, for the Twu-Coon-SRK model in the direct method, the activity coefficient models vary from the NRTL, Van Laar, and Uniquac. Figures 5.54 to 5.72 alternate between P vs. x, y and y vs. x for each system at each temperature.

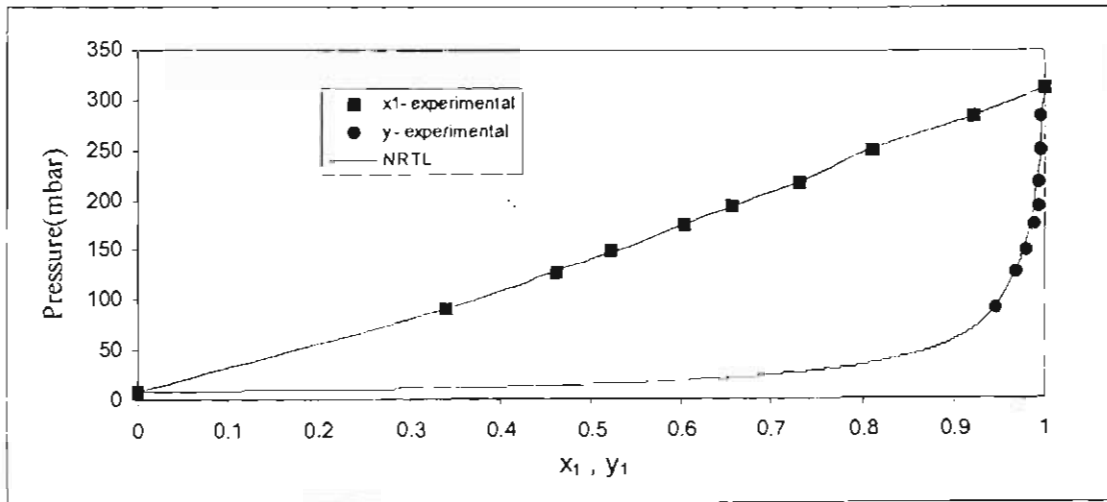


Figure 5. 55: Plot of P vs. x, y for NRTL fit of Water (1) + NMP (2) at 70 °C

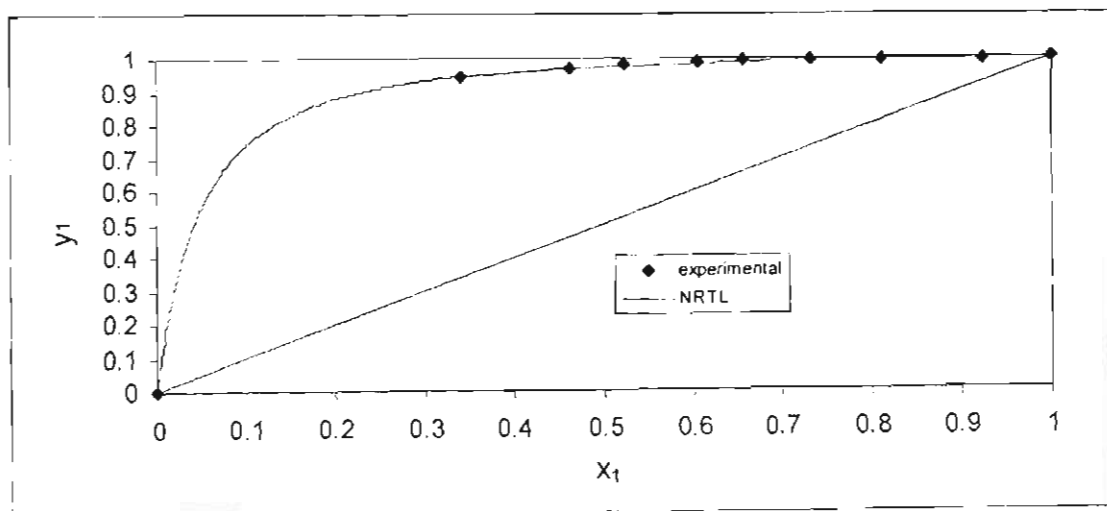


Figure 5. 56: Plot of y vs. x for NRTL fit of Water (1) + NMP (2) at 70 °C

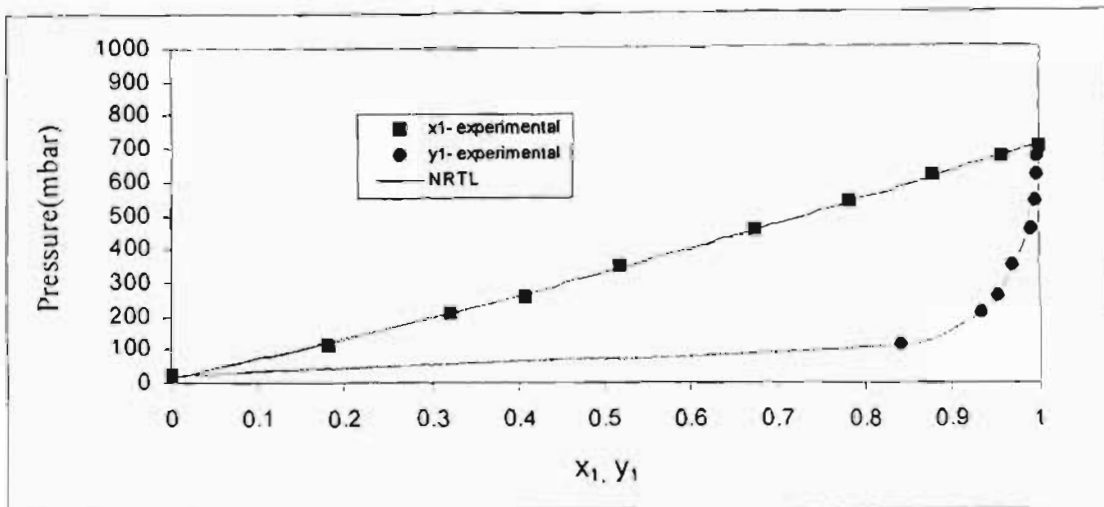


Figure 5.57: Plot of P vs. x, y for NRTL fit of Water (1) + NMP (2) at 90 °C

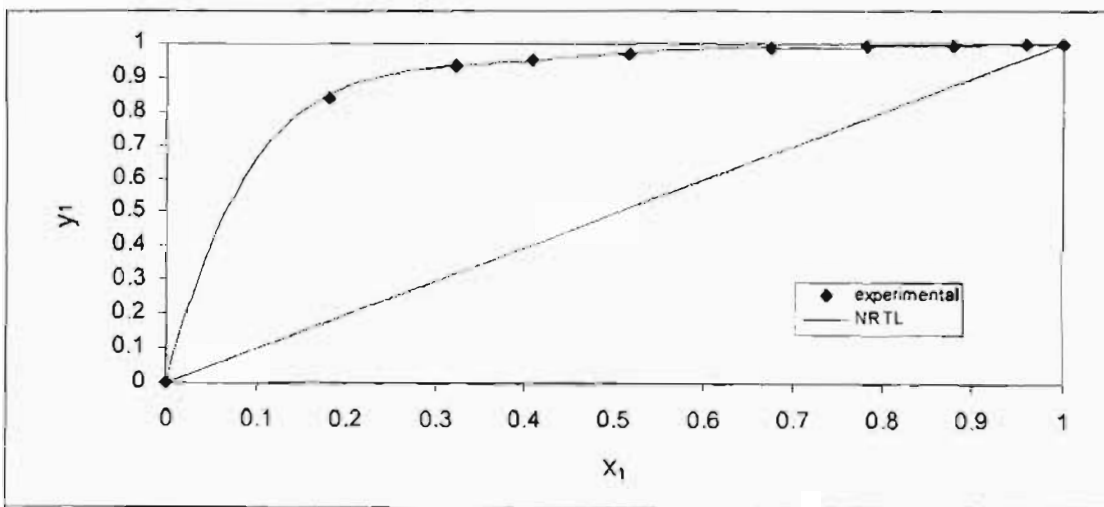


Figure 5.58: Plot of y vs. x for NRTL fit of Water (1) + NMP (2) at 90 °C

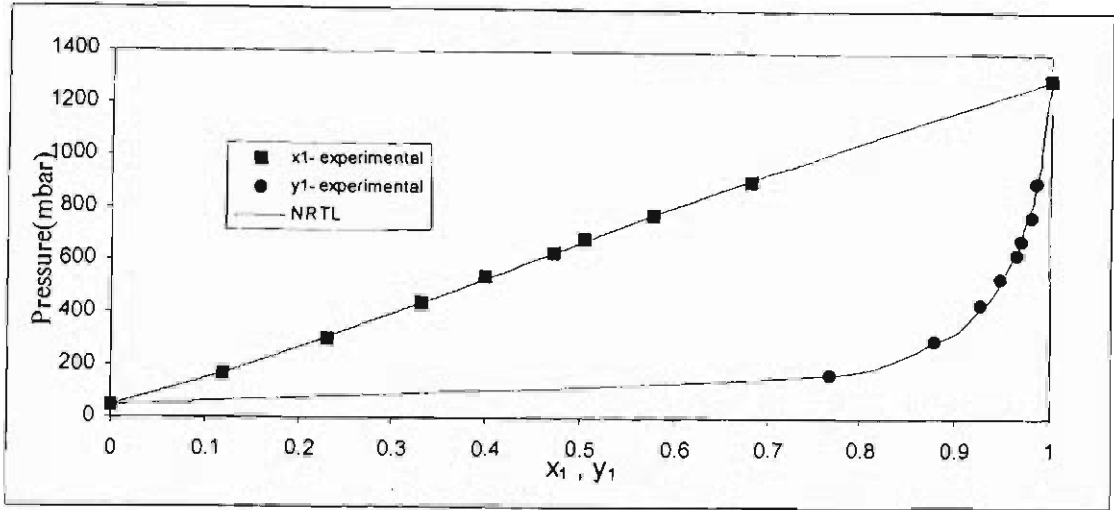


Figure 5. 59: Plot of P vs. x, y for NRTL fit of Water (1) + NMP (2) at 107 °C

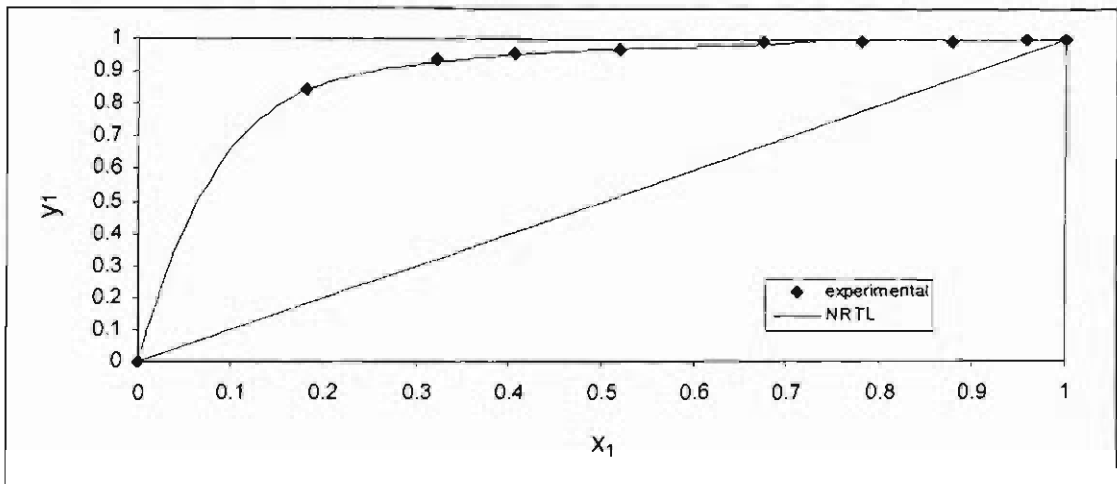


Figure 5. 60: Plot of y vs. x for NRTL fit of Water (1) + NMP (2) at 107 °C

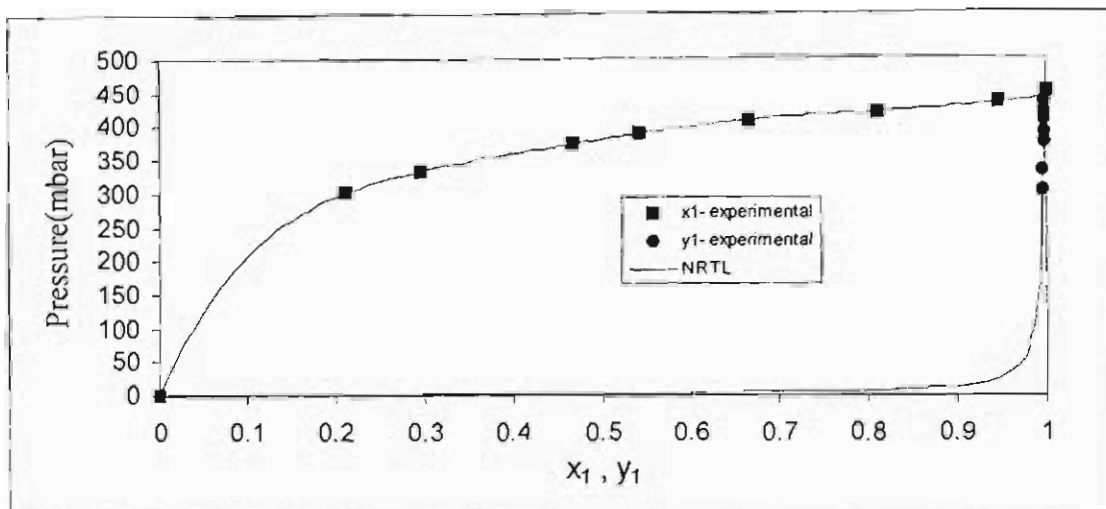


Figure 5. 61: Plot of P vs. x, y for NRTL fit of Hexene (1) + NMP (2) at 40 °C

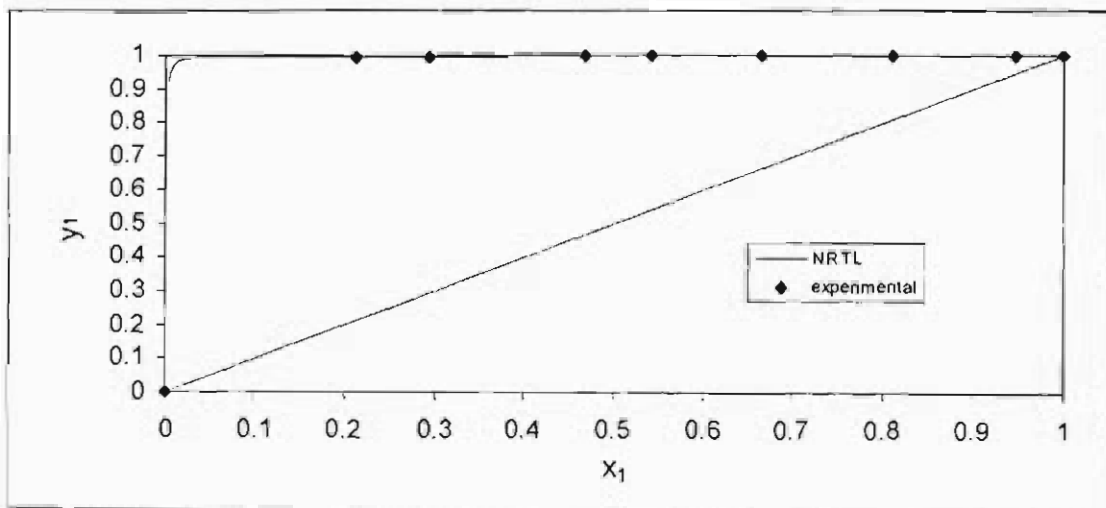


Figure 5. 62: Plot of y vs. x for NRTL fit of Hexene (1) + NMP (2) at 40 °C

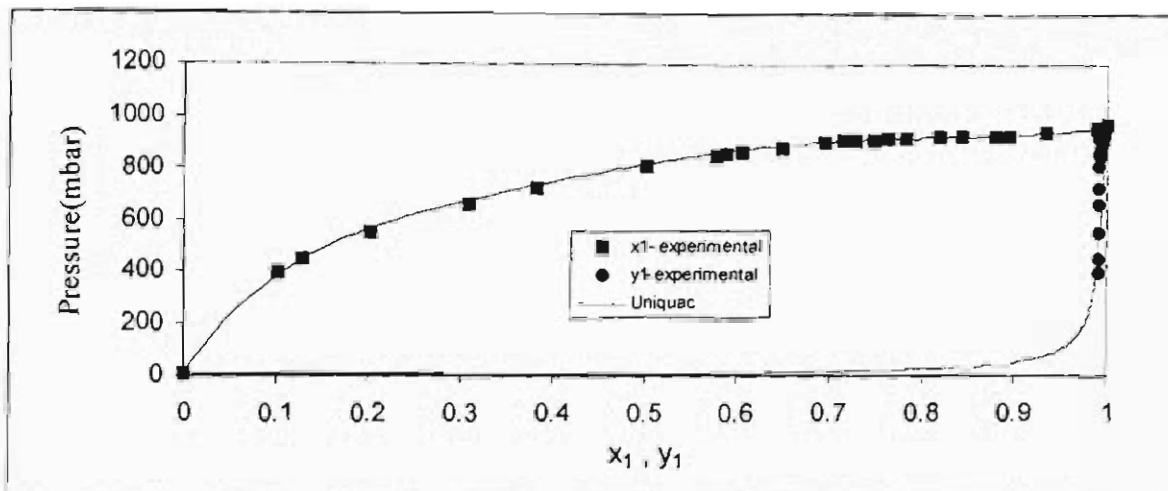


Figure 5. 63: Plot of P vs. x, y for Uniquac fit of Hexene (1) + NMP (2) at 62 °C

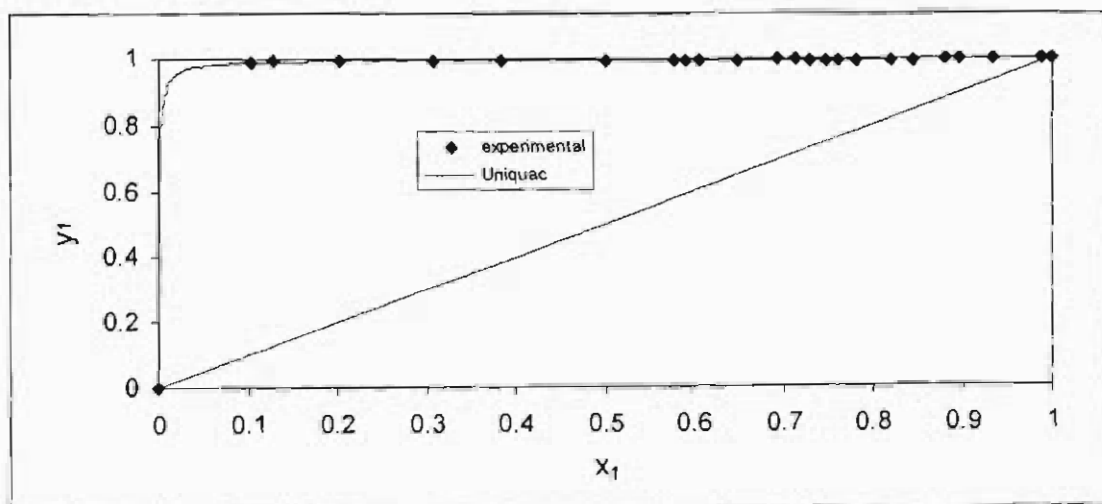


Figure 5. 64: Plot of y vs. x for Uniquac fit of Hexene (1) + NMP (2) at 62 °C

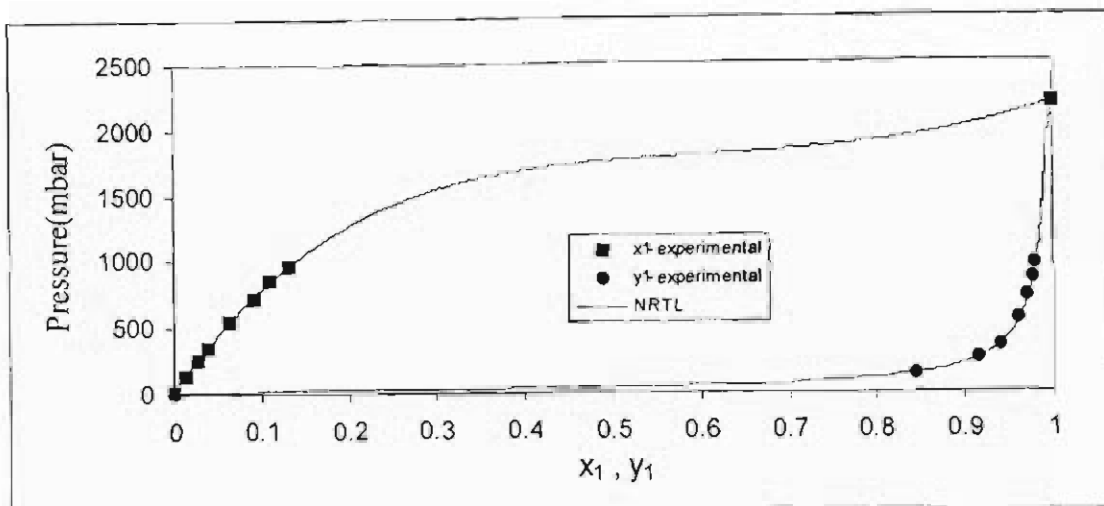


Figure 5. 65: Plot of P vs. x, y for NRTL fit of Hexene (1) + NMP (2) at 90 °C

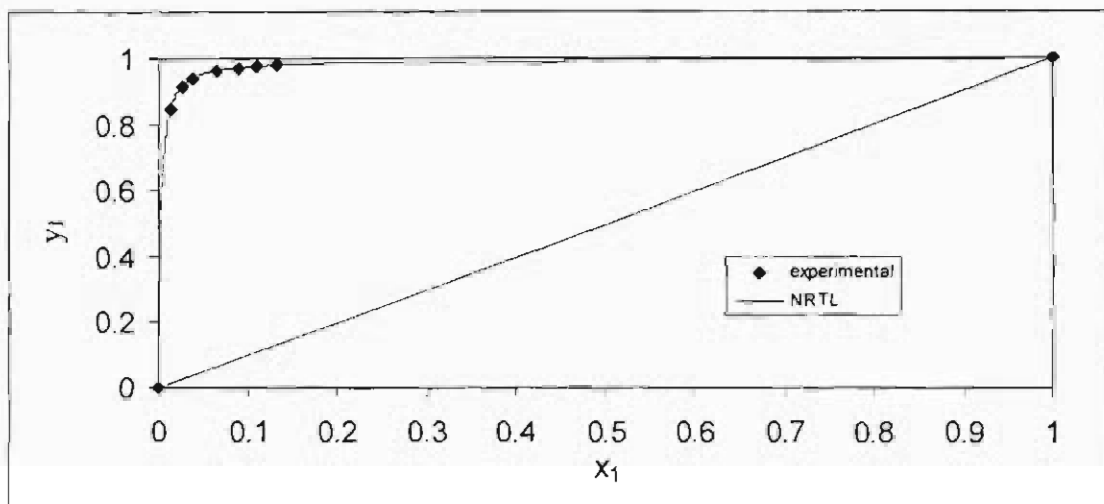


Figure 5. 66: Plot of y vs. x for NRTL fit of Hexene (1) + NMP (2) at 90 °C

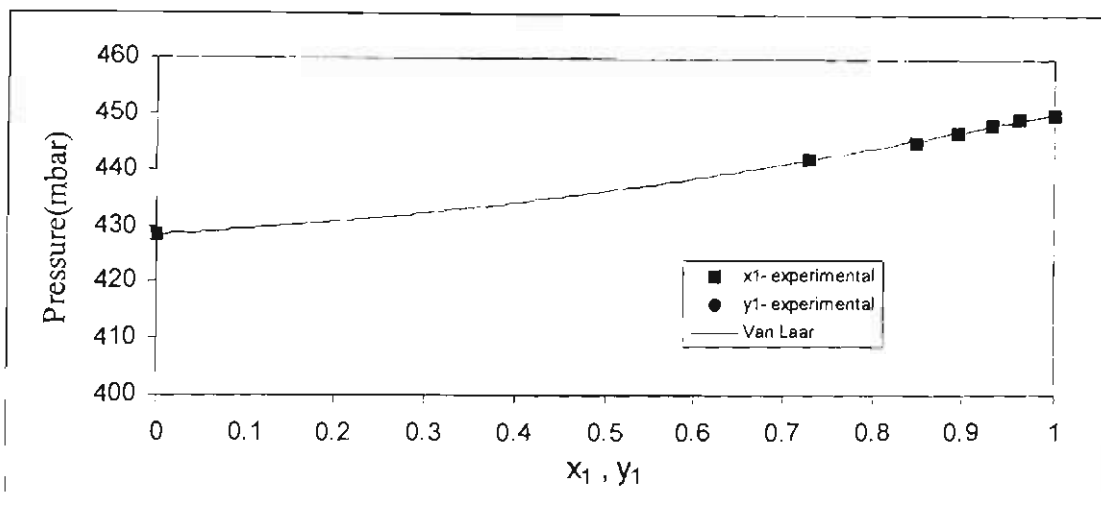


Figure 5. 67: Plot of P vs. x, y for Van Laar fit of Hexene (1) + 3MCP (2) at 40 °C

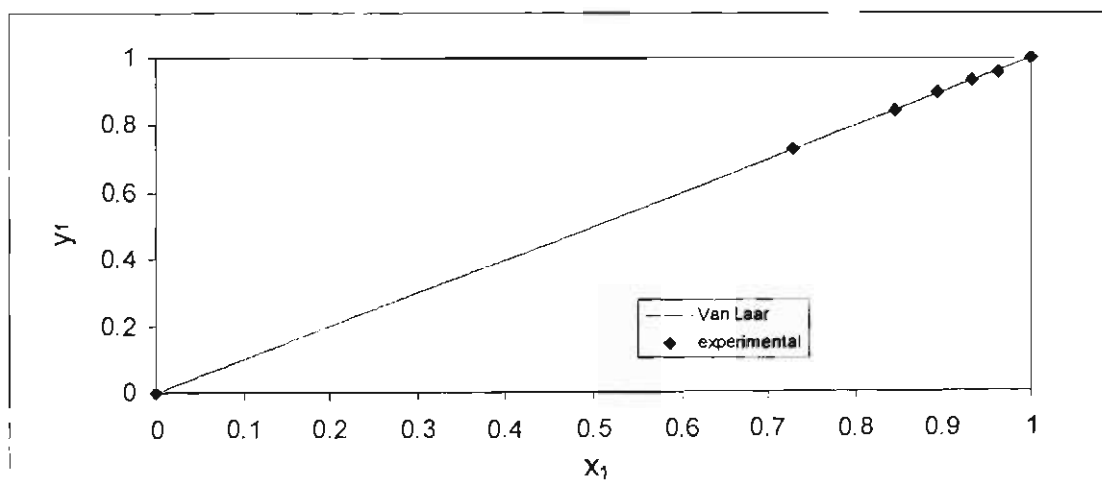


Figure 5. 68: Plot of y vs. x for Van Laar fit of Hexene (1) + 3MCP (2) at 40 °C

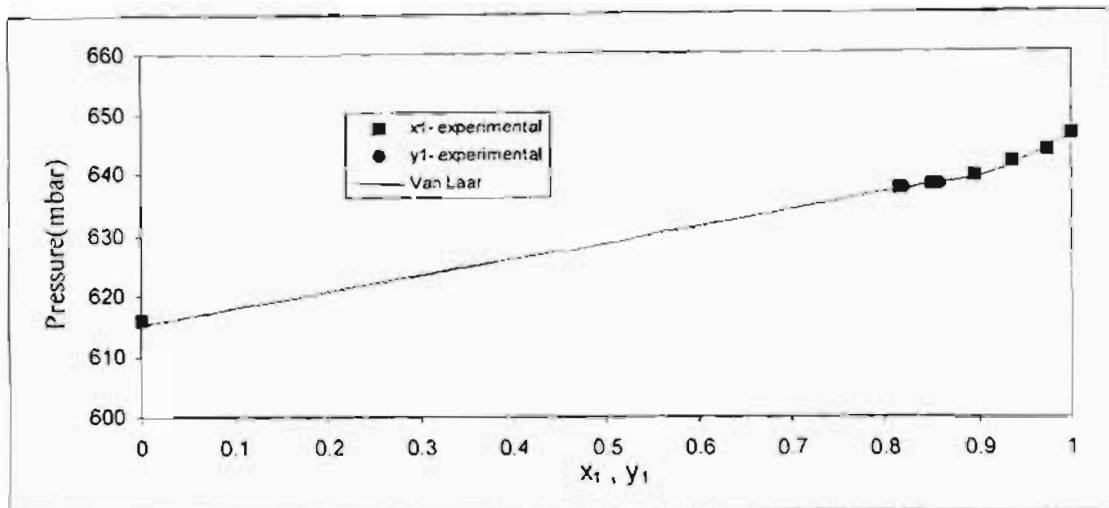


Figure 5. 69: Plot of P vs. x, y for Van Laar fit of Hexene (1) + 3MCP (2) at 50 °C

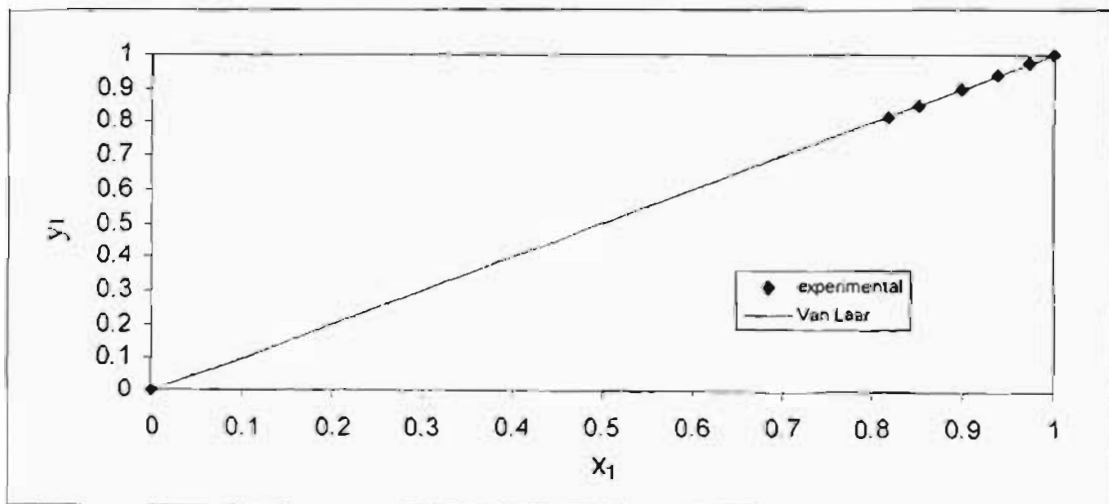


Figure 5. 70: Plot of y vs. x for Van Laar fit of Hexene (1) + 3MCP (2) at 50 °C

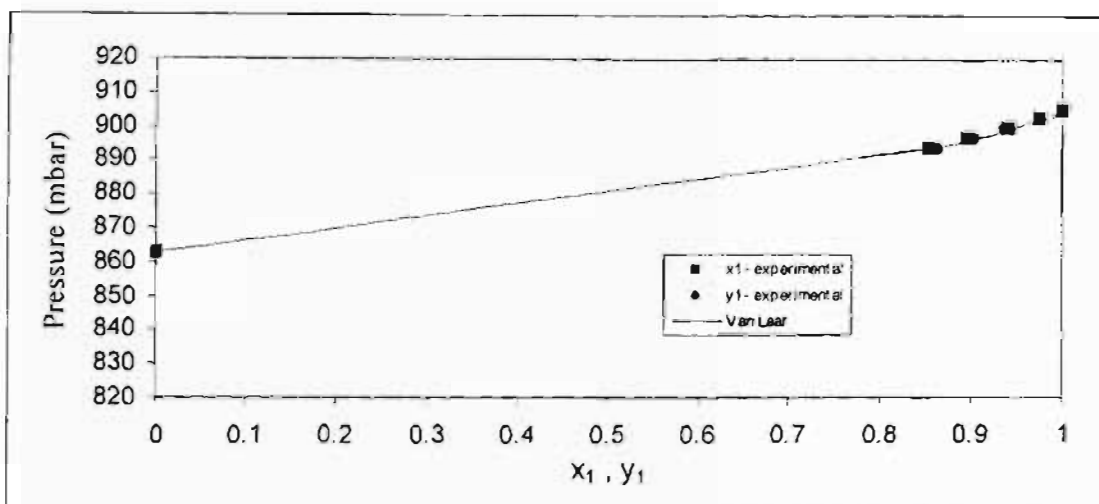


Figure 5. 71: Plot of P vs. x, y for Van Laar fit of Hexene (1) + 3MCP (2) at 60 °C

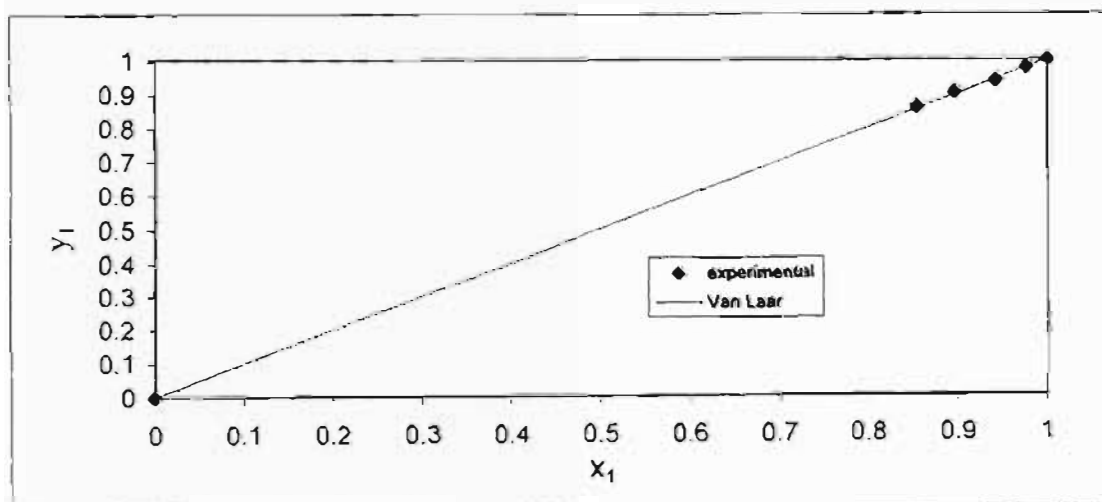


Figure 5. 72: Plot of y vs. x for Van Laar fit of Hexene (1) + 3MCP (2) at 60 °C

5.2.5 Direct Method- Twu-Coon PRSV

From Table 5.3, for the Twu-Coon-PRSV model in the direct method, the activity coefficient models that best fit the experimental data are the NRTL and Van Laar. Figures 5.73 to 5.90 alternate between P vs. x, y and y vs. x for each system at each temperature.

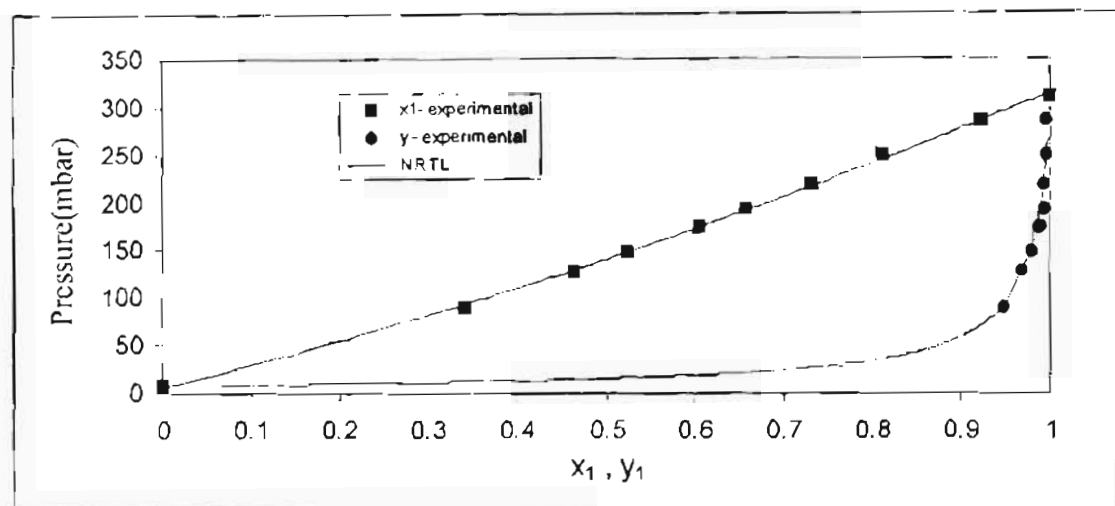


Figure 5. 73: Plot of P vs. x, y for NRTL fit of Water (1) + NMP (2) at 70 °C

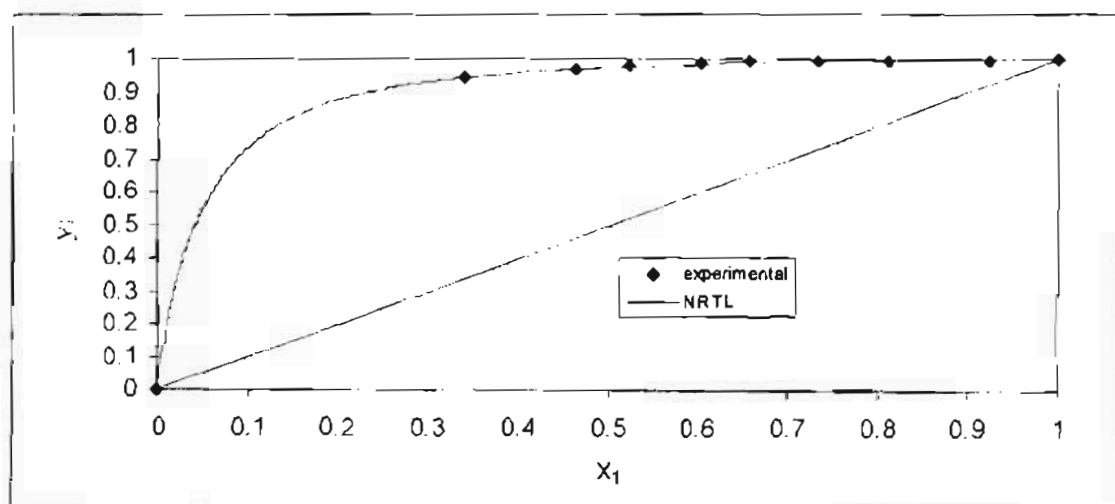


Figure 5. 74: Plot of y vs. x for NRTL fit of Water (1) + NMP (2) at 70 °C

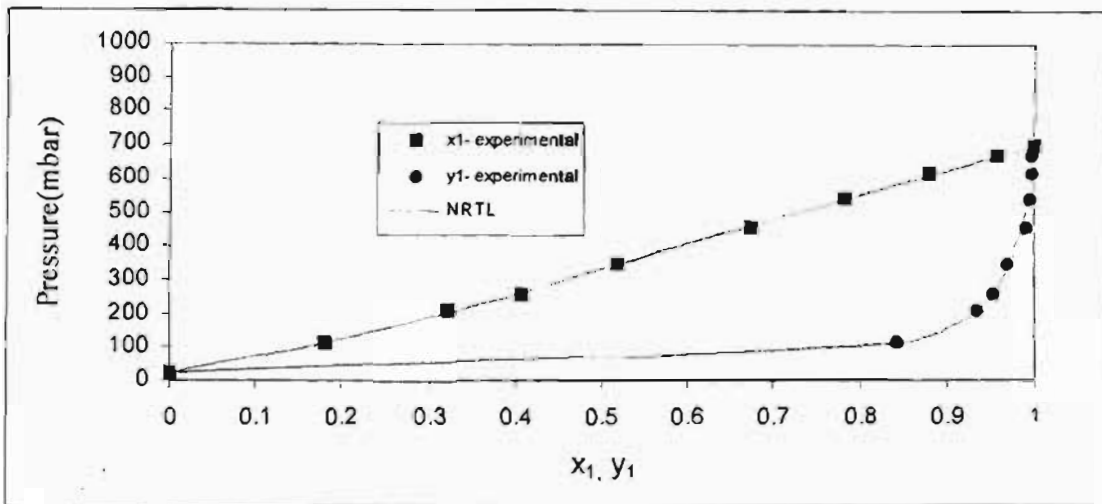


Figure 5. 75: Plot of P vs. x, y for NRTL fit of Water (1) + NMP (2) at 90 °C

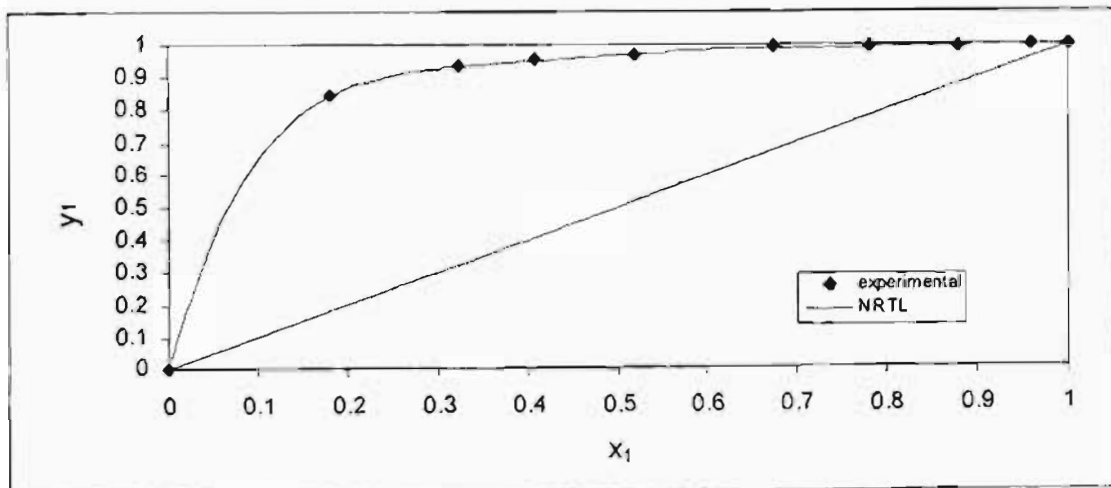


Figure 5. 76: Plot of y vs. x for NRTL fit of Water (1) + NMP (2) at 90 °C

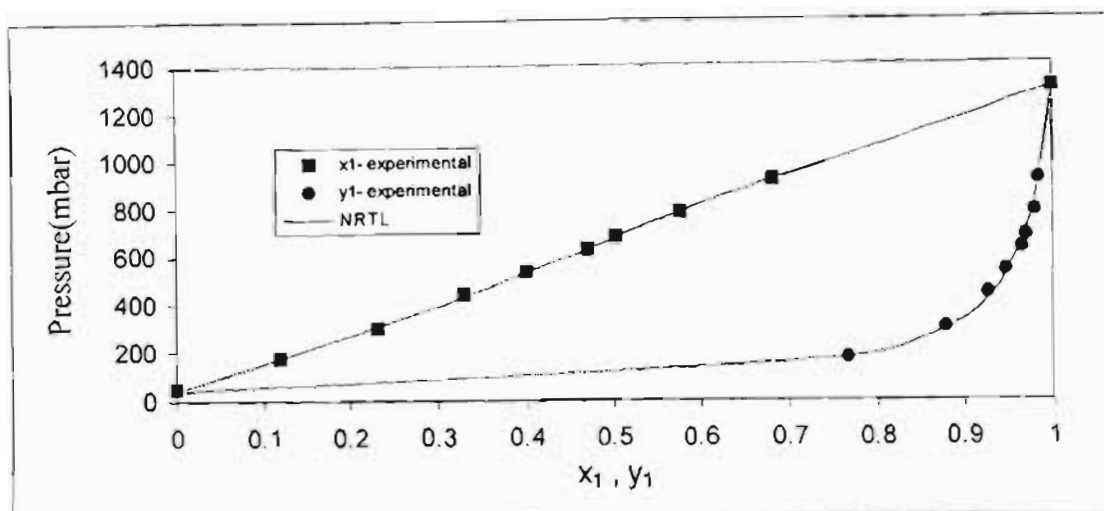


Figure 5. 77: Plot of P vs. x, y for NRTL fit of Water (1) + NMP (2) at 107 °C

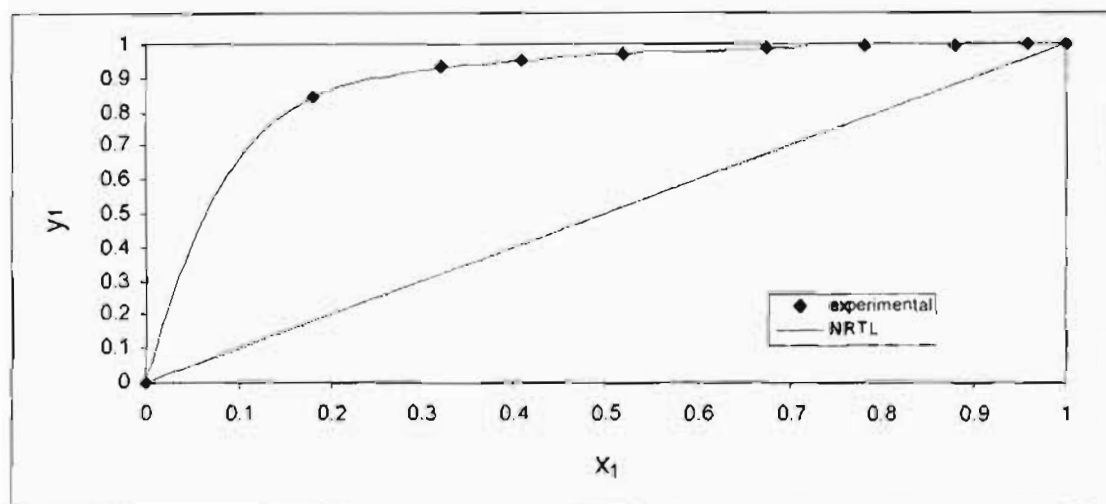


Figure 5. 78: Plot of y vs. x for NRTL fit of Water (1) + NMP (2) at 107 °C

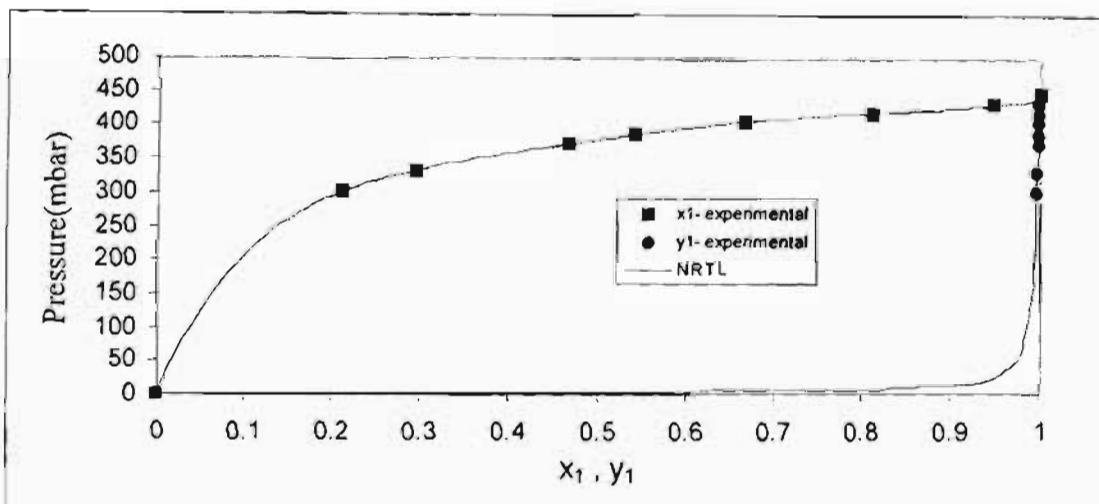


Figure 5.79: Plot of P vs. x, y for NRTL fit of Hexene (1) + NMP (2) at 40 °C

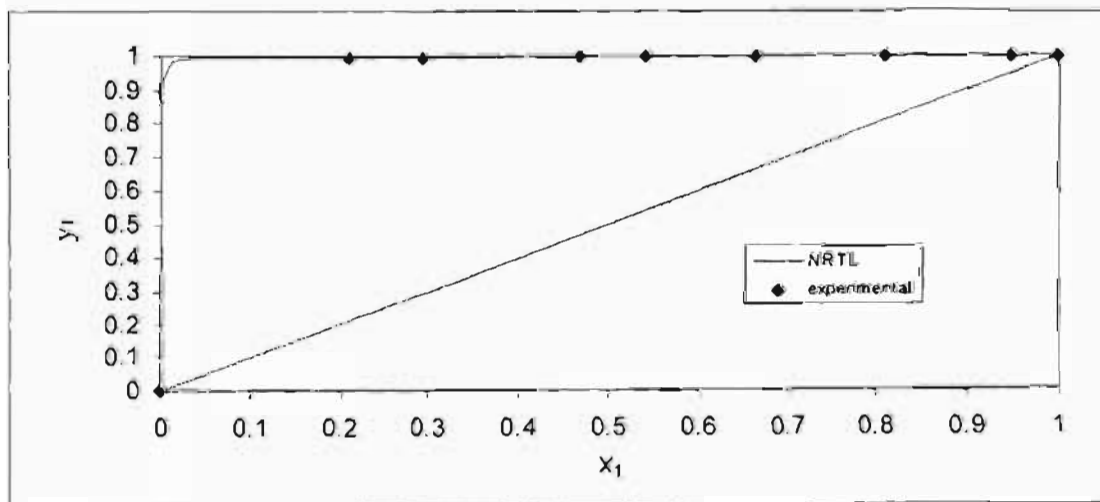


Figure 5.80: Plot of y vs. x for NRTL fit of Hexene (1) + NMP (2) at 40 °C

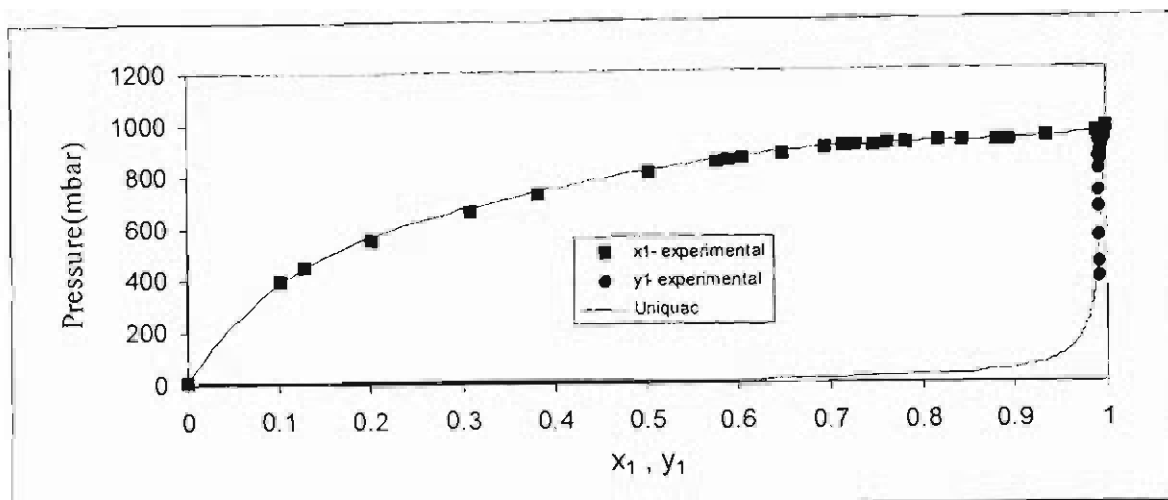


Figure 5. 81: Plot of P vs. x, y for Uniquac fit of Hexene (1) + NMP (2) at 62 °C

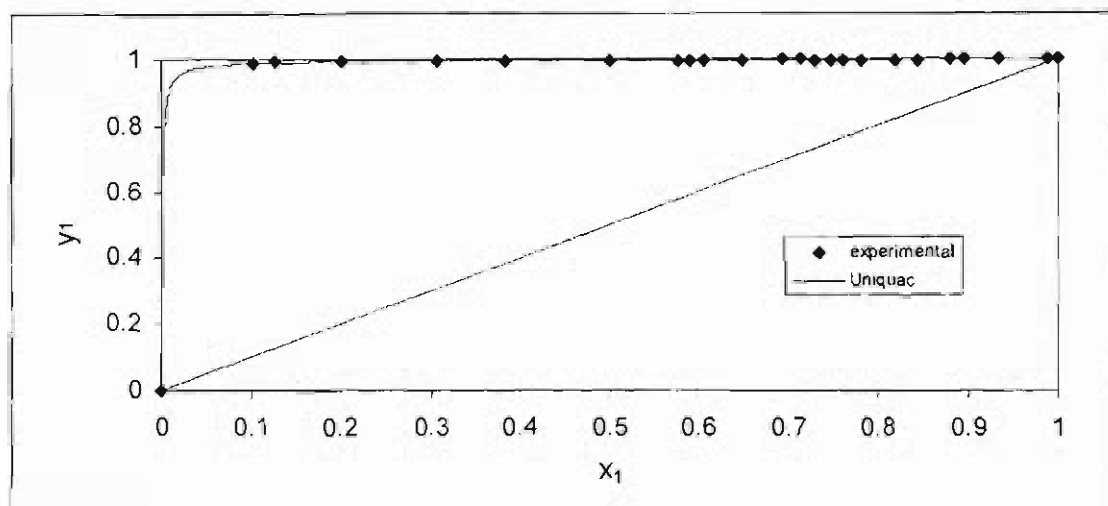


Figure 5. 82: Plot of y vs. x for Uniquac fit of Hexene (1) + NMP (2) at 62 °C

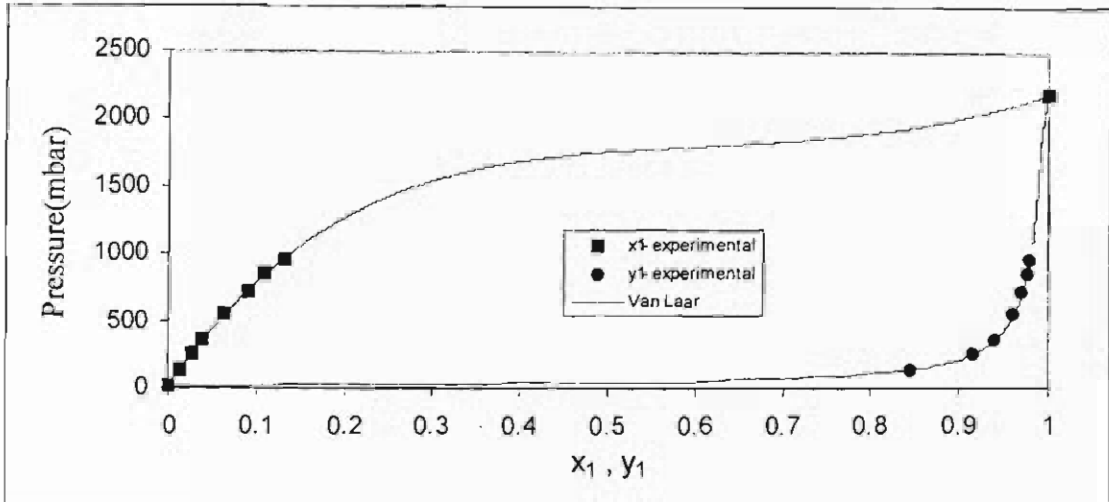


Figure 5. 83: Plot of P vs. x, y for Van Laar fit of Hexene (1) + NMP (2) at 90 °C

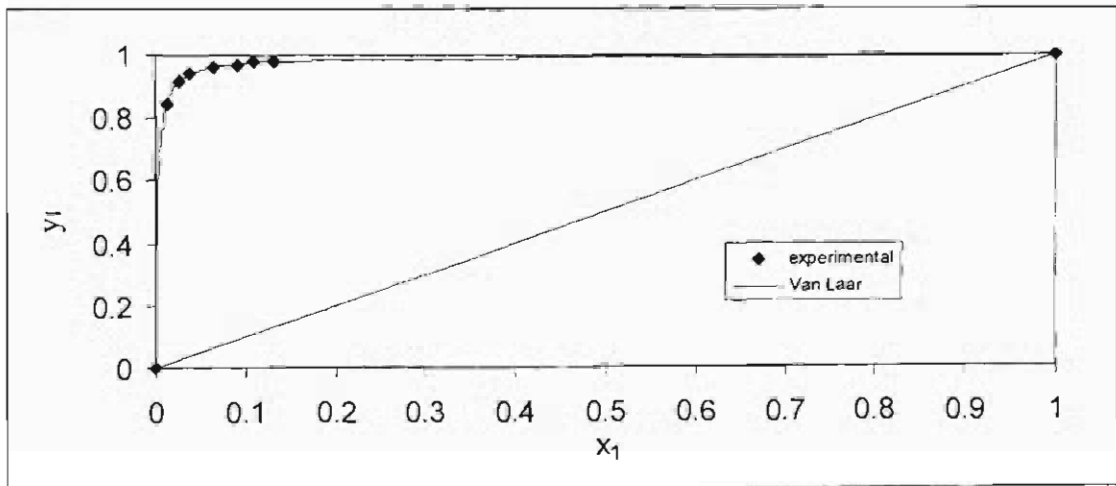


Figure 5. 84: Plot of y vs. x for Van Laar fit of Hexene (1) + NMP (2) at 90 °C

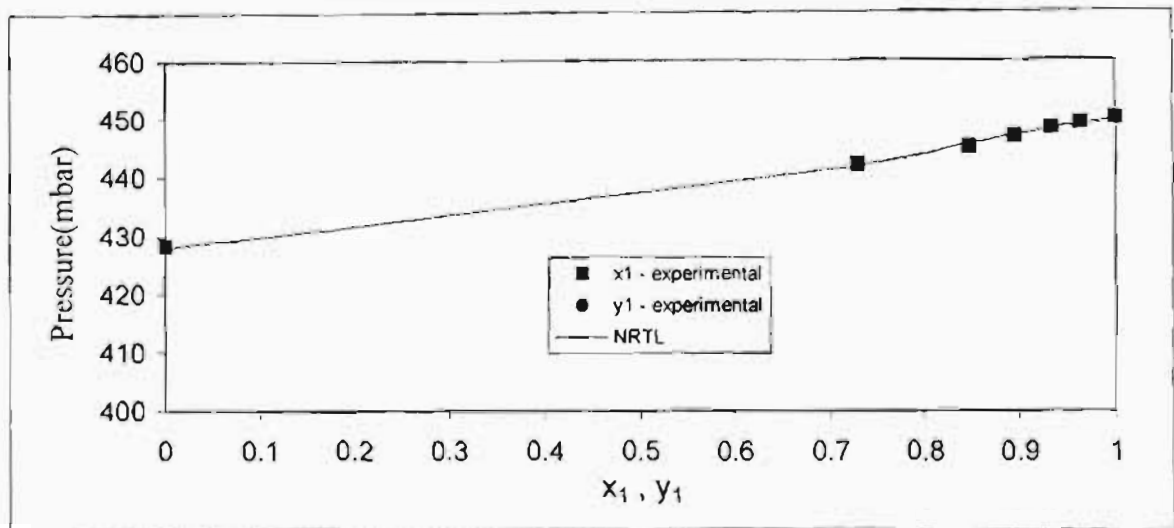


Figure 5.85: Plot of P vs. x, y for NRTL fit of Hexene (1) + 3MCP (2) at 40 °C

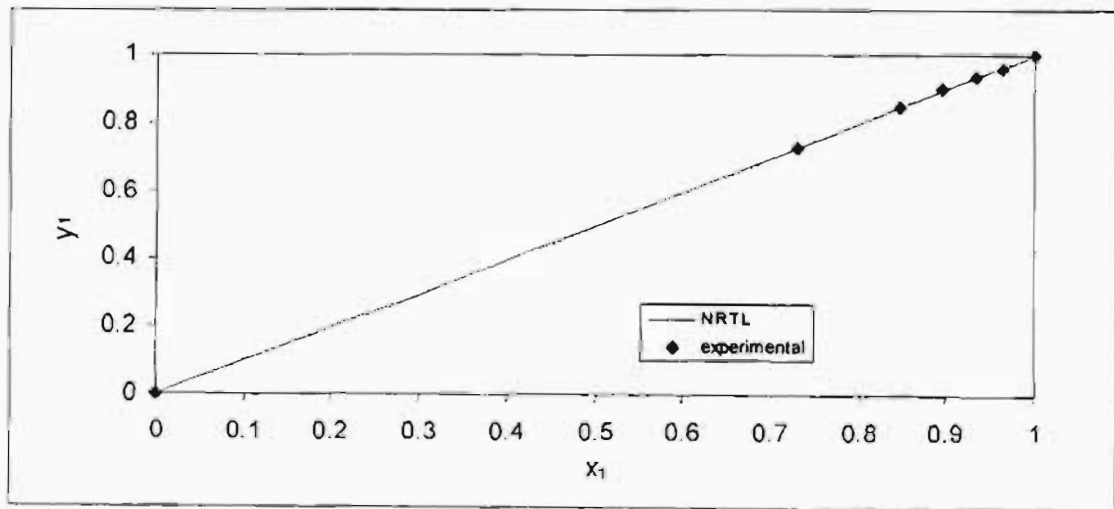


Figure 5.86: Plot of y vs. x for NRTL fit of Hexene (1) + 3MCP (2) at 40 °C

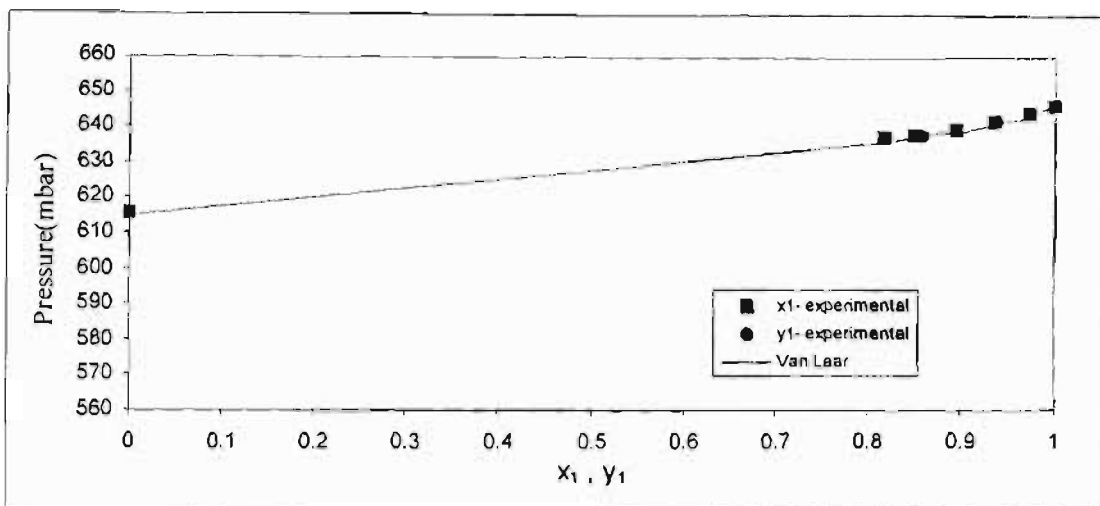


Figure 5. 87: Plot of P vs. x, y for Van Laar fit of Hexene (1) + 3MCP (2) at 50 °C

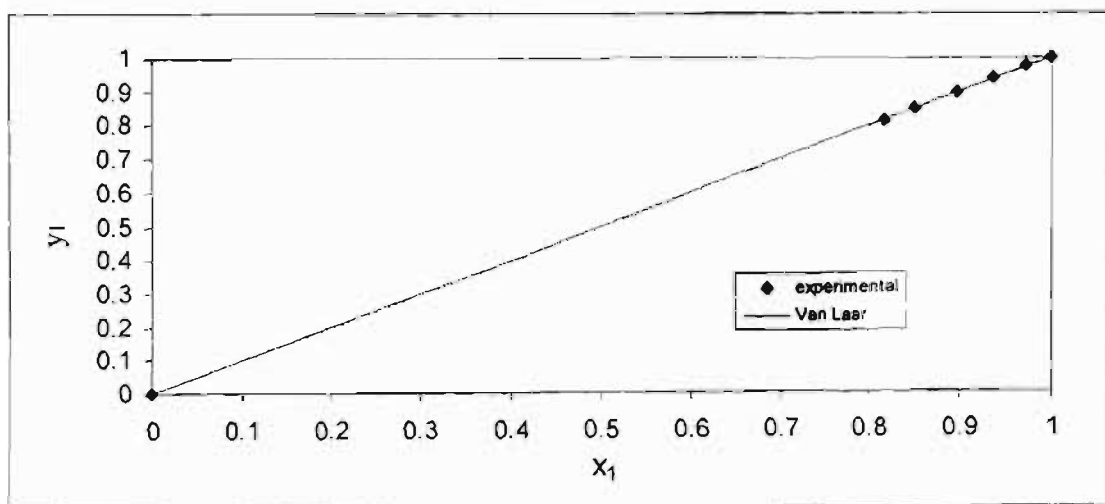


Figure 5. 88: Plot of y vs. x for Van Laar fit of Hexene (1) + 3MCP (2) at 50 °C

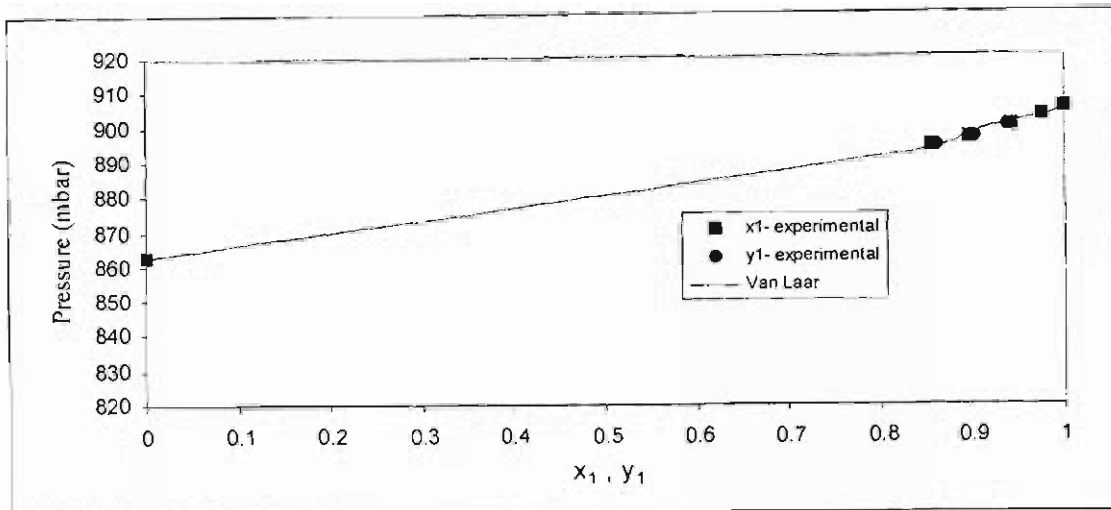


Figure 5. 89: Plot of P vs. x, y for Van Laar fit of Hexene (1) + 3MCP (2) at 60 °C

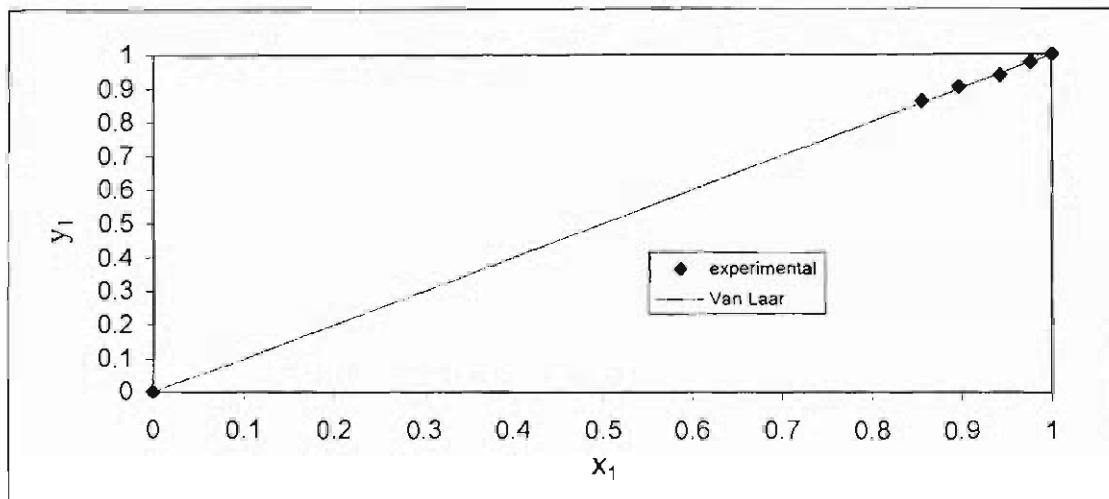


Figure 5. 90: Plot of y vs. x for Van Laar fit of Hexene (1) + 3MCP (2) at 60 °C

5.3 Thermodynamic Consistency Tests

In Chapter 2, Section 2.7 dealt with the theory of the various thermodynamic consistency tests available for data measured for low pressure measurements i.e. area, point and direct test. As explained in Section 2.7.1, the area test is not a sufficient condition for a consistency test as it is considered too mild, therefore this project has concentrated on the point and direct tests for the five different methods of data reduction used.

For the point test, the thermodynamic consistency of the system is judged by the vapour composition residual as experimental uncertainty is likely greatest for y . To successfully pass the point test, the vapour composition residual (δy) must scatter randomly about the x-axis, with the additional requirement of the average absolute deviation of the vapour composition being below 0.02. The plots of δy vs. x for the combined method can be found in Section 5.3.1 below and for the direct method in Appendix B.

For the direct test, data is regressed using the objective function based on the excess Gibbs energy residual, $\delta(\ln(\gamma_1/\gamma_2))$ as discussed in Chapter 2. For thermodynamically consistent data, the first measurement is that data in a plot of $\delta(\ln(\gamma_1/\gamma_2))$ vs. x_1 will scatter randomly about the x-axis, across the composition range. The plots for all systems measured for the combined method satisfy this requirement and can be found below in Section 5.3.1 and plots for the direct method can be found in Appendix B.

The second measurement for thermodynamically consistent data is comparing the RMS (root mean square) of the residual $\delta(\ln(\gamma_1/\gamma_2))$ to the Van Ness (1995) scale provided in Table 2.4 in Chapter 2. The scale ranges from a value of 1 (data of the highest quality) to 10 (data of poor quality). The Van Ness (1995) rating for the combined method can be found in Table 5.9.

This chapter focuses on the discussion of the point and direct test results for the combined method as the combined method performance is superior to the direct method in both the consistency tests. For the point test, the direct method shows either a

negative or positive bias, with average absolute δy values greater than 0.002 for the majority of the measured systems. For the direct method Van Ness tests, the index on the consistency scale ranges from 2 (very good) to 4 (satisfactory), with an average index of 4. The direct method consistency tests can be found in Appendix B.

5.3.1 Thermodynamic Consistency Tests for Combined Method

For the combined method, the graphical results of the point and the direct consistency tests for all systems measured can be found in Figures 5.91 to 5.108 alternatively.

The first requirement of the point test is satisfied for all the systems as the residuals δy scatter randomly across the x-axis. The second requirement of the point test is also achieved as the average absolute δy values as shown in Tables 5.4 to 5.8 are less than 0.002 for all measured systems.

The direct consistency test (Van Ness test) scale for the combined method of modeling can be found in Table 5.9. For the Van Ness test, the average index for all systems measured is 2 (very good), with the worst rating of 3 (good) for water (1) + NMP (2) at 70 °C and the best rating of 1 (excellent) for 1-hexene (1) + NMP (2) at 90 °C.

Table 5.9: Direct Test Scale for the Combined Method

Activity	water (1) + NMP (2)			1-hexene(1) + NMP(2)			1-hexene(1) + 3MCP (2)		
Coefficient Model									
Temperature									
T °C	70	90	107	40	62	90	40	50	60
Index	3	2	2	2	2	1	2	2	2

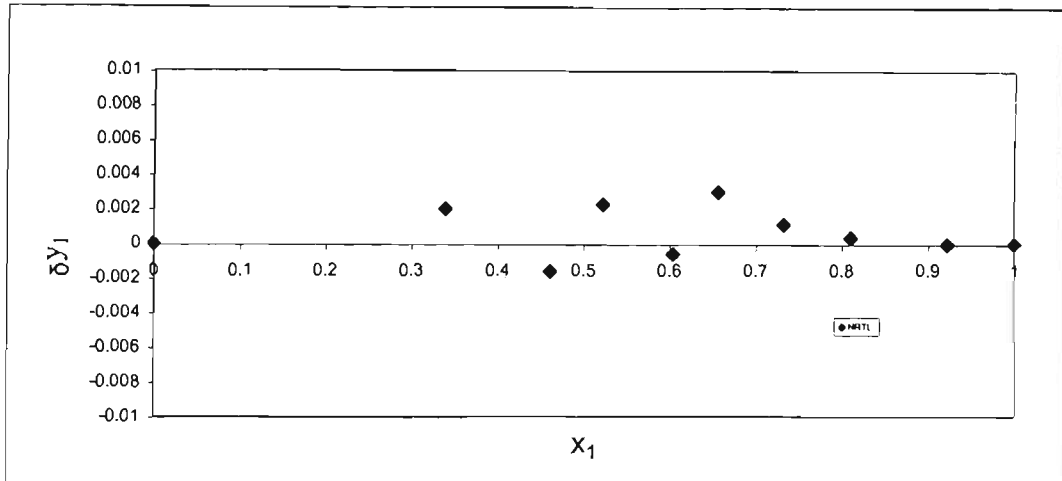


Figure 5. 91: Point Test for Water (1) + NMP (2) at 70 °C

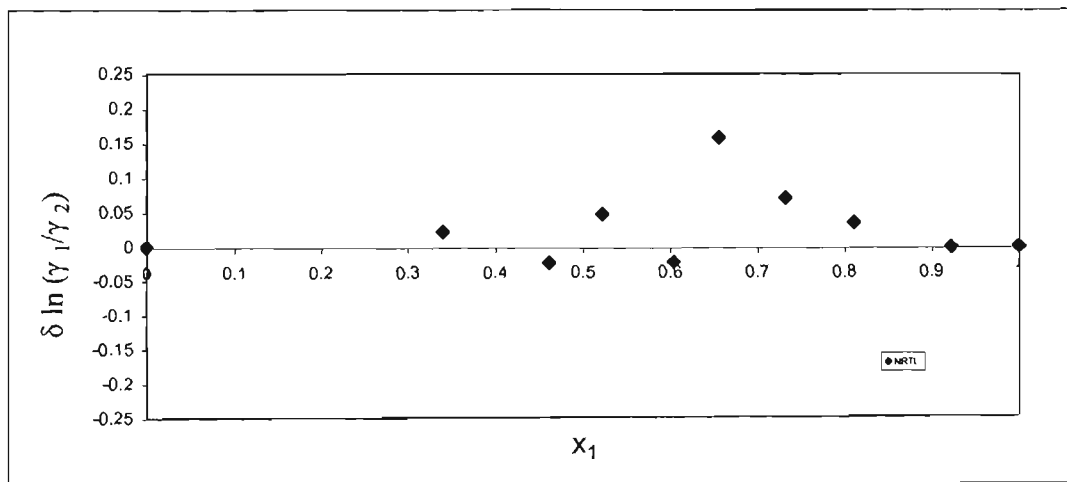


Figure 5. 92: Direct Test for Water (1) + NMP (2) at 70 °C

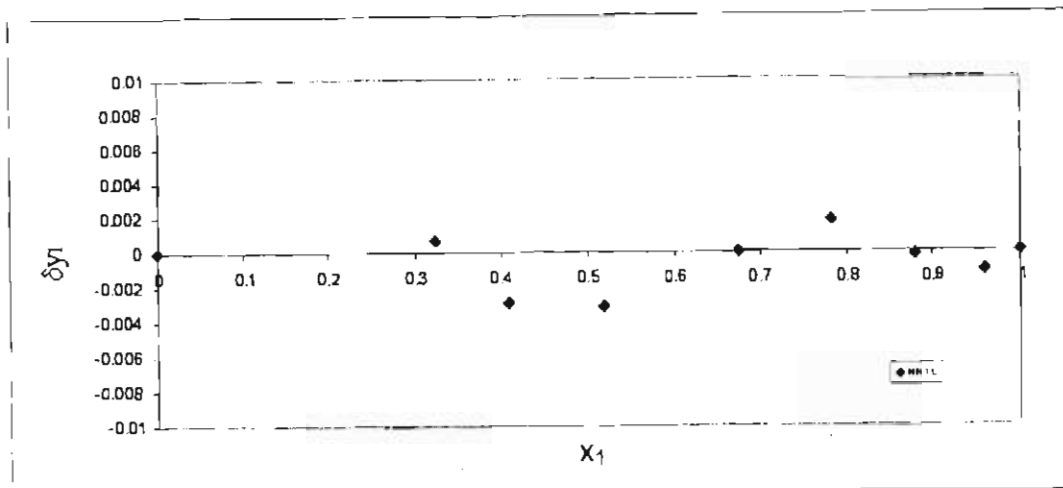


Figure 5.93: Point Test for Water (1) + NMP (2) at 90 °C

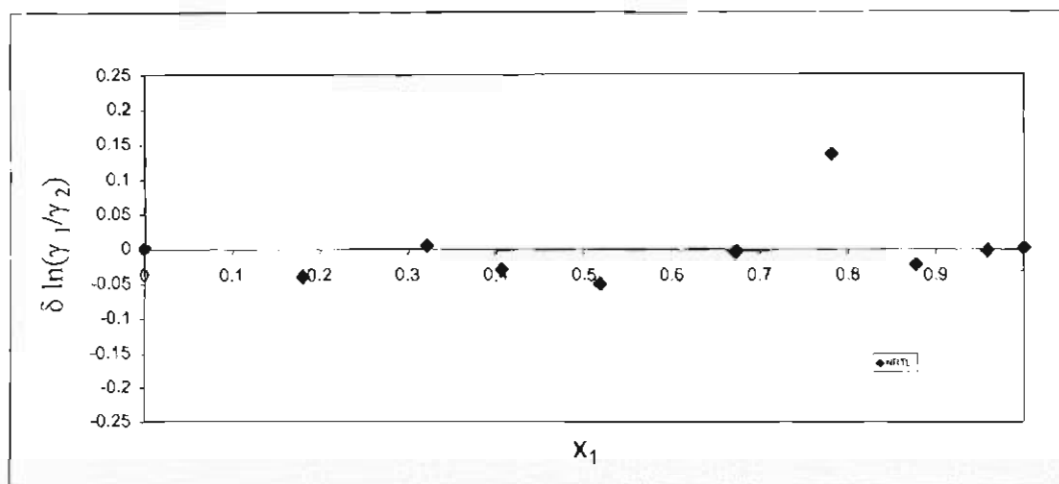


Figure 5.94: Direct Test for Water (1) + NMP (2) at 90 °C

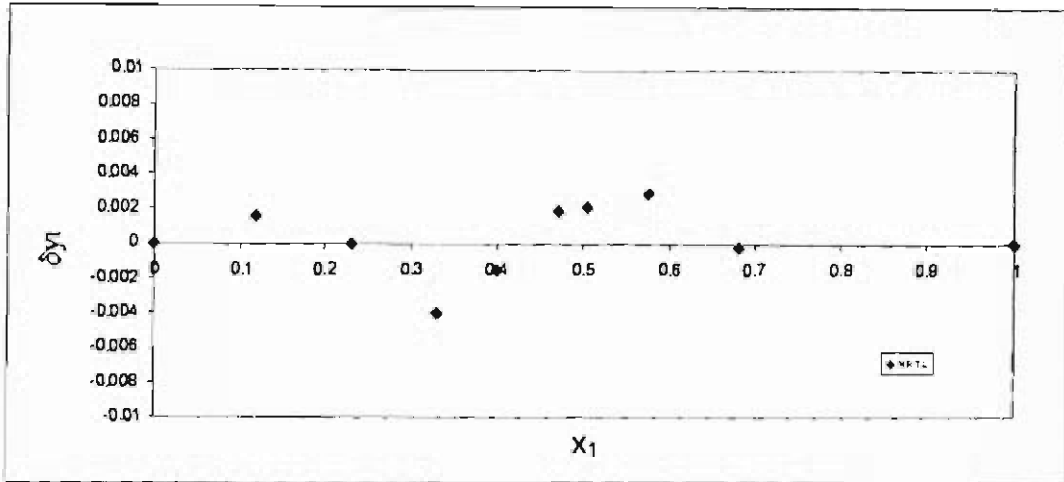


Figure 5.95: Point Test for Water (1) + NMP (2) at 107 °C

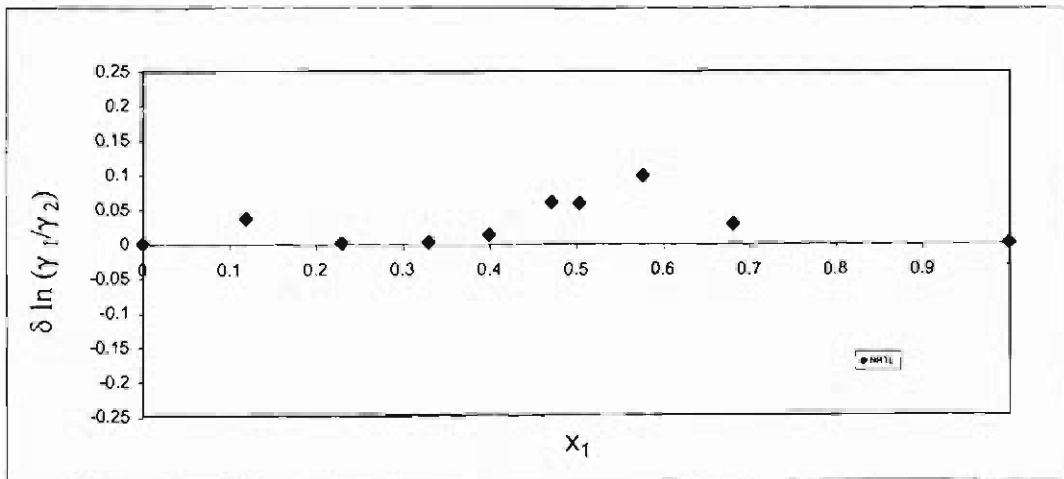


Figure 5.96: Direct Test for Water (1) + NMP (2) at 107 °C

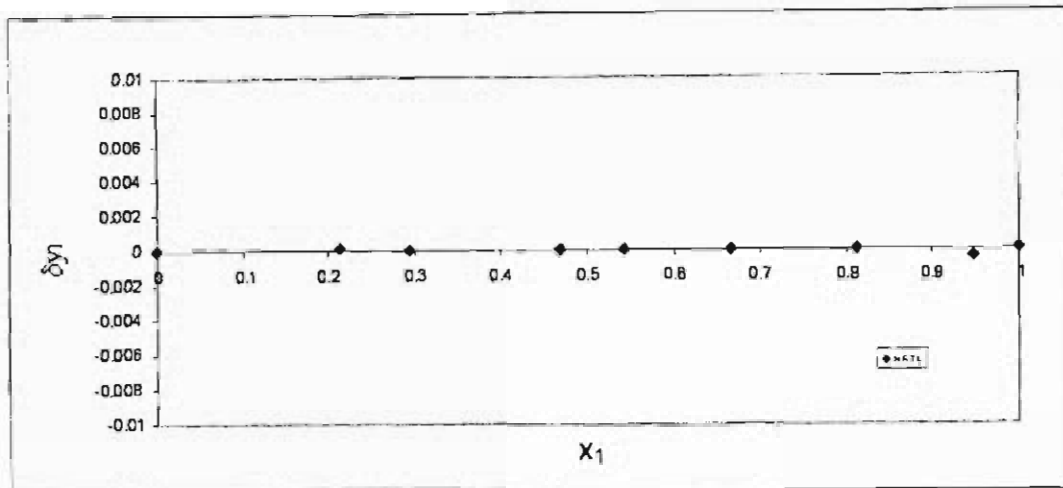


Figure 5.97: Point Test for Hexene (1) + NMP (2) at 40 °C

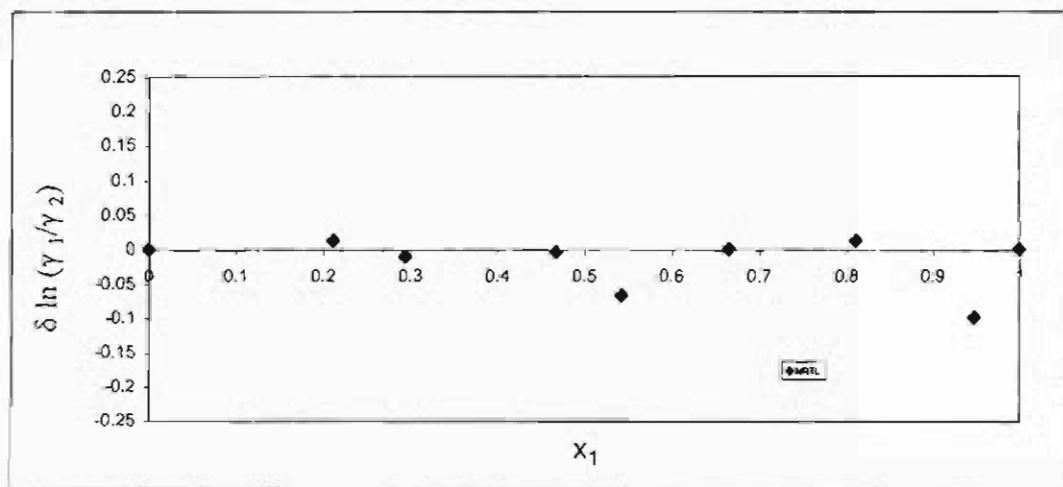


Figure 5.98: Direct Test for Hexene (1) + NMP (2) at 40 °C

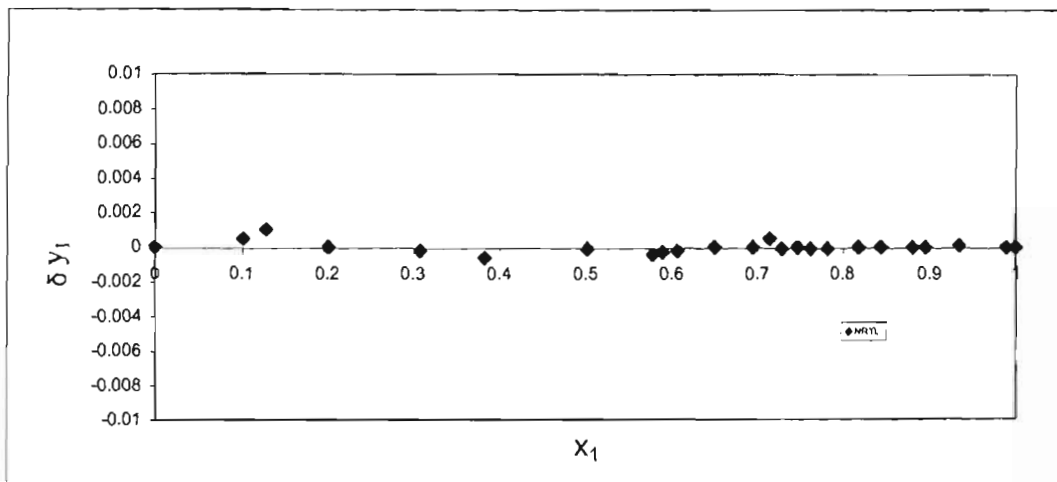


Figure 5.99: Point Test for Hexene (1) + NMP (2) at 62 °C

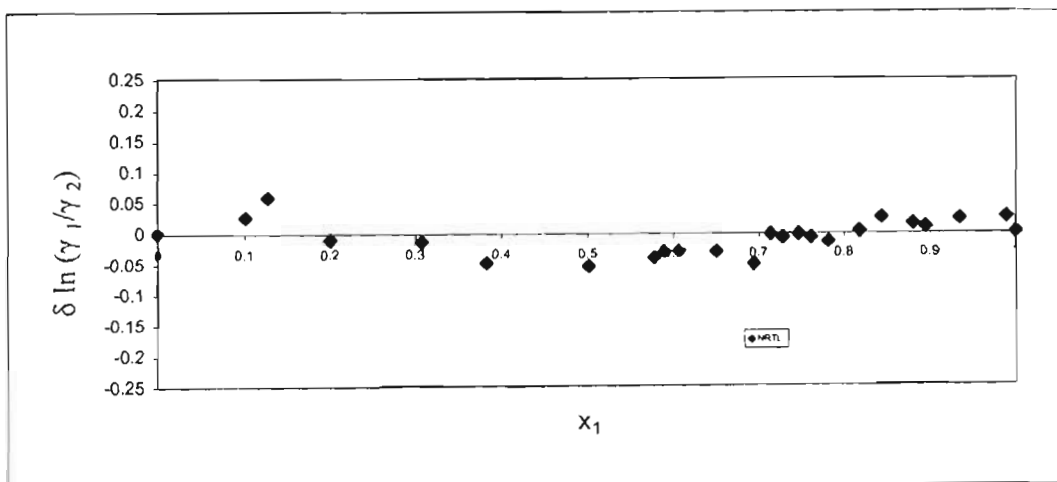


Figure 5.100: Direct Test for Hexene (1) + NMP (2) at 62 °C

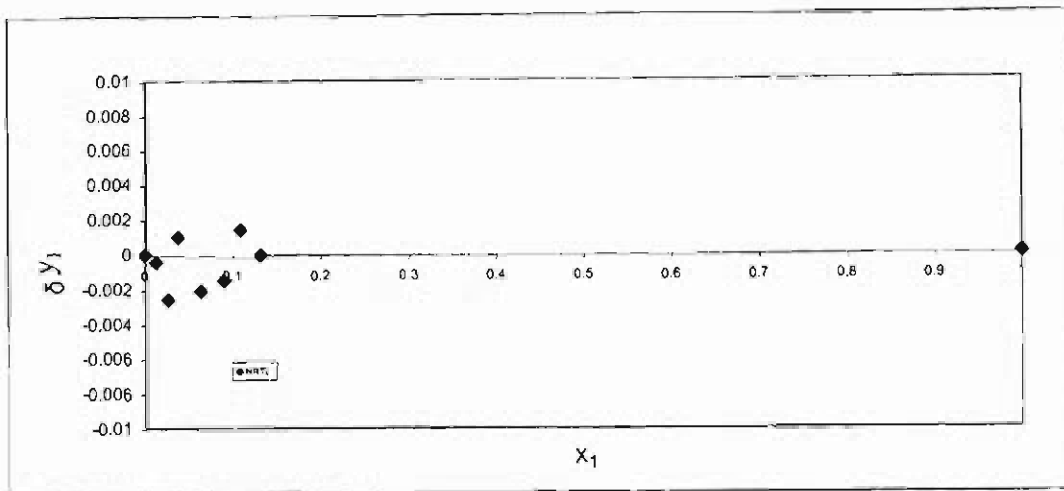


Figure 5. 101: Point Test for Hexene (1) + NMP (2) at 90 °C

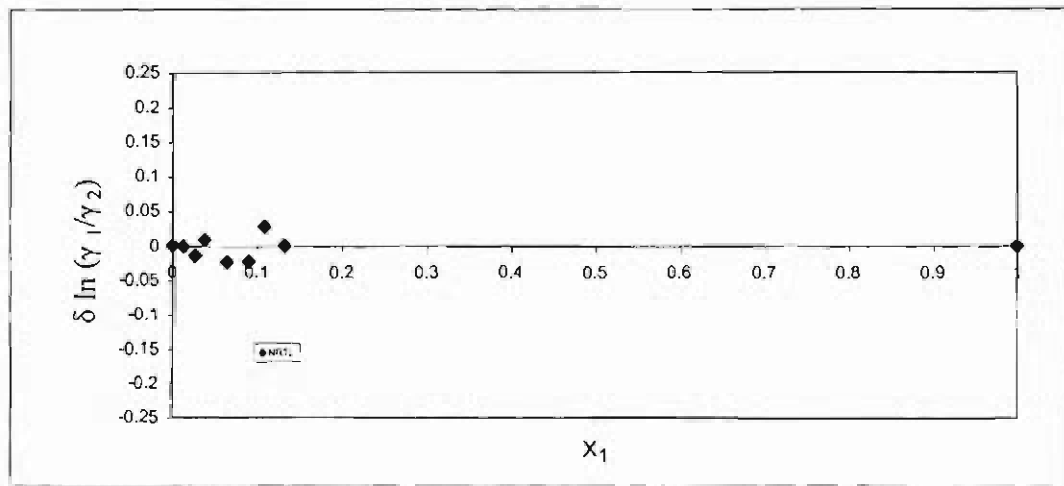


Figure 5. 102: Direct Test for Hexene (1) + NMP (2) at 90 °C

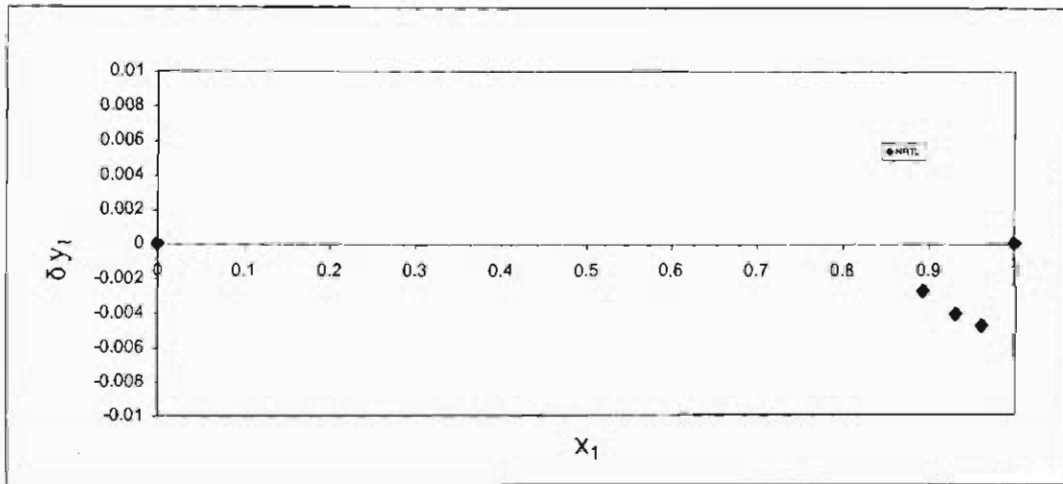


Figure 5.103: Point Test for Hexene (1) + 3MCP (2) at 40 °C

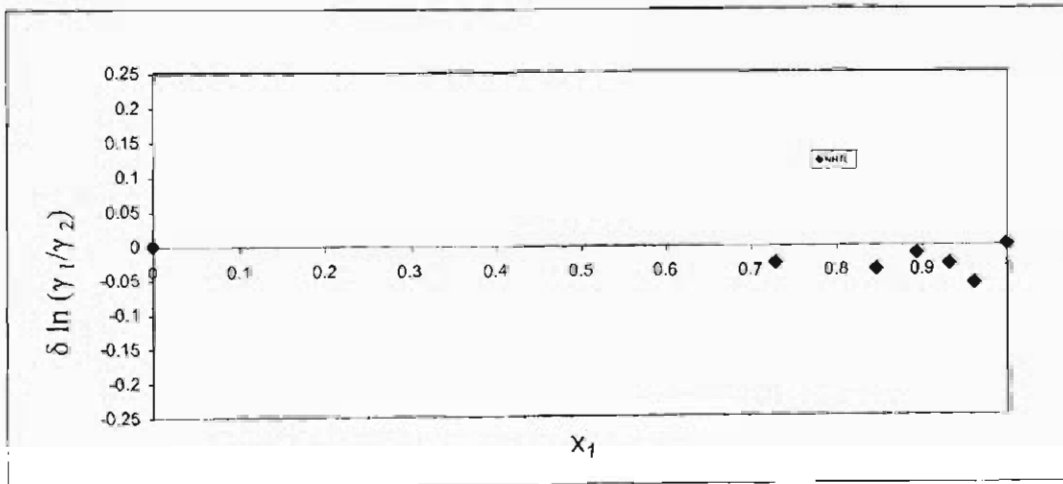


Figure 5.104: Direct Test for Hexene (1) + 3MCP (2) at 40 °C

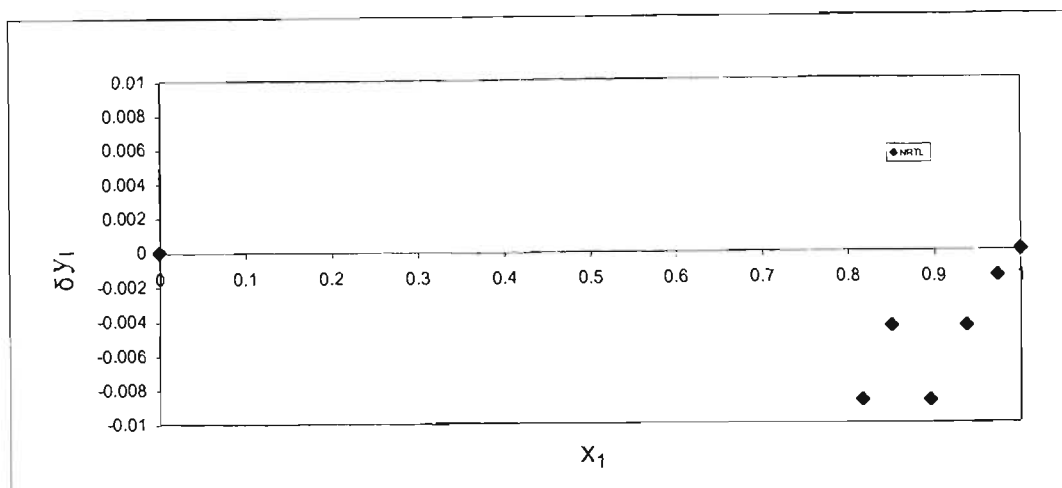


Figure 5. 105: Point Test for Hexene (1) + 3MCP (2) at 50 °C

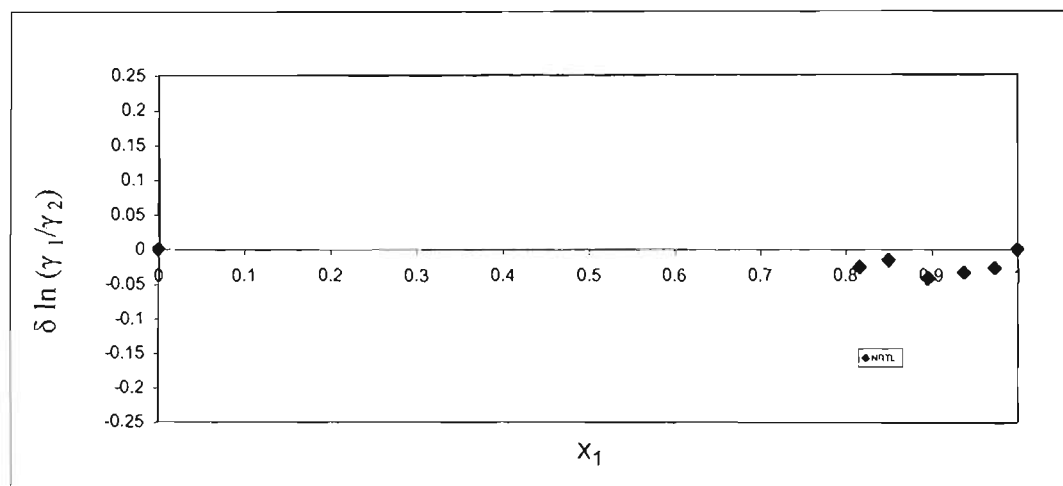


Figure 5. 106: Direct Test for Hexene (1) + 3MCP (2) at 50 °C

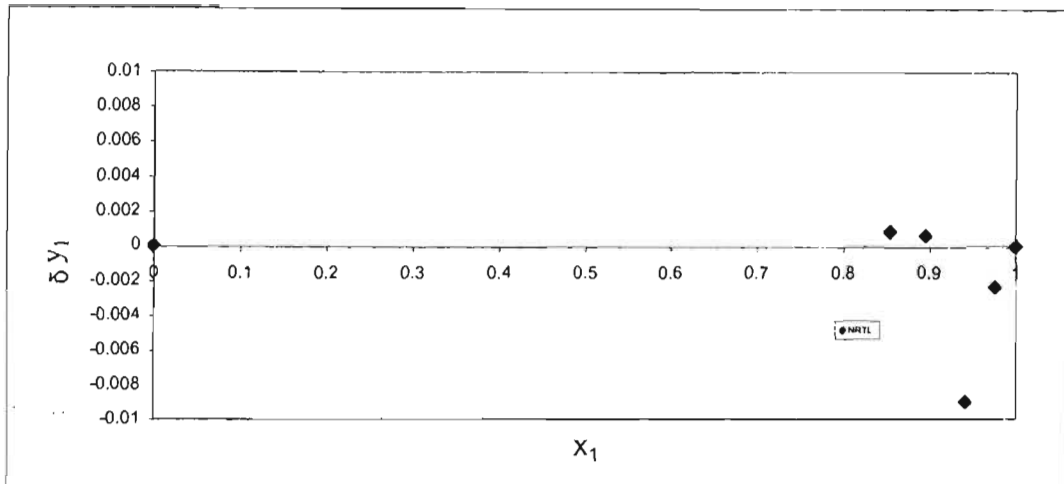


Figure 5.107: Point Test for Hexene (1) + 3MCP (2) at 60 °C

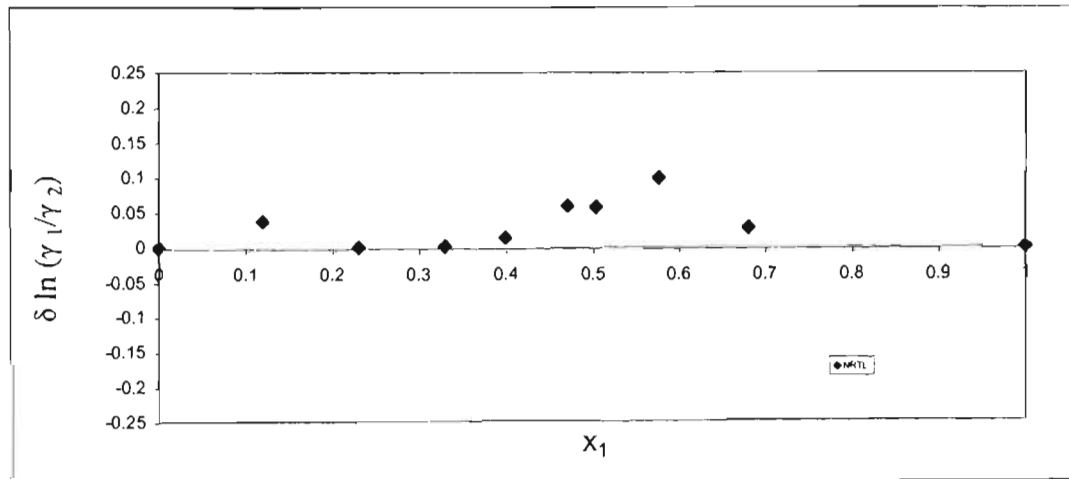


Figure 5.108: Direct Test for Hexene (1) + 3MCP (2) at 60 °C

5.4 Temperature Dependence of Thermodynamic Modelled Parameters

The parameters obtained for the activity coefficient models i.e. Wilson, NRTL, Van Laar and Uniquac in the combined and direct method of modeling can be found in Tables 5.4 to 5.8 for all measured systems. The temperature dependence of these parameters is vitally important for the interpolation and extrapolation of data.

The combined method performed the best in the consistency tests and therefore focus in this section will be on the combined method. The direct method results can be found in Appendix D.

5.4.1 Temperature Dependence of Thermodynamic Modelled Parameters-Combined Method

The following graphs plot the modeled parameters against the measured temperatures for the combined method. The activity coefficient models are represented in the order of Van Laar, Uniquac, Wilson and NRTL. Due to the wide range of values, some figures have been split into two parts e.g. the NRTL model has been split into Figure a showing parameters 'g₁₂-g₁₁' and 'g₁₂-g₂₂', with Figure b showing parameter 'alpha'.

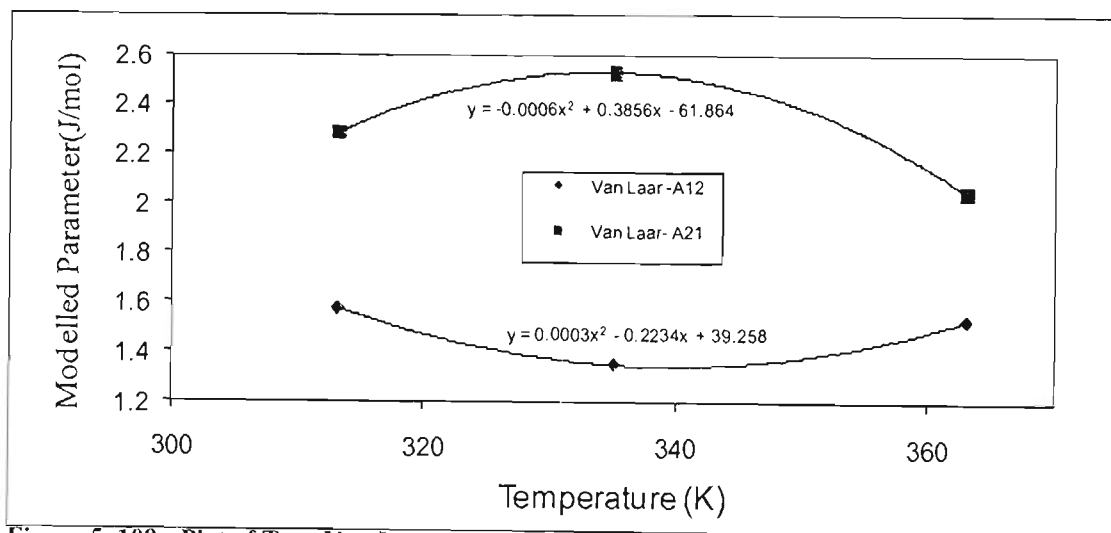


Figure 5.109: Plot of T vs. Van Laar modelled parameters for system 1-hexene (1) + NMP (2)

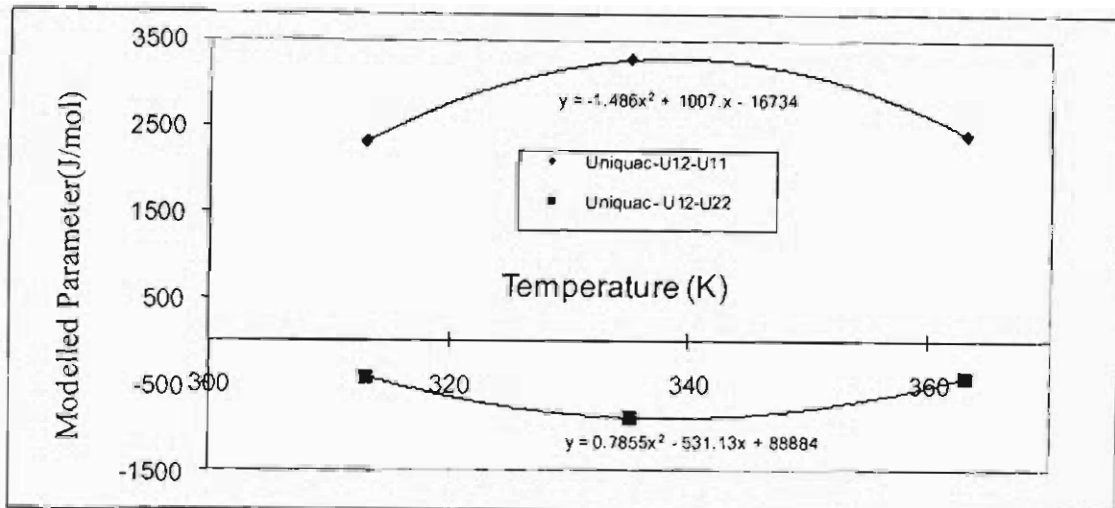


Figure 5.110: Plot of T vs. Uniquac modelled parameters for system 1-hexene (1) + NMP (2)

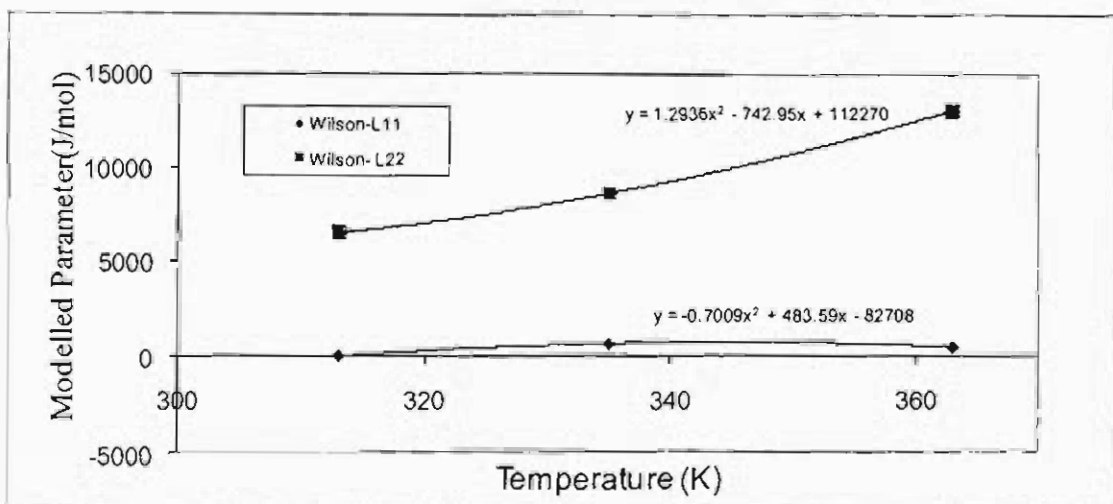


Figure 5.111: Plot of T vs. Wilson modelled parameters for system 1-hexene (1) + NMP (2)

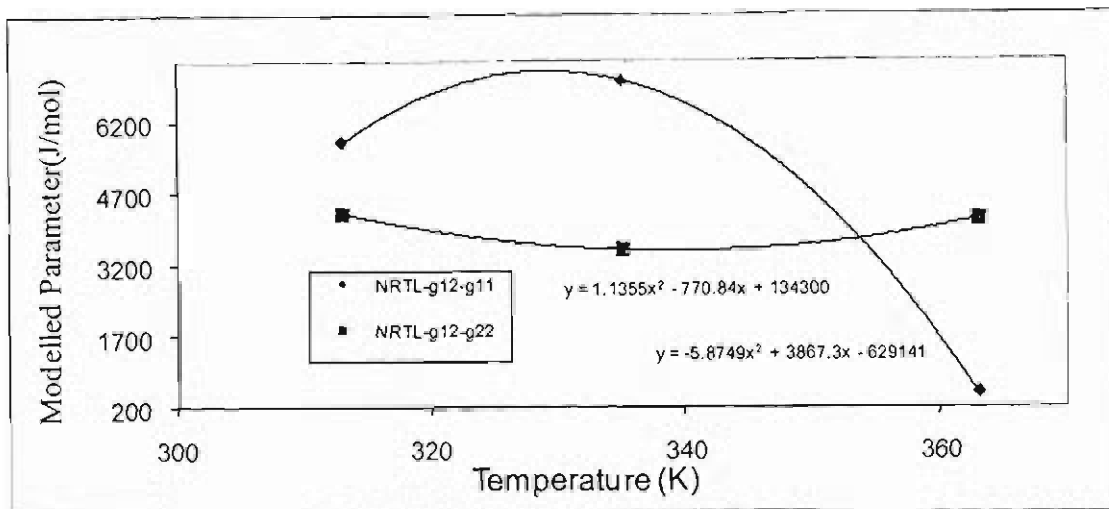


Figure 5.112a: Plot of T vs. NRTL modelled parameters for system 1-hexene (1) + NMP (2)

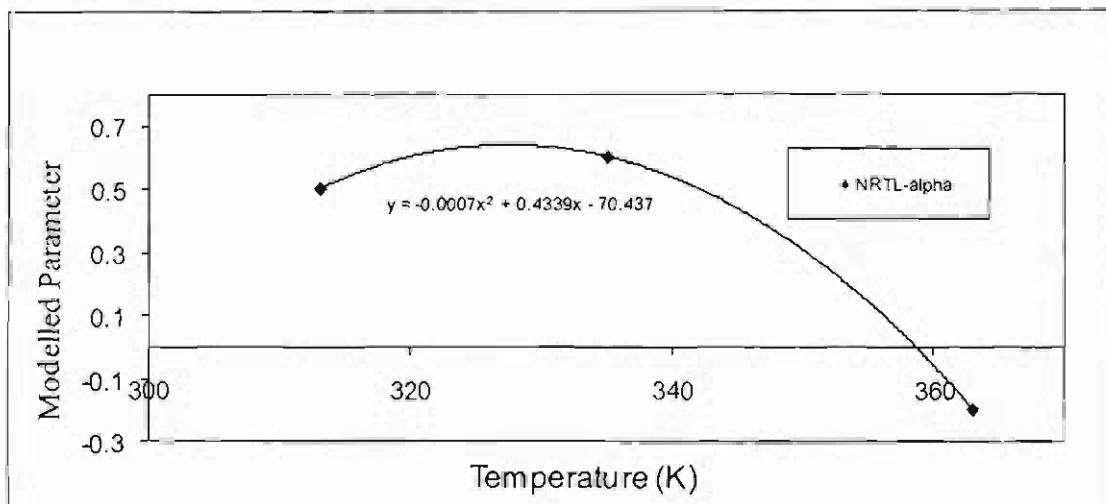


Figure 5.112b: Plot of T vs. NRTL modelled parameters for system 1-hexene (1) + NMP (2)

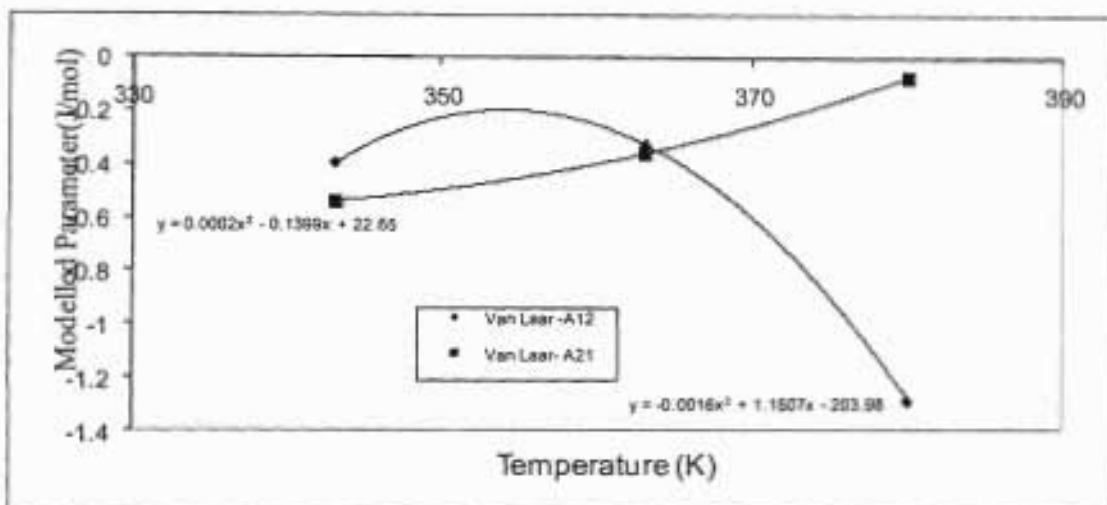


Figure 5.113: Plot of T vs. Van Laar modelled parameters for system water (1) + NMP (2)

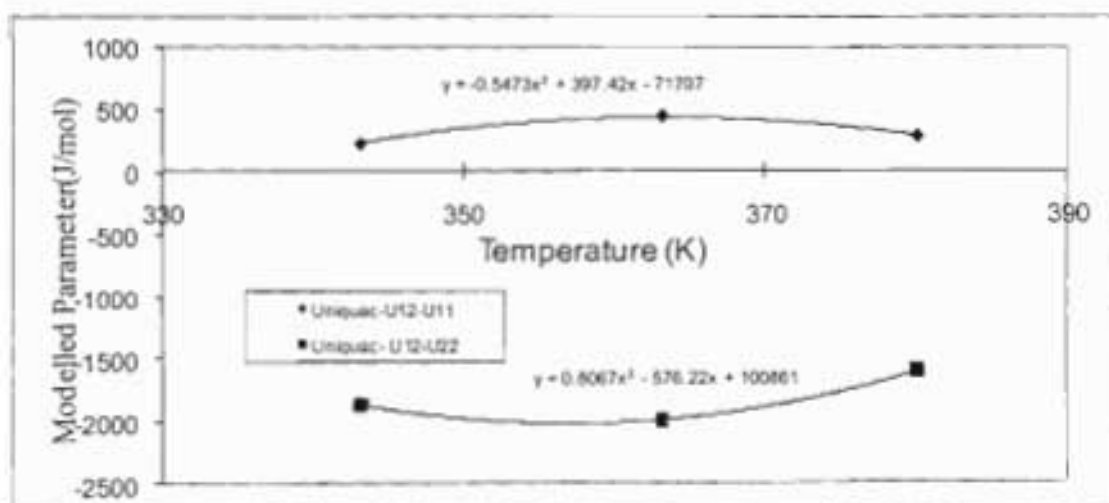


Figure 5.114: Plot of T vs. Uniquac modelled parameters for system water (1) + NMP (2)

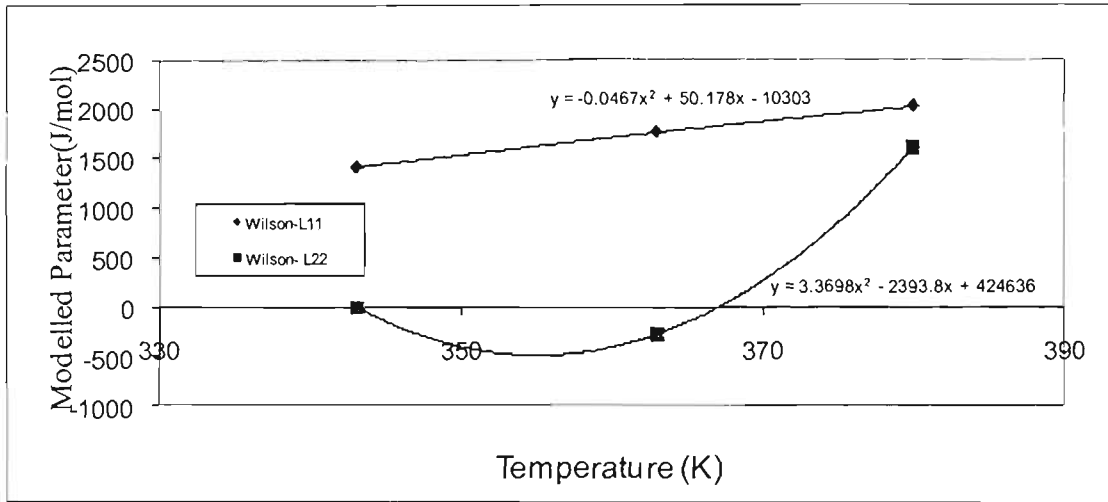


Figure 5.115: Plot of T vs. Wilson modelled parameters for system water (1) + NMP (2)

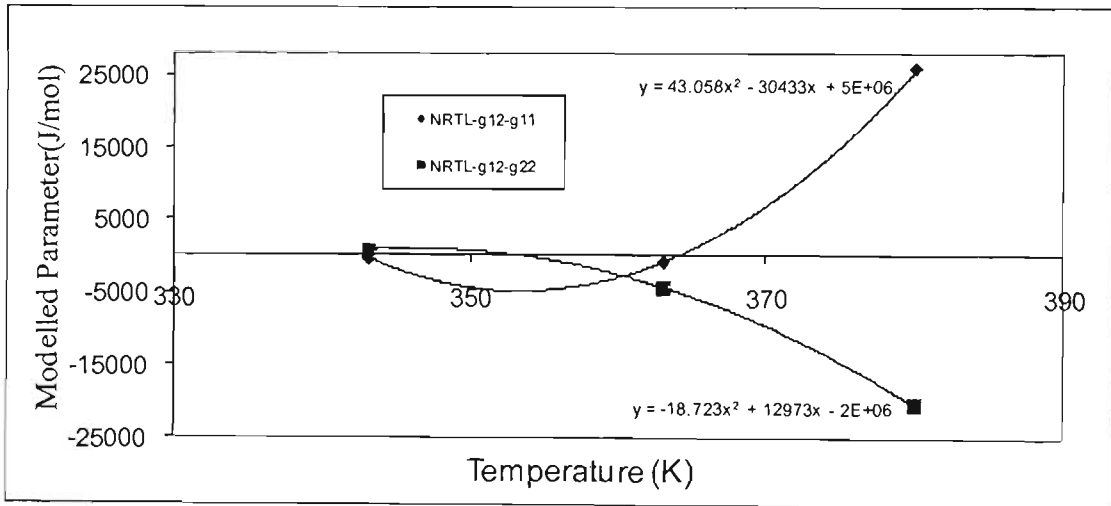


Figure 5.116a: Plot of T vs. NRTL modelled parameters for system water (1) + NMP (2)

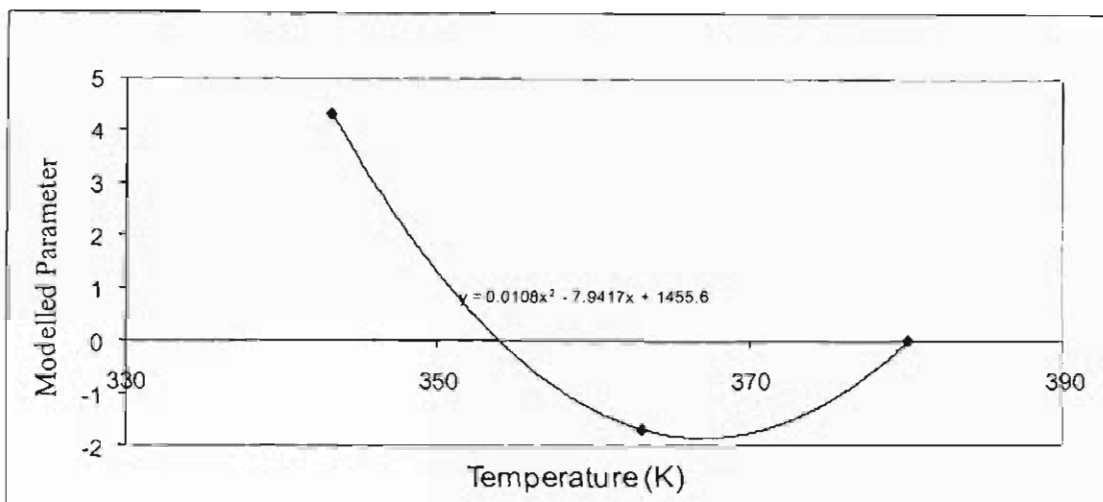


Figure 5.116b: Plot of T vs. NRTL modelled parameters for system water (1) + NMP (2)

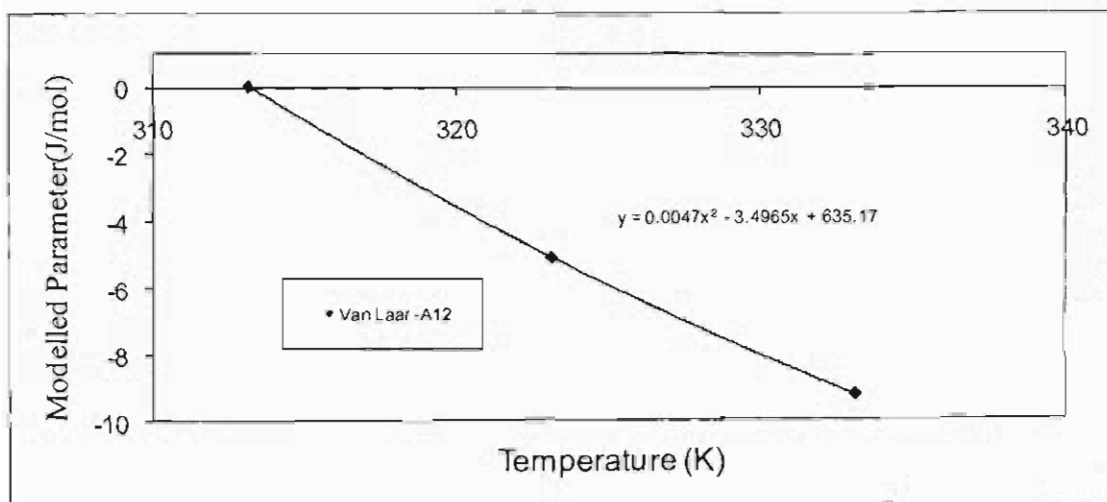


Figure 5.117a: Plot of T vs. Van Laar modelled parameters for system 1-hexene (1) + 3MCP (2)

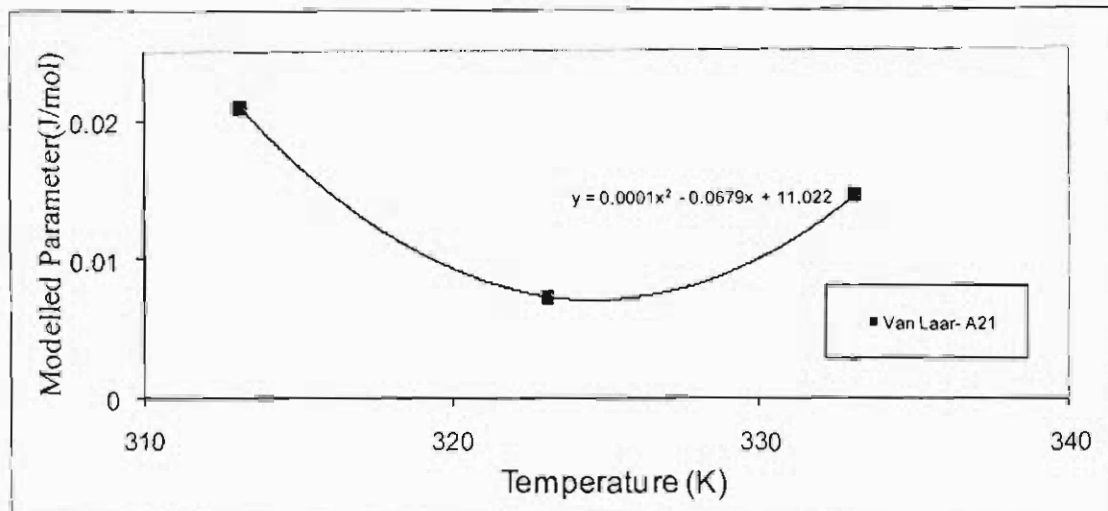


Figure 5. 117b: Plot of T vs. Van Laar modelled parameters for system 1-hexene (1) + 3MCP (2)

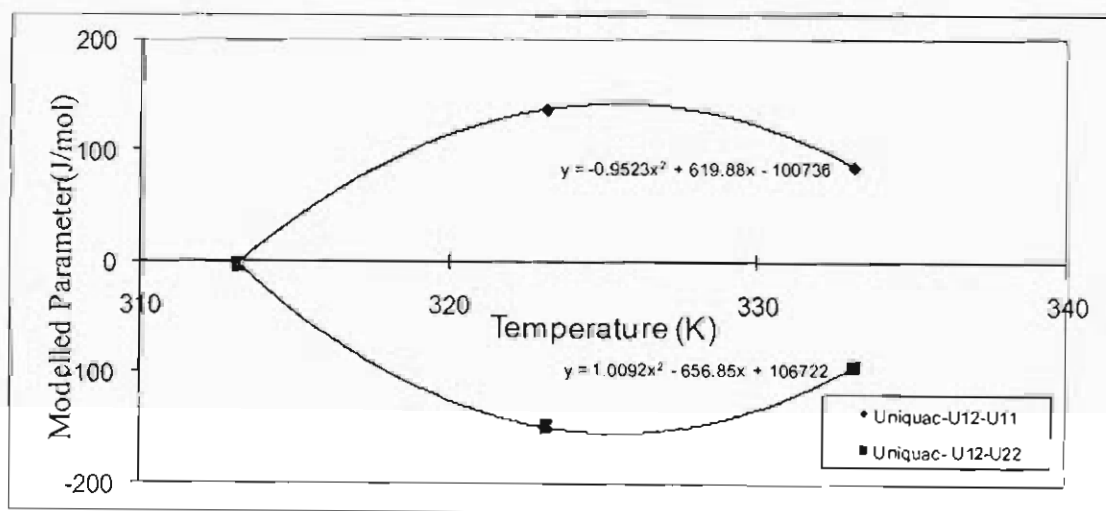


Figure 5. 118: Plot of T vs. Uniquac modelled parameters for system 1-hexene (1) + 3MCP (2)

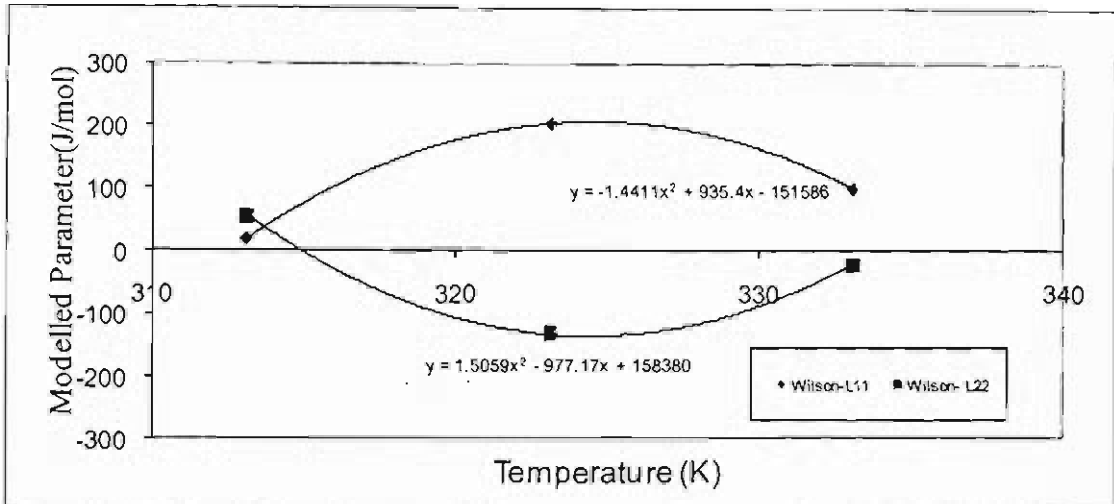


Figure 5.119: Plot of T vs. Wilson modelled parameters for system 1-hexene (1) + 3MCP (2)

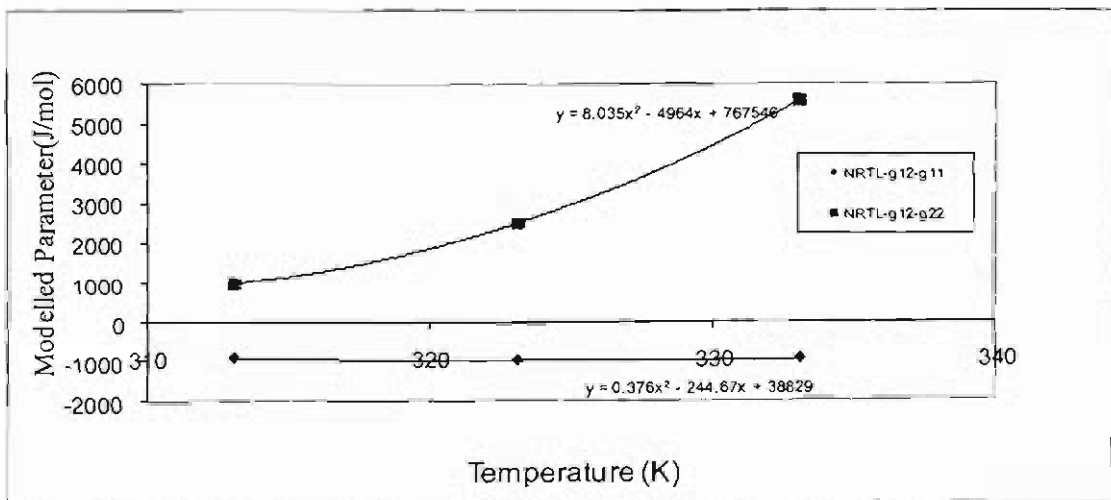


Figure 5.120a: Plot of T vs. NRTL modelled parameters for system 1-hexene (1) + 3MCP (2)

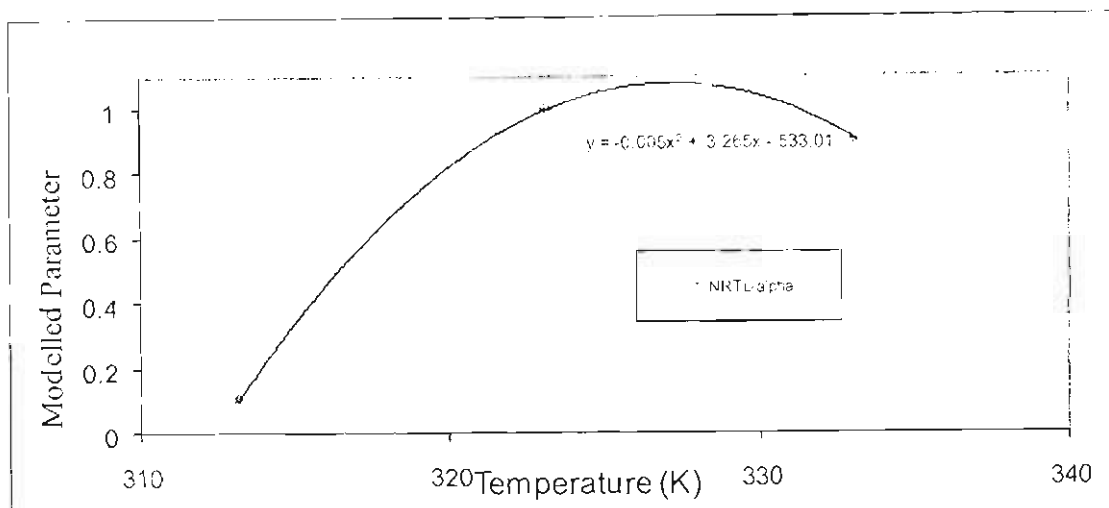


Figure 5.120b: Plot of T vs. NRTL modelled parameters for system 1-hexene (1) + 3MCP (2)

5.5 Verification of Available Experimental Data

A literature search was conducted to locate P-x-y experimental data on the systems measured during this study. The aim of the search was the verification of the experimental data's integrity. The systems found were the experimental data of P-x for water (1) + NMP (2) at 107 °C and P-x for water (1) + NMP (2) at 70 °C. The plots comparing this literature data to the measured data can be viewed in Figure 5.109 and 5.110 respectively. The first plot of P vs. x for water (1) + NMP (2) at 107 °C show excellent correlation while the second plot of P vs. x for water (1) + NMP (2) at 70 °C show a positive bias of the experimental data between x1 of 0.3 and 0.8. This positive bias does not pose a major concern as the experimental work conducted for all systems in this project has successfully passed stringent thermodynamic consistency tests.

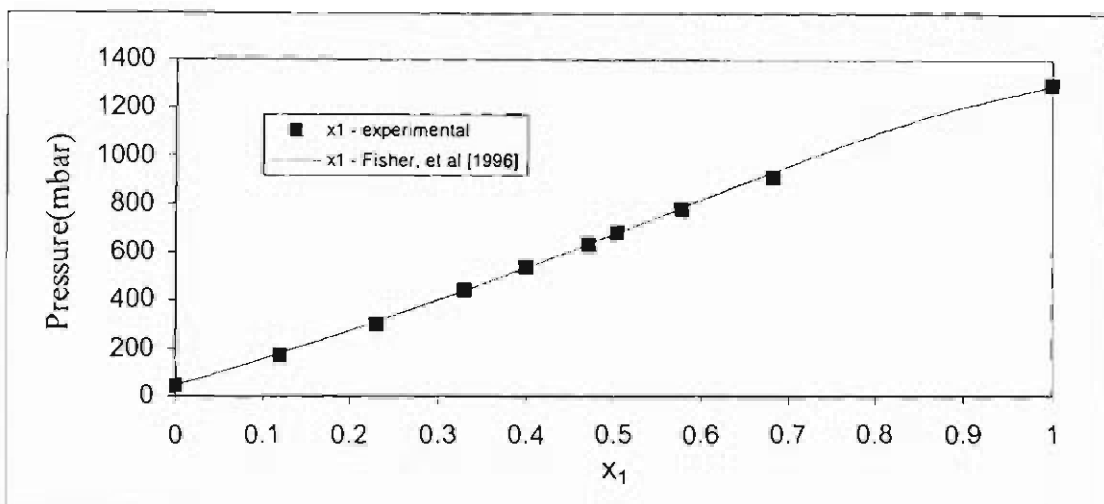


Figure 5.121: Plot of P vs. x for available data of Water (1) + NMP (2) at 107 °C

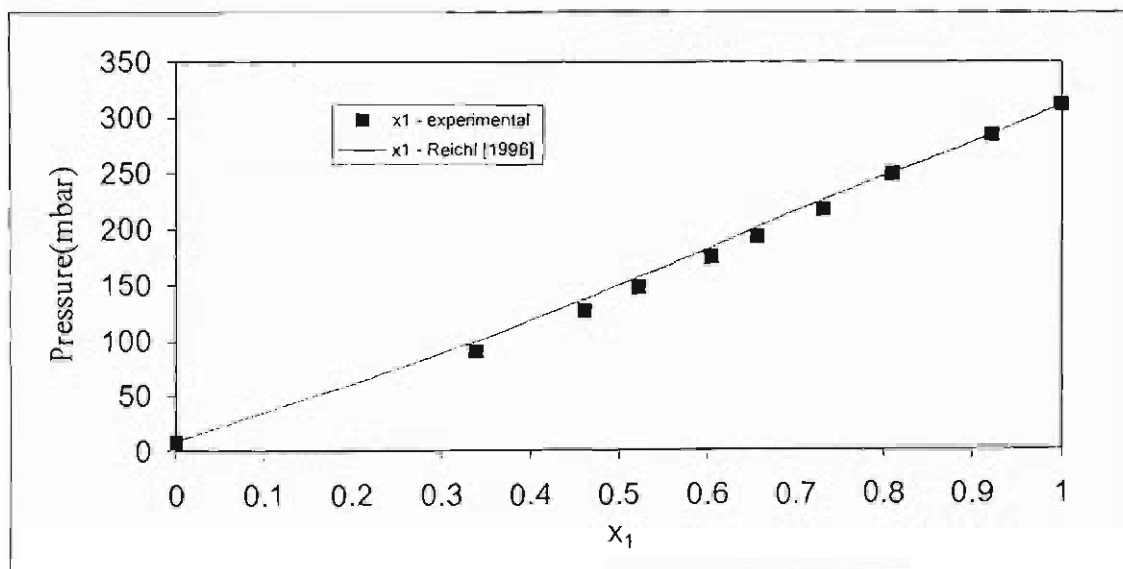


Figure 5.122: Plot of P vs. x for available data of Water (1) + NMP (2) at 70 °C

CONCLUSION

The objective of this thesis was to generate data for the development of a modelling package that would enable the petrochemical company SASOL to successfully run their 1-hexene plant. The following conclusions can be obtained from the project:

- The vapour-liquid equilibrium (VLE) data was successfully measured at low pressure using the dynamic equilibrium still as designed by Raal (Raal & Muhlbauer, 1998).
- The combined method modelled the low pressure VLE data more effectively than the direct method as observed in the thermodynamic consistency tests conducted.
- The activity coefficient model that performed the best was the NRTL model as it is the most flexible from the models used.
- The direct and point consistency tests achieved best results for the combined method of modelling data due to flexibility of the combined method as compared to the direct method of modelling.

REFERENCES

Abbott, MM, (1986), "Low Pressure Phase Equilibria: Measurement of VLE," *Fluid Phase Equilibria*, Vol. 29, Pg. 193-207.

Abrams, DS and Prausnitz, JM. (1975), "Statistical Thermodynamics of Liquid Mixtures: A New Expression for the Excess Gibbs Energy of Partly or Completely Miscible Systems," *American Institute of Chemical Engineers Journal*, Vol. 21, Pg. 116-128.

Altsheler, WB, Unger, ED and Kolachov, P, (1951), "Improved Still for Liquid-Vapor Equilibria Data on Systems: Ethanol-Water and Acetic Acid-Water," *Industrial and Engineering Chemistry*, Vol. 43, Pg. 2559-.

Barker, C. (1953), "Determination of Activity Coefficients from Total Pressure Measurements," *Australian Journal of Chemistry*, Vol. 6, Pg. 207-210.

Black, C, (1958), "Phase Equilibria in Binary and Multicomponent Systems," *Industrial and Engineering Chemistry*, Vol. 50, Pg. 403-412 .

Cottrell, FG, (1919), "On the Determination of Boiling Points of Solutions," *Journal of the American Chemical Society*, Vol. 41, Pg. 721-728.

Fredenslund A, Gmehling, J, Michelson, ML, Rasmussen, P and Prausnitz, JM, (1977a), "Computerized Design of Multicomponent Distillation Columns Using the UNIFAC Group Contribution Method for

Calculation of Activity Coefficients," *Industrial and Engineering Chemistry: Process Design and Development*, Vol. 16, Pg. 450-462.

Fredenslund, A, Gmehling, J and Rasmussen, P, (1977b), "Vapour-Liquid Equilibria Using UNIFAC: A Group Contribution Method," Amsterdam: Elsevier, North Holland.

Fredenslund, A, Jones, JL and Prausnitz, JM, (1975), "Group Contribution Method for the Estimation of Activity Coefficients in Non-Ideal Solutions," *American Institute of Chemical Engineers Journal*, Vol. 21, Pg. 1086.

Gautreaux, MF and Coates, J, (1955), "Activity Coefficients at Infinite Dilution," *American Institute of Chemical Engineers Journal*, Vol. 1, No. 4, Pg. 496-500.

Gibbs, RE and Van Ness, HC, (1972), "Vapor-Liquid Equilibria from Total-Pressure Measurements. A New Apparatus," *Industrial and Engineering Chemistry Fundamentals*, Vol. 11, Pg. 410-413.

Gillespie, DTC, (1946), "Vapor-liquid Equilibrium for Miscible Liquids," *Industrial and Engineering Chemistry, Analytical Edition*, Vol. 18, Pg. 575-577.

Hála, E, Pick, J, Fried, V and Vilím, O, (1957), "Vapour-Liquid Equilibrium," Pergamon Press, New York.

Hayden, JG and O'Connell, JP, (1975), "A Generalized Method for Predicting Second Virial Coefficients," *Industrial and Engineering Chemistry: Process Design and Development*, Vol. 14, Pg. 209-215.

Heertjes, PM, (1960), "Determination of Vapour-Liquid Equilibria of Binary Systems," *Chemical and Process Engineering*, Vol. 41, Pg. 385-386.

Jones, CA, Schoenborn, EM and Colburn, AP, (1943), "Equilibrium Still for Miscible Liquids," *Industrial and Engineering Chemistry*, Vol. 35, Pg. 666-672.

Joseph, MA, (2001), "Computer-Aided Measurement of Vapour-Liquid Equilibria in a Dynamic Still at Sub-Atmospheric Pressures," MSc. Eng. Thesis, University of Natal.

Joseph, MA, Ramjugernath, D and Raal, JD, (2001), "Phase Equilibrium Properties for Binary Systems with Diacetyl from a Computer Controlled Vapour-Liquid Equilibrium Still," *Fluid Phase Equilibria*, Vol. 182, Pg. 157-176.

Joseph, MA, Ramjugernath, D and Raal, JD, (2002), "Computer-Aided Measurement of Vapour-Liquid Equilibria in a Dynamic Still at Sub-Atmospheric Pressures," *Developments in Chemical Engineering and Mineral Processing*, Vol. 10, No. 5-6, Pg. 615-638. . .

Maher, PJ and Smith, BD, (1979), "A New Total Pressure Vapour-Liquid Equilibrium Apparatus. The Ethanol + Aniline System at 313.15K, 350.81K and 386.67K," *Journal of Chemical and Engineering Data*, Vol. 24, Pg. 16-22.

Malanowski, S, (1982). "Experiemental Methods for Vapour-Liquid Equilibria. Part I. Circulation Methods," *Fluid Phase Equilibria*, Vol. 8, Pg. 197-219.

Marquardt, DW. (1963), "An Algorithm for Least-Squares Estimation of Non-Linear Parameters," *Journal of the Society of Industrial and Applied Mathematics*, Vol. 11, Pg. 431441.

Mixon, FO, Gumowski, B and Carpenter, BH,(1965), "Computation of Vapor-Liquid Equilibrium from Solution Vapour Pressure Measurements," *Industrial and Engineering Chemistry Fundamentals*, Vol. 4, Pg. 455-459. .

Nothnagel, KH, Abrams, DS and Prausnitz, JM, (1973), "Generalized Correlation for the Fugacity Coefficients in Mixtures at Moderate Pressures," *Industrial and Engineering Chemistry: Process Design and Development*, Vol. 12, No. 1, Pg. 25-35.

O' Connell, JP and Prausnitz, JM, (1967), "Empirical Correlation of Second Virial Coefficients for Vapor-Liquid Equilibrium Calculations," *Industrial and Engineering Chemistry: Process Design and Development*, Vol. 6, No. 2, Pg. 245-250.

Othmer, DF, (1928), "Composition of Vapors from Boiling Binary Solutions. Improved Equilibrium Still," *Industrial and Engineering Chemistry*, Vol. 20, Pg. 743-766.

Othmer, DF, (1948), "Composition of Vapors from Boiling Binary Solutions. Improved Equilibrium Still," *Analytical Chemistry*, Vol. 20, Pg. 763-766.

Palmer, DA, (1987), "Handbook of Applied Thermodynamics," CRC Press, Inc., Florida

Peng, DY, and Robinson, DB, (1976), "A New Equation of State," *Industrial and Engineering Fundamentals*, Vol. 15, Pg. 59-64.

Perry, RH and Green, DW, (1998), "Perry's Chemical Engineers' Handbook," 7th edition, McGraw-Hill, New York.

Pitzer, KS and Brewer, L, (1961), "Thermodynamics," McGraw-Hill, New York.

Pitzer, KS and Curl, RF Jr., (1957), "The Volumetric and Thermodynamic Properties of Fluids: Empirical Equation for the Second Virial Coefficient," *Journal of the American Chemical Society*, Vol. 79, Pg. 2369-2370.

Prausnitz, JM, Anderson, TF, Grens, EA, Eckert, CA, Hsieh and O'Connell, JP, (1980), "Computer Calculations for Multicomponent Vapor-Liquid and Liquid-Liquid Equilibria," Prentice-Hall, Englewood Cliffs, New Jersey.

Prausnitz, JM, Ruediger, NL and de Azevedo, EG, (1986), "Molecular Thermodynamics of Fluid-Phase Equilibria," 2nd Edition, Prentice-Hall, Englewood Cliffs, New Jersey.

Raal, JD and Mühlbauer, AL, (1998), "Phase Equilibria: Measurement and Computation," Taylor and Francis, Bristol PA.

Raal, JD, (2003), "Experimental Thermodynamics," Vol. 7, Chapter 2a, Elsevier, In Press.

Redlich, O and Kister, AT, (1948), "Algebraic Representation of Thermodynamic Properties and the Classification of Solutions," *Industrial and Engineering Chemistry*, Vol. 40, Pg. 3453-48.

Redlich, O and Kwong, JNS, (1949), "On the Thermodynamics of Solutions. V. An Equation of State. Fugacities of Gaseous Solutions," *Chemical Reviews* Vol. 44, Pg. 233-244.

Reid, RC, Prausnitz, JM and Poling, BE, (1988), "Properties of Gases and Liquids," McGraw-Hill, New York.

Renon, H and Prausnitz, JM, (1968), "Local Composition in the Thermodynamic Excess Functions for Liquid Mixtures," *American Institute of Chemical Engineers Journal*, Vol. 14, Pg. 135-144.

Smith, JM, Van Ness, HC and Abbott, MM, (1996), "Introduction to Chemical Engineering Thermodynamics," McGraw-Hill, New York.

Soave, (1972), "Equilibrium Constants from a Modified Redlich-Kwong Equation of State," *Chemical Engineering Science*, Vol. 27, Pg. 1197-1203.

Tsonopoulos, C, (1974), "An Empirical Correlation of Second Virial Coefficients," *American Institute of Chemical Engineers Journal*, Vol. 20, Pg. 263-272.

Van Ness, HC and Abbott. MM, (1982), "Classical Thermodynamics of Non Electrolyte Solutions: With Applications to Phase Equilibria," McGraw-Hill, New York.

Van Ness, HC, (1995), "Thermodynamics in the Treatment of Vapor /Liquid Equilibrium (VLE) Data," *Pure and Applied Chemistry*, Vol. 67, Pg. 859-872.

Walas, SM, (1985), "Phase Equilibria in Chemical Engineering," Butterworth Publishers, Boston.

Wong, and Sandler, (1992), "A Theoretically Correct Mixing Rule for Cubic Equations of State," *American Institute of Chemical Engineers Journal*, Vol. 38, Pg. 671-680.

THERMODYNAMIC RELATIONSHIPS

Chapter 2 reviewed the theory behind the modelling of the experimental data. To elaborate on the subjects of equilibrium, chemical potential, fugacity and excess properties, Sections A.1-4 discusses these concepts. Section A.5 deals with the formulation of the Wong-Sandler mixing rule used in the direct modelling of data.

A.1 Energy Functions

The internal energy of a closed, homogeneous system can be expressed as:

$$dU = TdS - PdV \quad (\text{A-1})$$

where, U is the internal energy, S is the entropy and V is the volume. For a system to be at equilibrium, at constant entropy and volume, the internal energy must be at a minimum:

$$dU_{S,V} = 0$$

Calculations of internal energy using Equation (A-1) require expressions explicit in entropy and volume to integrate the terms on the right hand side. Rearrangement of

Equation (A-1) enables the use of temperature, pressure or volume explicit expressions in the calculation of energy, if the,

Enthalpy, H, is defined as:

$$H = U + PV \quad (\text{A-3})$$

Helmholtz energy, A, is defined as:

$$A = U - TS \quad (\text{A-4})$$

and, Gibbs energy, G, is defined as:

$$G = H - TS \quad (\text{A-5})$$

Differentiation and substitution into Equation (A-1) yields:

$$dH = TdS + VdP \quad (\text{A-6a})$$

$$dA = -SdT - PdV \quad (\text{A-6b})$$

$$dG = -SdT + VdP \quad (\text{A-6c})$$

A.2 Chemical potential

A closed system consisting of two separate phases may be closed with respect to its surroundings but matter can be exchanged between the two phases across a common interface. At equilibrium, their pressures and temperatures must be equal. Additionally the potential for mass transfer between the two phases must be zero. This condition is derived by the definition of the chemical potential for each species i , μ_i in terms of the internal energy:

$$\mu_i = \left(\frac{\partial nU}{\partial n_i} \right)_{S,V,n_j} \quad (\text{A-7})$$

where, n_i and n_j are mole numbers, with all mole numbers other than n_i kept constant.

For a system containing n moles of material, Equation (A-1) becomes:

$$d(nU) = Td(nS) - Pd(nV) + \sum \mu_i dn_i \quad (\text{A-8})$$

Similarly,

$$d(nG) = -(nS)dT + (nV)dP + \sum \mu_i dn_i \quad (\text{A-9})$$

At constant temperature, pressure and n_i ,

$$\mu_i = \left(\frac{\partial nG}{\partial n_i} \right)_{T,P,n_j} \quad (\text{A-10})$$

The partial differentiation in Equation (A-10) is the partial molar Gibbs energy.

A.3 Fugacity

With respect to the phase equilibrium conditions, the temperature and pressure can be measured whereas the chemical potential cannot. This was rectified by the introduction of a quantity known as the fugacity f (units of pressure) by G. N. Lewis. For an ideal gas and pure material at constant temperature and pressure, Equation (A-3c) reduces to:

$$dG = RT d \ln f \quad (\text{A-11})$$

For a component i in a solution (gaseous or liquid), the fugacity is defined by \hat{f}_i . Therefore,

$$d\bar{G}_i = RT d \ln \hat{f}_i \quad (\text{A-12})$$

where,

$$\bar{G} = \left(\frac{\partial nG}{\partial n_i} \right)_{T,P,n_j} = \mu_i \quad (\text{A-13})$$

Therefore,

Therefore,

$$d\mu_i = d\bar{G}_i = RT d \ln \hat{f}_i \quad (\text{A-14})$$

Analogous to the equilibrium condition for a liquid and vapour phase,

$$\mu_i^L = \mu_i^V \quad (\text{A-15})$$

we obtain,

$$\hat{f}_i^L = \hat{f}_i^V \quad (\text{A-16})$$

The fugacity then replaces the chemical potential as the criterion for equilibrium and it is through the fugacity that the conditions of equilibrium will be expressed in terms of the experimental quantities of pressure, temperature, volume and phase composition.

A.4 Excess Properties

Using the concept of excess properties where for property M , at the same temperature and pressure,

Excess value = Actual value - Ideal solution value,

i.e.
$$M^E = M - M^{id},$$

we obtain for the Gibbs energy, G:

$$\bar{G}^E = \bar{G}_i - \bar{G}_i^{id} = \mu_i - \mu_i^{id}$$

$$\bar{G}^E = G_i + RT \ln x_i - G_i - RT \ln \gamma_i x_i$$

$$\bar{G}^E = RT \ln \gamma_i \quad (\text{A-17})$$

and

$$\ln \gamma_i = \frac{\bar{G}_i^E}{RT}$$

For pure material at constant temperature, fugacity is related to pressure via:

$$dG_i = V_i dP - S_i dT = RT d \ln f_i \quad (\text{A-18})$$

At constant temperature, Equation (A-18) reduces to:

$$d \ln f_i = \frac{V_i^L}{RT} dP \quad (\text{A-19})$$

Integration from P_i^{sat} to P gives:

$$f_i = f_i^{sat} \exp \left[\frac{1}{RT} \int_{P_i^{sat}}^P V_i^L dP \right] \quad (\text{A-20})$$

where, V_i^L = liquid molar volume and P_i^{sat} = saturation pressure. The exponential term is the Poynting correction. This correction is close to unity unless the pressure of the system is substantially higher than P_i^{sat} . Assuming V_i^L independent of pressure (i.e. an incompressible liquid), Equation (A-17) reduces to:

$$f_i = \phi_i^{sat} P_i^{sat} \exp \left[\frac{V_i^L (P - P_i^{sat})}{RT} \right] \quad (\text{A-21})$$

where, f_i^{sat} has been eliminated by $f_i^{sat} = \phi_i^{sat} P_i^{sat}$

A.5 Formulation of the Wong-Sandler Mixing Rule

The following analysis of the Wong-Sandler mixing rule is accomplished via the Peng-Robinson EOS with the NRTL activity coefficient correlation as undertaken in Wong and Sandler, 1991.

The Peng-Robinson EOS is:

$$P = \frac{RT}{\bar{V} - B} - \frac{a(T)}{\bar{V}^2 + 2b\bar{V} - b^2} \quad (\text{A-22})$$

The Helmholtz free energy departure function for the Peng-Robinson EOS at a given temperature, pressure and composition is:

$$\frac{(\bar{A} - \bar{A}^{IGM})}{RT} = -\ln \left[\frac{P(\bar{V} - b)}{RT} \right] + \frac{a}{2\sqrt{2}RT} \ln \left[\frac{\bar{V} + (1 - \sqrt{2})b}{\bar{V} + (1 + \sqrt{2})b} \right] \quad (\text{A-23})$$

Taking the limit as pressure approaches infinity:

$$\lim_{P \rightarrow \infty} \frac{(\bar{A} - \bar{A}^{IGM})}{RT} = \frac{a}{bRT} C \quad (\text{A-24})$$

with the constant C being:

$$C = \frac{1}{\sqrt{2}} \ln(\sqrt{2} - 1) \quad (\text{A-25})$$

The excess Helmholtz free energy at infinite pressure then:

$$\frac{\bar{A}_\infty^E}{CRT} = \frac{a_m}{b_m RT} - \sum_i x_i \frac{a_i}{b_i RT} \quad (\text{A-26})$$

The expressions for the EOS parameters a_m and b_m :

$$\frac{a_m}{RT} = Q \frac{D}{1-D} \quad (\text{A-27})$$

and

$$b_m = \frac{Q}{(1-D)} \quad (\text{A-28})$$

with Q and D defined as:

$$Q = \sum_i \sum_j x_i x_j \left(b - \frac{a}{RT} \right)_{ij} \quad (\text{A-29})$$

and

$$D = \sum_i x_i \frac{a_i}{b_i RT} + \frac{\bar{A}_\infty^E}{CRT} \quad (\text{A-30})$$

The fugacity coefficient is computed from:

$$\ln \phi_i = \int_{\bar{V}}^{\infty} \left[\frac{1}{RT} \left(\frac{\partial P}{\partial n_i} \right)_{T, V, n_j} - \frac{1}{\bar{V}} \right] d\bar{V} - \ln \left(\frac{P\bar{V}}{RT} \right) \quad (\text{A-31})$$

For the Peng-Robinson EOS and an arbitrary set of mixing rules for a_m and b_m , one obtains:

$$\begin{aligned} \ln \phi_i = & -\ln \left[\frac{P(\bar{V} - b_m)}{RT} \right] + \frac{1}{b_m} \left(\frac{\partial n b_m}{\partial n_i} \right) \left(\frac{P\bar{V}}{RT} - 1 \right) + \\ & \frac{1}{2\sqrt{2}} \left(\frac{a_m}{b_m RT} \right) \left[\frac{1}{a_m} \left(\frac{1}{n} \frac{\partial n^2 a_m}{\partial n_i} \right) - \frac{1}{b_m} \left(\frac{\partial n b_m}{\partial n_i} \right) \right] \ln \left[\frac{\bar{V} + b_m(1 - \sqrt{2})}{\bar{V} + b_m(1 + \sqrt{2})} \right] \end{aligned} \quad (\text{A-32})$$

The partial derivatives of a_m and b_m are:

$$\frac{1}{RT} \left(\frac{1}{n} \frac{\partial n^2 a_m}{\partial n_i} \right) = D \frac{\partial n b_m}{\partial n_i} + b_m \frac{\partial n D}{\partial n_i} \quad (\text{A-33})$$

and

$$\frac{\partial n b_m}{\partial n_i} = \frac{1}{(1-D)} \left(\frac{1}{n} \frac{\partial n^2 Q}{\partial n_i} \right) - \frac{Q}{(1-D)^2} \left(1 - \frac{\partial n D}{\partial n_i} \right) \quad (\text{A-34})$$

with the partial derivative of Q and D given by:

$$\left(\frac{1}{n} \frac{\partial n^2 Q}{\partial n_i} \right) = 2 \sum_j x_j \left(b - \frac{a}{RT} \right)_{ij} \quad (\text{A-35})$$

and

$$\frac{\partial n D}{\partial n_i} = \frac{a_i}{b_i RT} + \frac{\ln \gamma_{\infty i}}{C} \quad (\text{A-36})$$

with

$$\ln \gamma_{\infty i} = \frac{1}{RT} \frac{\partial n \bar{A}_{\infty}^{-E}}{\partial n_i} \quad (\text{A-37})$$

Using the NRTL model for the Helmholtz energy at infinite pressure:

$$\frac{\bar{A}_{\infty}^{-E}}{RT} = \sum_i x_i \left(\frac{\sum_j x_j \tau_{ji} g_{ji}}{\sum_k x_k g_{ki}} \right) \quad (\text{A-38})$$

with

$$g_{ij} = \exp(-\alpha_{ij} \tau_{ij}) \quad (\text{A-39})$$

and

$$(\alpha_{ij} = \alpha_{ji}) \quad (\text{A-40})$$

Applying Equation (A-38) to the NRTL model one obtains:

$$\ln \gamma_{\infty i} = \frac{\sum_j x_j \tau_{ji} g_{ji}}{\sum_k x_k g_{ki}} + \sum_j \frac{x_j g_{ij}}{\sum_k x_k g_{kj}} \left(\tau_{ij} - \frac{\sum_l x_l \tau_{lj} g_{lj}}{\sum_k x_k g_{kj}} \right) \quad (\text{A-41})$$

THERMODYNAMIC CONSISTENCY TESTS

Chapter 5 covered the thermodynamic consistency tests of the point and direct test for the combined method. Appendix B deals with the point and direct consistency tests as well, but with respect to the direct method results.

B.1: Thermodynamic Consistency Tests for Wong-Sandler

SRK

For the direct method using the Wong-Sandler-SRK combination, the graphical results of the point and the direct consistency tests for all systems measured can be found in Figures B.1 to B.18 alternatively. The direct consistency test scale can be found in Table B.1. The vapour composition residuals can be found in Chapter 5, Table 5.5.

Table B.1: Direct Test Scale for the Direct Method: Wong-Sandler-SRK

Systems	water (1) + NMP (2)			1-hexene(1) + NMP(2)			1-hexene(1) + 3MCP (2)		
Temperature									
$T^{\circ}C$	70	90	107	40	62	90	40	50	60
Index	3	4	4	3	3	3	2	3	2

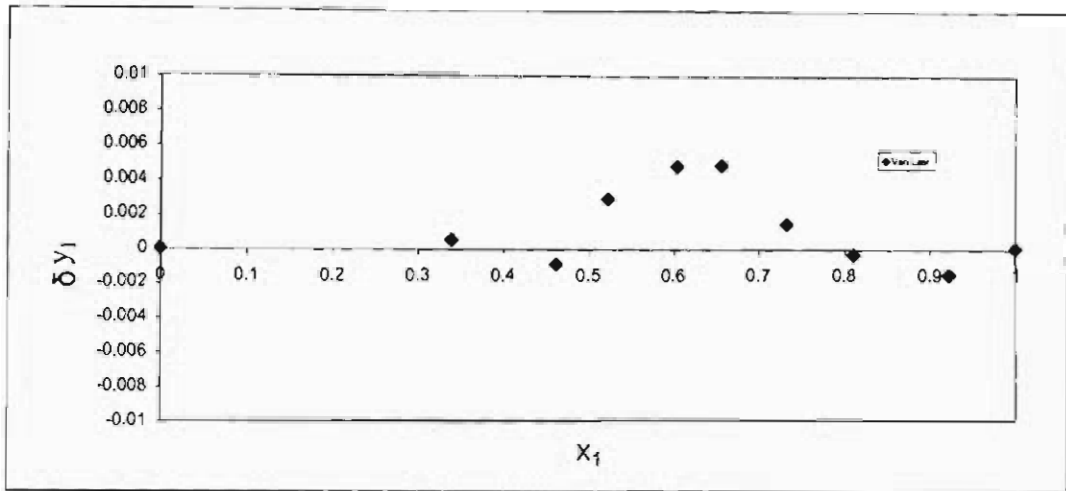


Figure B.1: Point Test for Water (1) and NMP (2) at 70 °C

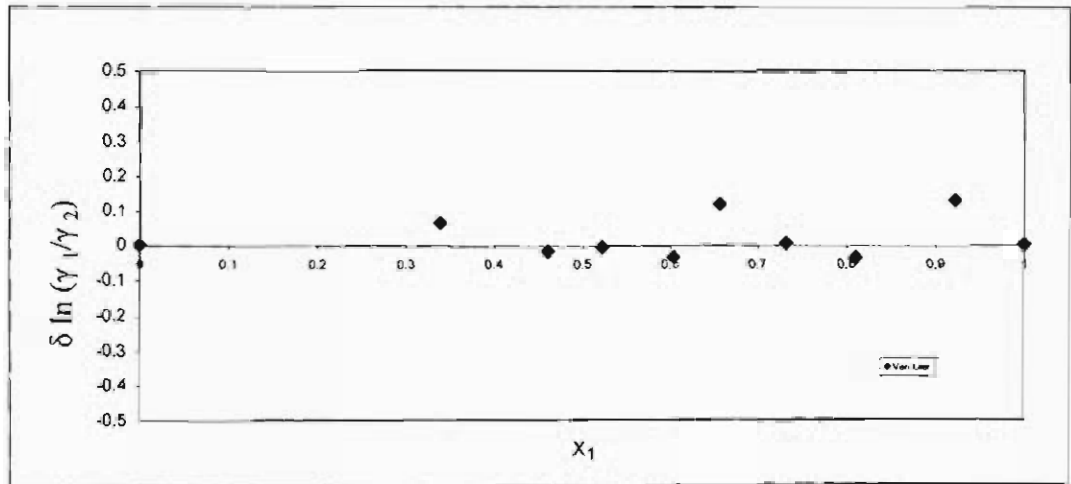


Figure B.2: Direct Test for Water (1) and NMP (2) at 70 °C

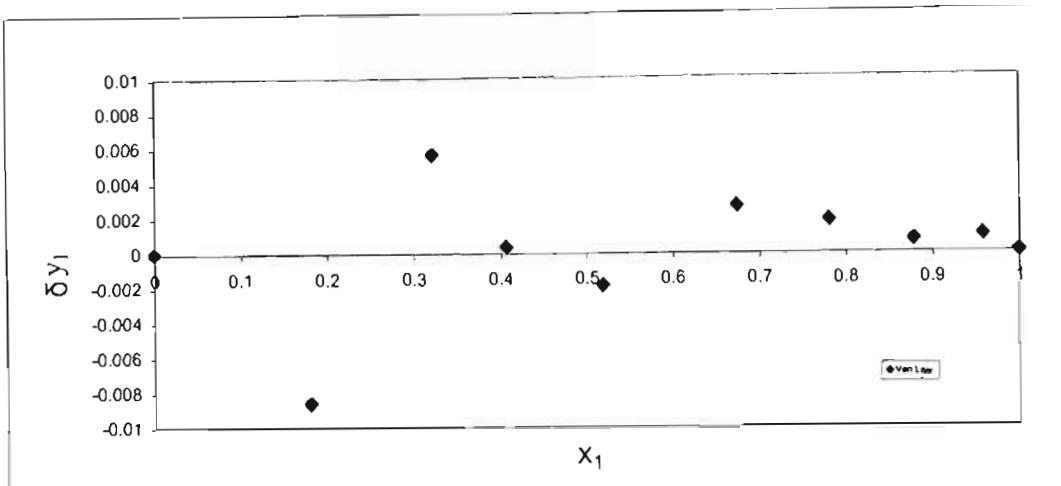


Figure B.3: Point Test for Water (1) and NMP (2) at 90 °C

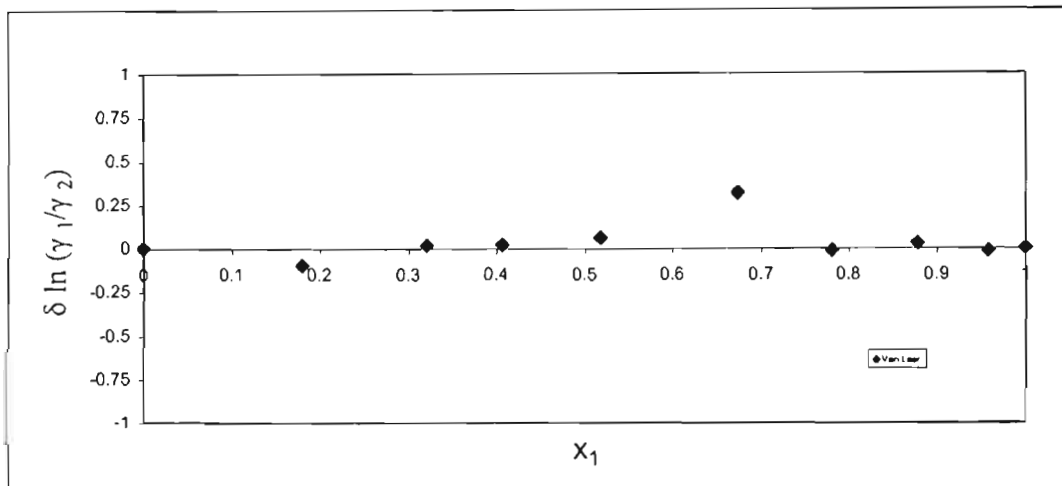


Figure B.4: Direct Test for Water (1) and NMP (2) at 90 °C

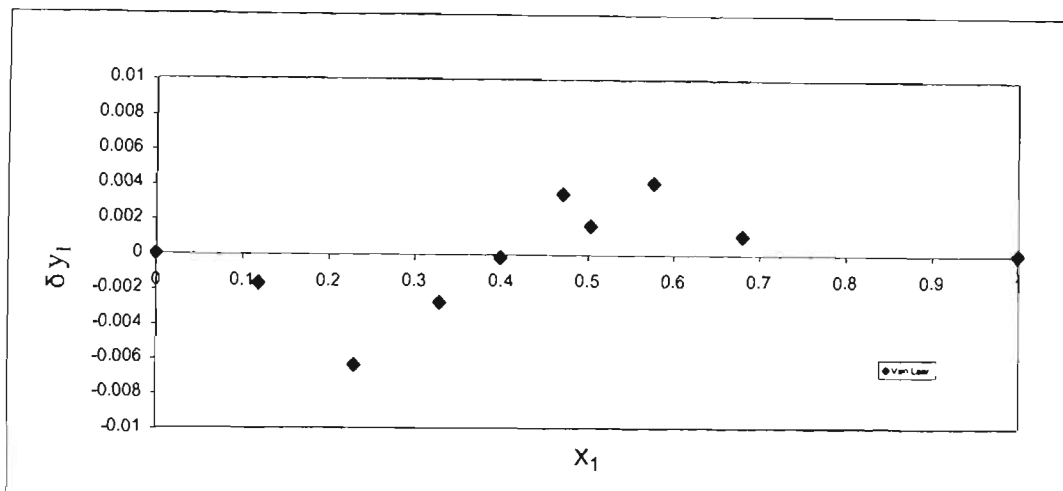


Figure B.5: Point Test for Water (1) and NMP (2) at 107 °C

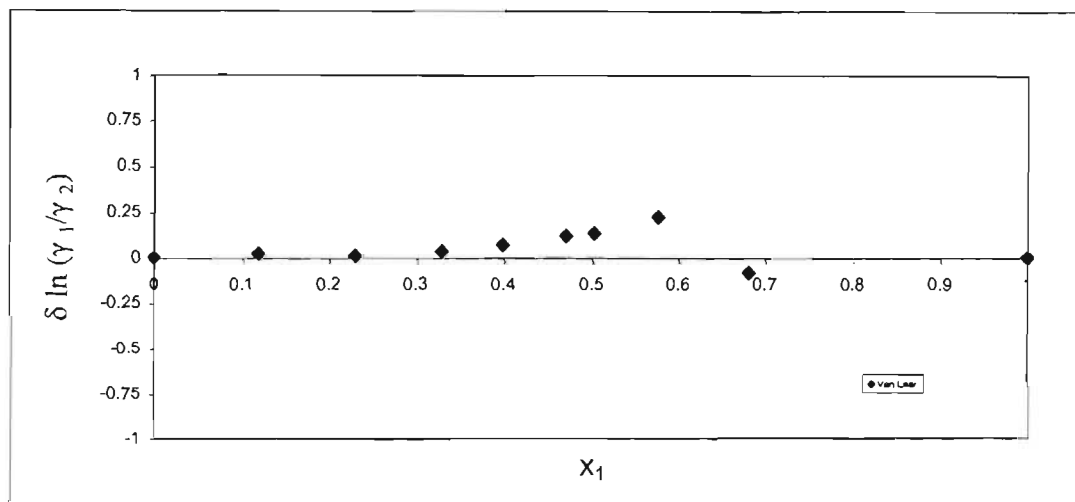


Figure B.6: Point Test for Water (1) and NMP (2) at 107 °C

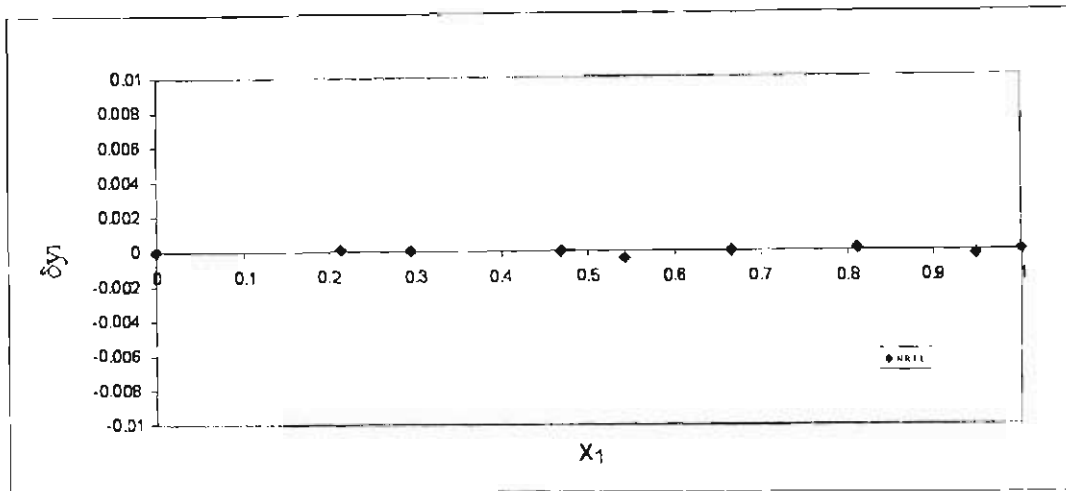


Figure B.7: Point Test for Hexene (1) and NMP (2) at 40 °C

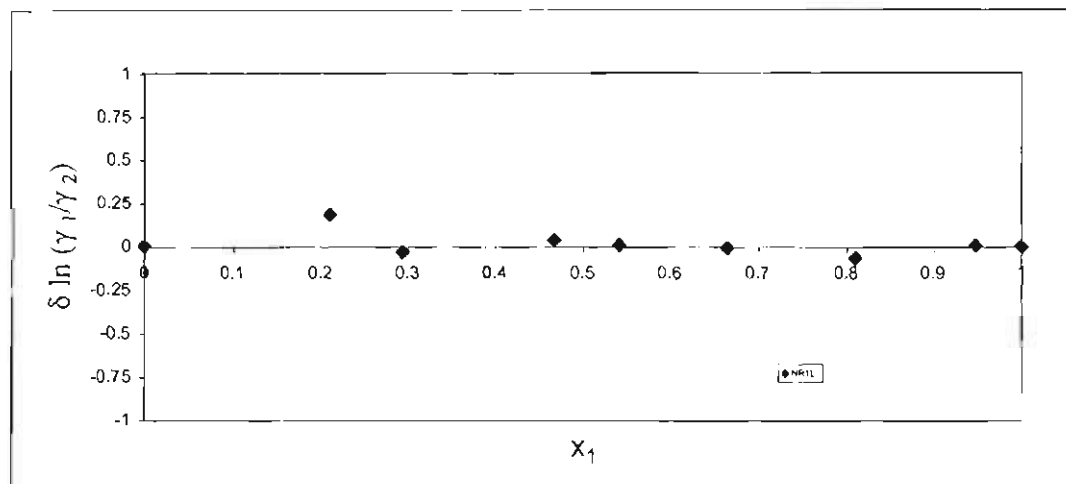


Figure B.8: Direct Test for Hexene (1) and NMP (2) at 40 °C

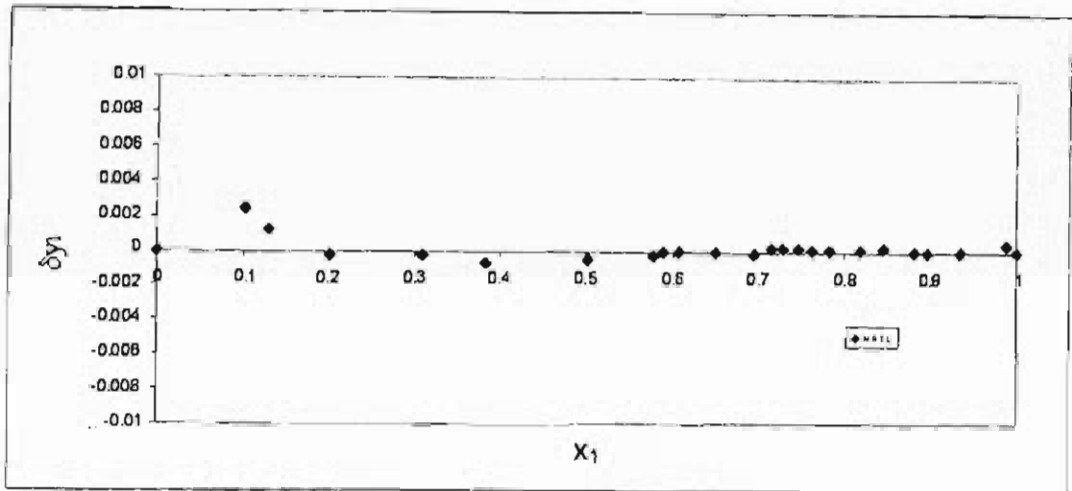


Figure B.9: Point Test for Hexene (1) and NMP (2) at 62 °C

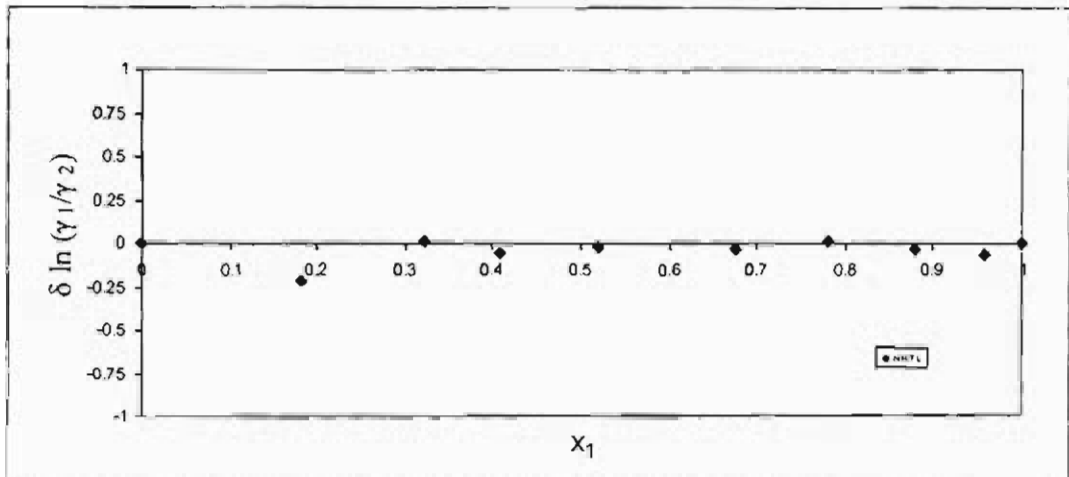


Figure B.10: Direct Test for Hexene (1) and NMP (2) at 62 °C

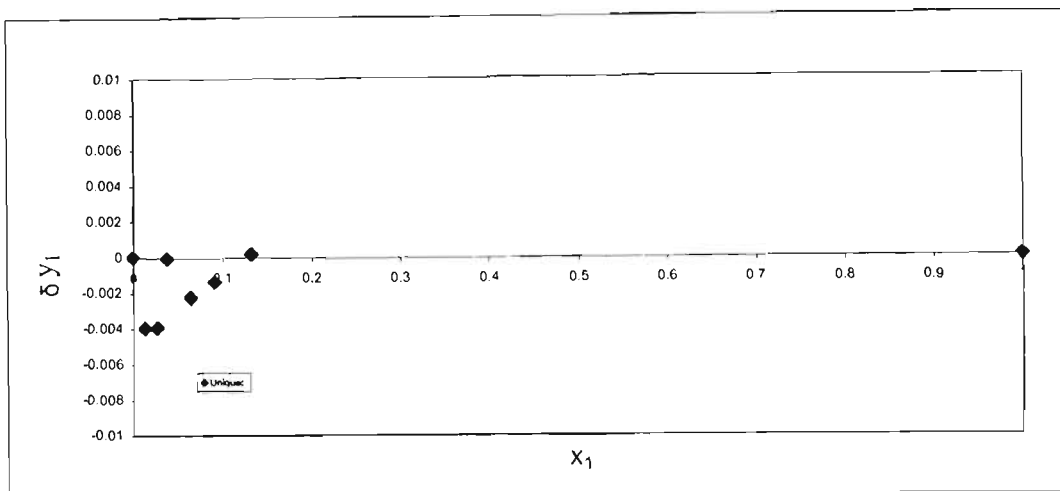


Figure B.11: Point Test for Hexene (1) and NMP (2) at 90 °C

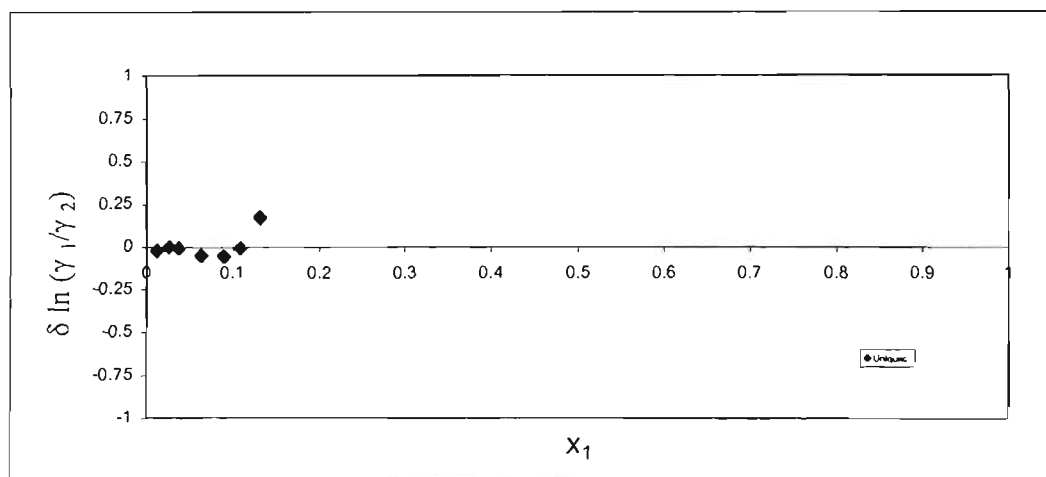


Figure B.12: Direct Test for Hexene (1) and NMP (2) at 90 °C

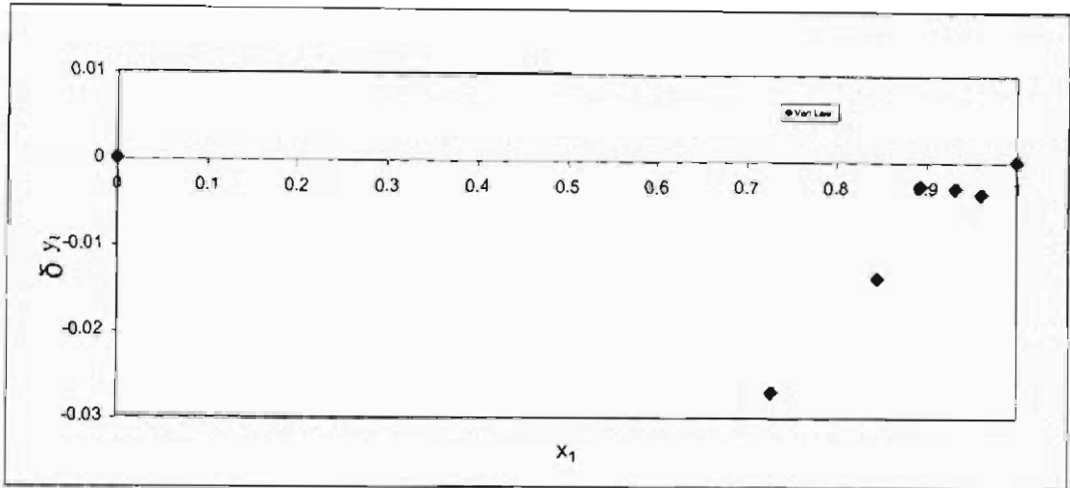


Figure B.13: Point Test for Hexene (1) and 3MCP (2) at 40 °C

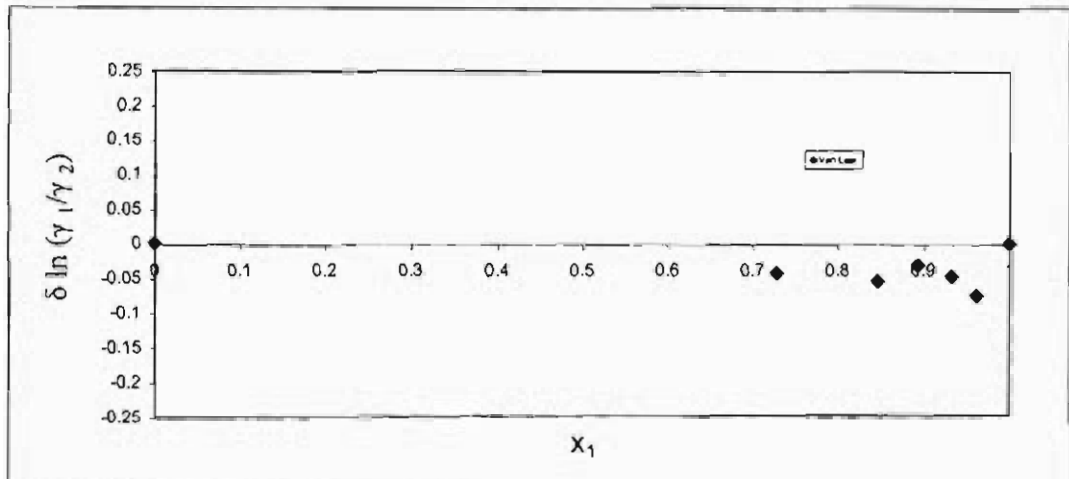


Figure B.14: Direct Test for Hexene (1) and 3MCP (2) at 40 °C

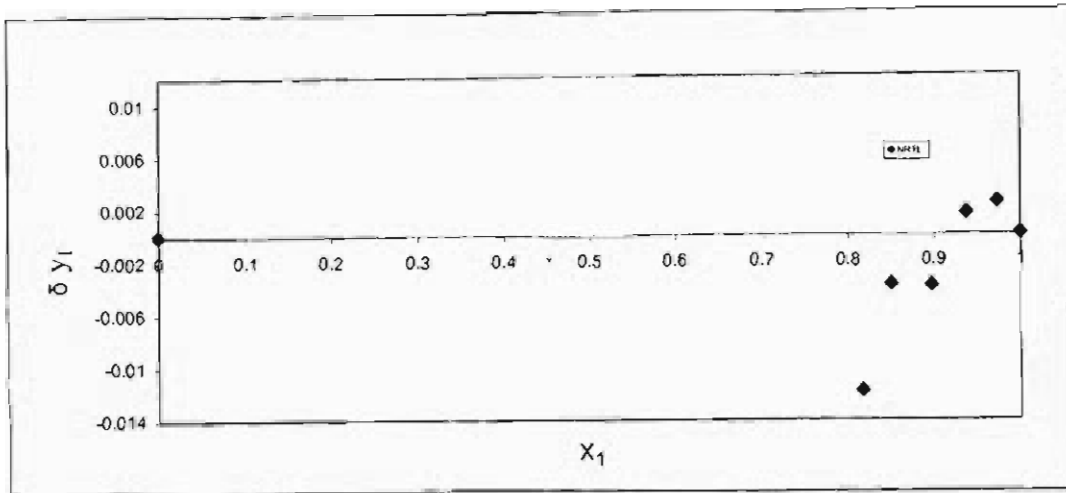


Figure B.15: Point Test for Hexene (1) and 3MCP (2) at 50 °C

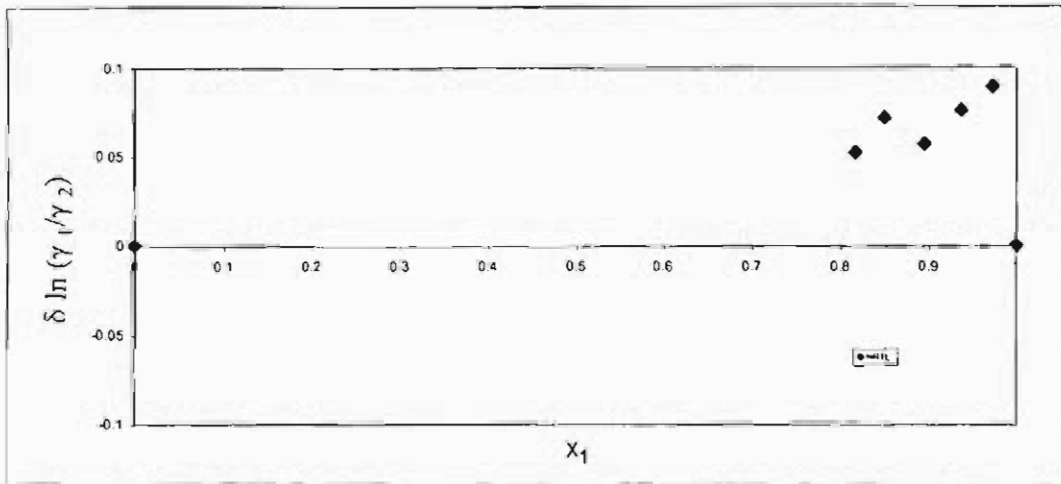


Figure B.16: Direct Test for Hexene (1) and 3MCP (2) at 50 °C

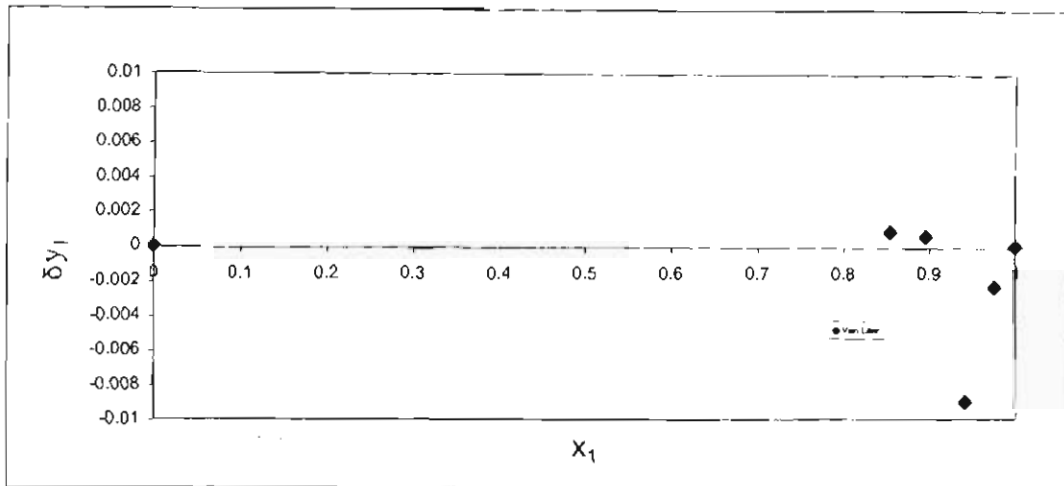


Figure B.17: Point Test for Hexene (1) and 3MCP (2) at 60 °C

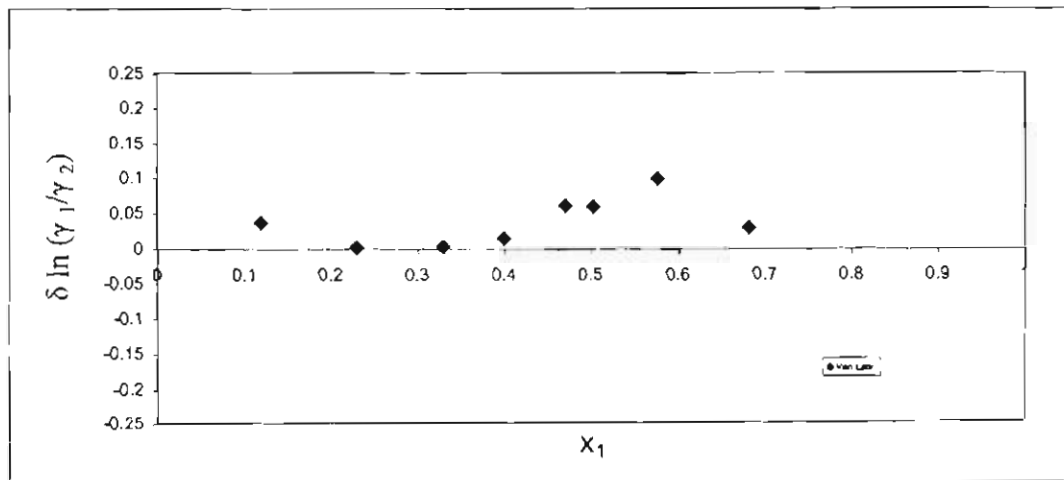


Figure B.18: Point Test for Hexene (1) and 3MCP (2) at 60 °C

B.2: Thermodynamic Consistency Tests for Direct Method:

Wong-Sandler-PRSV

For the direct method using the Wong-Sandler-PRSV combination, the graphical results of the point and the direct consistency tests for all systems measured can be found in Figures B.19 to B.36 alternatively. The direct consistency test scale can be found in Table B.2. The vapour composition residuals can be found in Chapter 5, Table 5.6.

Table B.2: Direct Test Scale for the Direct Method: Wong-Sandler-PRSV

Systems	water (1) + NMP (2)			1-hexene(1) + NMP(2)			1-hexene(1) + 3MCP (2)		
Temperature									
$T^{\circ}C$	70	90	107	40	62	90	40	50	60
<i>Idx</i>	4	4	4	4	3	4	3	1	2

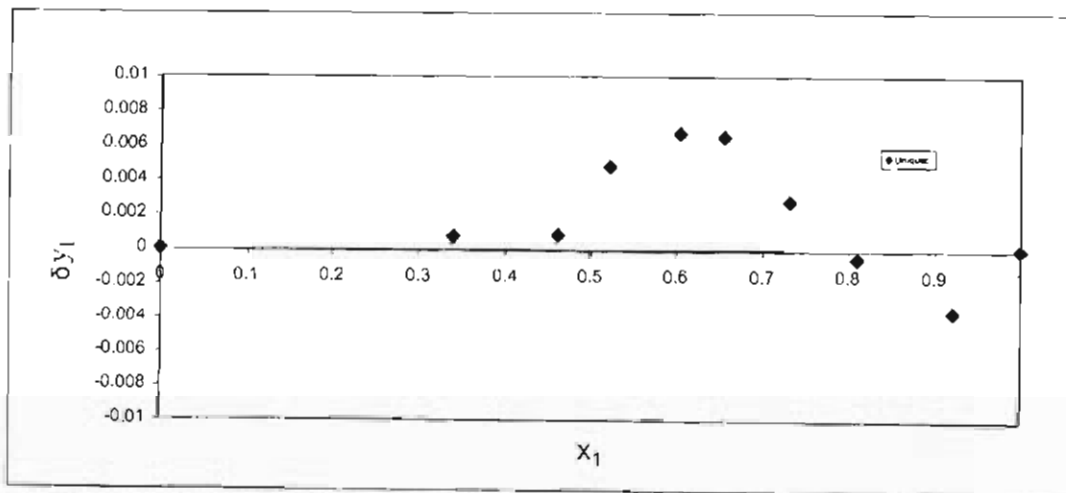


Figure B.19: Point Test for Water (1) and NMP (2) at 70 °C

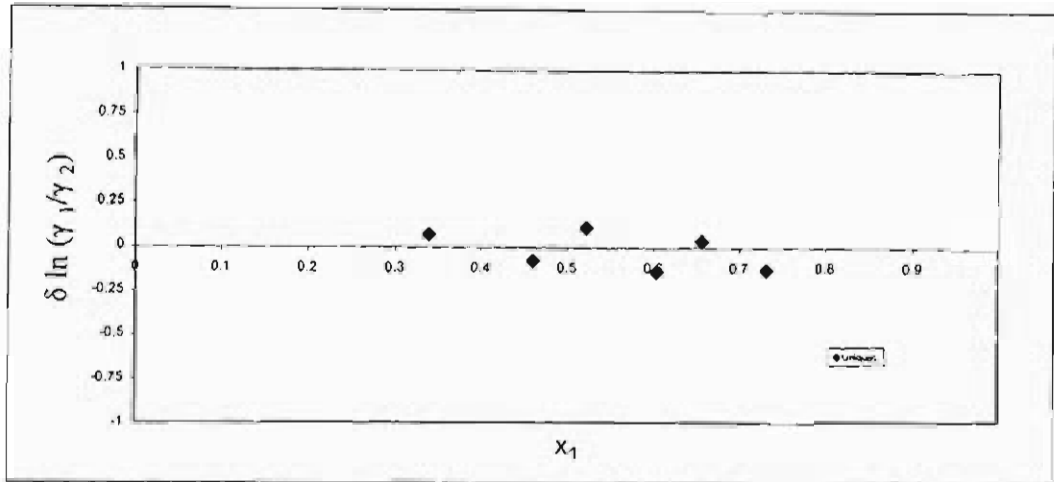


Figure B.20: Direct Test for Water (1) and NMP (2) at 70 °C

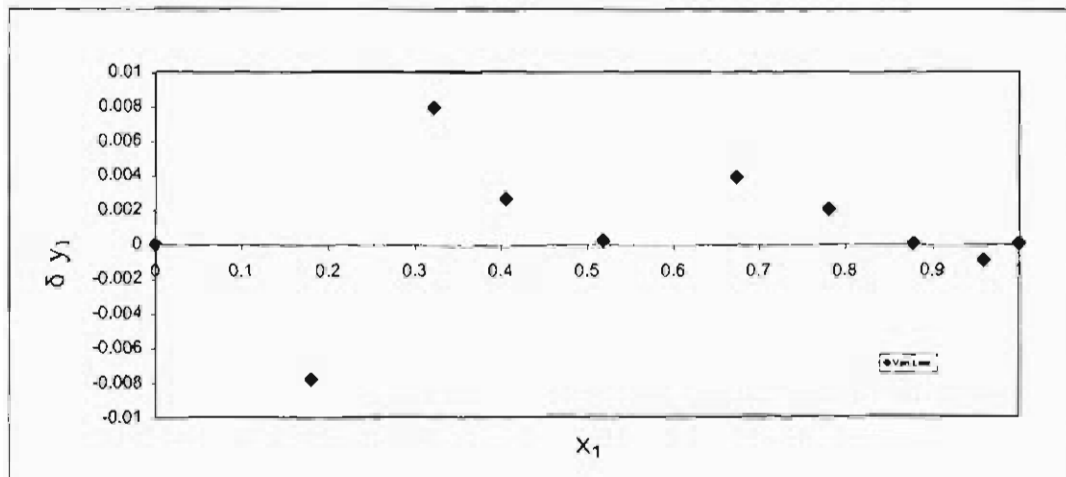


Figure B.21: Point Test for Water (1) and NMP (2) at 90 °C

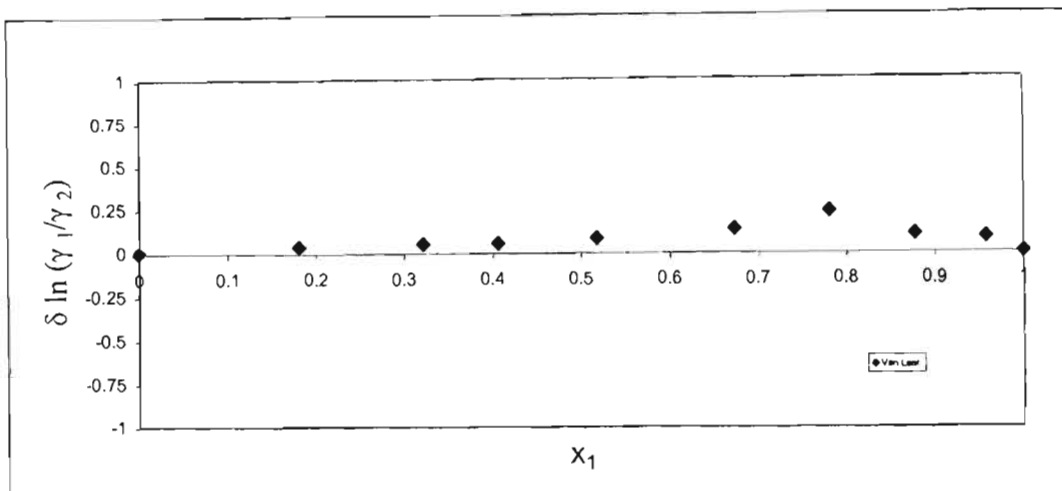


Figure B.22: Direct Test for Water (1) and NMP (2) at 90 °C

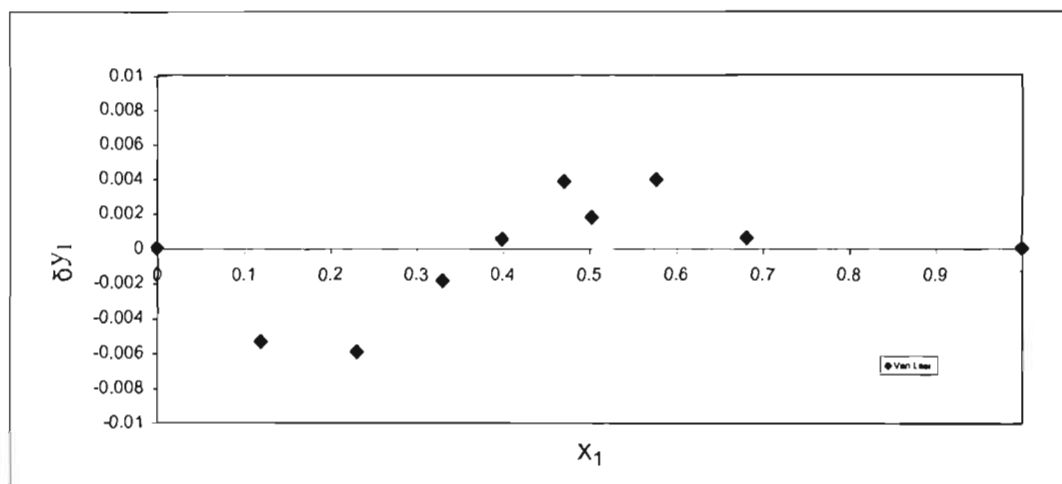


Figure B.23: Point Test for Water (1) and NMP (2) at 107 °C

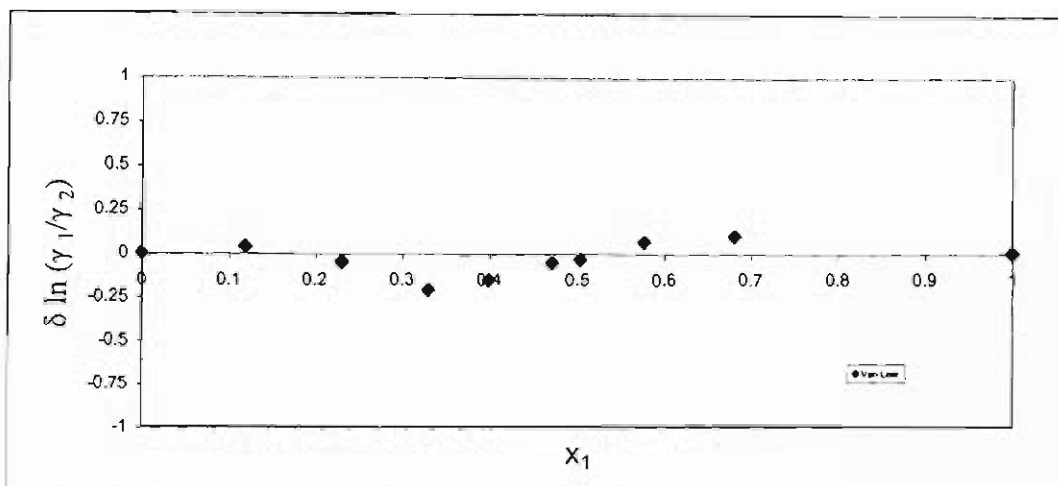


Figure B.24: Direct Test for Water (1) and NMP (2) at 107 °C

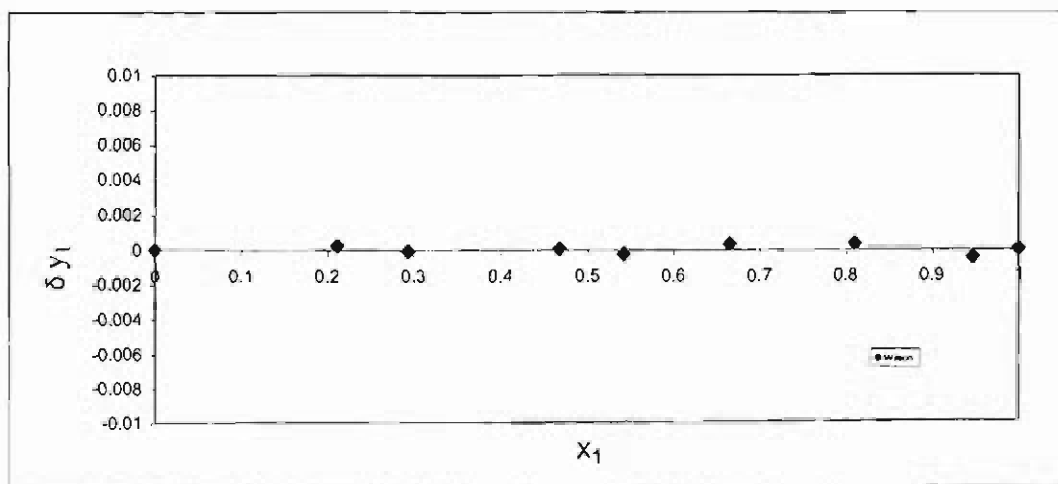


Figure B.25: Point Test for Hexene (1) and NMP (2) at 40 °C

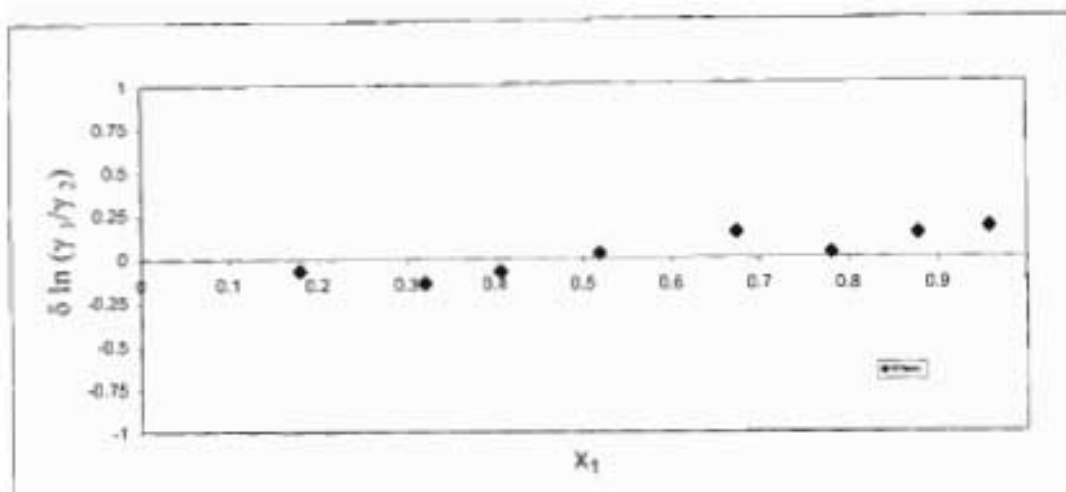


Figure B.26: Direct Test for Hexene (1) and NMP (2) at 40 °C

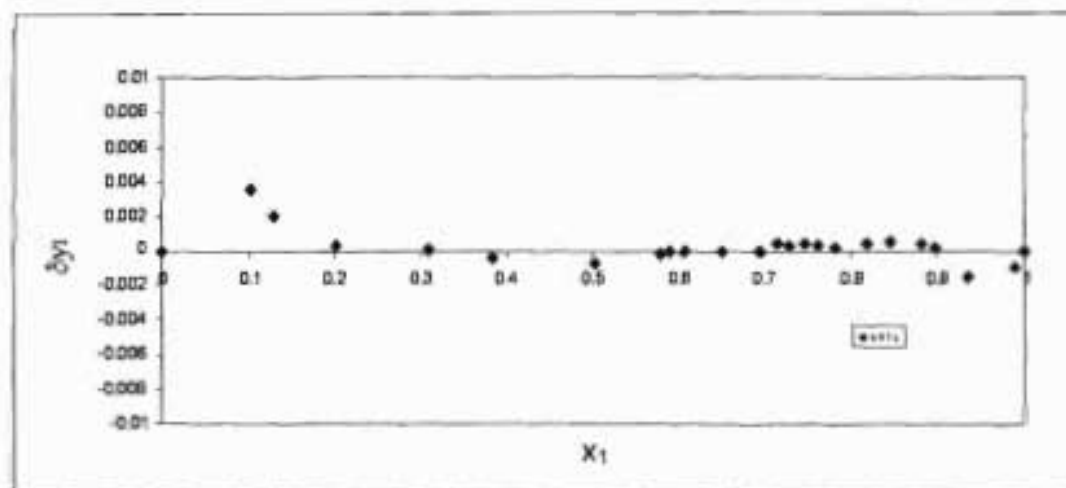


Figure B.27: Point Test for Hexene (1) and NMP (2) at 62 °C

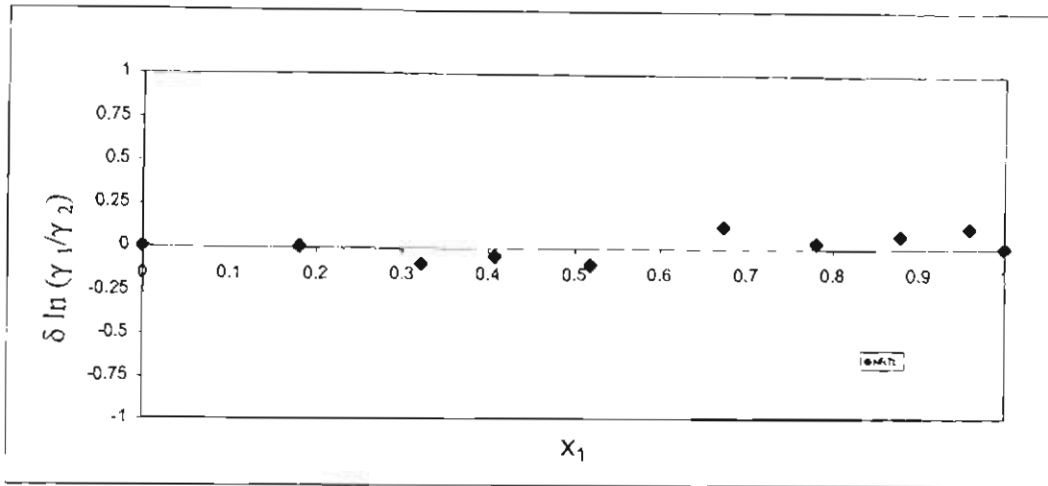


Figure B.28: Direct Test for Hexene (1) and NMP (2) at 62 °C

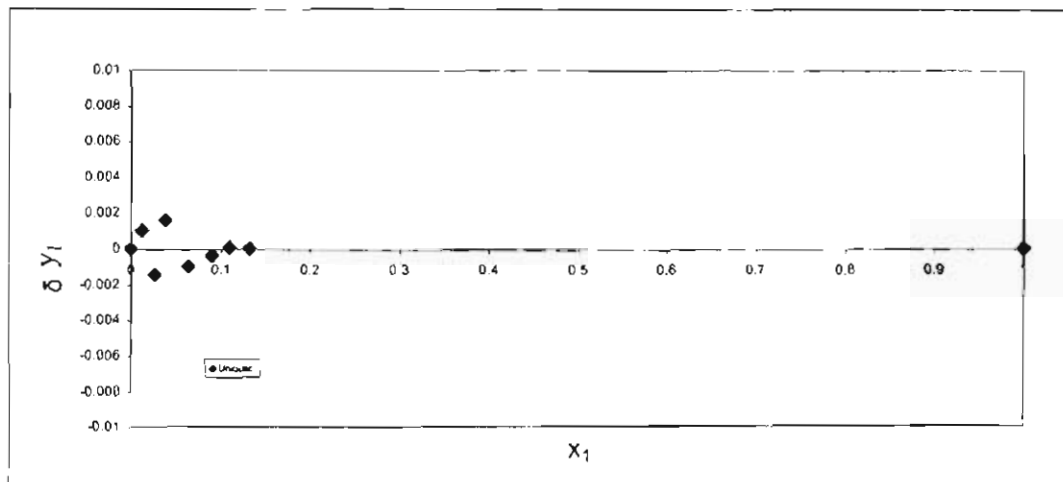


Figure B.29: Point Test for Hexene (1) and NMP (2) at 90 °C

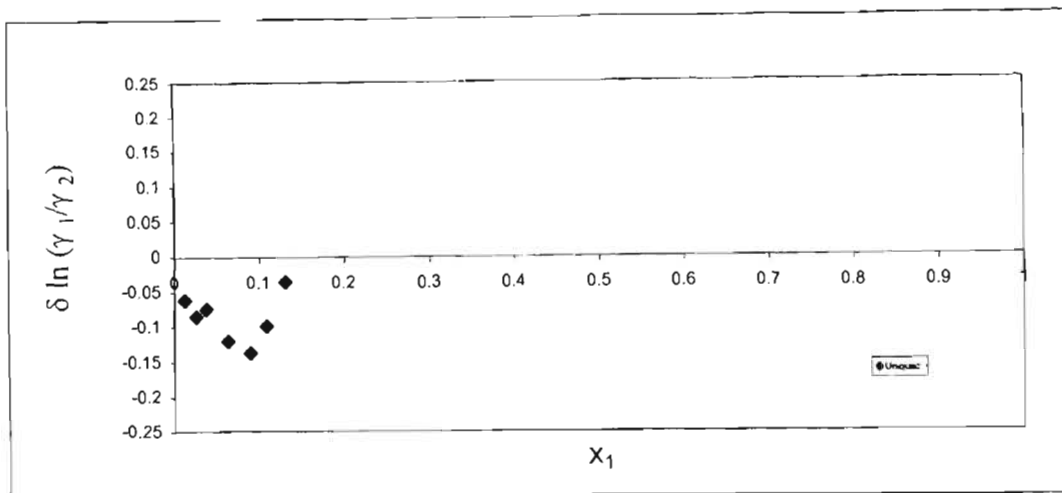


Figure B.30: Direct Test for Hexene (1) and NMP (2) at 90 °C

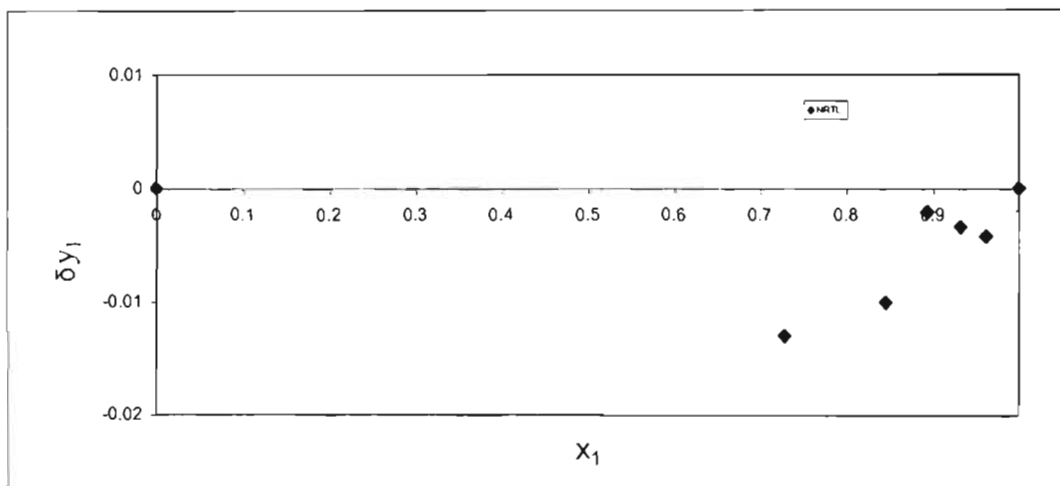


Figure B.31: Point Test for Hexene (1) and 3MCP (2) at 40 °C

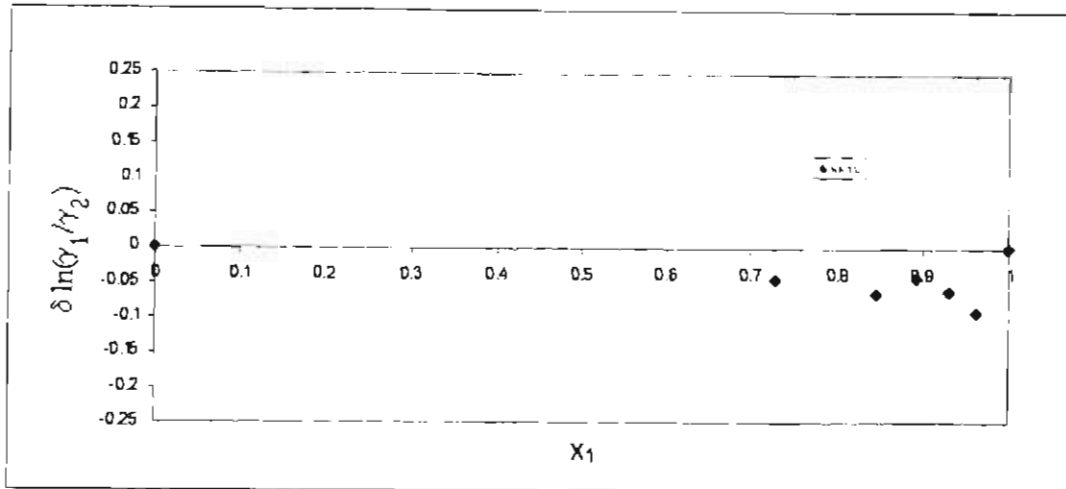


Figure B.32: Direct Test for Hexene (1) and 3MCP (2) at 40 °C

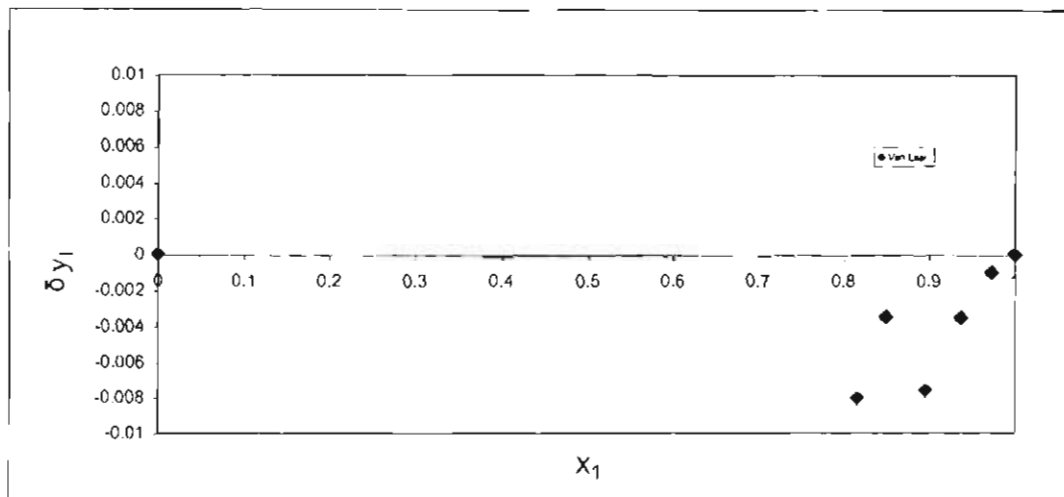


Figure B.33: Point Test for Hexene (1) and 3MCP (2) at 50 °C

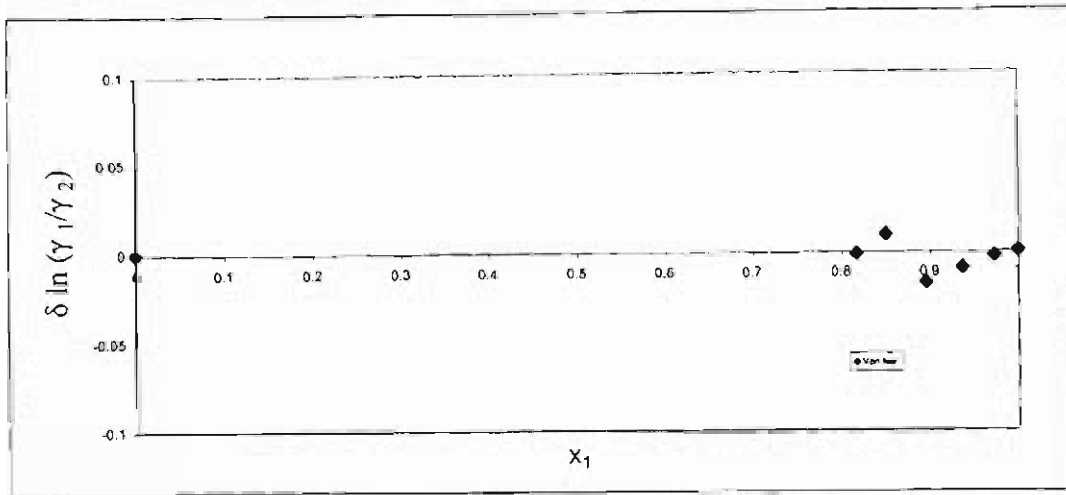


Figure B.34: Direct Test for Hexene (1) and 3MCP (2) at 50 °C

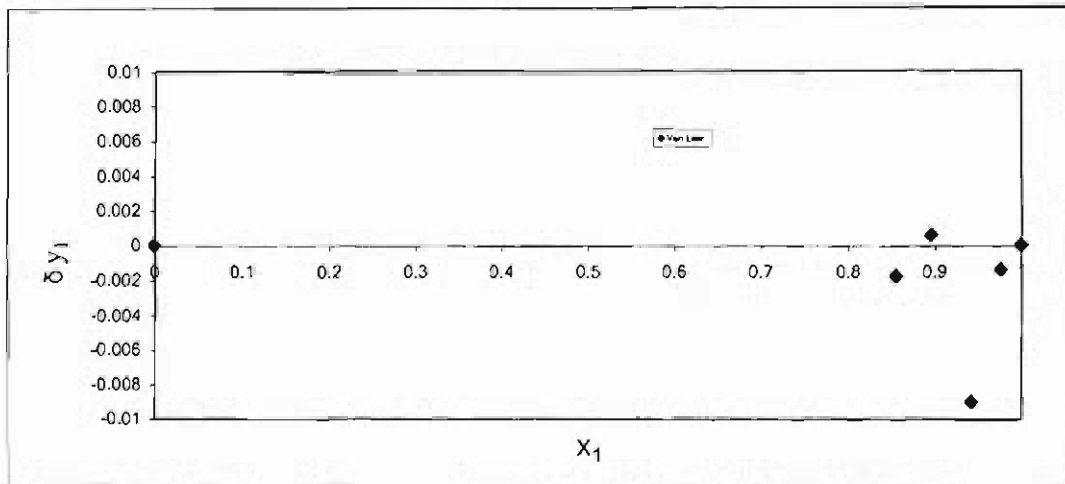


Figure B.35: Point Test for Hexene (1) and 3MCP (2) at 60 °C

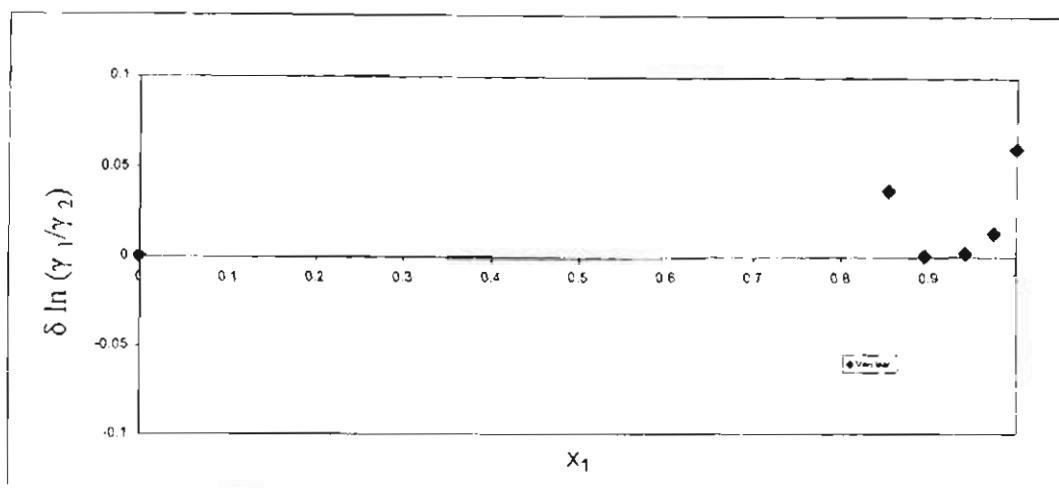


Figure B.36: Point Test for Hexene (1) and 3MCP (2) at 60 °C

B.3 Thermodynamic Consistency Tests for Direct Method: Twu-Coon-SRK

For the direct method using the Twu-Coon-SRK combination, the graphical results of the point and the direct consistency tests for all systems measured can be found in Figures B.37 to B.54 alternatively. The direct consistency test scale can be found in Table B.3. The vapour composition residuals can be found in Chapter 5, Table 5.7.

Table B.3: Direct Test Scale for the Direct Method: Twu-Coon-SRK

Systems	water (1) + NMP (2)			1-hexene(1) + NMP(2)			1-hexene(1) + 3MCP (2)		
Temperature									
$T^{\circ}C$	70	90	107	40	62	90	40	50	60
Index	4	4	2	3	4	4	4	4	2

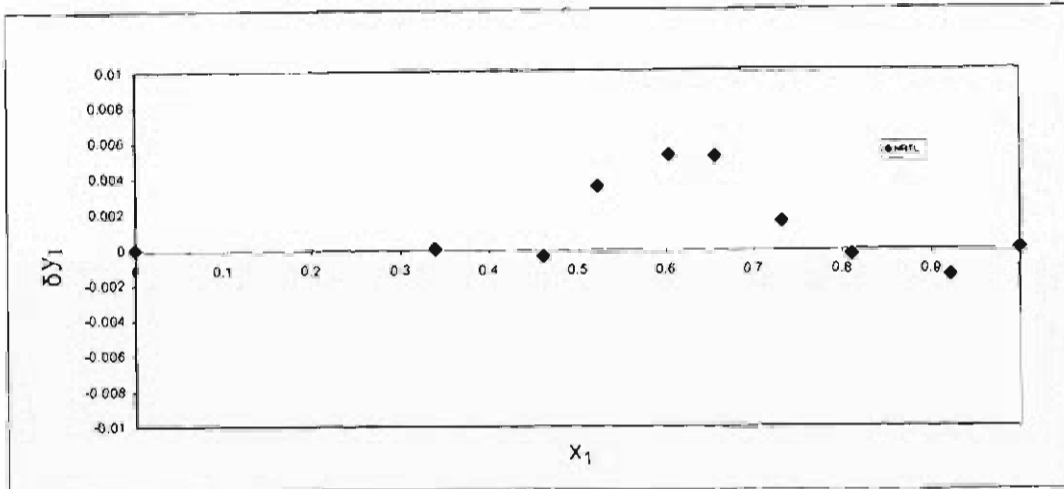


Figure B.37: Point Test for Water (1) and NMP (2) at 70 °C

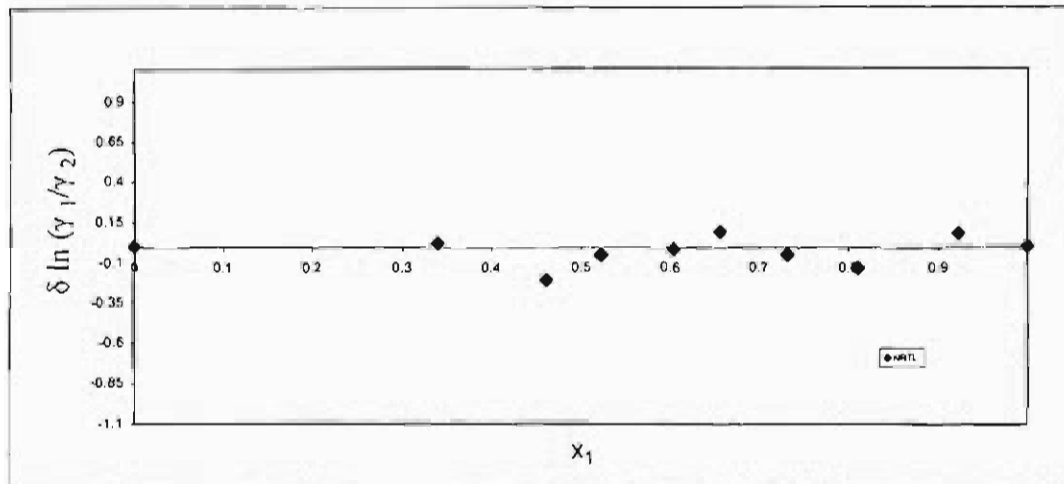


Figure B.38: Direct Test for Water (1) and NMP (2) at 70 °C

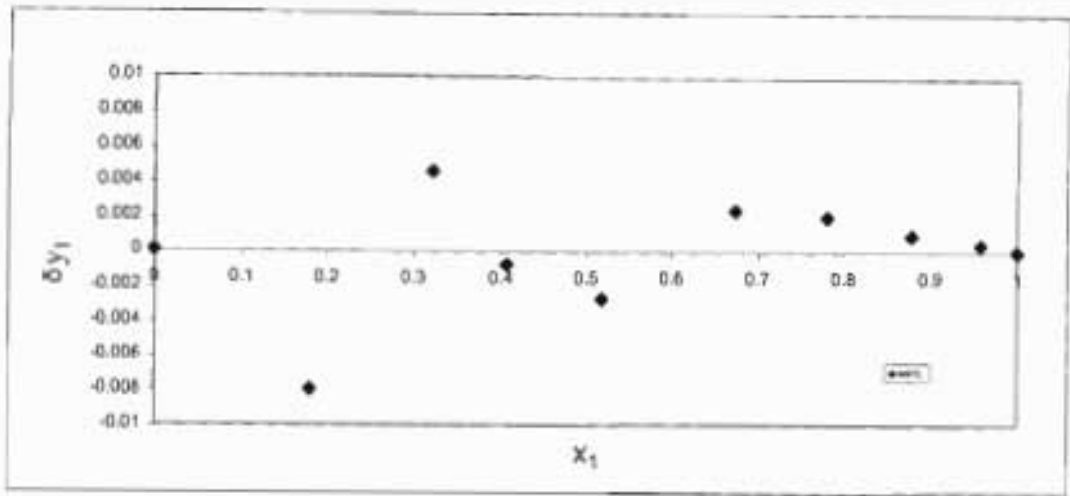


Figure B.39: Point Test for Water (1) and NMP (2) at 90 °C

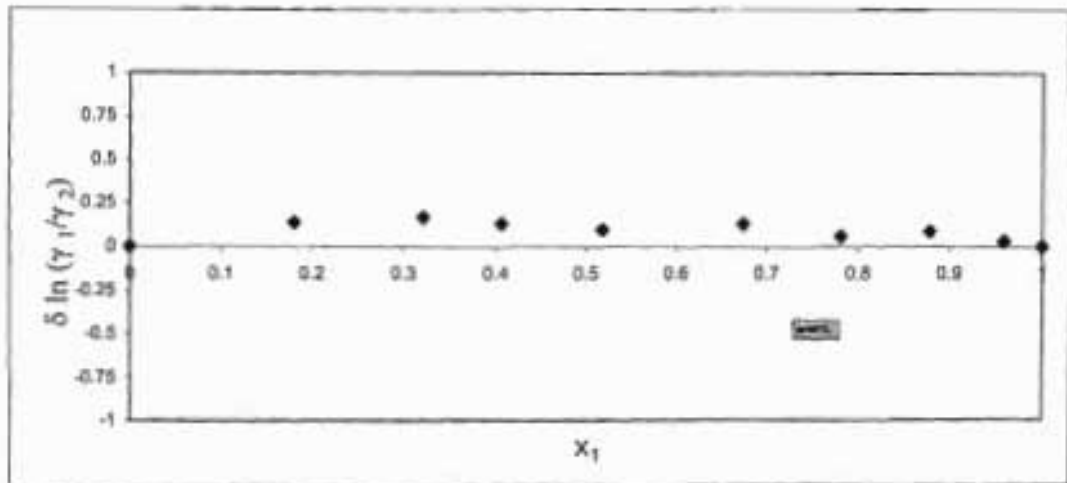


Figure B.40: Direct Test for Water (1) and NMP (2) at 90 °C

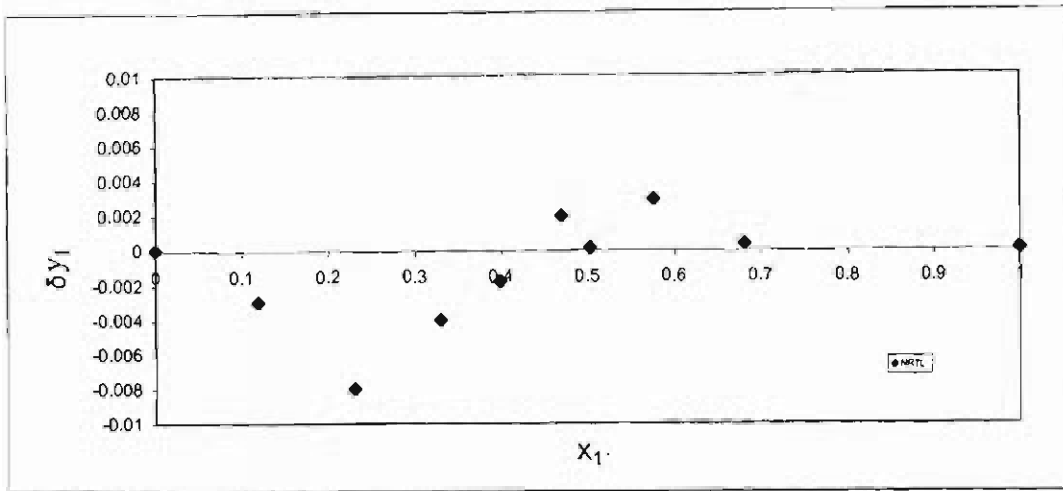


Figure B.41: Point Test for Water (1) and NMP (2) at 107 °C

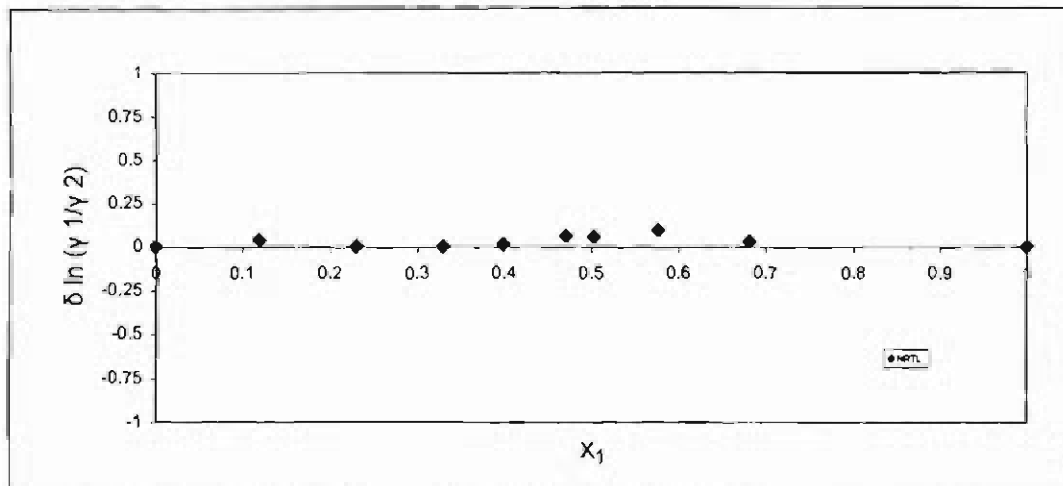


Figure B.42: Direct Test for Water (1) and NMP (2) at 107 °C

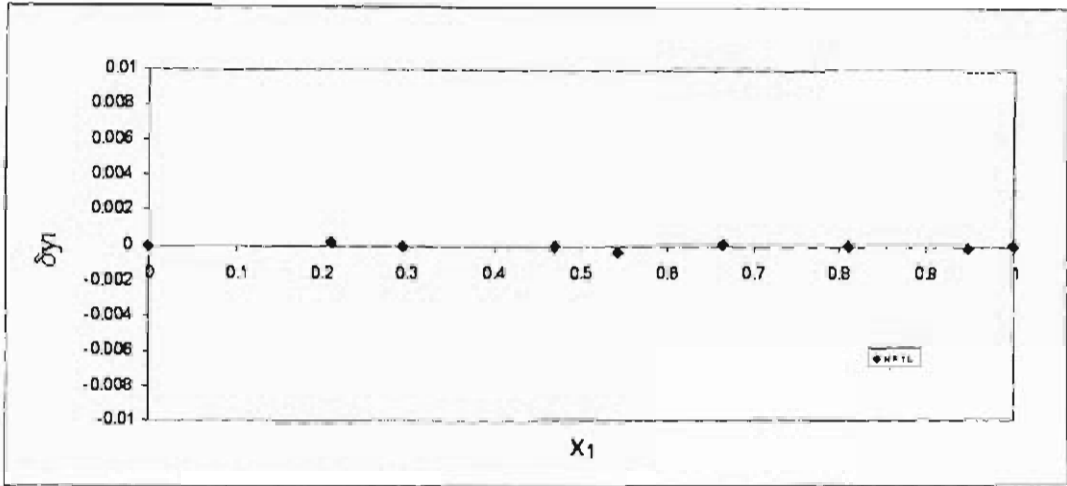


Figure B.43: Point Test for Hexene (1) and NMP (2) at 40 °C

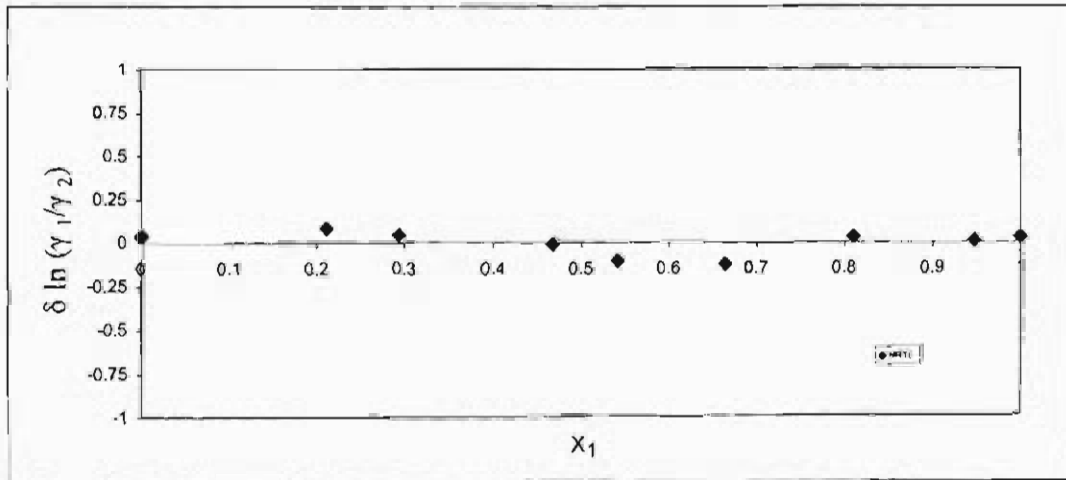


Figure B.44: Direct Test for Hexene (1) and NMP (2) at 40 °C

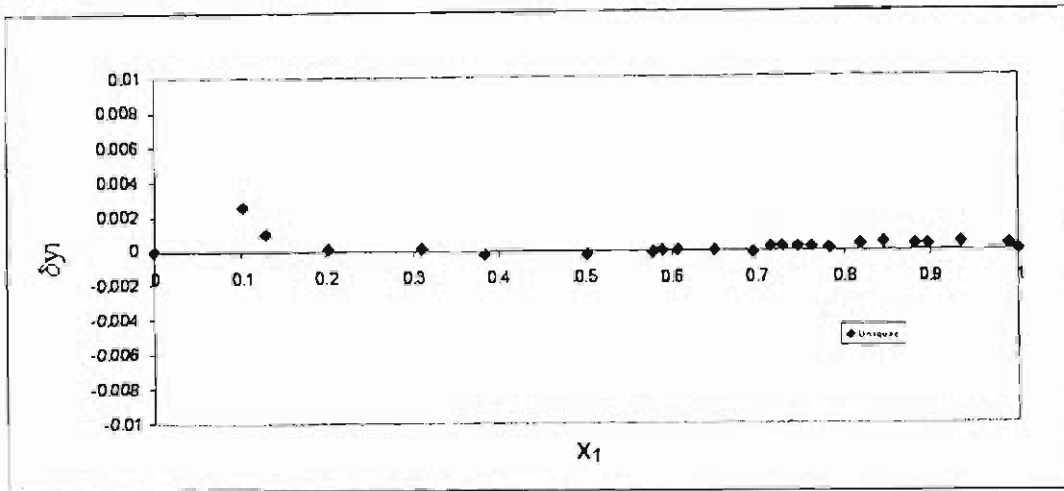


Figure B.45: Point Test for Hexene (1) and NMP (2) at 62 °C

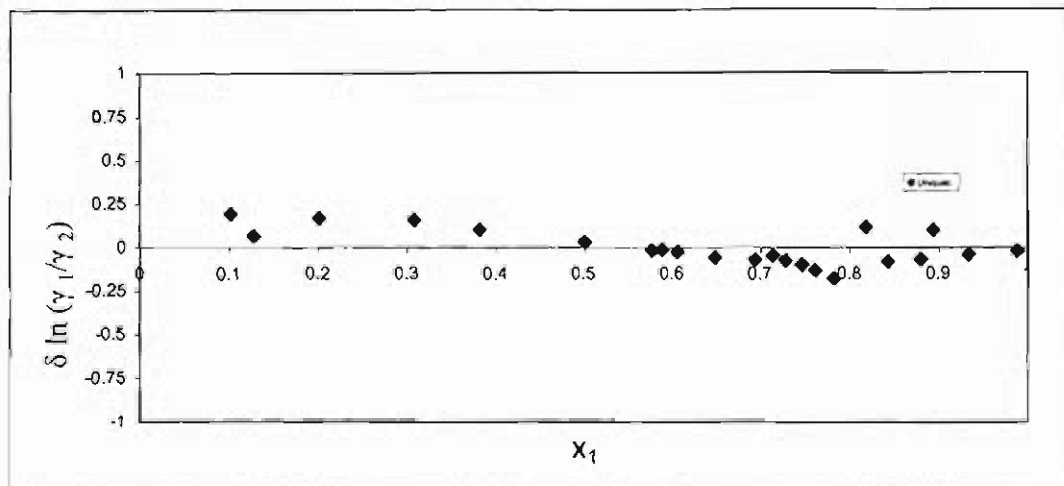


Figure B.46: Direct Test for Hexene (1) and NMP (2) at 62 °C

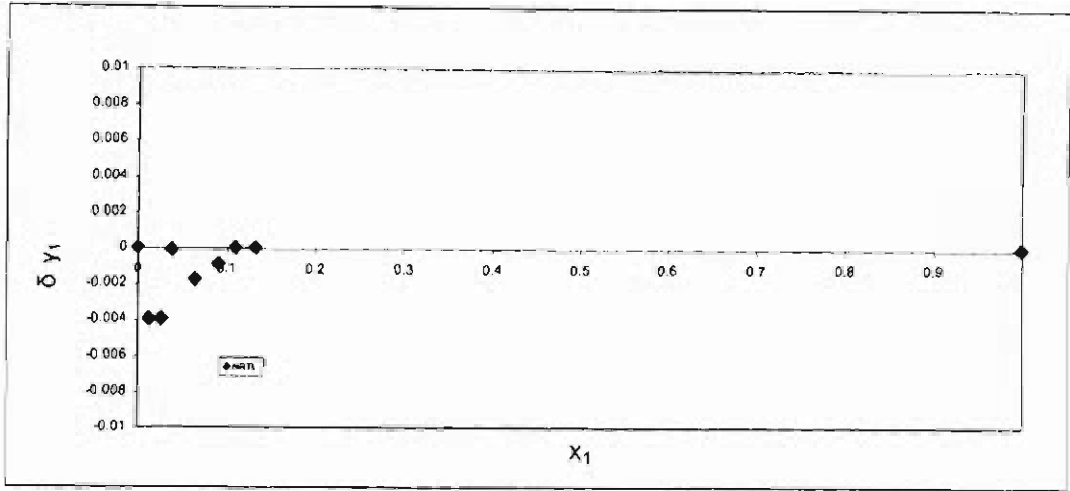


Figure B.47: Point Test for Hexene (1) and NMP (2) at 90 °C

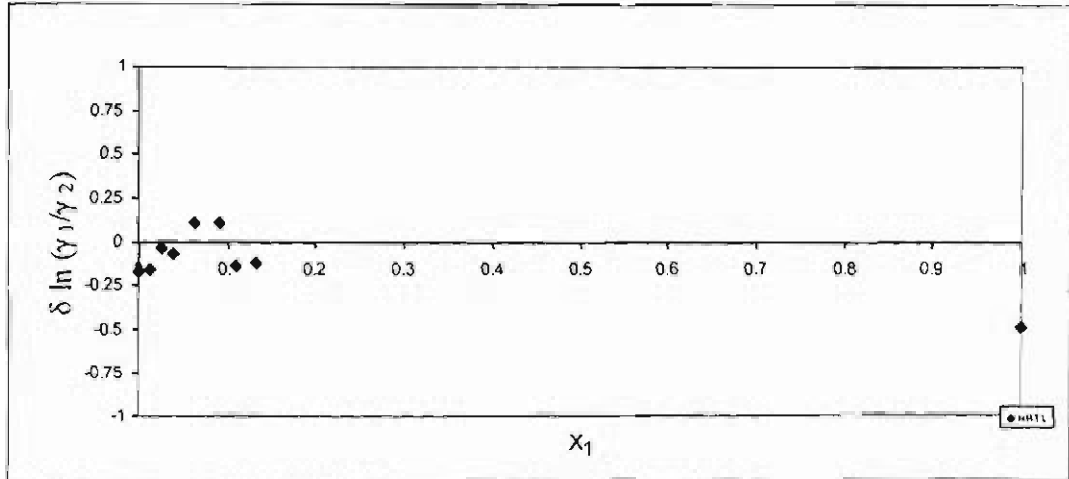


Figure B.48: Direct Test for Hexene (1) and NMP (2) at 90 °C

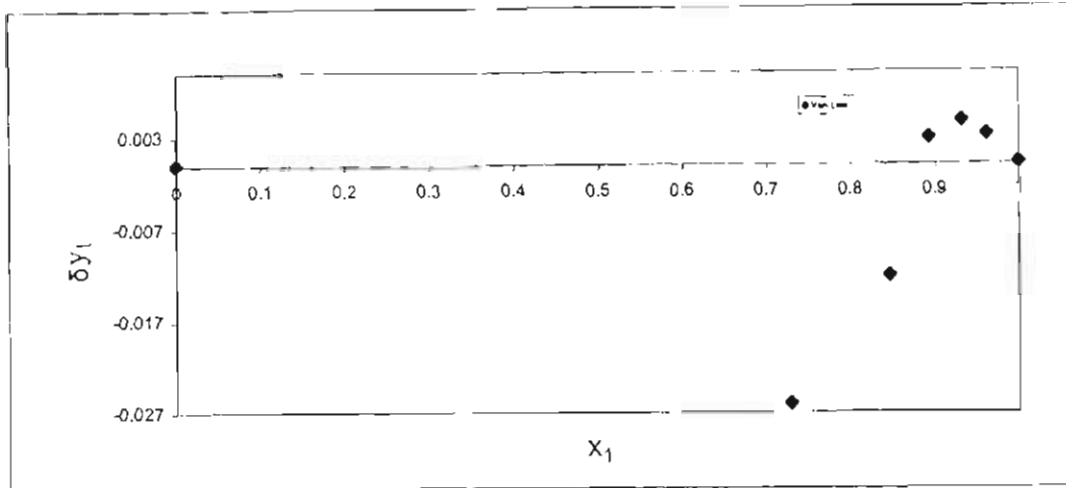


Figure B.49: Point Test for Hexene (1) and 3MCP (2) at 40 °C

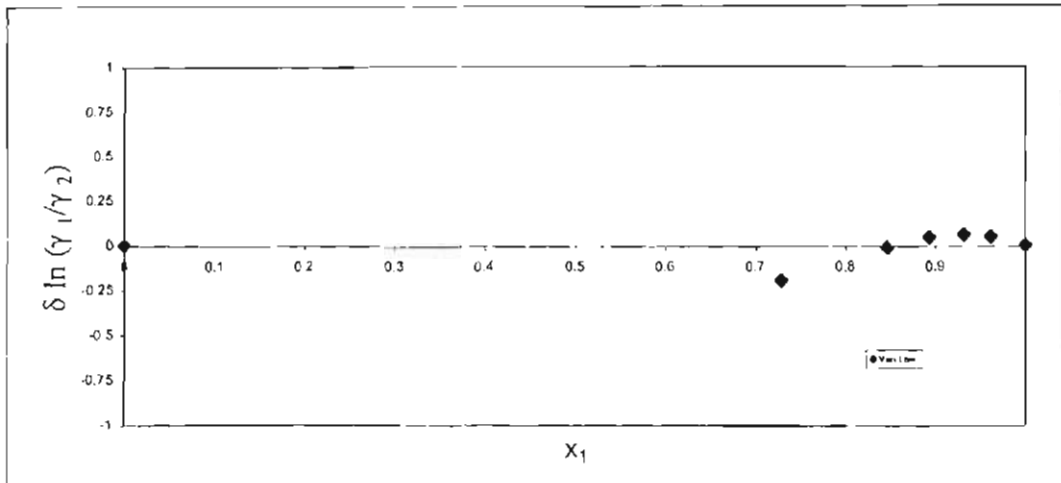


Figure B.50: Direct Test for Hexene (1) and 3MCP (2) at 40 °C

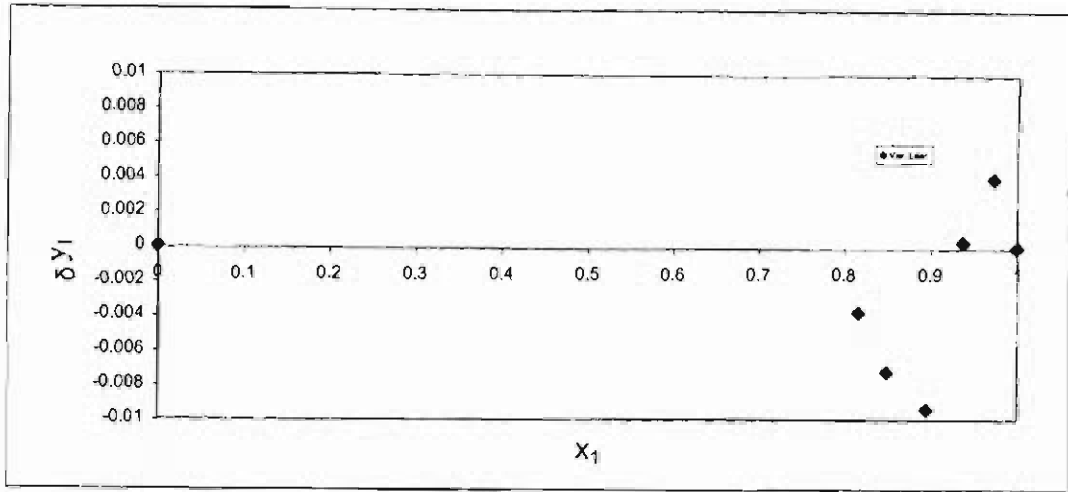


Figure B.51: Point Test for Hexene (1) and 3MCP (2) at 50 °C

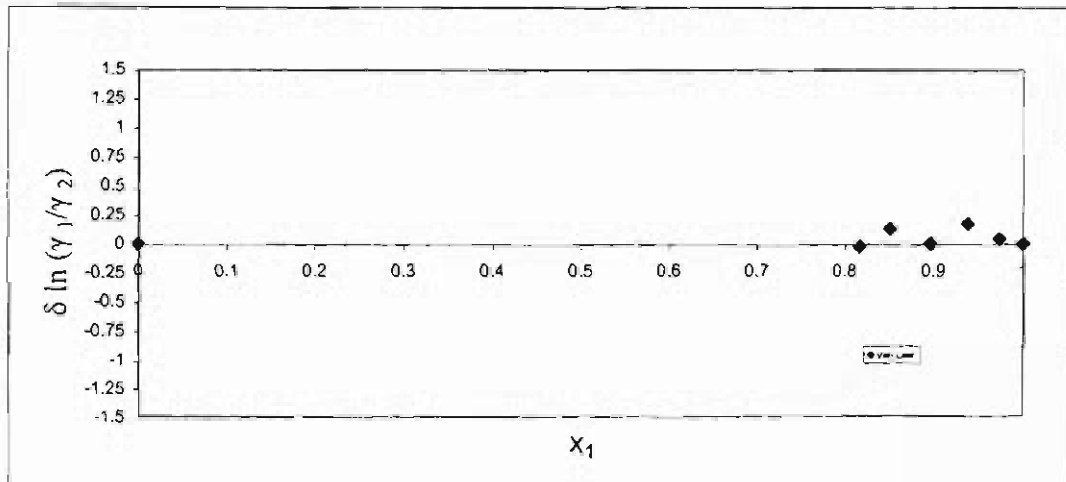


Figure B.52: Direct Test for Hexene (1) and 3MCP (2) at 50 °C

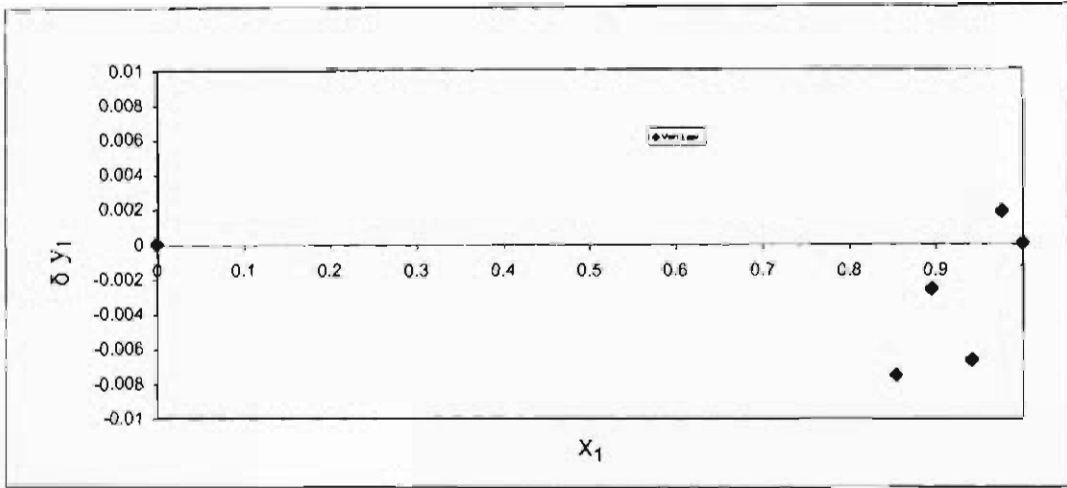


Figure B.53: Point Test for Hexene (1) and 3MCP (2) at 60 °C

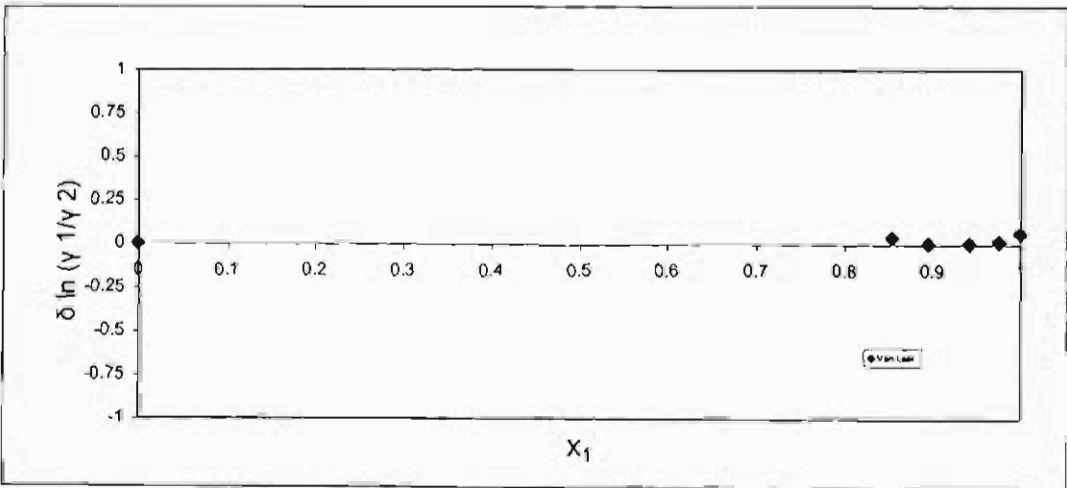


Figure B.54: Direct Test for Hexene (1) and 3MCP (2) at 60 °C

B.4 Thermodynamic Consistency Tests for Direct Method: Twu-Coon-PRSV

For the direct method using the Twu-Coon-PRSV combination, the graphical results of the point and the direct consistency tests for all systems measured can be found in Figures B.55 to B.72 alternatively. The direct consistency test scale can be found in Table B.4. The vapour composition residuals can be found in Chapter 5, Table 5.8.

Table B.4: Direct Test Scale for the Direct Method: Twu-Coon-PRSV

Systems	water (1) + NMP (2)			1-hexene(1) + NMP(2)			1-hexene(1) + 3MCP (2)		
Temperature									
$T^{\circ}C$	70	90	107	40	62	90	40	50	60
Index	4	4	4	4	4	4	3	4	4

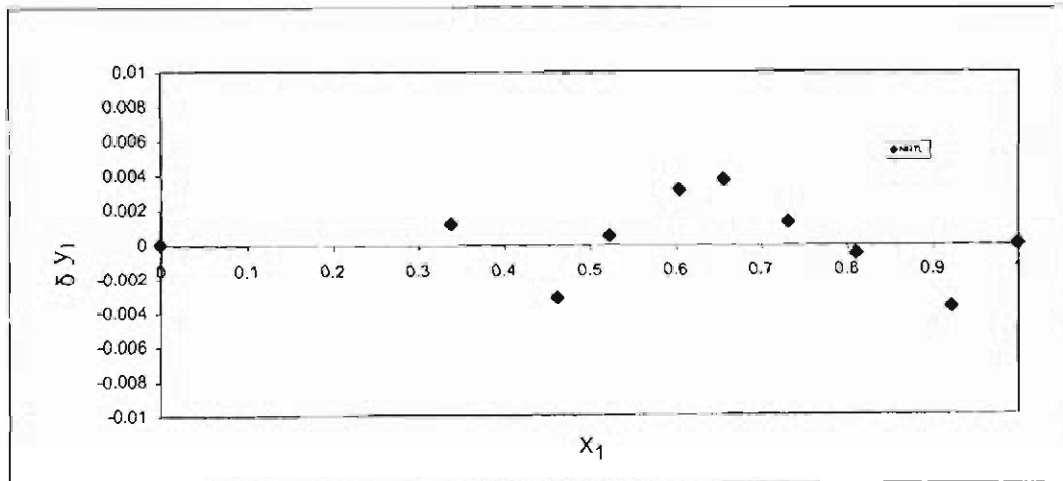


Figure B.55: Point Test for Water (1) and NMP (2) at 70 °C

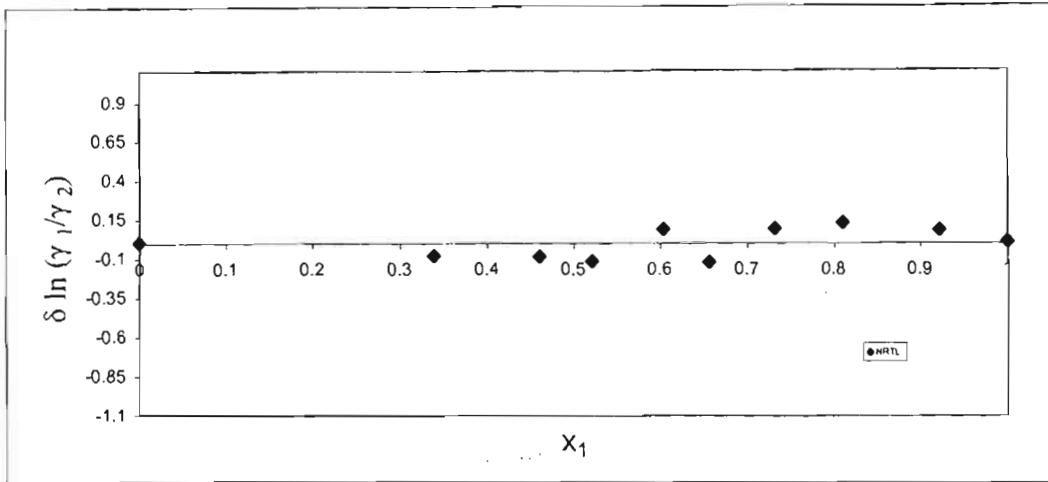


Figure B.56: Direct Test for Water (1) and NMP (2) at 70 °C

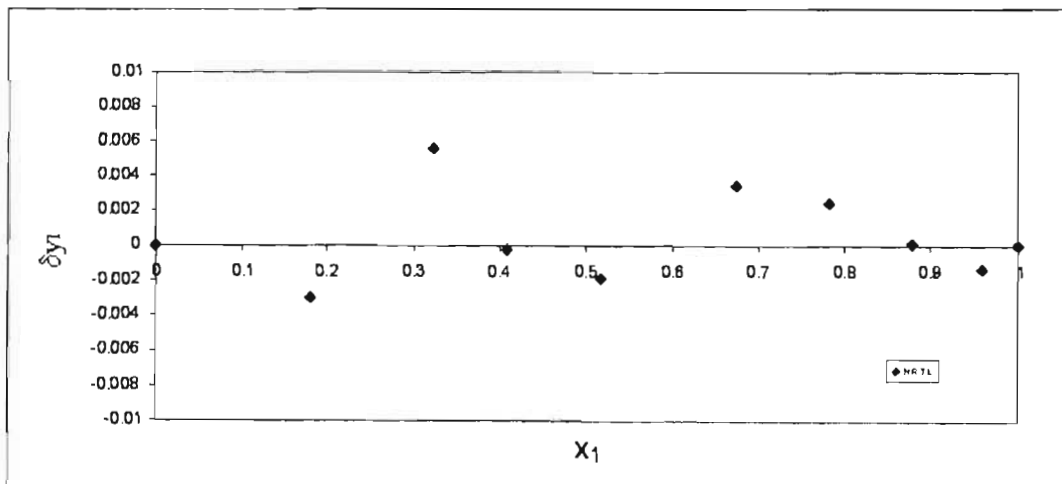


Figure B.57: Point Test for Water (1) and NMP (2) at 90 °C

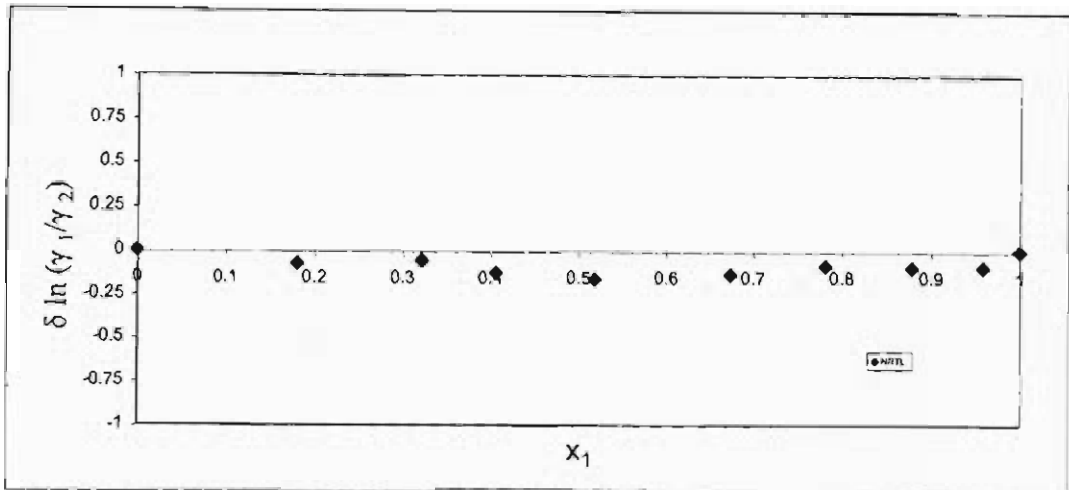


Figure B.58: Direct Test for Water (1) and NMP (2) at 90 °C

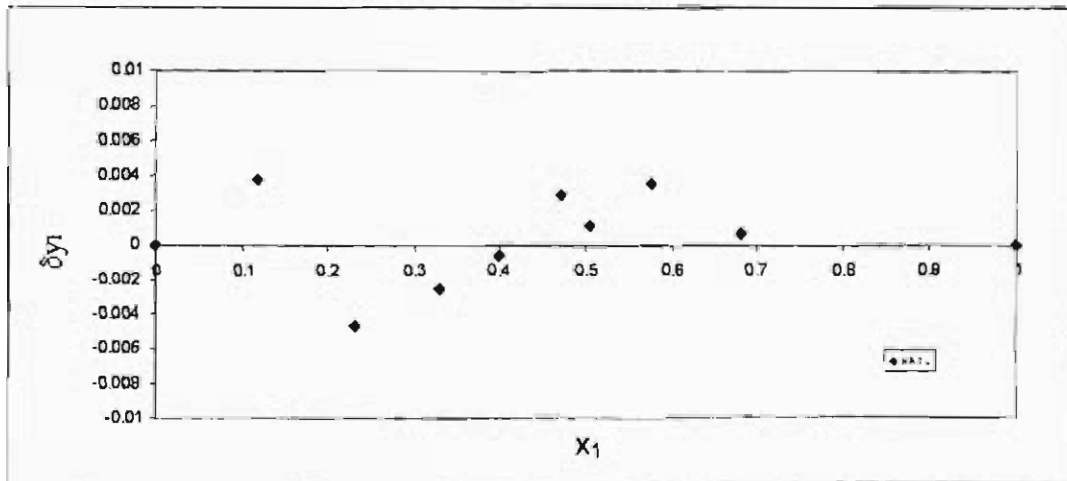


Figure B.59: Point Test for Water (1) and NMP (2) at 107 °C

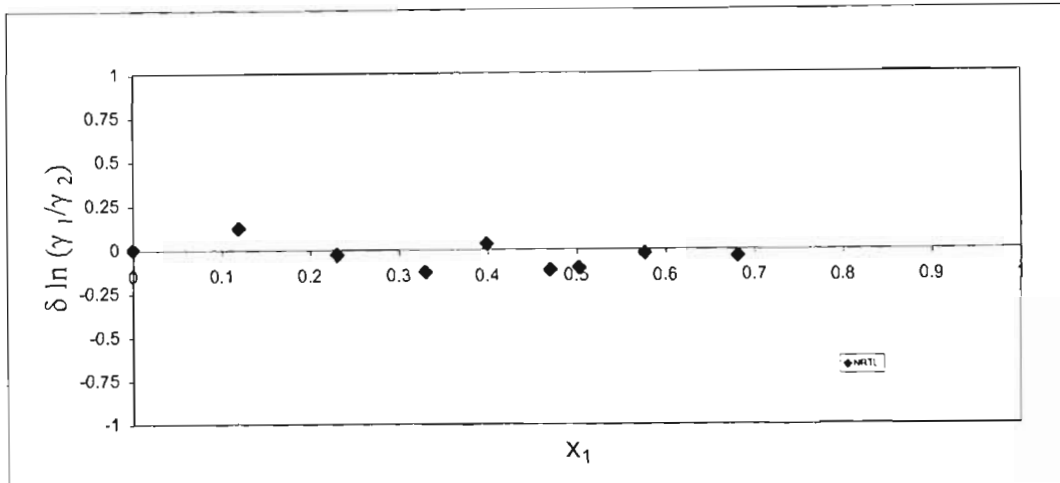


Figure B.60: Direct Test for Water (1) and NMP (2) at 107 °C

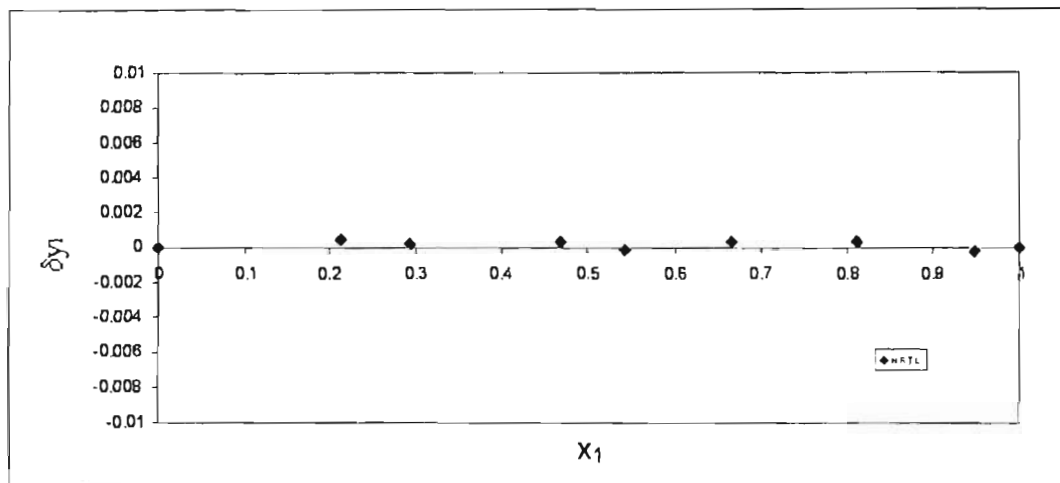


Figure B.61: Point Test for Hexene (1) and NMP (2) at 40 °C

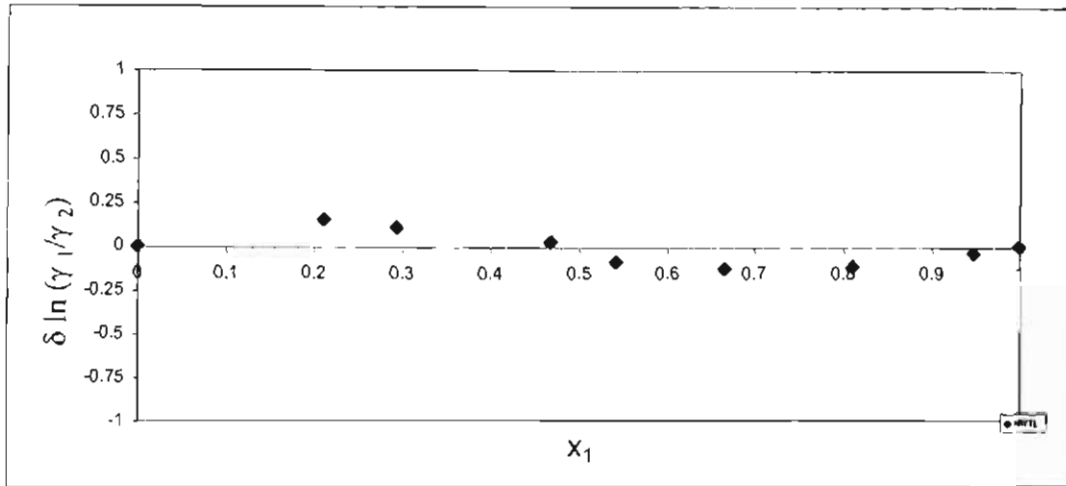


Figure B.62: Direct Test for Hexene (1) and NMP (2) at 40 °C

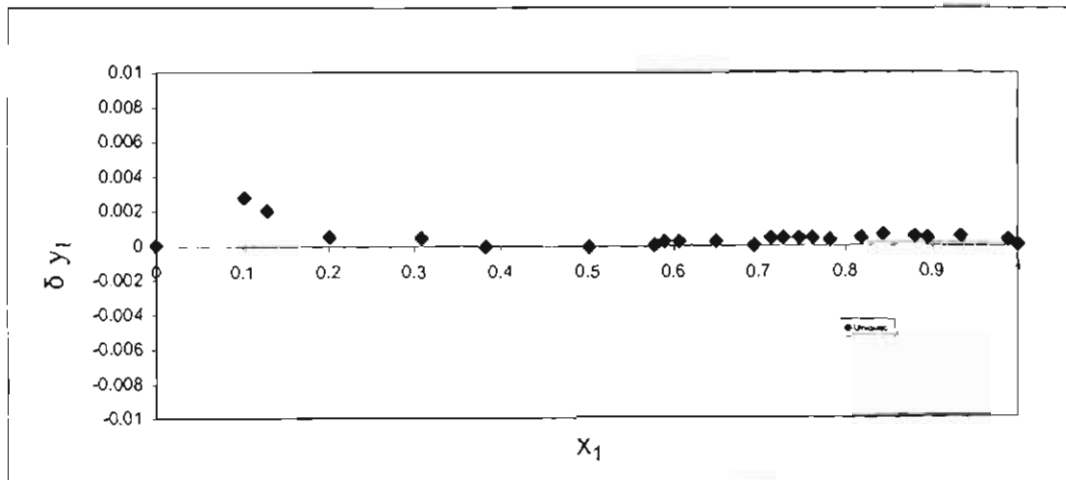


Figure B.63: Point Test for Hexene (1) and NMP (2) at 62 °C

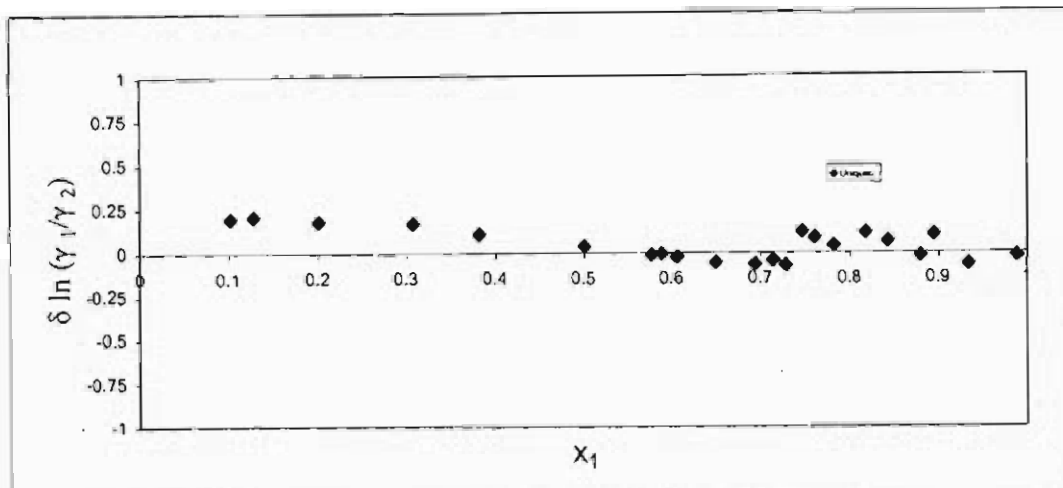


Figure B.64: Direct Test for Hexene (1) and NMP (2) at 62 °C

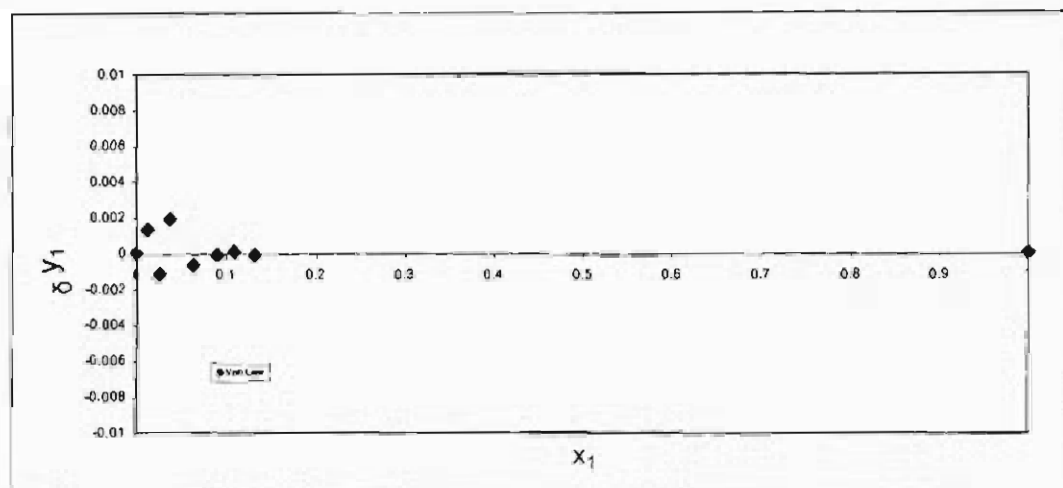


Figure B.65: Point Test for Hexene (1) and NMP (2) at 90 °C

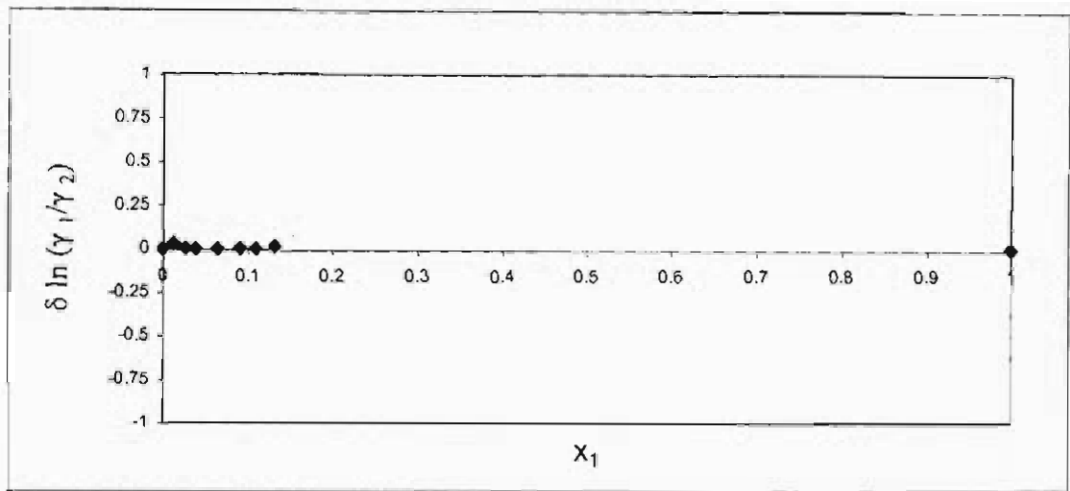


Figure B.66: Direct Test for Hexene (1) and NMP (2) at 90 °C

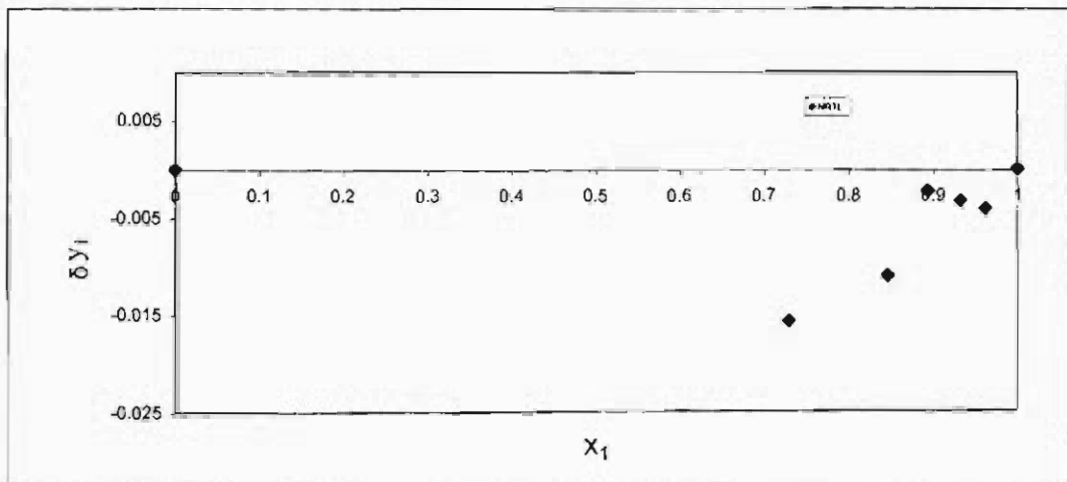


Figure B.67: Point Test for Hexene (1) and 3MCP (2) at 40 °C

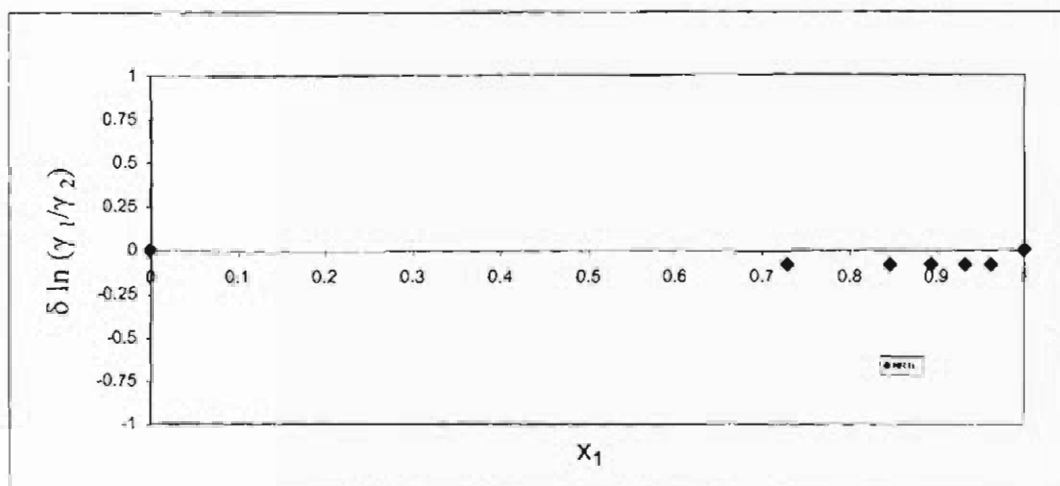


Figure B.68: Direct Test for Hexene (1) and 3MCP (2) at 40 °C

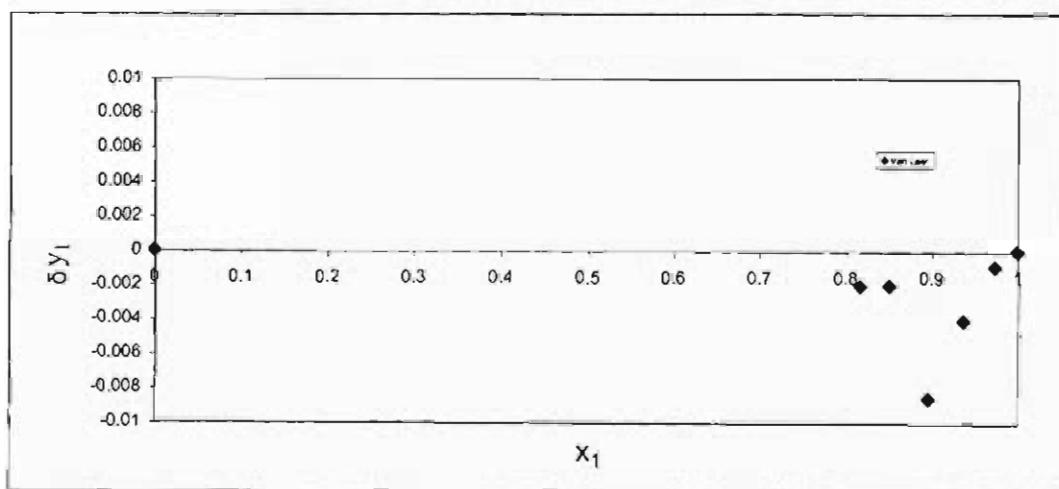


Figure B.69: Point Test for Hexene (1) and 3MCP (2) at 50 °C

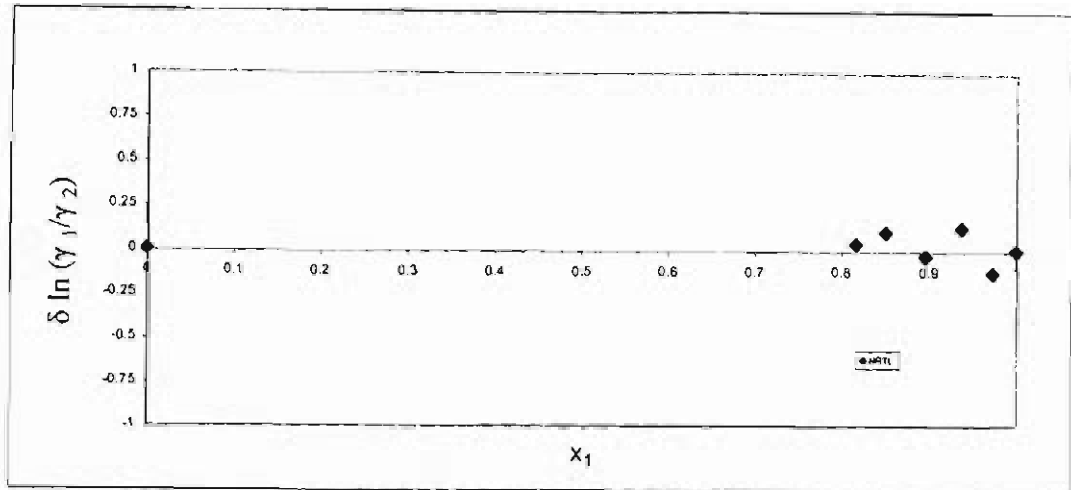


Figure B.70: Point Test for Hexene (1) and 3MCP (2) at 50 °C

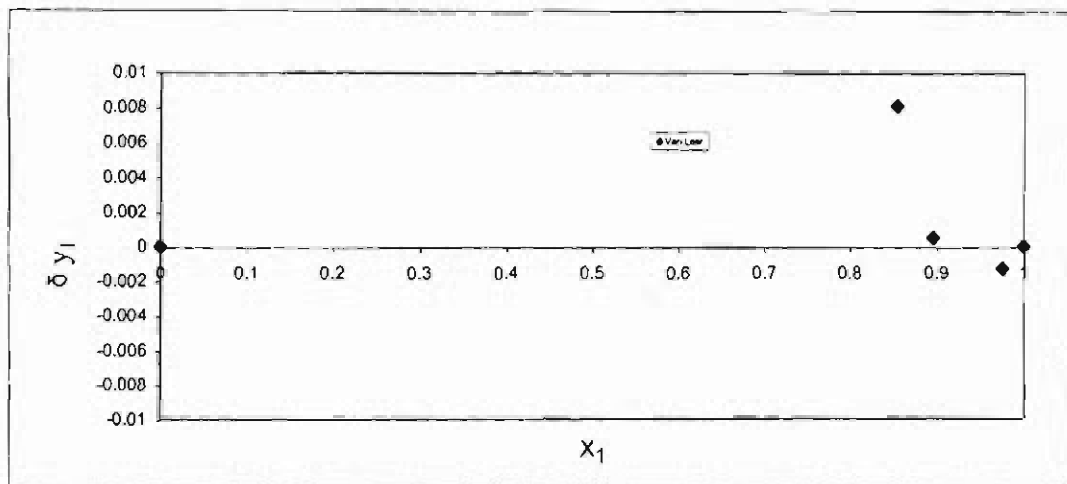


Figure B.71: Point Test for Hexene (1) and 3MCP (2) at 60 °C

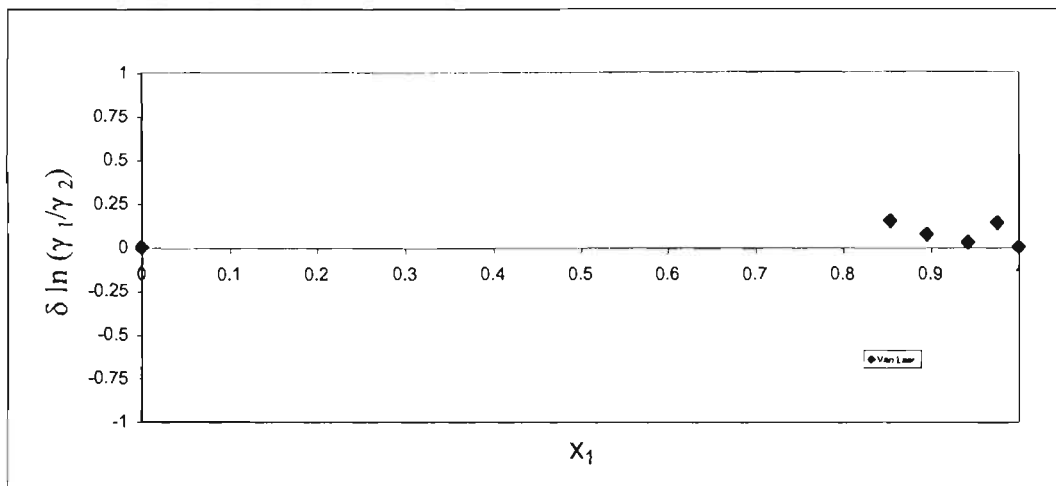


Figure B.72: Direct Test for Hexene (1) and 3MCP (2) at 60 °C

GAS CHROMATOGRAPH CALIBRATIONS

Chapter 3 reviewed the method behind the calibration of the gas chromatograph (GC), with the GC specifications and operating conditions. The plot of A_1/A_2 vs. x_1/x_2 and A_2/A_1 vs. x_2/x_1 the system of cyclohexane + ethanol is provided as an example in Chapter 3, with the calibration of all the systems shown below in Figures C.1 to C.6.

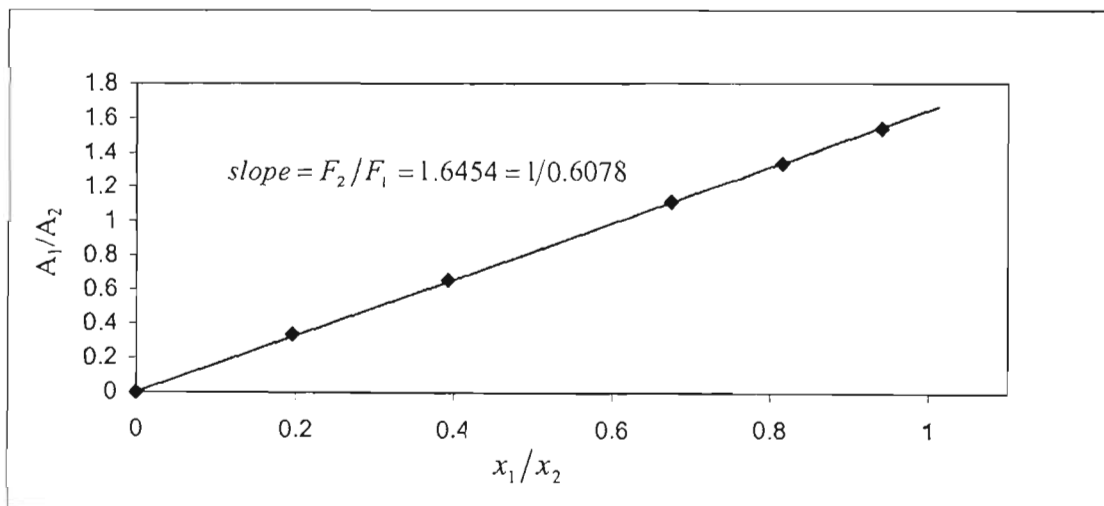


Figure C.1: Plot of A_1/A_2 vs. x_1/x_2 for 1-hexene (1) + NMP (2)

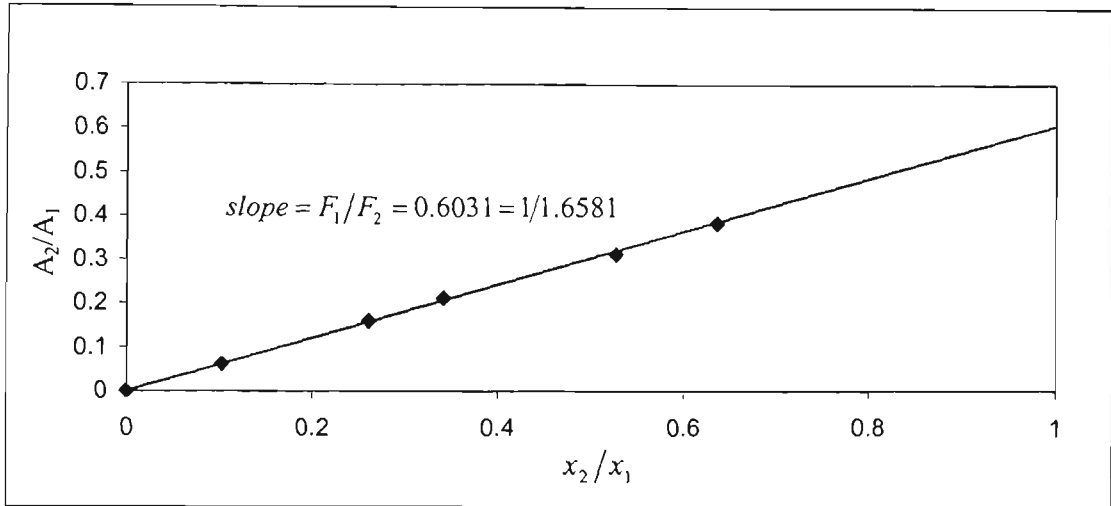


Figure C.2: Plot of A_2/A_1 vs. x_2/x_1 for 1-hexene (1) + NMP (2)

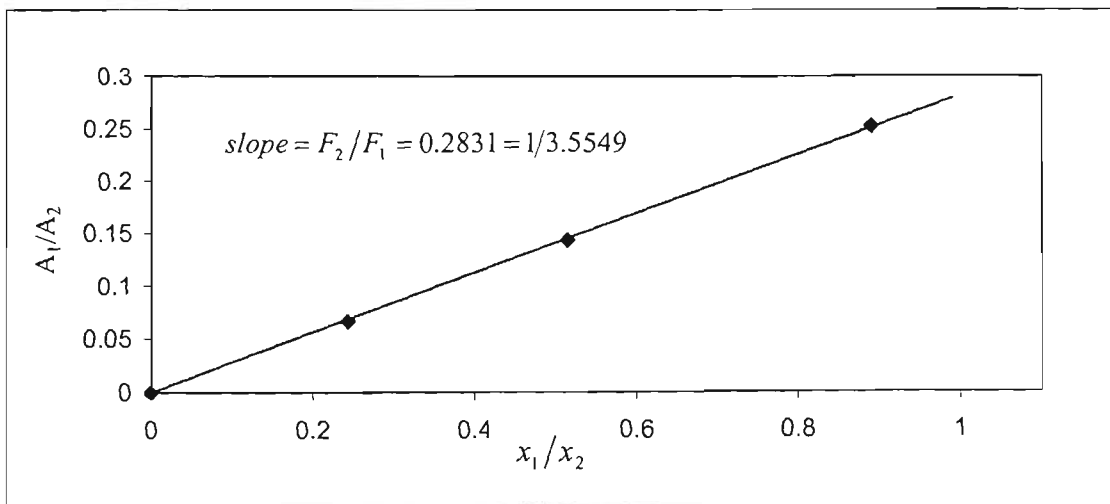


Figure C.3: Plot of A_1/A_2 vs. x_1/x_2 for water (1) + NMP (2)

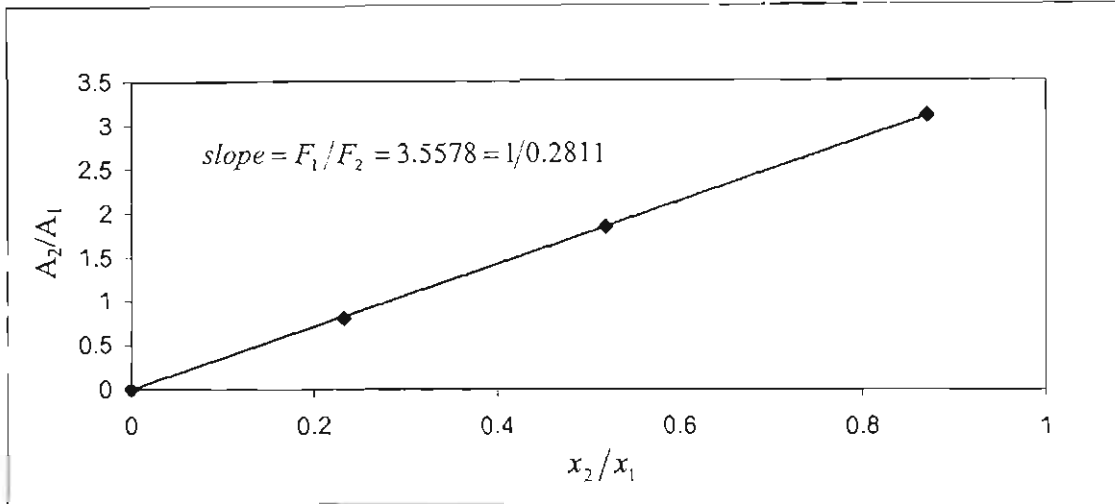


Figure C.4: Plot of A_2/A_1 vs. x_2/x_1 for water (1) + NMP (2)

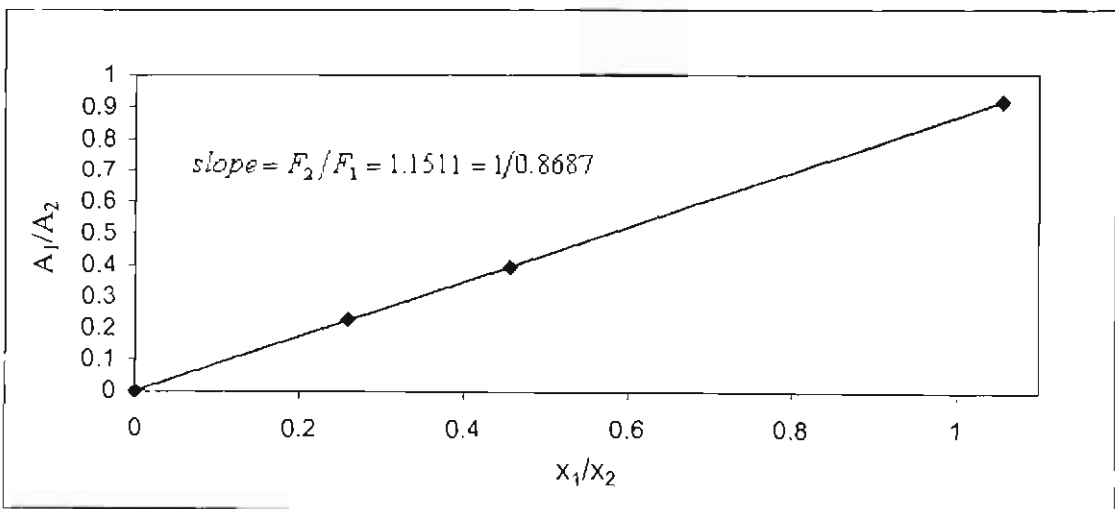


Figure C.5: Plot of A_1/A_2 vs. x_1/x_2 for 1-hexene (1) + 3MCP (2)

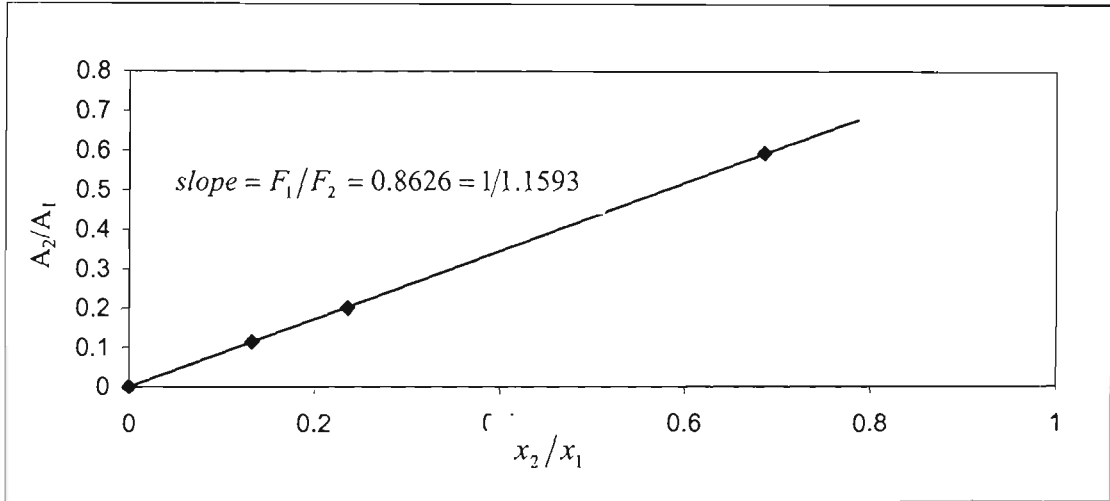


Figure C.6: Plot of A_2/A_1 vs. x_2/x_1 for 1-hexene (1) + 3MCP (2)

TEMPERATURE DEPENDENCE OF MODELLED PARAMETERS

The following graphs plot the modeled parameters against the measured temperatures for the direct method: Wong-Sandler-SRK, Wong-Sandler-PRSV, Twu-Coon-SRK and Twu-Coon-PRSV. The activity coefficient models are represented in the order of Van Laar, Uniquac, Wilson and NRTL. Due to the wide range of values, some figures have been split into two parts e.g. the NRTL model has been split into Figure a showing parameters ' $g_{12}-g_{11}$ ' and ' $g_{12}-g_{22}$ ', with Figure b showing parameter ' α '.

D.1 Temperature Dependence of Thermodynamic Modelled Parameters- Direct Method i.e. Wong-Sandler-SRK

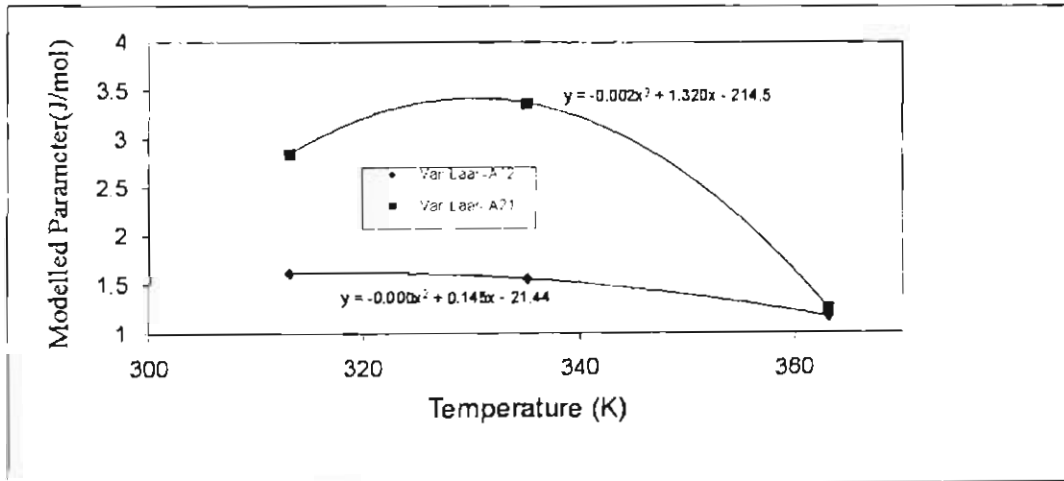


Figure D.1: Plot of T vs. Van Laar modelled parameters for system 1-hexene (1) + NMP (2)

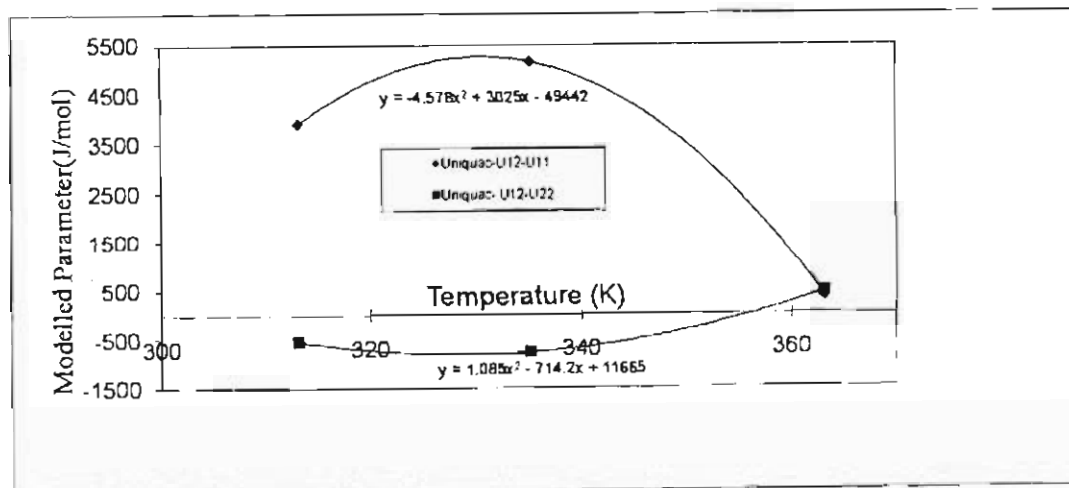


Figure D.2: Plot of T vs. Uniquac modelled parameters for system 1-hexene (1) + NMP (2)

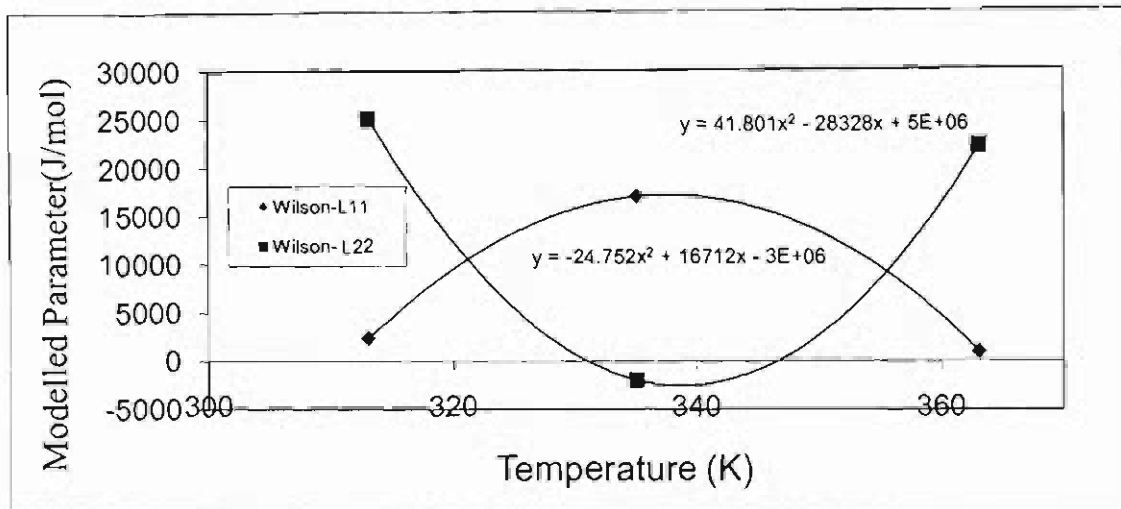


Figure D.3: Plot of T vs. Wilson modelled parameters for system 1-hexene (1) + NMP (2)

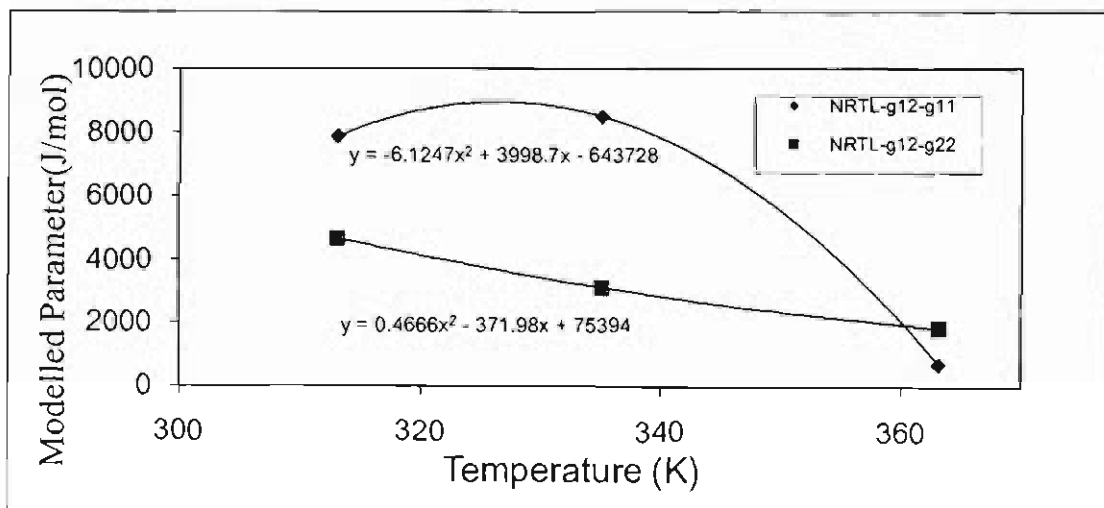


Figure D.4a: Plot of T vs. NRTL modelled parameters for system 1-hexene (1) + NMP (2)

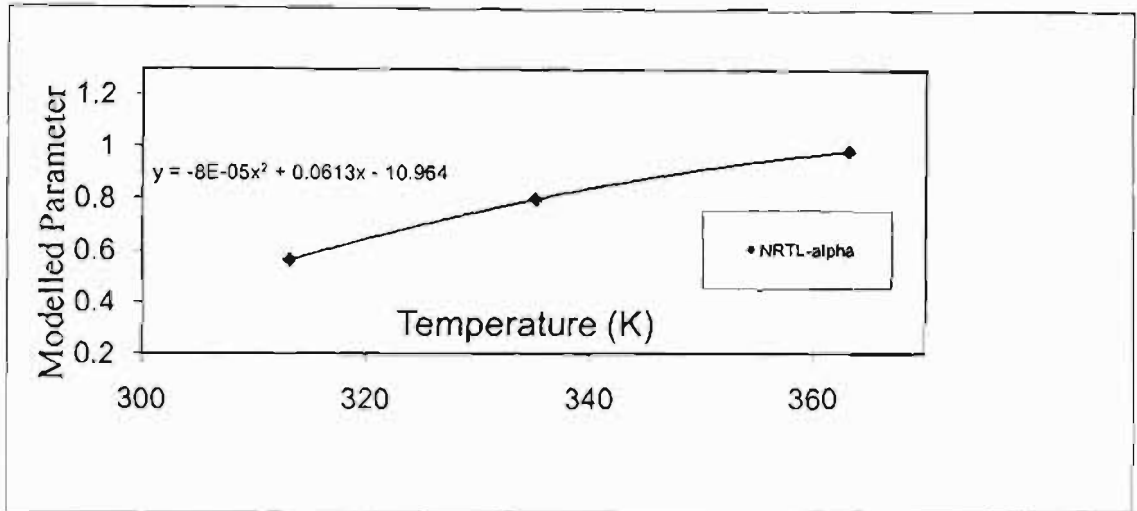


Figure D.4b: Plot of T vs. NRTL modelled parameters for system 1-hexene (1) + NMP (2)

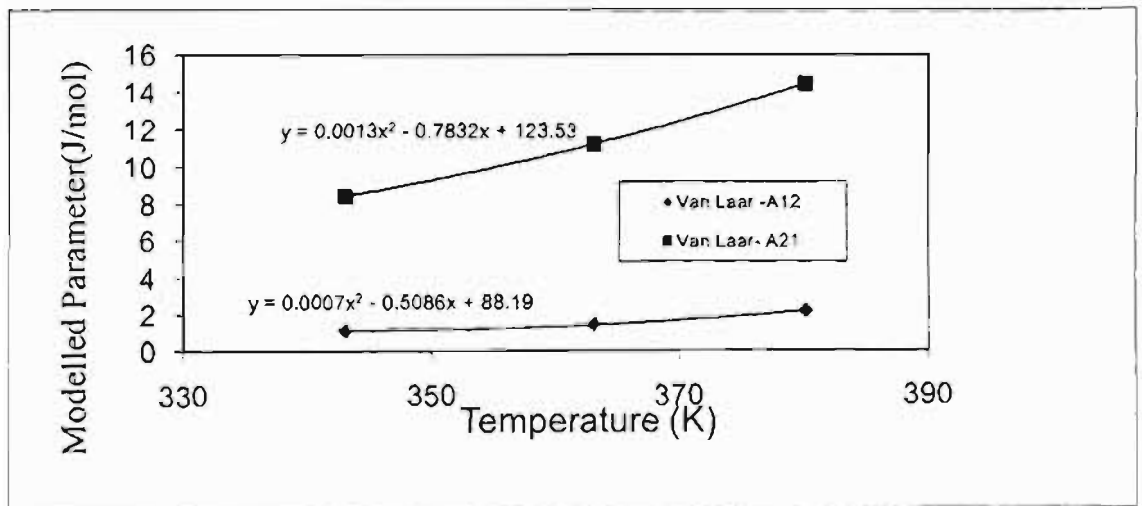


Figure D.5: Plot of T vs. Van Laar modelled parameters for system water (1) + NMP (2)

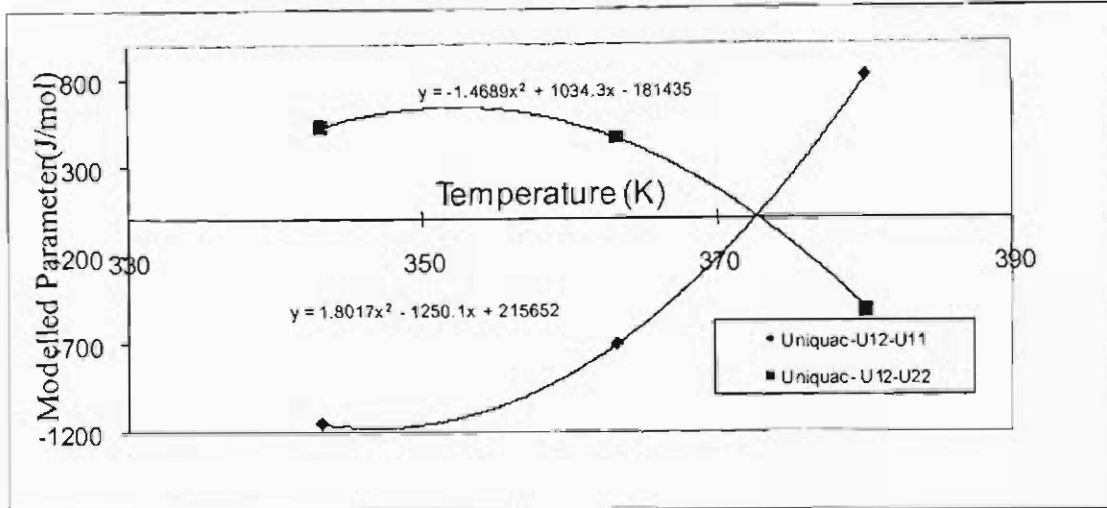


Figure D.6: Plot of T vs. Uniquac modelled parameters for system water (1) + NMP (2)

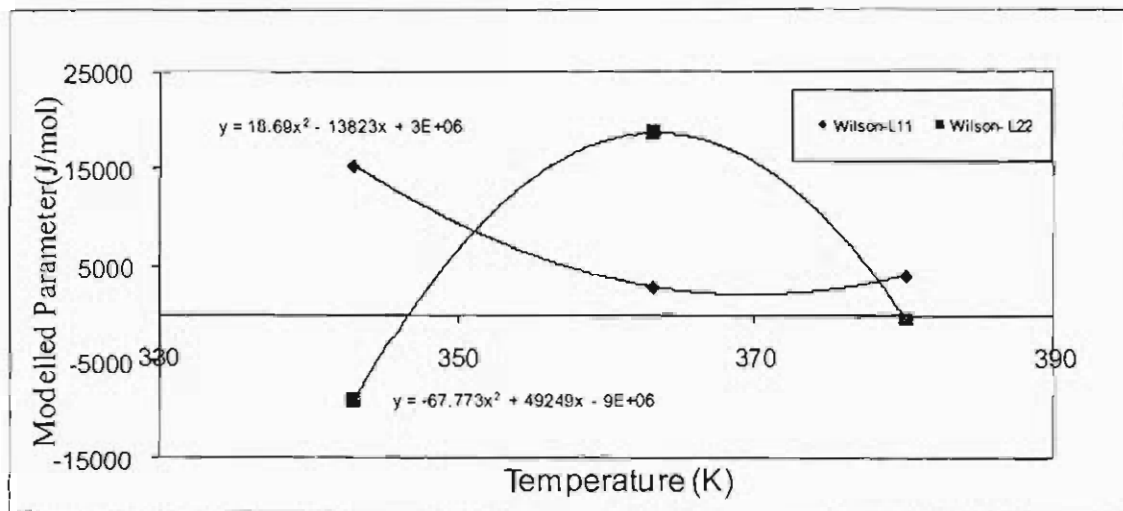


Figure D.7: Plot of T vs. Wilson modelled parameters for system water (1) + NMP (2)

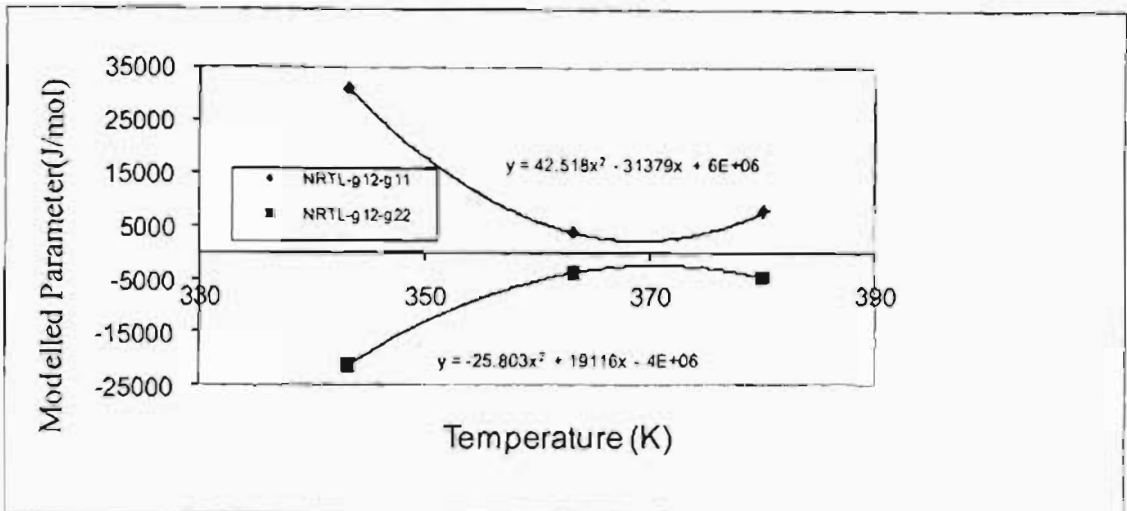


Figure D.8a: Plot of T vs. NRTL modelled parameters for system water (1) + NMP (2)

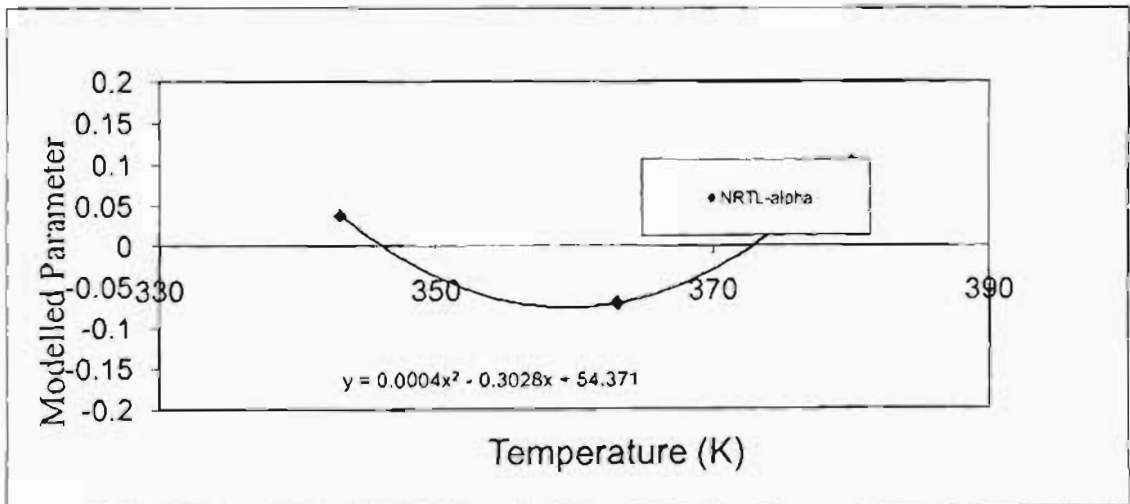


Figure D.8b: Plot of T vs. NRTL modelled parameters for system water (1) + NMP (2)

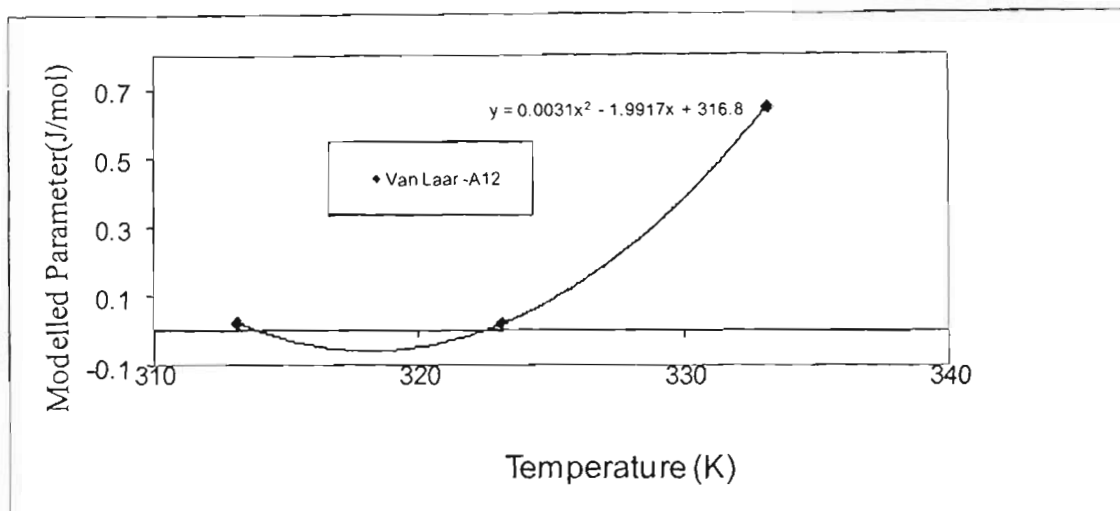


Figure D.9a: Plot of T vs. Van Laar modelled parameters for system 1-hexene (1) + 3MCP (2)

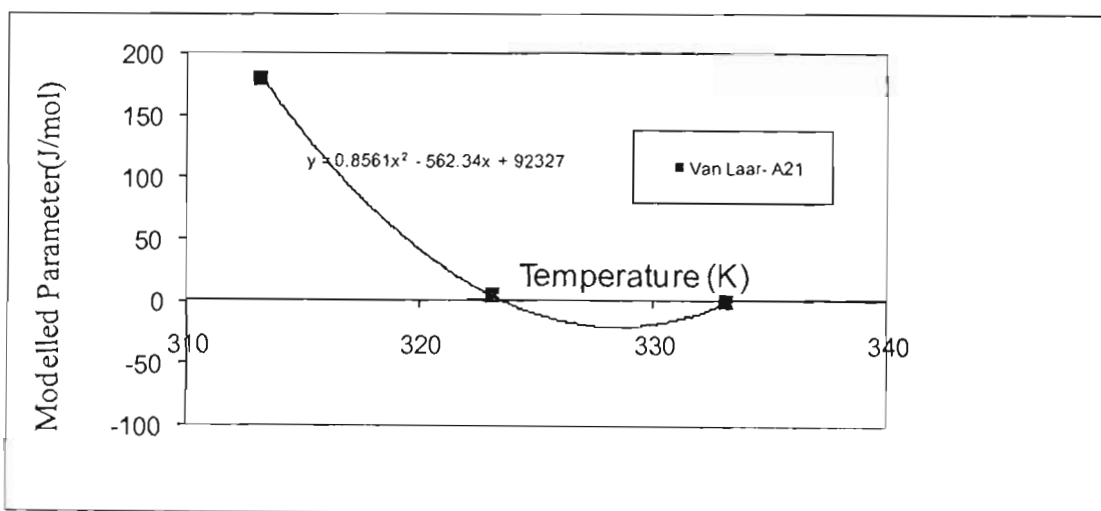


Figure D.9b: Plot of T vs. Van Laar modelled parameters for system 1-hexene (1) + 3MCP (2)

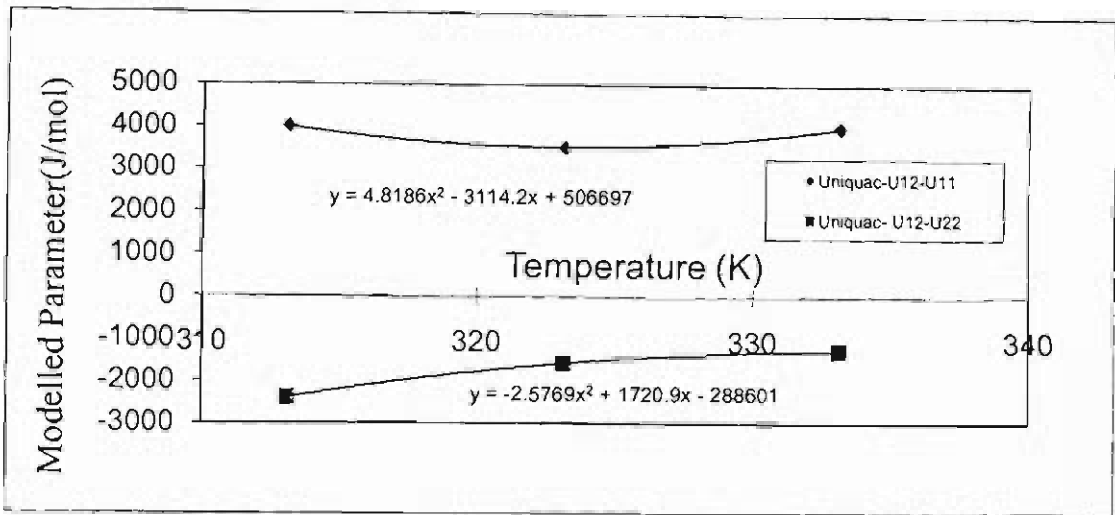


Figure D.10: Plot of T vs. Uniquac modelled parameters for system 1-hexene (1) + 3MCP (2)

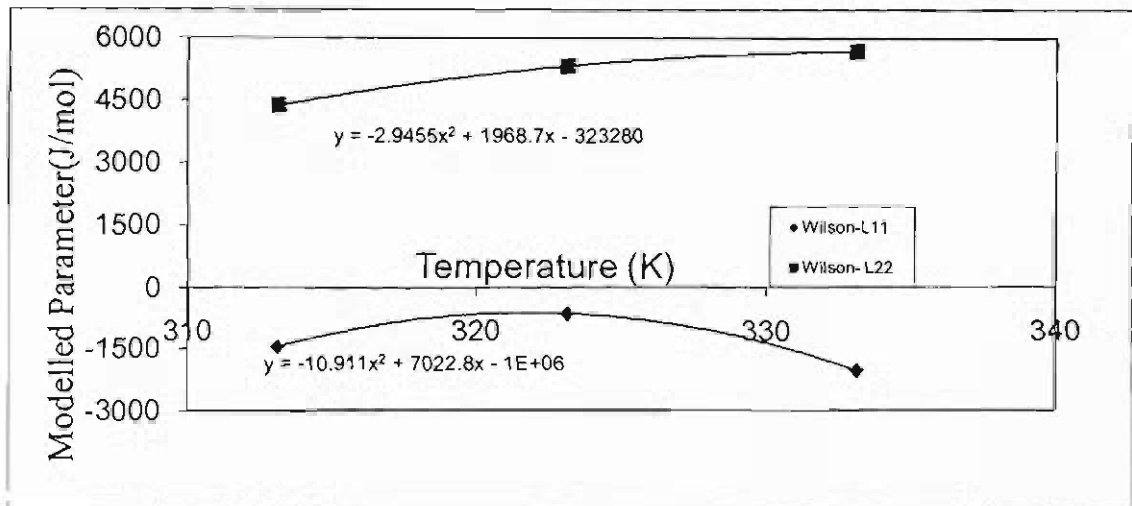


Figure D.11: Plot of T vs. Wilson modelled parameters for system 1-hexene (1) + 3MCP (2)

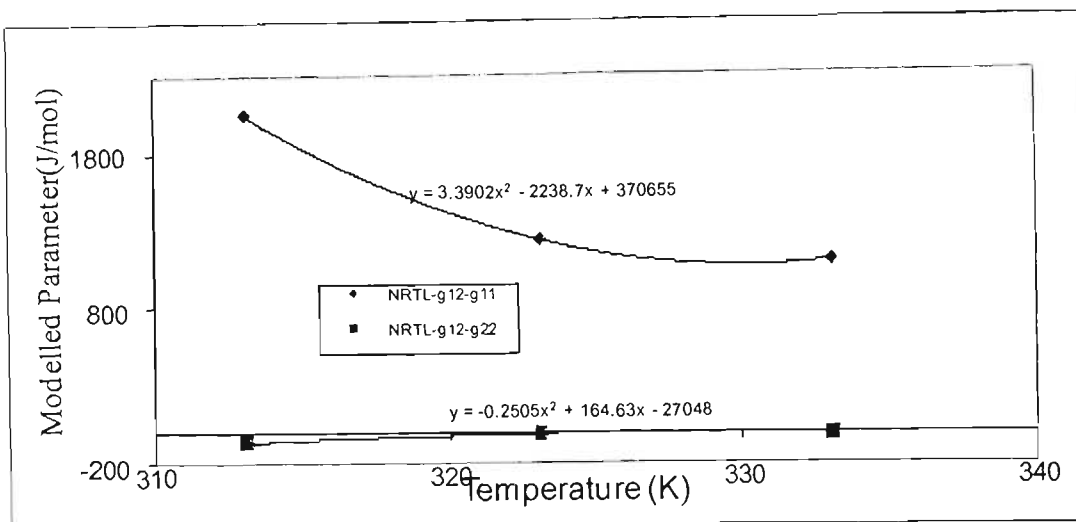


Figure D.12a: Plot of T vs. NRTL modelled parameters for system 1-hexene (1) + 3MCP (2)

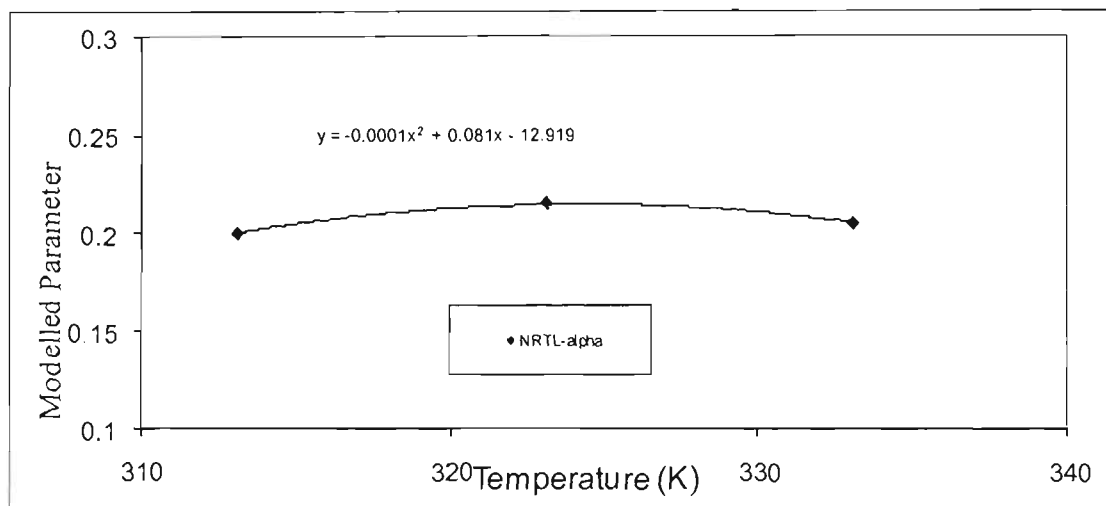


Figure D.12b: Plot of T vs. NRTL modelled parameters for system 1-hexene (1) + 3MCP (2)

D.2 Temperature Dependence of Thermodynamic Modelled Parameters- Direct Method i.e. Wong-Sandler-PRSV

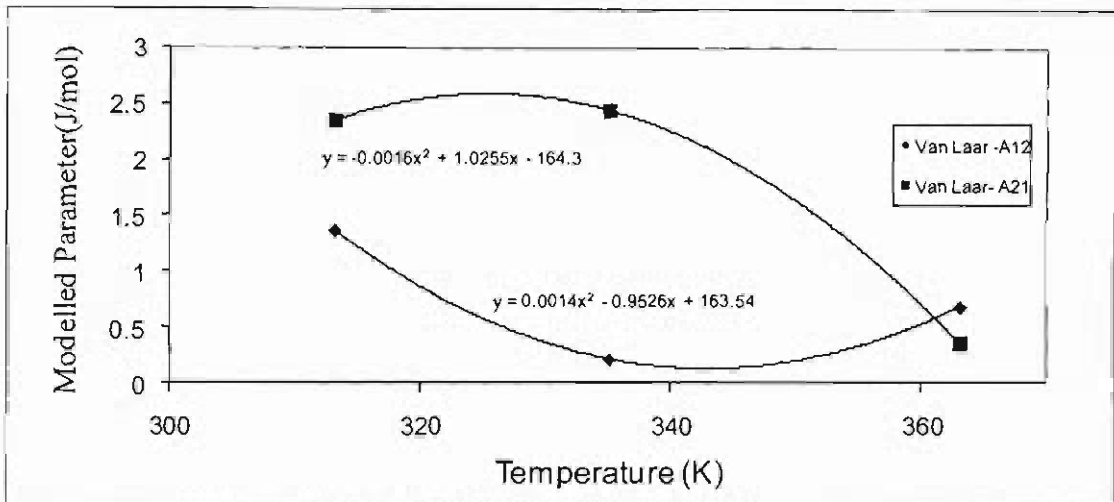


Figure D.13: Plot of T vs. Van Laar modelled parameters for system 1-hexene (1) + NMP (2)

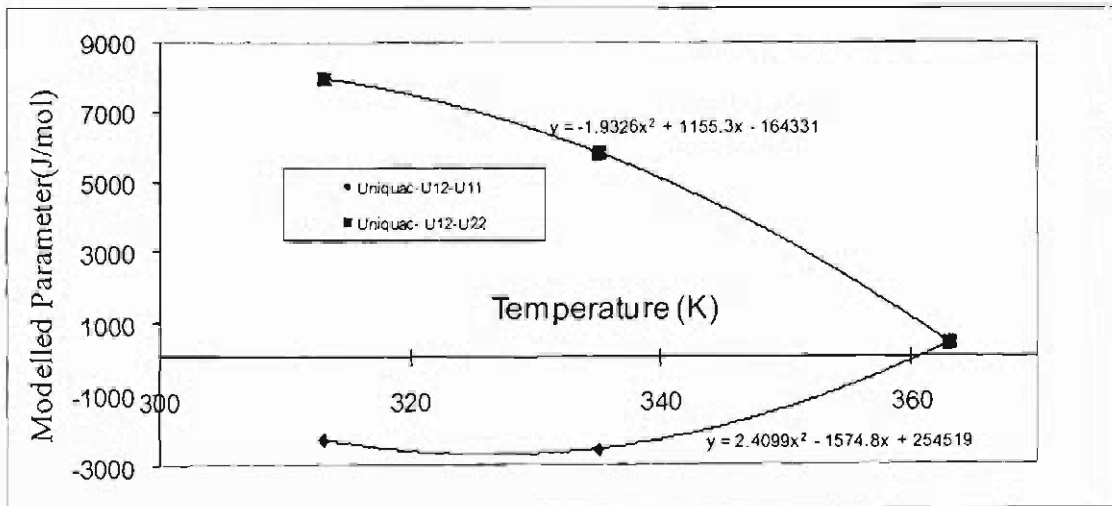


Figure D.14: Plot of T vs. Uniquac modelled parameters for system 1-hexene (1) + NMP (2)

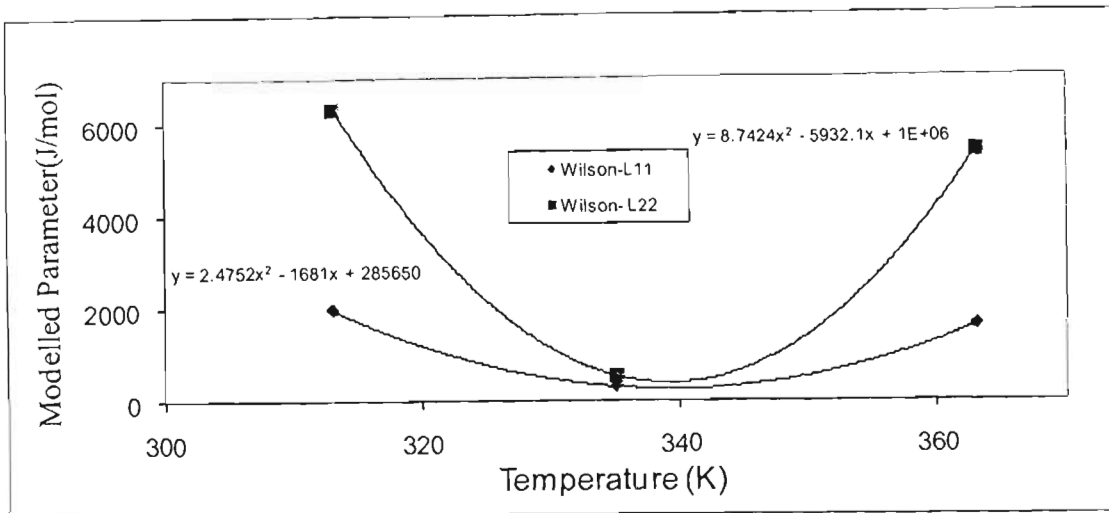


Figure D.15: Plot of T vs. Wilson modelled parameters for system 1-hexene (1) + NMP (2)

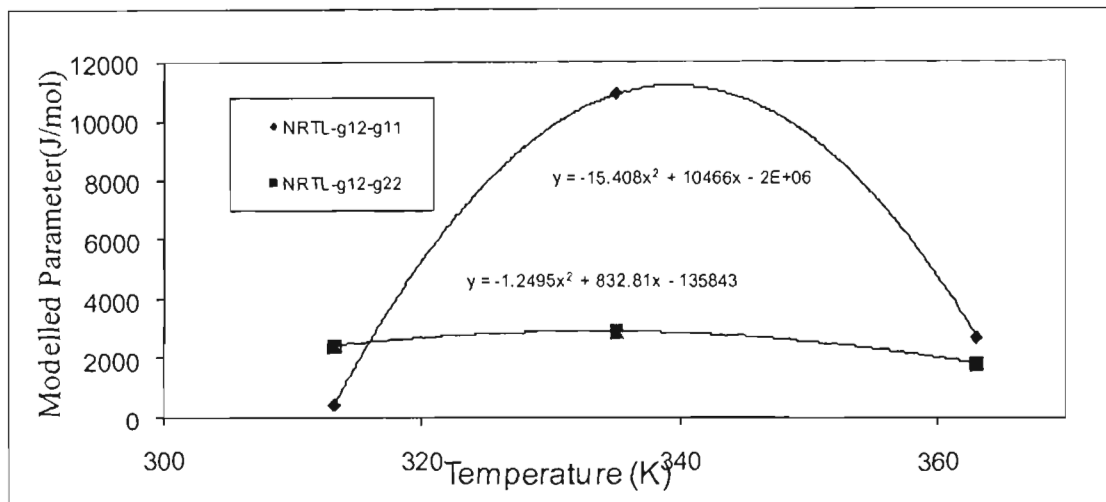


Figure D.16a: Plot of T vs. NRTL modelled parameters for system 1-hexene (1) + NMP (2)

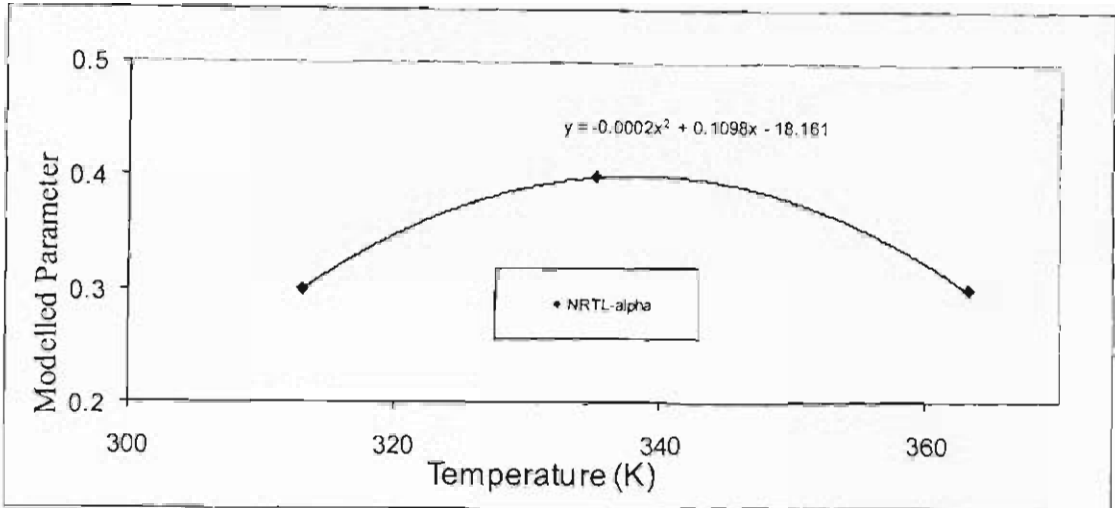


Figure D.16b: Plot of T vs. NRTL modelled parameters for system 1-hexene (1) + NMP (2)

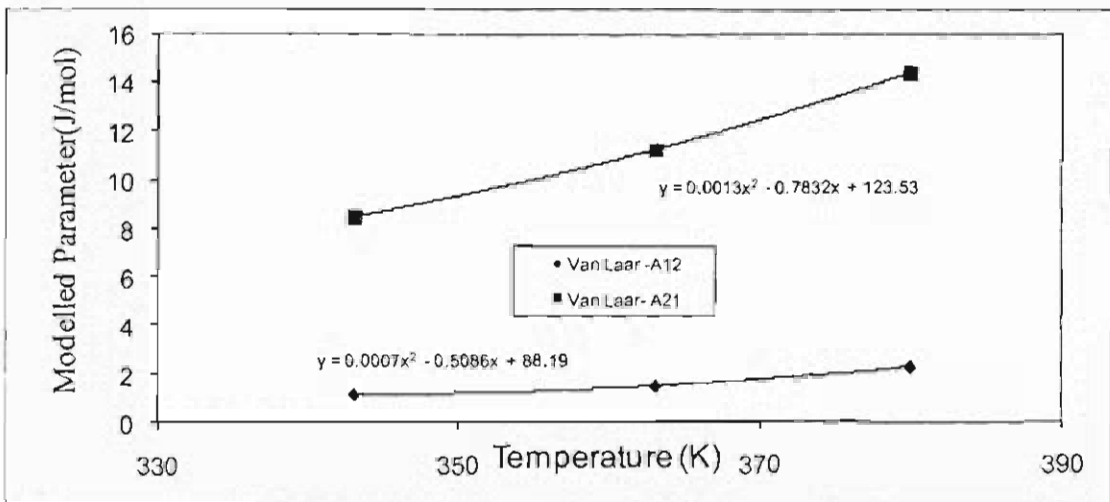


Figure D.17: Plot of T vs. Van Laar modelled parameters for system water (1) + NMP (2)

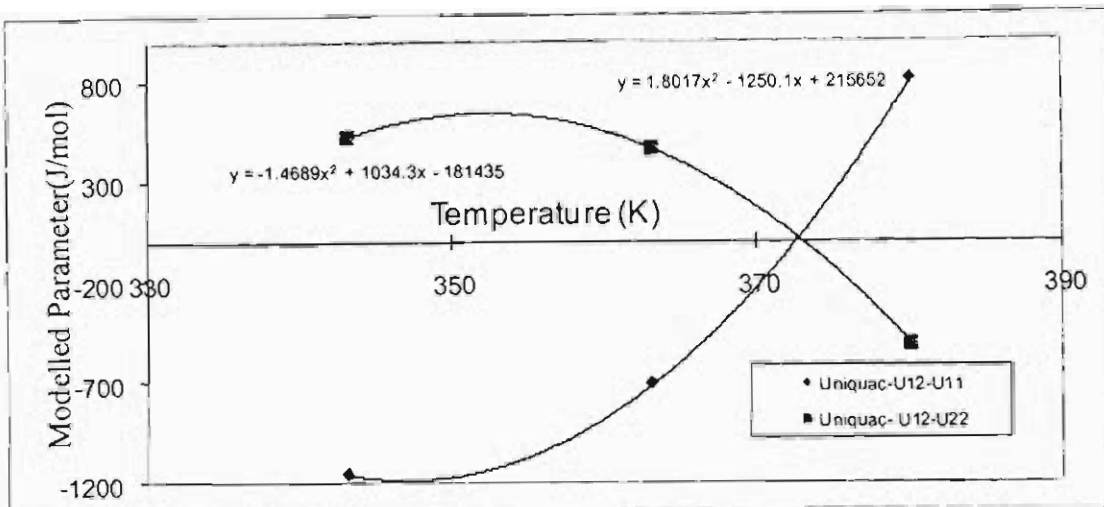


Figure D.18: Plot of T vs. Uniquac modelled parameters for system water (1) + NMP (2)

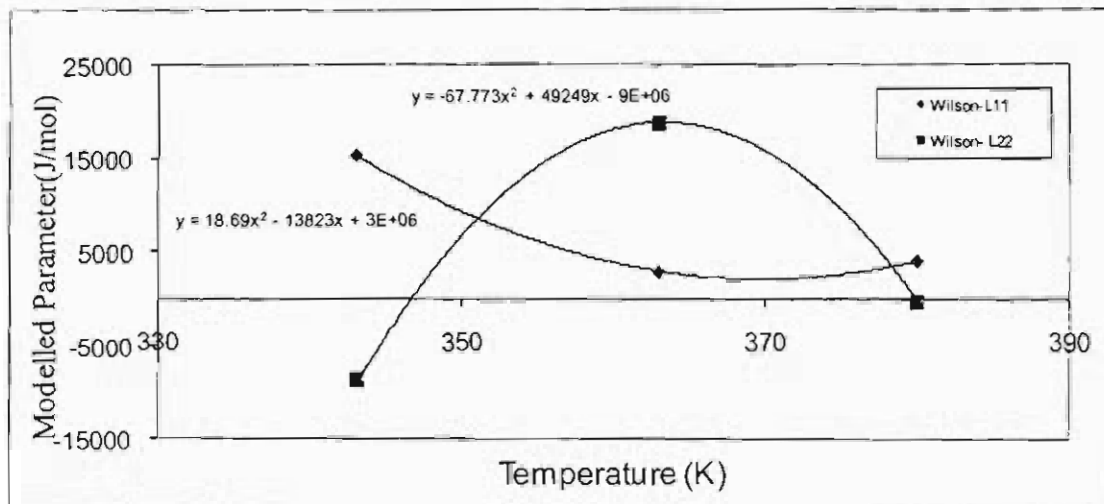


Figure D.19: Plot of T vs. Wilson modelled parameters for system water (1) + NMP (2)

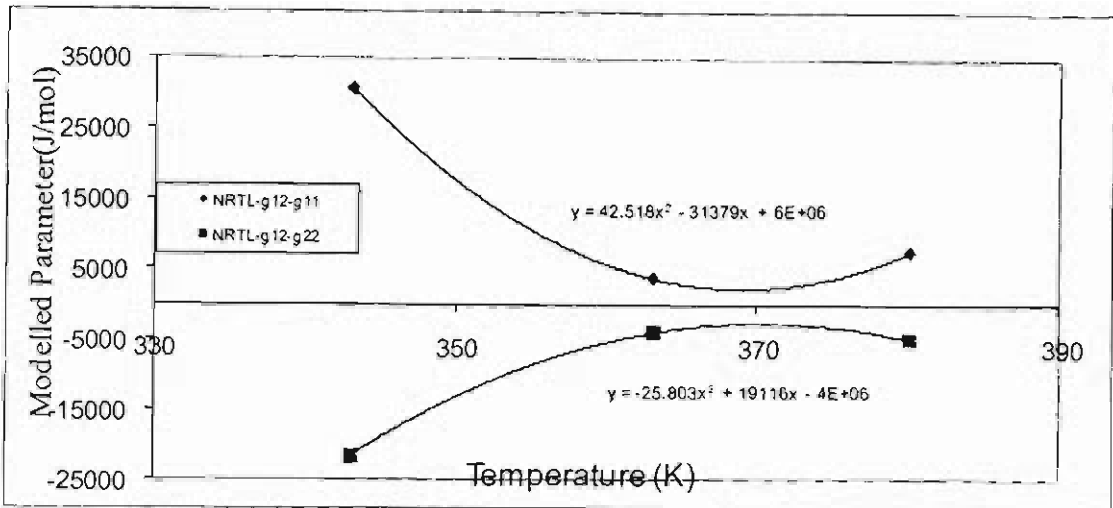


Figure D.20a: Plot of T vs. NRTL modelled parameters for system water (1) + NMP (2)

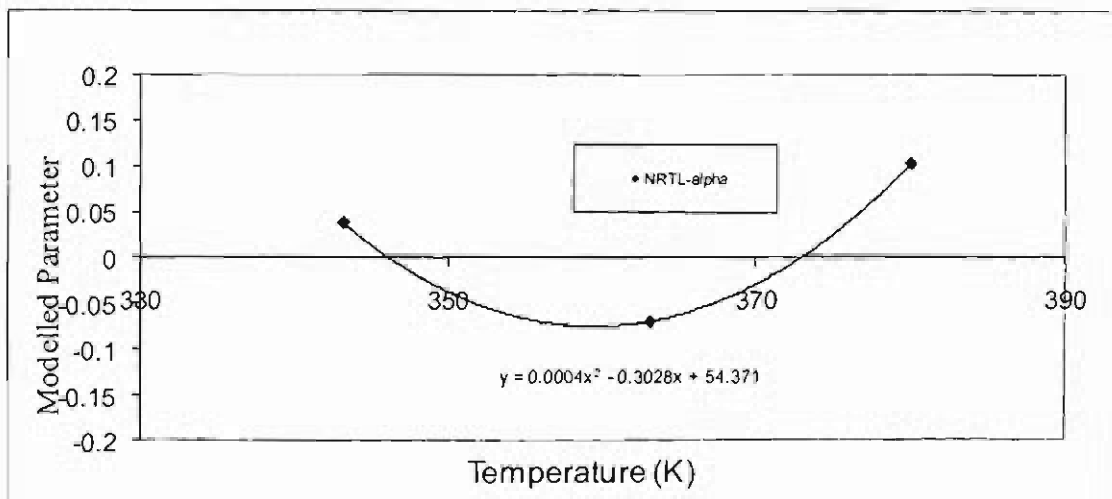


Figure D.20b: Plot of T vs. NRTL modelled parameters for system water (1) + NMP (2)

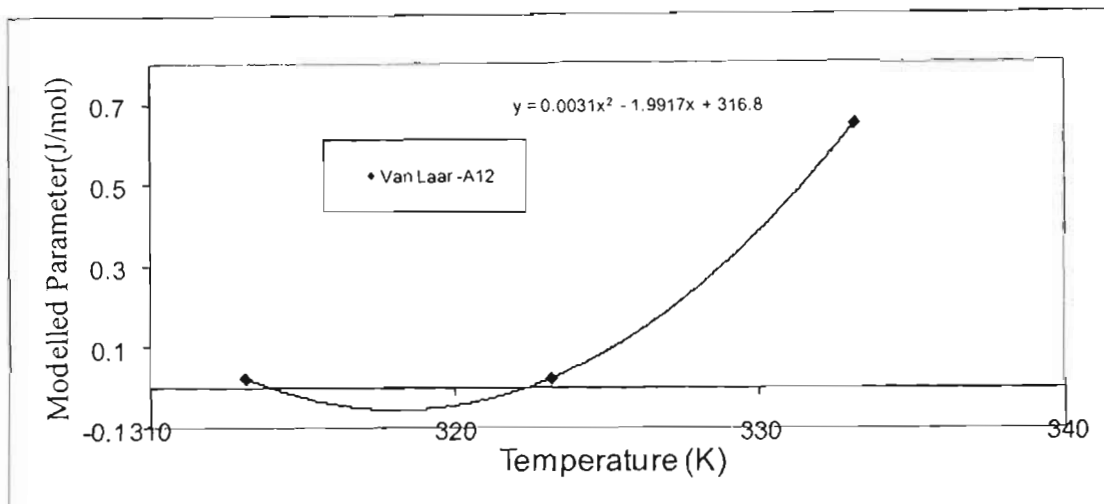


Figure D.21a: Plot of T vs. Van Laar modelled parameters for system 1-hexene (1) + 3MCP (2)

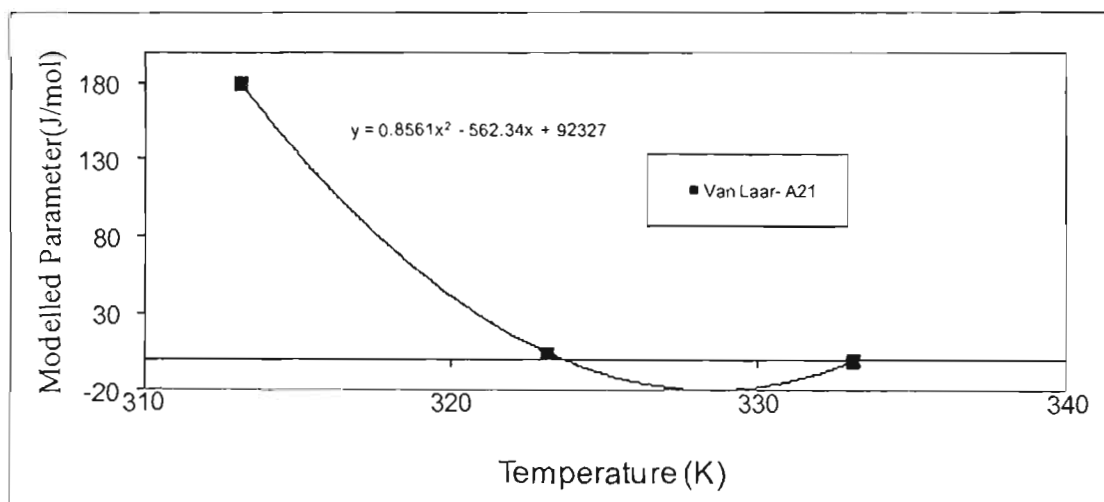


Figure D.21b: Plot of T vs. Van Laar modelled parameters for system 1-hexene (1) + 3MCP (2)

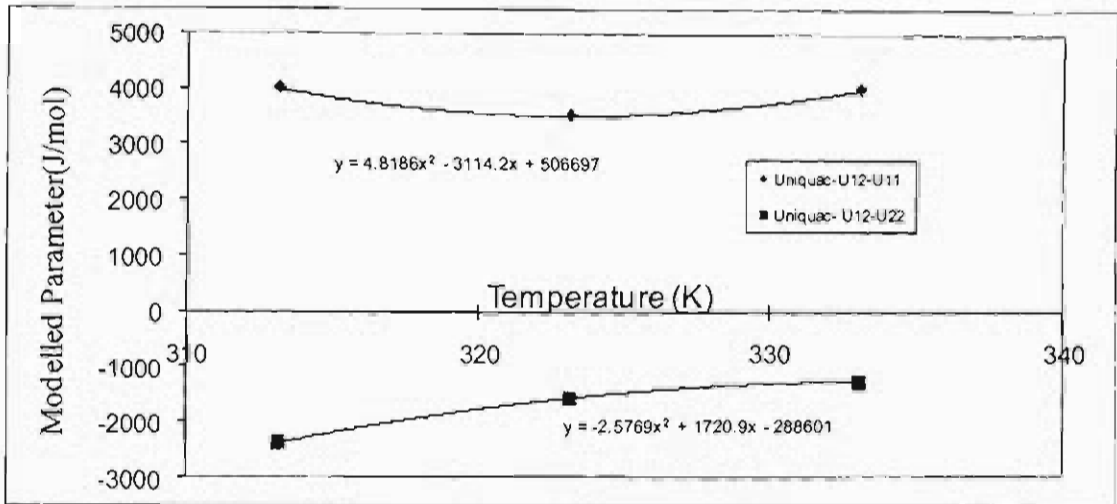


Figure D.22: Plot of T vs. Uniquac modelled parameters for system 1-hexene (1) + 3MCP (2)

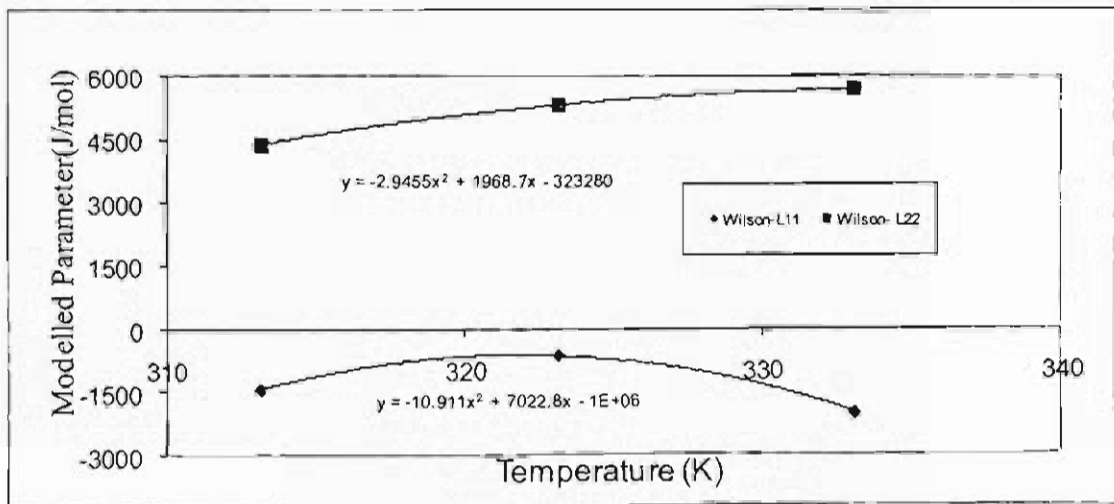


Figure D.23: Plot of T vs. Wilson modelled parameters for system 1-hexene (1) + 3MCP (2)

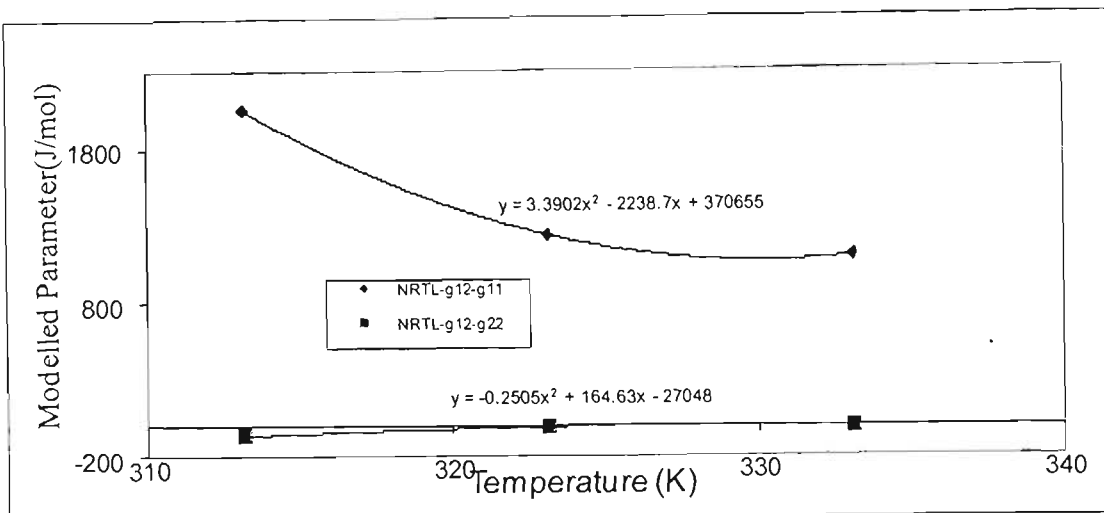


Figure D.24a: Plot of T vs. NRTL modelled parameters for system 1-hexene (1) + 3MCP (2)

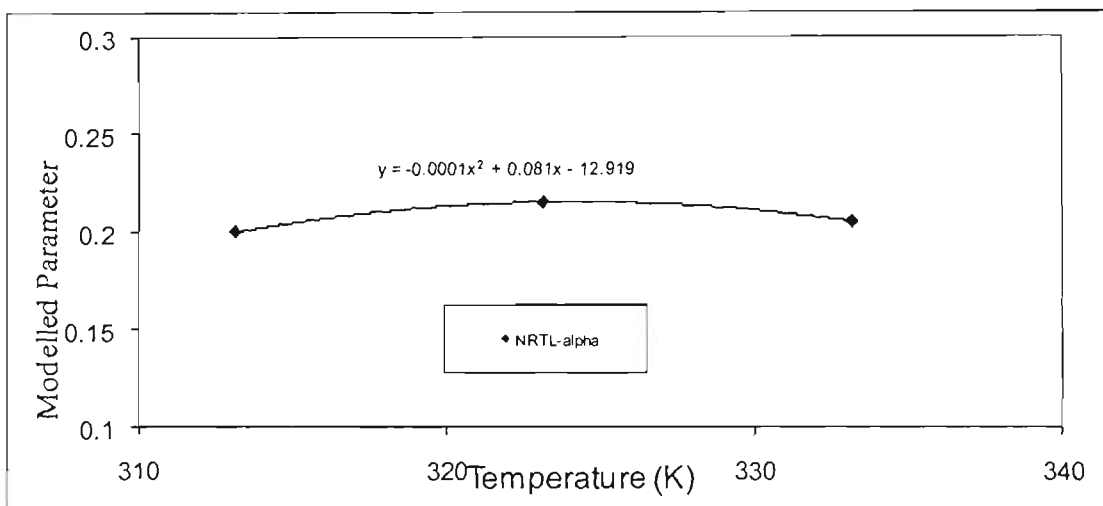


Figure D.24b: Plot of T vs. NRTL modelled parameters for system 1-hexene (1) + 3MCP (2)

D.3 Temperature Dependence of Thermodynamic Modelled Parameters- Direct Method i.e. Twu-Coon-SRK

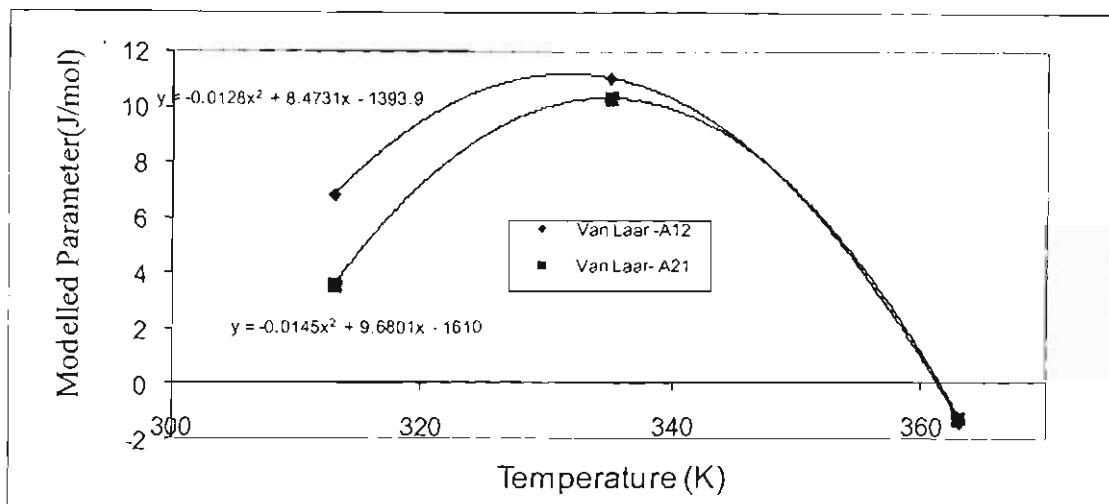


Figure D.25: Plot of T vs. Van Laar modelled parameters for system 1-hexene (1) + NMP (2)

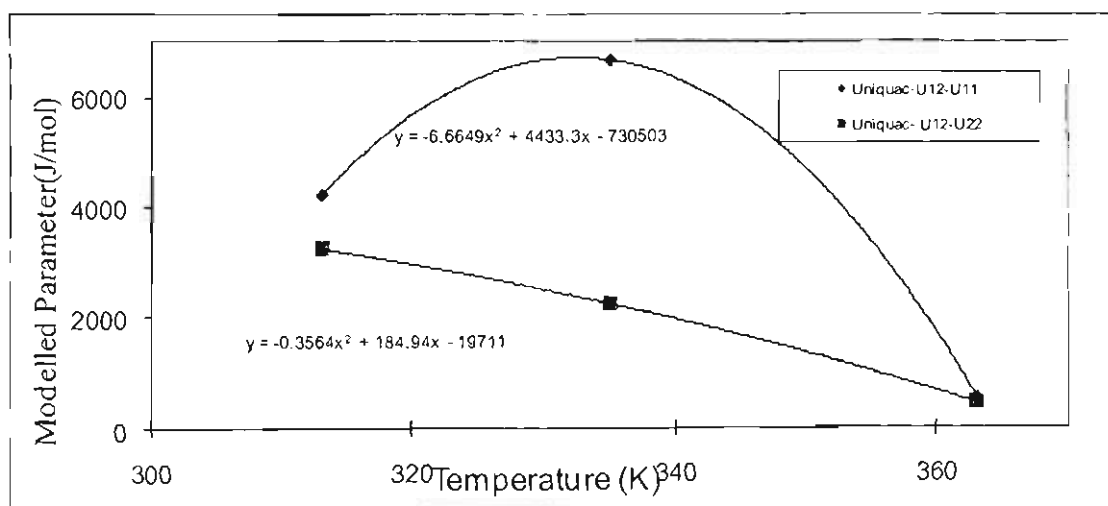


Figure D.26: Plot of T vs. Uniquac modelled parameters for system 1-hexene (1) + NMP (2)

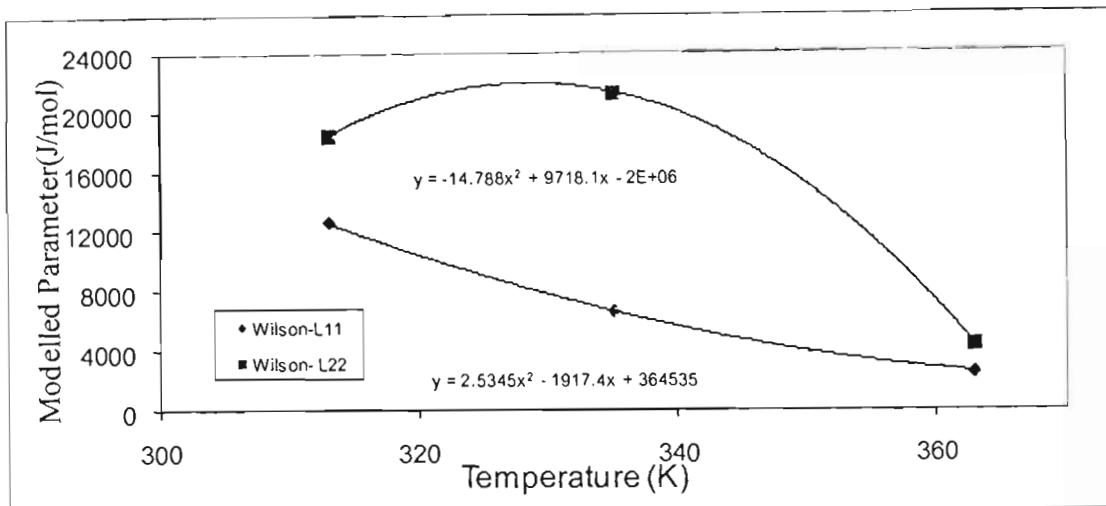


Figure D.27: Plot of T vs. Wilson modelled parameters for system 1-hexene (1) + NMP (2)

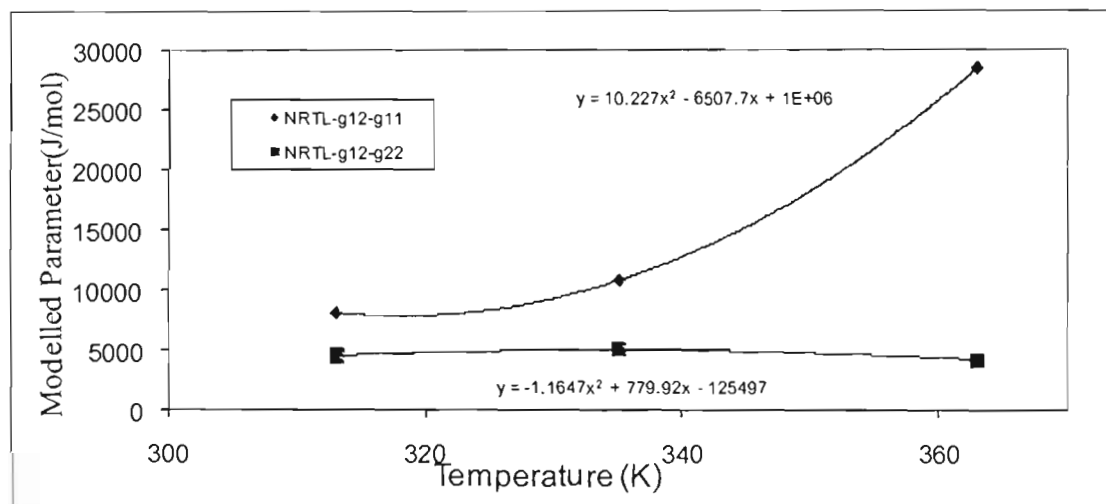


Figure D.28a: Plot of T vs. NRTL modelled parameters for system 1-hexene (1) + NMP (2)

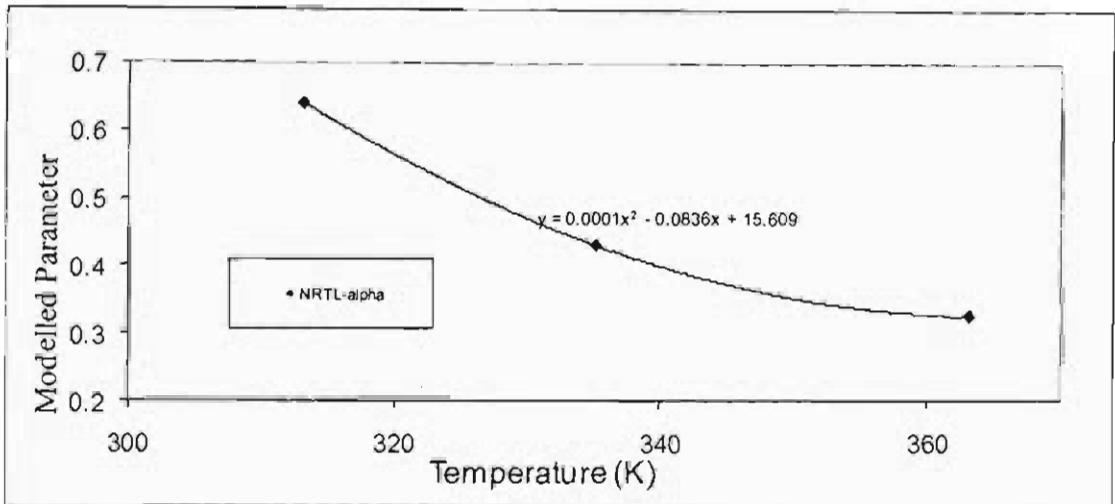


Figure D.28b: Plot of T vs. NRTL modelled parameters for system 1-hexene (1) + NMP (2)

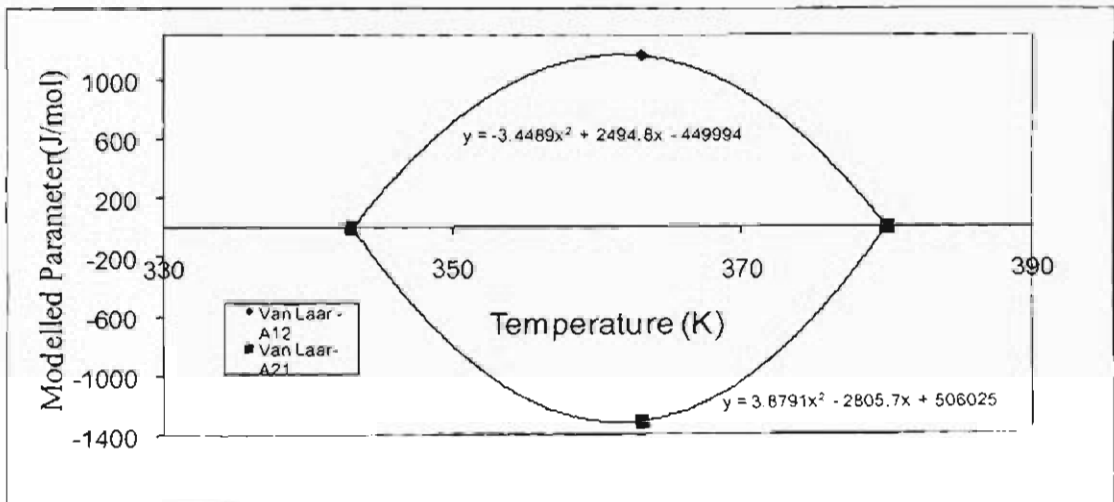


Figure D.29: Plot of T vs. Van Laar modelled parameters for system water (1) + NMP (2)

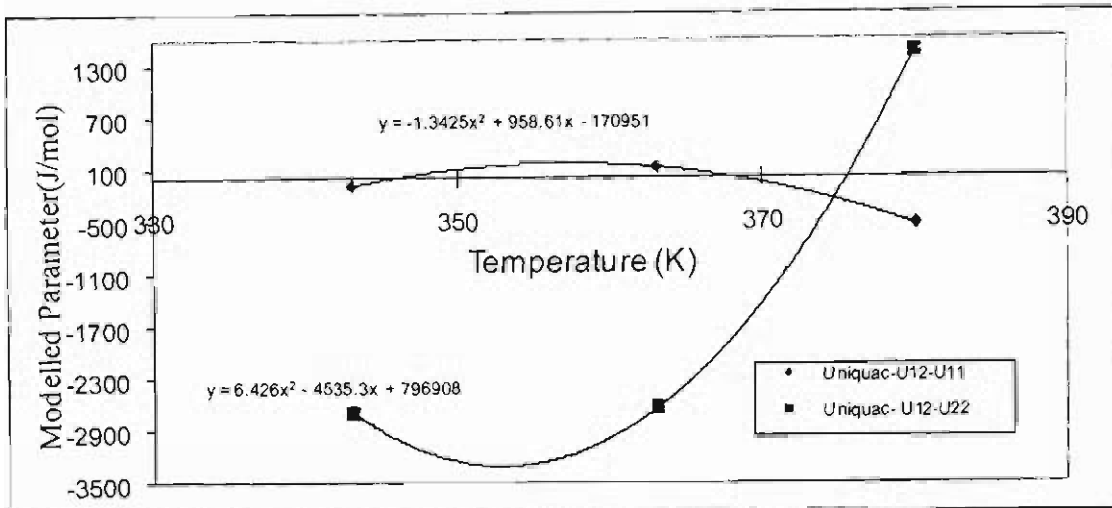


Figure D.30: Plot of T vs. Uniquac modelled parameters for system water (1) + NMP (2)

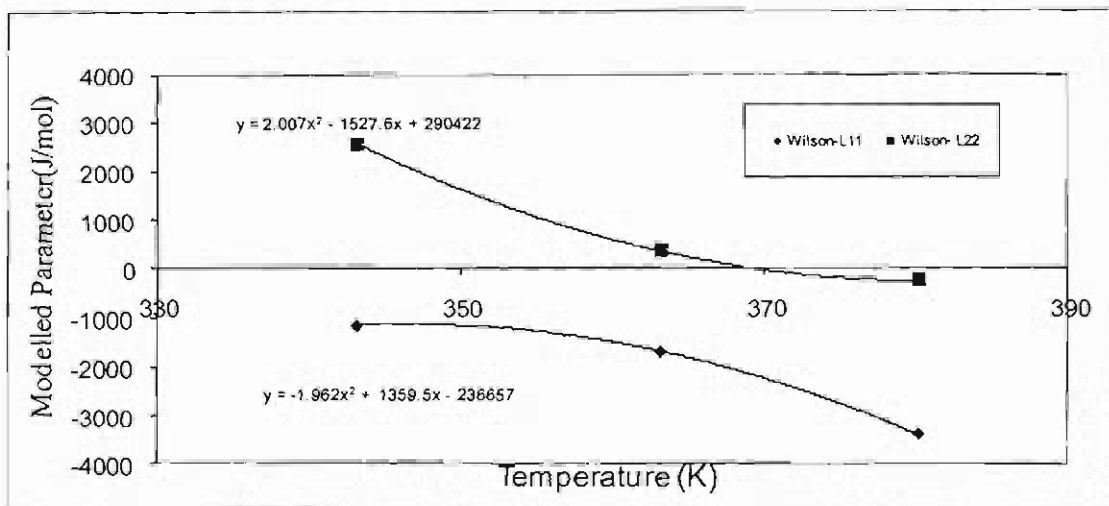


Figure D.31: Plot of T vs. Wilson modelled parameters for system water (1) + NMP (2)

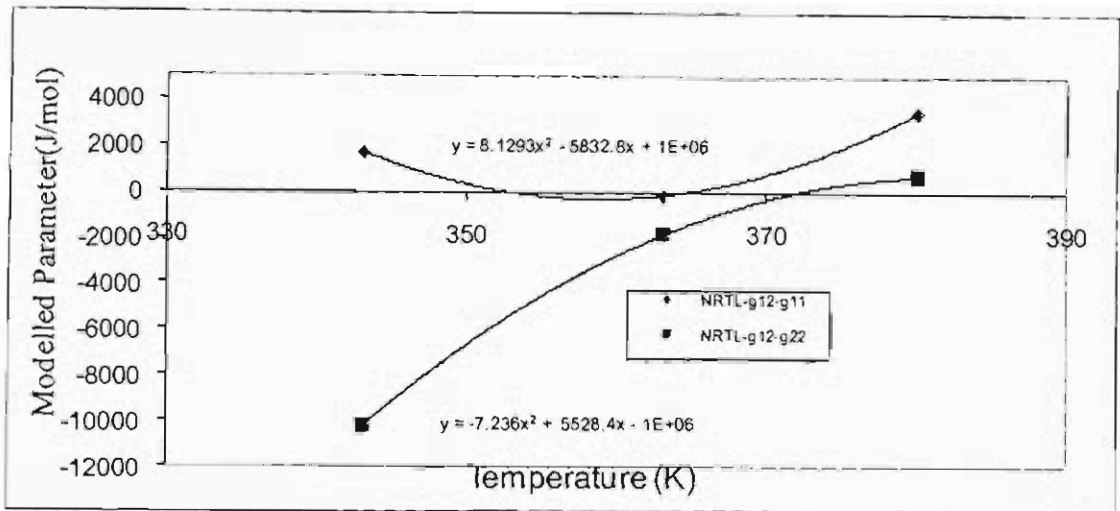


Figure D.32a: Plot of T vs. NRTL modelled parameters for system water (1) + NMP (2)

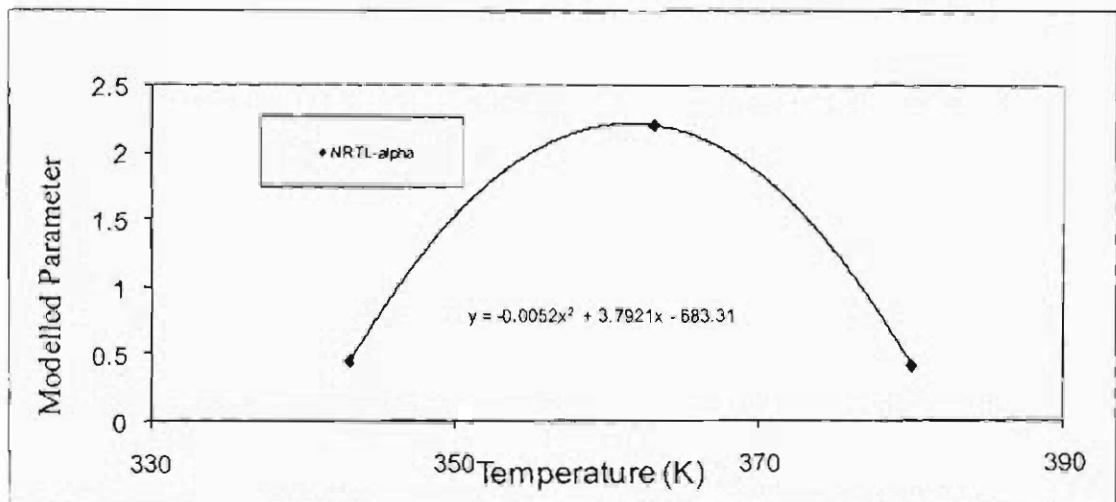


Figure D.32b: Plot of T vs. NRTL modelled parameters for system water (1) + NMP (2)

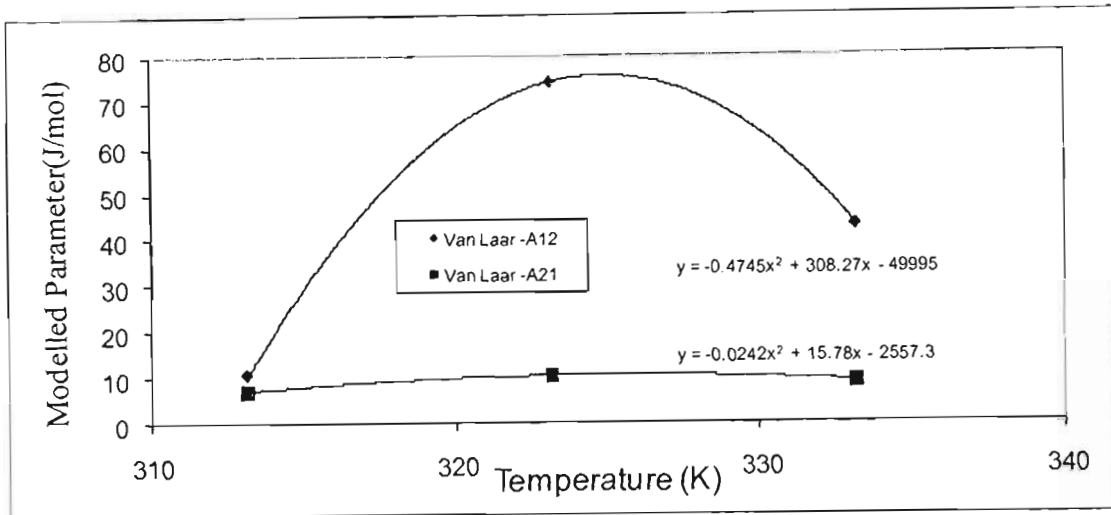


Figure D.33: Plot of T vs. Van Laar modelled parameters for system 1-hexene (1) + 3MCP (2)

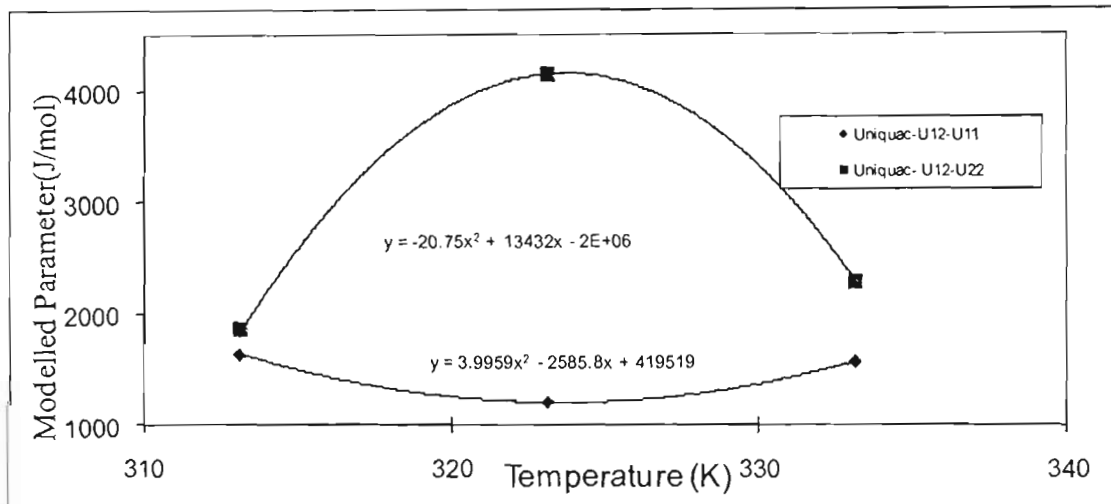


Figure D.34: Plot of T vs. Uniquac modelled parameters for system 1-hexene (1) + 3MCP (2)

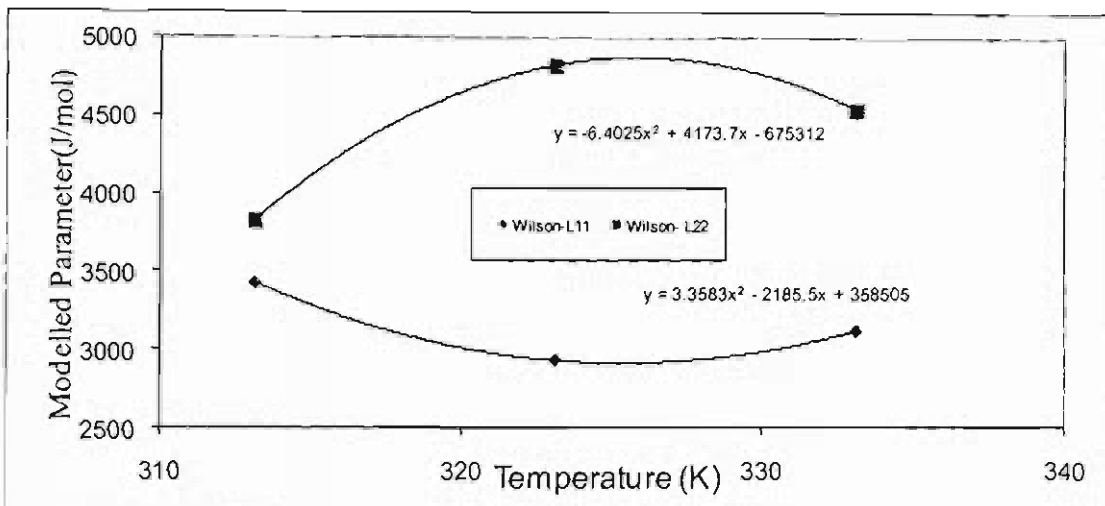


Figure D.35: Plot of T vs. Wilson modelled parameters for system 1-hexene (1) + 3MCP (2)

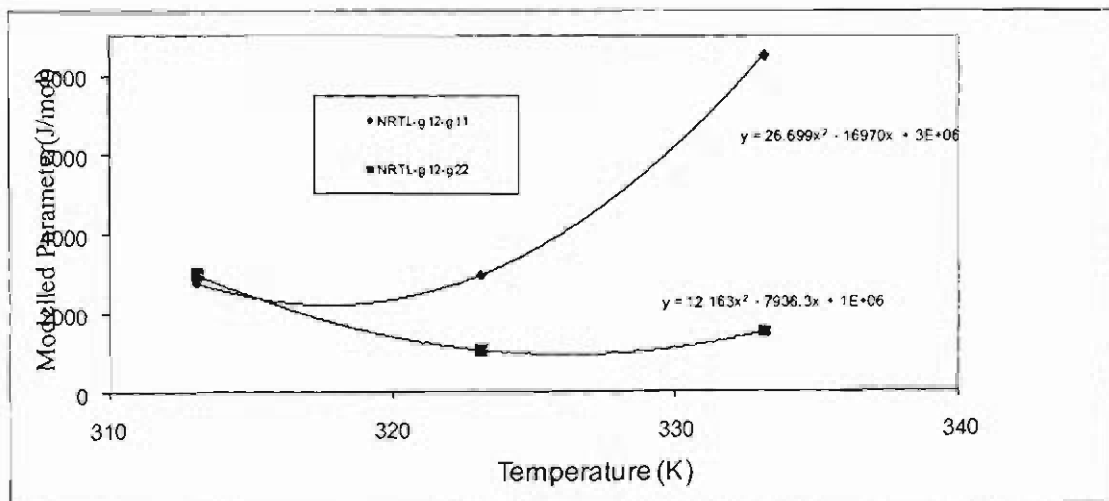


Figure D.36a: Plot of T vs. NRTL modelled parameters for system 1-hexene (1) + 3MCP (2)

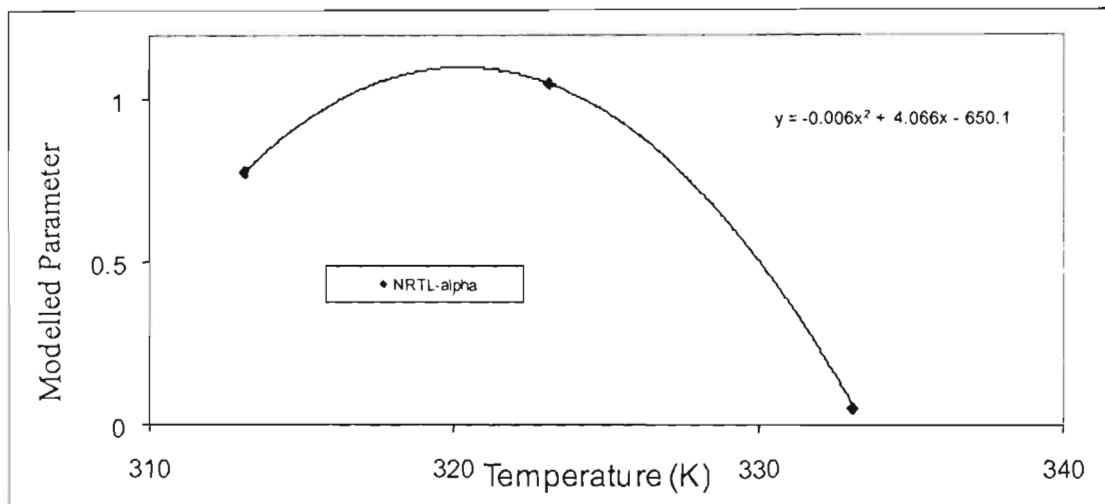


Figure D.36b: Plot of T vs. NRTL modelled parameters for system 1-hexene (1) + 3MCP (2)

D.4 Temperature Dependence of Thermodynamic Modelled Parameters- Direct Method i.e. Twu-Coon-PRSV

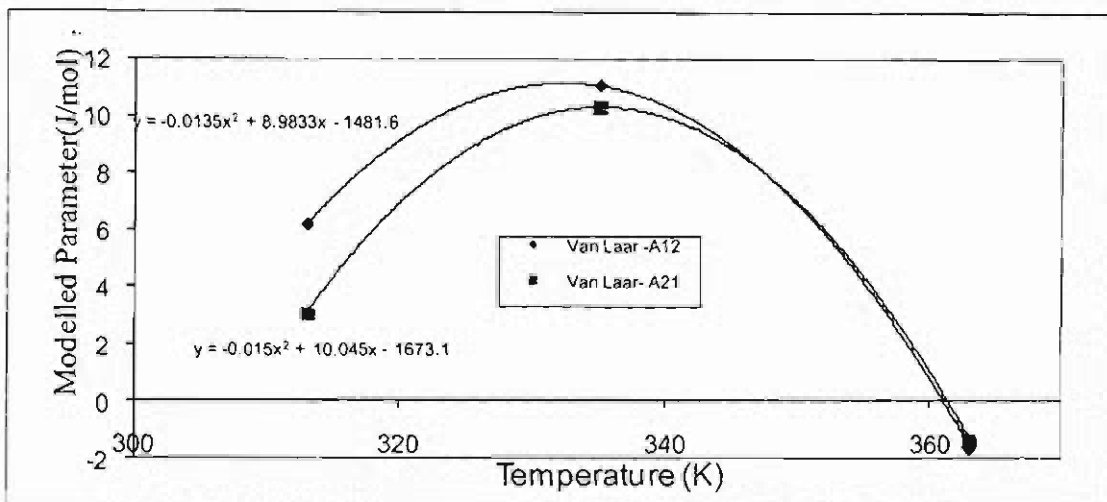


Figure D.37: Plot of T vs. Van Laar modelled parameters for system 1-hexene (1) + NMP (2)

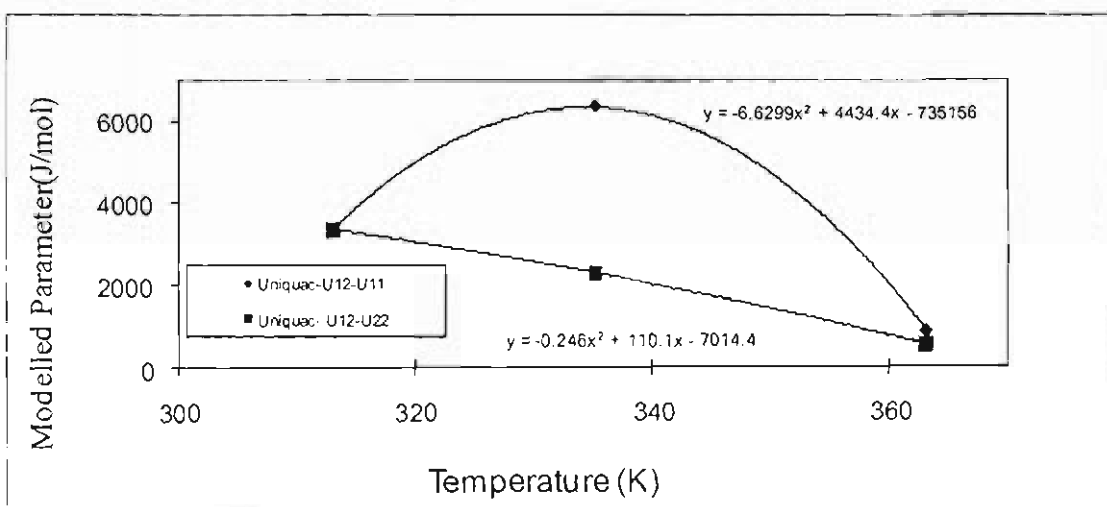


Figure D.38: Plot of T vs. Uniquac modelled parameters for system 1-hexene (1) + NMP (2)

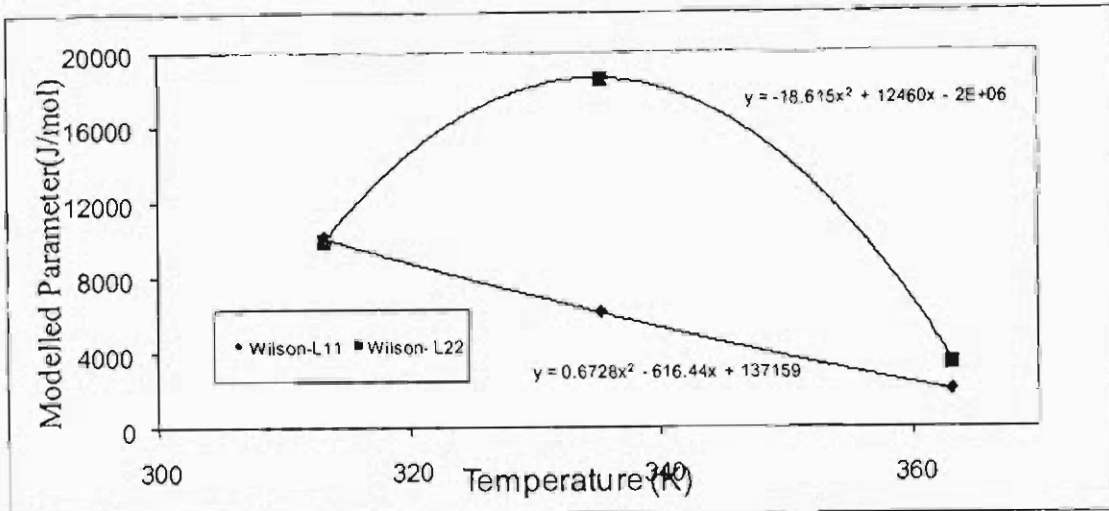


Figure D.39: Plot of T vs. Wilson modelled parameters for system 1-hexene (1) + NMP (2)

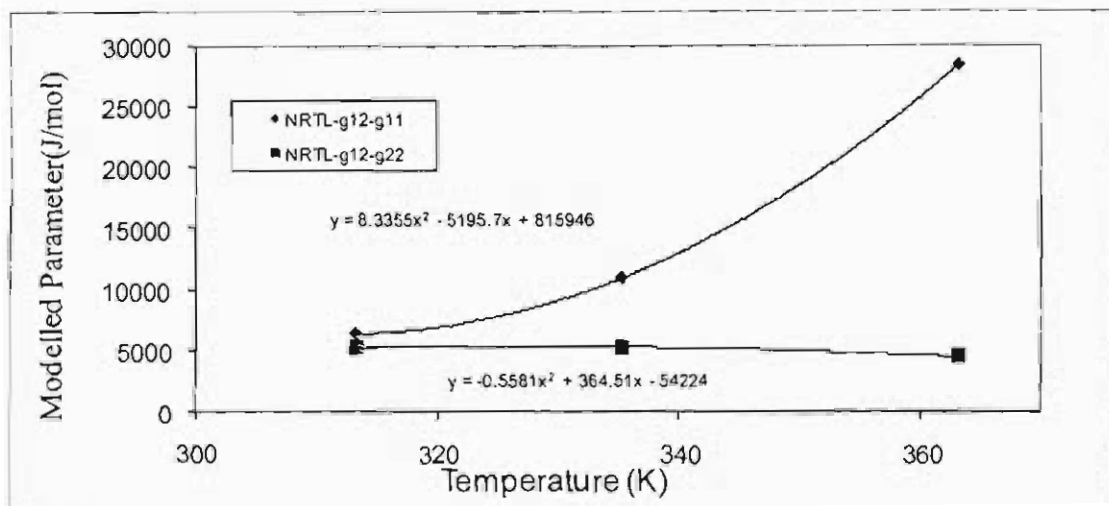


Figure D.40a: Plot of T vs. NRTL modelled parameters for system 1-hexene (1) + NMP (2)

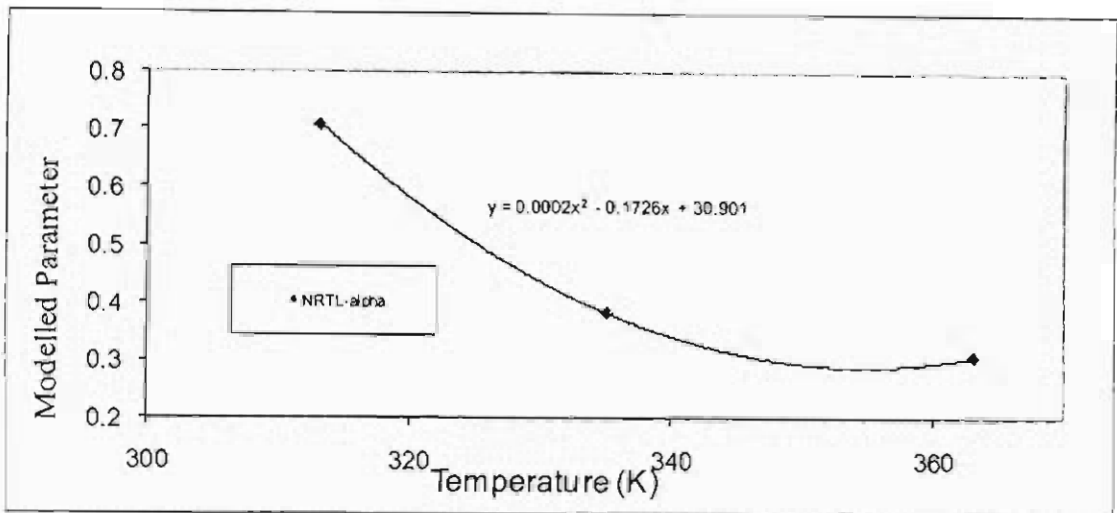


Figure D.40b: Plot of T vs. NRTL modelled parameters for system 1-hexene (1) + NMP (2)

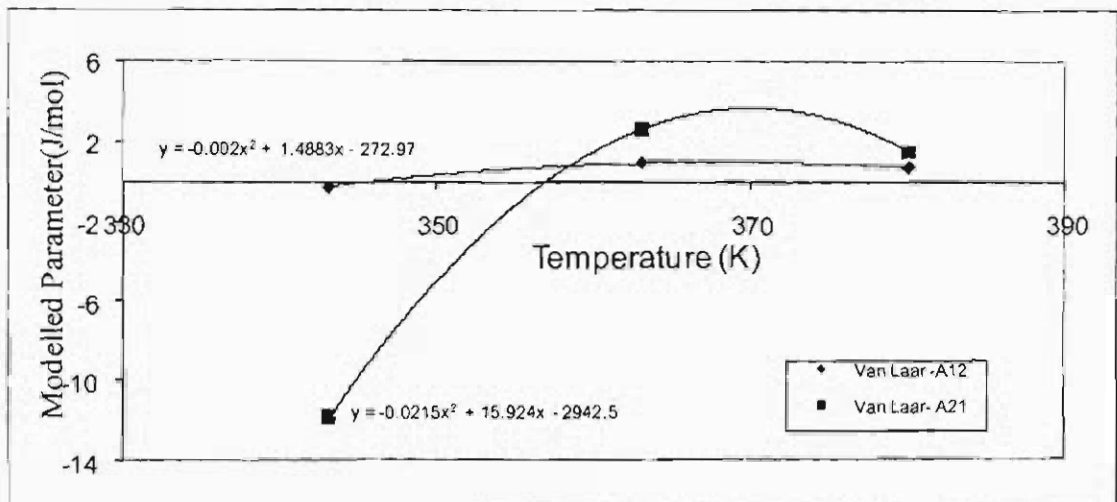


Figure D.41: Plot of T vs. Van Laar modelled parameters for system water (1) + NMP (2)

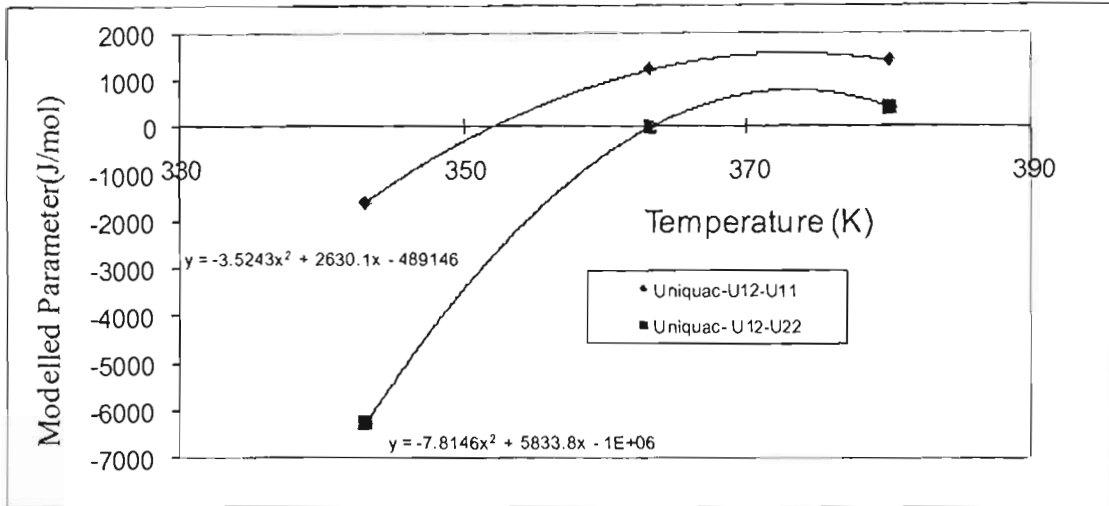


Figure D.42: Plot of T vs. Uniquac modelled parameters for system water (1) + NMP (2)

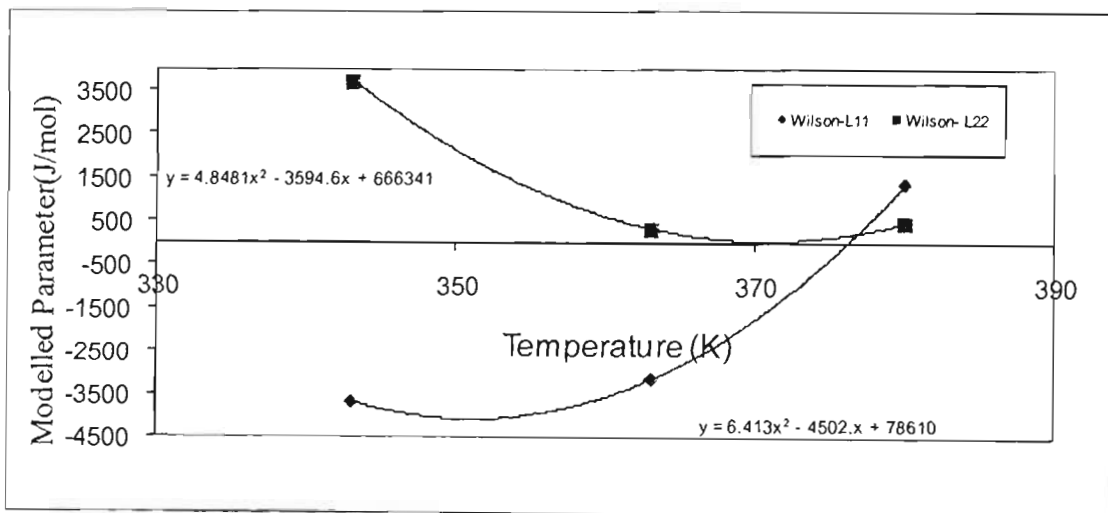


Figure D.43: Plot of T vs. Wilson modelled parameters for system water (1) + NMP (2)

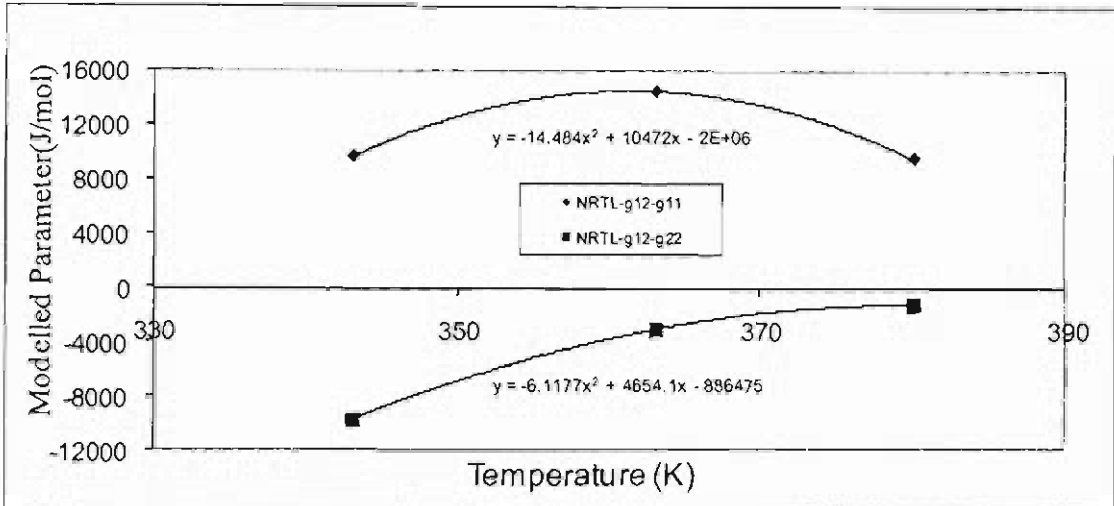


Figure D.44a: Plot of T vs. NRTL modelled parameters for system water (1) + NMP (2)

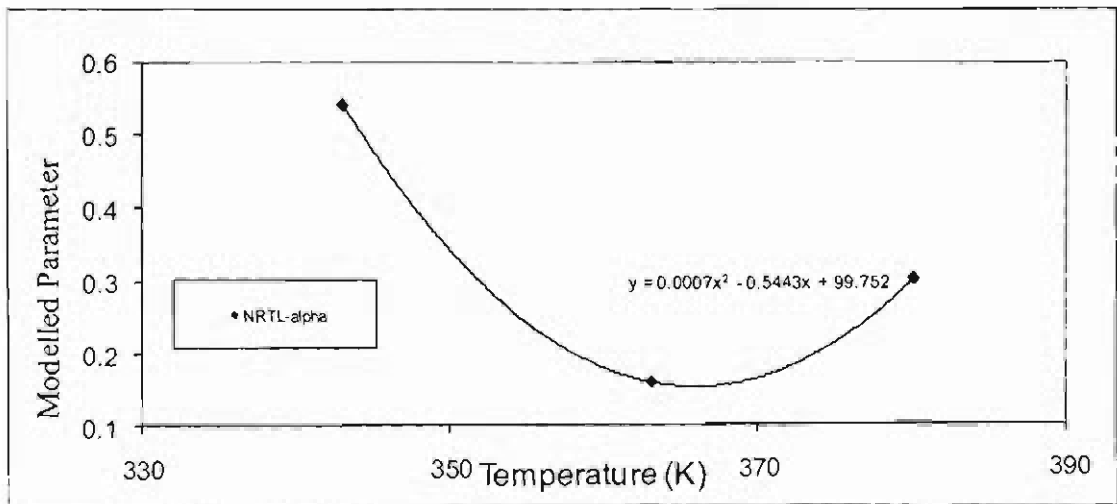


Figure D.44b: Plot of T vs. NRTL modelled parameters for system water (1) + NMP (2)

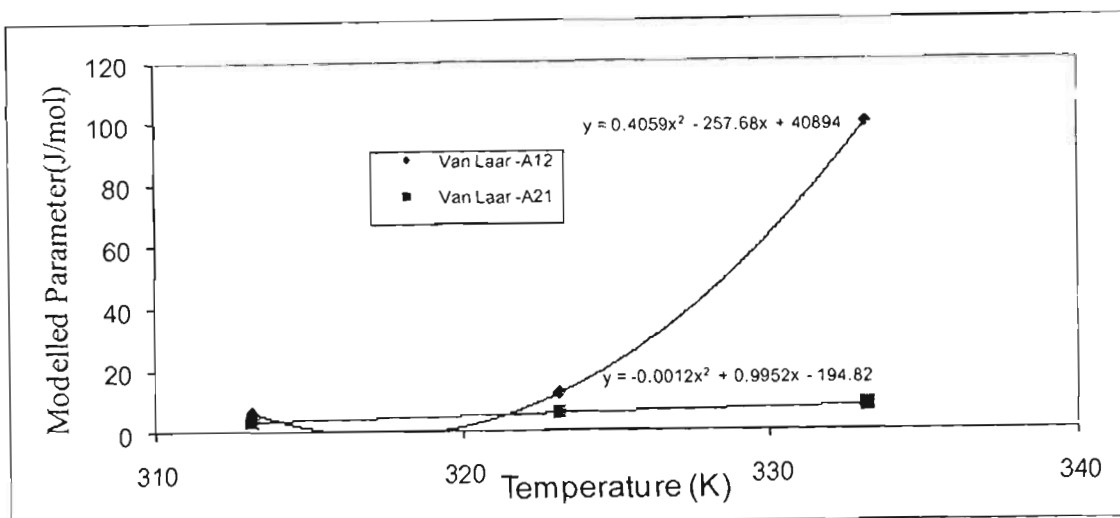


Figure D.45: Plot of T vs. Van Laar modelled parameters for system 1-hexene (1) + 3MCP (2)

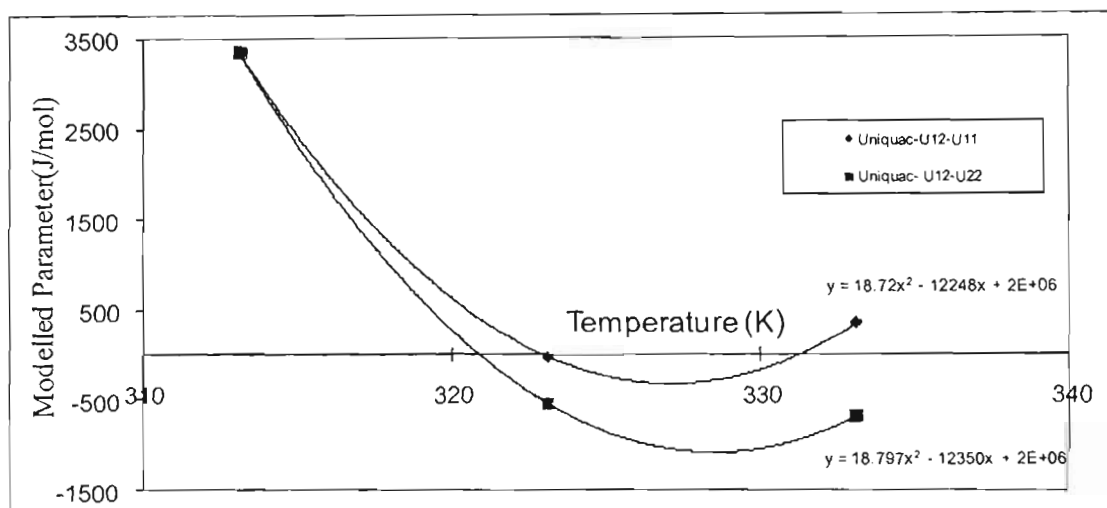


Figure D.46: Plot of T vs. Uniquac modelled parameters for system 1-hexene (1) + 3MCP (2)

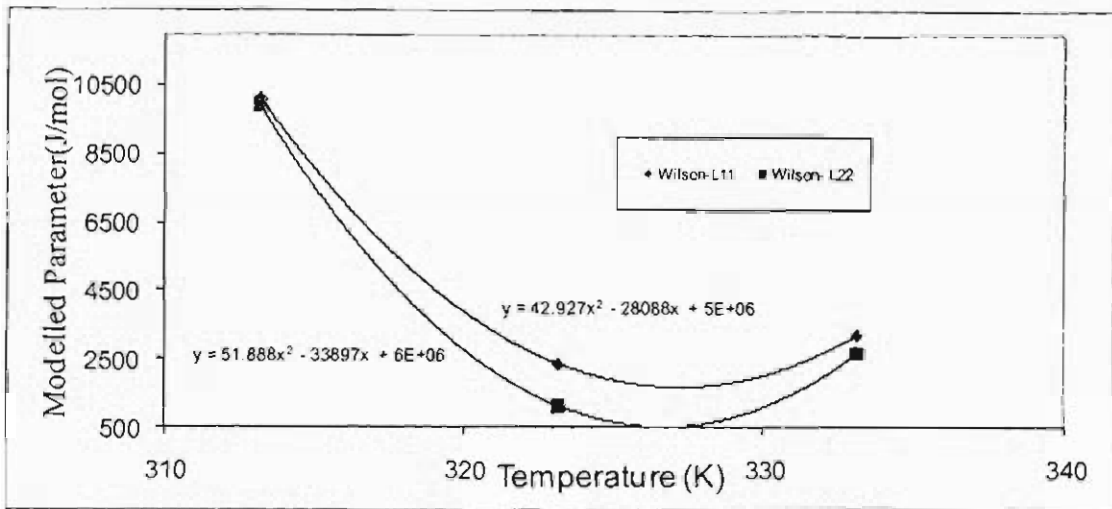


Figure D.47: Plot of T vs. Wilson modelled parameters for system 1-hexene (1) + 3MCP (2)

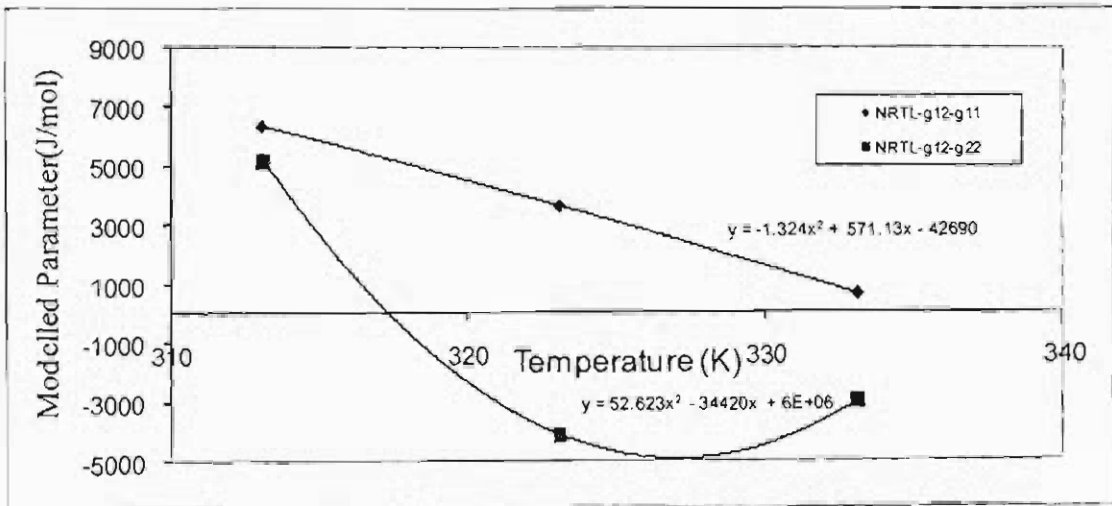


Figure D.48a: Plot of T vs. NRTL modelled parameters for system 1-hexene (1) + 3MCP

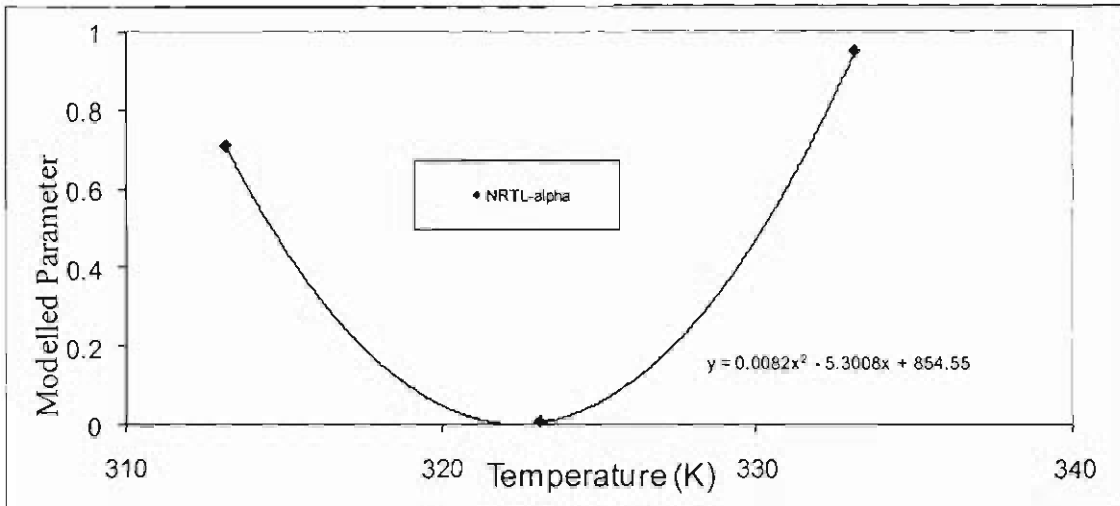


Figure D.48b: Plot of T vs. NRTL modelled parameters for system 1-hexene (1) + 3MCP (2)